THE STUDY OF MAGNETIC PROPERTIES AND MAGNETIC INTERACTIONS IN AMORPHOUS MAGNETIC MULTILAYER THIN FILMS

A thesis submitted

by

Camelia Das

to

Indian Institute of Technology Guwahati

in

Partial fulfillment of the requirement for the award of the degree of
Doctor of Philosophy in Physics

Department of Physics
Indian Institute of Technology Guwahati
Guwahati 781 039, Assam, India
May 2018

THE STUDY OF MAGNETIC PROPERTIES AND MAGNETIC INTERACTIONS IN AMORPHOUS MAGNETIC MULTILAYER THIN FILMS

A thesis submitted

by

Camelia Das

to

Indian Institute of Technology Guwahati

in

Partial fulfillment of the requirement for the award of the degree of
Doctor of Philosophy in Physics

Department of Physics
Indian Institute of Technology Guwahati
Guwahati 781 039, Assam, India
May 2018

STATEMENT

The work contained in the thesis entitled "***The study of magnetic properties and magnetic interactions in amorphous magnetic multilayer thin films***" has been carried out by me under the supervision of Prof. Perumal Alagarsamy at the Department of Physics, Indian Institute of Technology Guwahati. This work has not been submitted elsewhere for the award of any degree.

May 2018

(Camelia Das)
Roll No: 136121020
Department of Physics
Indian Institute of Technology Guwahati
Guwahati – 781039
India.

CERTIFICATE

It is certified that the work contained in the thesis entitled "***The study of magnetic properties and magnetic interactions in amorphous magnetic multilayer thin films***" submitted by Ms. Camelia Das (Roll No: 136121020), a Ph.D. student of the Department of Physics, Indian Institute of Technology Guwahati for the award of degree of Doctor of Philosophy has been carried out under the supervision of Prof. Perumal Alagarsamy. This work has not been submitted elsewhere for the award of any degree.

May 2018

(Dr. Perumal Alagarsamy)
Professor
Department of Physics
Indian Institute of Technology Guwahati
Guwahati – 781039
India.

Dedicated to

My beloved parents . . .

ACKNOWLEDGEMENTS

It is my privilege to express my deep sense of gratitude and profound regard to my thesis supervisor Prof. Perumal Alagarsamy for his patient guidance, insightful advice, tireless effort and careful supervision throughout my research work. His enthusiasm, constant encouragement and fruitful discussion helped me to understand the problem and had been a driving force for me to excel in my work. I am grateful to my doctoral committee members (Prof. D. Pal, Dr. S. Thota and Prof. S. Kanagaraj) for reviewing my research work regularly and providing useful remarks and invaluable suggestions for the improvement of my research work. I am thankful to Prof. Subhradip Ghosh, HOD Department of Physics, Prof. P. Poulose and Prof. S. Basu, the former HODs, Department of Physics for their immense supports.

I am very much thankful to Dr. Subhankar Bedanta, NISER Bhubaneswar, India and Dr. Jyoti Ranjan Mohanty, IIT Hyderabad, India for magnetic domain observation using Kerr microscope and MFM techniques.

I am grateful to Indian Institute of Technology Guwahati, and Government of India, Ministry of Human Resource Development for the financial support.

I express my sincere thanks to Dr. Sidananda Sarma, scientific officer in department of physics, for guiding me to operate various high precision instruments in department of physics. Also, I thank Mr. Chandan Borgohain, Dr. Kula Kamal Senapati and Mr. Kesho Singh, scientific officers of Central Instrument Facility, IIT Guwahati who have patiently and enthusiastically extended their expertise in handling various instruments that I have used for my research work.

I am fortunate to have seniors, Dr. Akhilesh Kr. Singh, Dr. P.C. Shyni, Mr. Bhagban Kisan, Dr. Bhargab Deka, Dr. R. Gopalrao, who helped me in various ways throughout my research work. Ravi bhaiya, Anabil da, Sambit, Jumal (late), Gobinda, Aneeta, Dolly, Sutanuka di, Aakansha, Rajkumar, Bibhuti bhaiya and Srinivas will always be remembered for the wonderful time we shared together. I am very much thankful to Jumal Das for his kind help and meaningful questions, which drove me to revise the work in various ways. I would like to thank all the members of our condensed matter group for the meaningful discussion on various topics, which has helped me a lot in understanding and carrying out the experiments in an easy and better way.

Special thanks to my hostel-mates Priya di, Mitali di, Richa di, Sanjukta, Trushna, Upasana, Sreya, Nandita and Bandita for making my stay easy and memorable from the very beginning at IITG. My adorable juniors, Dolly and Aakansha certainly deserve a special mention for their wonderful company and never ending support. All those wonderful and funny moments we shared together, will always be cherished. Eshita, Priyadarshini and Susmita, thanks for all your love and support. A big thanks to my best friend Subhadeep, for being so supportive all the time and helping me in various ways. Thank you all, for making my IITG life worth remembering.

I am deeply obligated to my beloved parents Bikash Ch. Das and Madhuri Das for their encouragement and moral support. Thanks dad, for being the best person in my life, my life mentor, friend, guardian and simply being there every time. My dear mom, there are not enough words, I can use to describe just how important you are to me and no one can ever replace you. Lots of love to my younger brother Antariksha Das for all decent criticism, love and support. You all are the wind beneath my wings. Without your unlimited motivation and support, it would not have been possible for me to complete my Ph.D work. Thanks to my dear boromasi and dadi, for all your love and blessings. Thanks for making me feel home with those surprise visits and the delicious foods. I sincerely thank all my family members for their love and encouragement.

I am thankful to my childhood buddies, especially Jhiki, Dibyashree and Nanda for their well wishes. I am thankful to my teachers for their kind blessings which motivated me to complete this voyage. Finally my sincere thanks are due to all those have been helped me in whatever manner and brought me to this position, some of whom I may have inadvertently forgotten to mention in this acknowledgement.

Camelia Das

PREFACE

A key trend in recent materials science and technology is the exploitation of fabrication of artificial materials which do not occur in nature and the phenomena occurring at length scales between 1 and 500 nm. One such important field has been that of magnetic multilayers where layers of magnetic materials are sandwiched between layers of non-magnetic materials. One of the most important milestones in the multilayers is the discovery of giant magnetoresistance in thin film structure, which finds application in hard disks, where the magnetoresistive read heads convert information stored in recording media by a small magnetic stray field into electrical signal with a high spatial resolution. Another notable achievement is the combination of tunnel magnetoresistance elements in read heads with perpendicular magnetic recording which steeply increases the storage density. Driven by technological applications, the study of thin films, interfaces, multilayer magnetism and magnetic interactions between layers is, in recent years, one of the most active research areas from both fundamental and applied research points of view. Another key advantage of artificial magnetic nanostructures is their ability to surpass the performance of naturally occurring magnetic compounds. Hence, the controlled growth and tailorable properties of such nanostructured multilayer films have become a very active field of research for the realization of futuristic magnetic devices. Recently, the technical committee of the IEEE Magnetics Society has selected seven research topics: 1) hard disk drives, 2) magnetic random access memories, 3) domain-wall devices, 4) permanent magnets, 5) sensors and actuators, 6) magnetic materials and 7) organic devices to develop their roadmaps. These developments are expected to be achieved not only by the development of these alloys but also by the fundamental understanding of the properties.

Among various magnetic thin films, Co based and Fe based amorphous thin films are found to be promising materials suitable for applications due to their tunable magnetic properties. In addition, amorphous thin films having excellent soft magnetic properties have gained a lot of interest after their successful implementation in tunnel junctions, as amorphous nature is usually free from pinning centers and leads to very smooth interface, which is ideal for subsequent growth of ultrathin interlayers. A careful literature review on these thin films reveals that the magnetic properties of the films are strongly dependent on film thickness, i.e., (i) films with thickness less than 7 nm exhibit a strong perpendicular

magnetic anisotropy. Hence, these films are proposed for magnetic tunnel junctions, magnetic random access memory, spin logic based devices, *etc*. The increase of film thickness above 7 nm and up to about 80 nm exhibits in-plane magnetic domains with magnetization oriented in the film plane. This allows them to be mainly used as flexible electronics, soft magnetic underlayers in perpendicular magnetic recording media, magnetic passives, energy transferring devices, magnetic flux amplifiers, magnetic recording heads, *etc*. On further increasing film thickness (> 80 nm), the stress quenched in the films overcomes the in-plane magnetic anisotropy and increases the degree of local disorder in the easy-axis of as-deposited films. This enhances the effective magnetic anisotropy and develops dense stripe domain with out-of-plane magnetic components in the as-deposited films. Therefore, thicker Co based and Fe based amorphous thin films become magnetically hard and display transcritical loop characterized by both in-plane and out-of-plane magnetization components.

Although thicker amorphous magnetic films are explored for various applications, the magnetic properties of the films degrade with increasing film thickness. Therefore, to obtain enhanced soft magnetic properties at higher film thickness, multilayer thin films having ferromagnetic layers separated by non-magnetic (metallic and non-metallic) layers are proposed. As the magnetic thin films are deposited sequentially with a fine non-magnetic spacer layers, magnetic interaction between ferromagnetic layers is rather unavoidable. One of the technological hurdles in multilayer films is to understand and control the interlayer magnetic coupling between ferromagnetic layers. Most of the earlier works on multilayer films have been focused from applications point of view at room temperature. Therefore, from the fundamental point of view, only limited studies have been reported to understand (i) the effect of spacer layers on the improvement of soft magnetic properties of multilayer thin films and (ii) their stability against the spacer layer thickness, number of spacer layers and the individual thicknesses of spacer layers and ferromagnetic layers and (iii) the effect of temperature on various types of magnetic coupling between ferromagnetic layers. The last one, especially as a function of temperature, is expected to produce multistep magnetization reversal behavior with different combination of switching in multilayer thin films. Furthermore, a comparison between multilayer thin films and single-layer thick films of equivalent thickness is very much essential to understand the advantage of multilayer films to improve the magnetic properties.

This motivated us to plan this thesis work on two different important amorphous magnetic thin films with the following objectives: (i) To study the effect of thickness on the

structural and magnetic properties of single-layer amorphous $Co_{40}Fe_{40}B_{20}$ (CoFeB) (x = 10 – 200 nm) and $Fe_{80}Ta_8C_{12}$ (FeTaC) (x = 5 – 100 nm) thin films over a wide range of thickness. (ii) To investigate the effect of number of spacer layers, spacer layer thickness and measurement temperature (T) on tuning the magnetic properties of films at higher thicknesses by utilizing the multilayer structures of [CoFeB (y nm)/Ta (z nm)]$_n$/CoFeB (y nm) and [FeTaC (y nm)/SiO_2 (z nm)]$_n$/FeTaC (y nm). (iii) To study the magnetic interaction between CoFeB films, exhibiting stripe domain magnetic structure, in stack structure of [CoFeB (100 nm)/Ta (z nm)]$_n$/CoFeB (100 nm) films with n = 0 – 4 and z = 0 – 1.5 as a function of n, z and T, and compare with the magnetic properties of single-layer CoFeB films of nearly equivalent thicknesses.

This thesis is organized as follows: **Chapter 1** presents a brief introduction to the content of the thesis along with a review of literatures relevant to the present thesis work. The motivation, aim and organization of the thesis work are also included in this chapter. **Chapter 2** covers the fundamental aspects and theoretical models including basics of magnetism, intrinsic properties of magnetic materials, magnetic anisotropy, magnetic domains and walls, interlayer magnetic coupling in multilayer films. In **chapter 3**, a short introduction of experimental methods and techniques used in this thesis work are described. These comprise the fabrication of samples and characterization tools. **Chapter 4** discusses thickness dependent magnetic properties of single-layer amorphous $Co_{40}Fe_{40}B_{20}$ (CoFeB) (x nm) films over a wide range of thickness from 10 to 200 nm at first and then tuning the magnetic properties of $Co_{40}Fe_{40}B_{20}$ films at higher thicknesses by utilizing multilayer structure of [CoFeB (y nm)/ Ta (z nm)]$_n$/ CoFeB (y nm) with a careful variation of thickness of CoFeB and Ta layers. The temperature dependent magnetic properties of CoFeB thin films in the temperature range between 30 and 650 K at different thicknesses are also examined in this chapter. **Chapter 5** focuses on the systematic investigation of the effects of number of spacer layer (n), spacer layer thickness (z) and T on the interlayer coupling between the CoFeB layers, exhibiting stripe domain magnetic structure, and their influences on the magnetic properties at room temperature and at the low temperature region (30 K – 300 K) in the stack structured [CoFeB (100 nm)/Ta (z nm)]$_n$/CoFeB (100 nm films with z = 0 - 1.5 and n = 0 - 4. In order to understand the modification in the magnetic properties of stack structured films, single-layer CoFeB films of nearly equivalent thickness are prepared and characterized for comparison. **Chapter 6** is meant for studying thickness dependent surface topography, magnetic properties and magnetic domain structures of single-layer amorphous $Fe_{80}Ta_8C_{12}$ (x nm) films with x = 5 – 100 nm and systematic investigations on

the effect of number of SiO_2 spacer layers (n), thickness of SiO_2 spacer layer (z), magnetic domains of FeTaC layers on the temperature dependent magnetization reversal behavior in multilayer films and their influences on the magnetic properties at room temperature and at lower temperatures (30 K – 300 K) in multilayer [FeTaC (y nm)/SiO_2 (z nm)]$_n$/FeTaC (y nm) films with y = 100/(n+1), n = 0 - 3 and z = 0 – 6. The summary of conclusions drawn from the thesis work along with a brief write-up about the future scope of research in these types of materials is presented in **Chapter 7**. References and list of publications, originated out of this thesis work and the publications from other collaborative research works, are listed at the end of the thesis.

CONTENTS

भारतीय प्रौद्योगिकी संस्थान गुवाहाटी
Indian Institute of Technology Guwahati

Chapter 1

Prologue

भारतीय प्रौद्योगिकी संस्थान गुवाहाटी
Indian Institute of Technology Guwahati

1.1. Introduction

A key trend in recent materials science and technology is the exploitation of fabrication of artificial materials which do not occur in nature and the phenomena occurring at length scales between 1 and 500 nm. One such important field has been that of magnetic multilayers where layers of magnetic materials are sandwiched between layers of non-magnetic materials [BENN1994, HART2000, NALW2002, DECH2012, HADJ2013, MORA2013, WEIS2013, MELE2015]. Such artificially structured multilayers have displayed a variety of magnetic, optical and electrical properties. Particularly in magnetism and related transport properties, one of the most important milestones in the multilayers is the discovery of giant magnetoresistance in thin film structure consisting of two ferromagnetic layers separated by a metallic non-magnetic spacer layer [BAIB1988, BINA1989, HART2000, REIG2013], which finds application in hard disks, where the magnetoresistive read heads convert information stored in recording media by a small magnetic stray field into electrical signal with a high spatial resolution [WOLF2001, PIRA2007, PIRA2011, MALL2012, HIRO2013]. Another important achievement is the combination of tunnel magnetoresistance elements in read heads with perpendicular recording which steeply increases the storage density [VILL2010, HIRO2015, SATO2015, FREI2016, TSYM2016, YOUC2017, ZHOU2017]. Magnetic random access memory, magnetic field sensors, lab-on-chip and reconfigurable magnetic logic are a few other examples of recent developments using multilayers [TANG2010, HEDI2013, IANN2014, LEON2014, DIEN2016, KURI2017, WANG2017].

Driven by technological applications, the study of thin films, interfaces, multilayer magnetism and magnetic interactions between layers is, in recent years, one of the most active research areas from both fundamental and applied research points of view. A number of differences with respect to potential technological important have been observed in the transport and magnetic properties of thin films and multilayers, as compared with bulk materials, and have been assigned to structural changes specific for systems with reduced dimension. In addition, from the fundamental point of view, such studies are also expected to provide an understanding of surface magnetism and transport phenomena, such as interlayer magnetic coupling [KORE2012, KRAV2012], dipolar interaction between ferromagnetic layers [HILL1993, MAJC2007], magnetostatic interaction induced by the interface roughness (topological coupling) [SHIZ1994, ZHAN19961], effects of thickness and number of spacer layers on structural and magnetic properties [HERN2008], disorder magnetic states, surface anisotropy, magneto-optical effect and different types of

magnetoresistance, *etc*. Another key advantage of artificial magnetic nanostructures is their ability to surpass the performance of naturally occurring magnetic compounds. Therefore, the controlled growth and tailorable properties of such nanostructured multilayer films have become a very active field of research for the realization of futuristic magnetic devices.

Recently, the technical committee of the IEEE Magnetics Society has selected seven research topics: 1) hard disk drives, 2) magnetic random access memories, 3) domain-wall devices, 4) permanent magnets, 5) sensors and actuators, 6) magnetic materials and 7) organic devices to develop their roadmaps, where major developments should be listed alongside expected timelines [HIRO2015]. Figure 1.01 displays the roadmap for magnetic materials to develop various nanoscale devices at room temperature. These developments are expected to be achieved not only by the development of these alloys but also by the fundamental understanding of the properties such that these materials can be implemented in futuristic magnetic devices within next two decades.

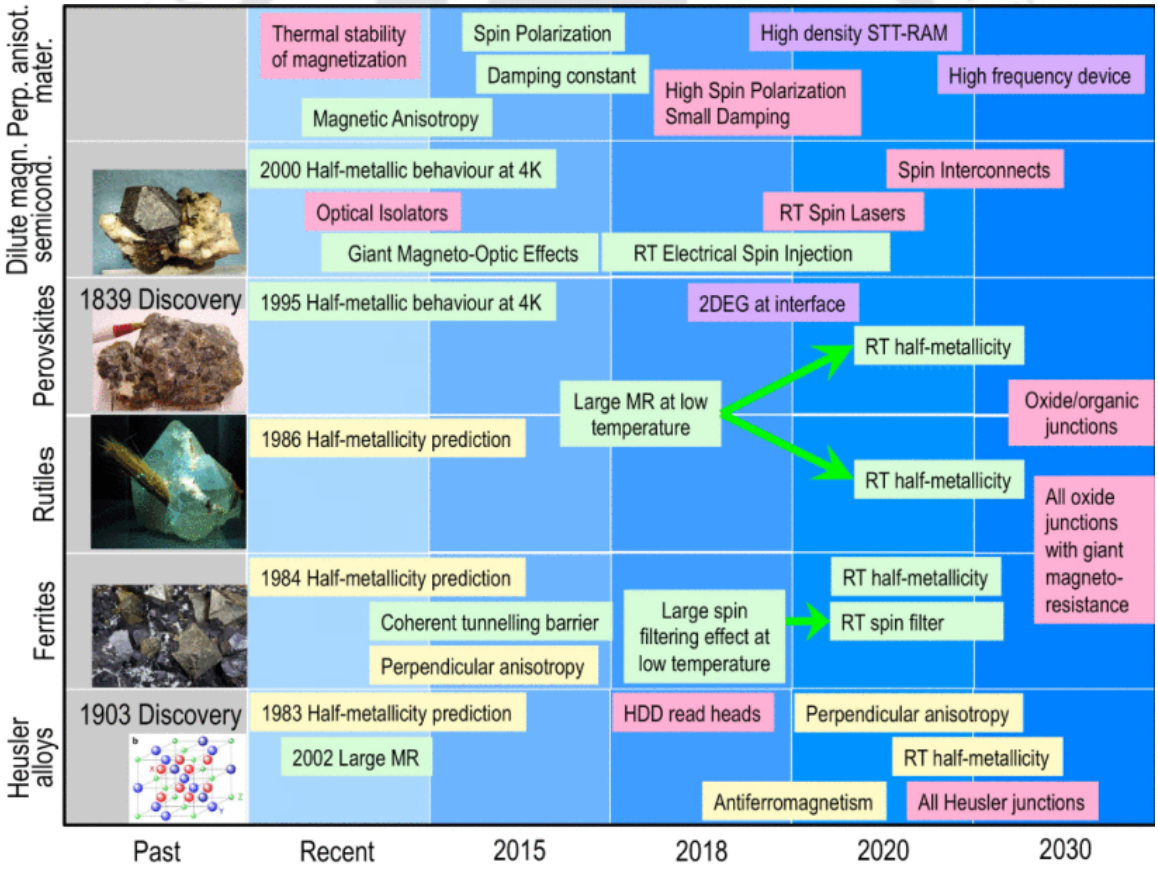

Figure 1.01: Roadmap for magnetic materials [HIRO2015].

1.2. Motivation behind the work

In order to obtain controllable magnetic properties suitable for various futuristic magnetic devices, it is very much essential to understand the correlation between the artificial

structure, microstructure and physical properties so that tunable magnetic domain structure with enhanced magnetic properties can be achieved in magnetic thin films. It may be noted that the equilibrium magnetic domain structure in magnetic thin films is governed by the competition of various energy terms (exchange, dipolar and anisotropy energies) and conversely the orientation of magnetization is determined by the effective anisotropy constant. To understand the correlation between structural and magnetic properties, extensive studies have been carried out since past two decades on various amorphous single-layer thin films such as FeCuNbSiB [NAOE1998, FUJI2006], FeAlSi [TATE1998], CoNbZr [HIRA2000], FeTa(C)N [WEIV2000, JIAN2005], FeTaC [TANA2002], Fe-Zr-N [CRAU2002], CoTaZr [LEED2006] and CoFeB [MUNA2005, GUER2007, HASH2007, HIND2011, KIPG2012, CUIB2013, KAZI2013, TANG2014, QIAO2016] and multilayer structured thin films of Fe/Ta and Fe:N/Ta:N [NAOE1996], Fe/Zr [CAST1997], FeCoTa:N/Ti [NAKA1997], FeCuNbSiB/Al [NAOE1998], Fe/Cu [OLIV1999], HITPERM/SiO_2 [HUAN2001, OKUM2003, OKUM2004] FeAlSi/C [NAKA2001], CoCrTa/Ru/CoTaZr and CoCrPt/Ru/CoFe [WUAY2002, JUNG2006], NiFe/IrMn/NiFe/CoTaZr [TANA20031], Fe(Ta,Ti,Nb)C/Ta [TANA20032, MISH2011, SING2013], CoTaZr/Ru/CoTaZr [ACHA2004], $[FeNi/SiO_2]_n$ [URSE2005], Nb/(Al,Pd,Cr)/Fe [NAVA2009], Fe/Al [BRAJ2010], $[CoPd]_4$/Au/$[CoPd]_2$ [LIUX2012], FeZr/AlZr [KORE2012], $[FeNi\text{-}O/SiO_2]_n$ [GENG2013], *etc*. Among various magnetic thin films, Co based and Fe based amorphous thin films are found to be promising materials suitable for applications in modern magneto-electronic devices due to their tunable magnetic properties. In addition, the amorphous nature of thin films having excellent soft magnetic properties has gained additional interest after their successful implementation in tunnel junctions, as amorphous nature of the films is usually free from pinning centers and leads to very smooth interface which is ideal for subsequent growth of ultrathin interlayers [DIMO2004, TEIX2006].

A careful literature review on these thin films reveals that the magnetic properties of the films are strongly dependent on film thickness, i.e., (i) films with thickness less than 7 nm exhibit a strong perpendicular magnetic anisotropy [IKED2010, MANT2013, WANG2014]. Hence, extensive studies have been carried out on these films to find their applicability in magnetic tunnel junctions, magnetic random access memory, spin logic based devices and various spin based applications [SONG2000, TEHR2000, PALU2006, UHRM2008, JIAN2009, IKED2010, LIUX20111, PARK2011, YAMA2011, ZHUY2012, MANT2013, ISHI2014, SATO2014, THOM2014, SULI2015, ZHAN2015, ZHAO2015,

CUCH2016, LIUY2016, VEMU2016, LEES2017, MAEK2017]. With increasing film thickness above 7 nm and up to about 80 nm, the perpendicular magnetic anisotropy observed in ultra-thin films transforms into in-plane magnetic anisotropy with magnetization oriented along the film plane [SATO1988, MAPP1991, NAOE1998, HUAN2001, NAKA2001, INGV2002, COIS2009, HIND2011, KIPG2012, SING2012, CUIB2013, TANG2014, QIAO2016, MASO2017]. The presence of such in-plane magnetic domains, high resistivity, high permeability, high saturation magnetization and appropriate anisotropy field in these films allows them to be mainly used as soft magnetic underlayers in perpendicular magnetic recording media, magnetic passives, energy transferring devices, magnetic flux amplifiers, magnetic recording heads, microwave integrated circuits, cores in high-frequency inductors, wireless inductors, microwave noise filters, electromagnetic wave absorbers, flexible electronics, *etc* [OKUM2003, OKUM2004, ITOS2005, MUNA2005, HASH2007, PIRA2007, PERU2010, PIRA2011, KAZI2013, YANG2013, TANG2014, QIAO2016, WUHA2017, SHEN2018]. On further increasing film thickness (≥ 100 nm), the effective magnetic anisotropy induced by the stress in the films overcomes the in-plane magnetic anisotropy and increases the degree of local disorder in the easy-axis of as-deposited films. This develops dense stripe domain with out-of-plane magnetic components in the as-deposited films [CRAU2002, CRAU2003, ITOS2005, SHAR2006, LIXW2007, COIS2009, PERU2009, MISH2011, SING2012, TANG2014, GAYE2017]. Therefore, thicker Fe based and Co based amorphous thin films become magnetically hard and display transcritical loop characterized by two magnetic components. Nevertheless, the majority of the reported works focused on studying the magnetic properties of the films at random thicknesses and compositions using different fabrication processes from the application point of view, while there are only limited reports or no systematic studies on the effects of film thickness over a wide range of thicknesses and measurement temperatures on the magnetic properties of thin films prepared by a single fabrication technique.

Although thicker amorphous magnetic films were explored for various applications, the magnetic properties of the films degrade with increasing film thickness due to the stress quenched in during the deposition of the films at a high deposition rate to form amorphous structure. In order to obtain enhanced soft magnetic properties at higher film thickness, multilayer thin films having ferromagnetic layers separated by non-magnetic (metallic and non-metallic) layers are proposed [NAKA1997, NAOE1998, HUAN2001, NAKA2001, OKUM2003, TANA20031, TANA20032, OKUM2004, URSE2005, KORE2012,

GENG2013, SING2013]. As the magnetic thin films are deposited sequentially with a fine non-magnetic spacer layers, the magnetic interaction between ferromagnetic layers is quite unavoidable. One of the technological hurdles in multilayer films is to understand and control the interlayer magnetic coupling between ferromagnetic layers, which originates in general from four different sources: (a) direct ferromagnetic coupling through pinholes in thin spacer layers [PONG2008], (b) indirect exchange coupling [KUDR1997, NIST2010], (c) orange peel (Néel) coupling due to correlated interfacial roughness [NEEL1954, NEEL1962, KOOL1999, ZHAN19961, ZHAN19962, CHOP2000, SCHR2000, TEGE2001, MORI2004], and (d) magnetostatic coupling either through magnetic poles at the edge of the films [CHOP2000, THOM2000, CHOP2005, BALT2007, STOB2009, LIUX2012] or through stray fields of domain walls [ANGU2000, CHOP2000, THOM2000, YUL2000, CHOP2005]. While most of the earlier works on multilayer films have been focused from applications point of view, there are only limited reports or no systematic studies have been reported from the fundamental point of view to understand (i) the effect of spacer layer on the improvement of soft magnetic properties of multilayer thin films and (ii) their stability against the spacer layer thickness, number of spacer layers and the individual thicknesses of spacer layer and ferromagnetic layers and (iii) the effect of temperature on various types of magnetic coupling between ferromagnetic layers. The last one, especially as a function of temperature, is expected to produce multistep magnetization reversal behavior with different combination of switching in multilayer thin films. Furthermore, a comparison between multilayer thin films and single-layer thick films of equivalent thickness is essential to understand the advantage of multilayer films to improve the magnetic properties. This motivated us to plan this thesis work on two different important amorphous magnetic thin films with the following objectives:

1.3. Objective of the thesis work

- To prepare single-layer amorphous $Co_{40}Fe_{40}B_{20}$ (CoFeB) (x = 10 – 200 nm) thin films directly on thermally oxidized Si substrates using magnetron sputtering technique at ambient temperature.
- To understand the effect of thickness on the structural and magnetic properties of amorphous CoFeB (x nm) films over a wide range of thicknesses at room temperature.
- To fabricate multilayer [CoFeB (y nm)/Ta (z nm)]$_n$/CoFeB (y nm) films with y = 200/(n+1), where n is the number of multilayers varied between 0 and 3, and z is the

spacer layer thickness controlled between 0 and 2 nm, on thermally oxidized Si substrates using magnetron sputtering technique at ambient temperature.

- To understand the effects of *n*, *z* and measurement temperature (*T*) on tuning the magnetic properties of films at higher thicknesses by utilizing above multilayer structure.
- To prepare stack structure of [CoFeB (100 nm)/Ta (*z* nm)]$_n$/CoFeB (100 nm) films with $n = 0 – 4$ and $z = 0 – 1.5$ on thermally oxidized Si substrates using magnetron sputtering technique at ambient temperature.
- To study the magnetic interaction between CoFeB films exhibiting stripe domain magnetic structure as a function of *n*, *z* and *T*, and compare with the magnetic properties of single-layer CoFeB films of nearly equivalent thickness.
- To prepare single-layer amorphous $Fe_{80}Ta_8C_{12}$ (FeTaC) ($x = 5 – 100$ nm) thin films on thermally oxidized Si substrate using magnetron sputtering technique at ambient temperature.
- To investigate the effect of thickness on the surface topography, magnetic properties and magnetic domain structure of amorphous FeTaC thin films.
- To fabricate multilayer [FeTaC (*y* nm)/SiO_2 (*z* nm)]$_n$/FeTaC (*y* nm) films with $y = 100/(n+1)$, $n = 0 - 3$ and $z = 0 – 6$ on thermally oxidized Si substrate using magnetron sputtering technique at ambient temperature.
- To study the effect of number of SiO_2 spacer layers (*n*), thickness of SiO_2 spacer layer (*z*), magnetic domains of FeTaC layers on the interlayer coupling between FeTaC layers and their influences on the magnetic properties at room temperature and at lower temperatures (30 K – 300 K) in multilayer [FeTaC (*y* nm)/SiO_2 (*z* nm)]$_n$/FeTaC (*y* nm) films.

This thesis is organized as follows: The **second chapter** covers the fundamental aspects and theoretical models including basics of magnetism, intrinsic properties of magnetic materials, magnetic anisotropy, magnetic domains and walls, interlayer magnetic coupling in multilayer films. In **chapter 3**, a short introduction of experimental methods and techniques used in this thesis is described. These comprise the fabrication of samples and characterization tools. **Chapter 4** discusses thickness dependent magnetic properties of single-layer amorphous $Co_{40}Fe_{40}B_{20}$ (CoFeB) (*x* nm) films over a wide range of thickness from 10 to 200 nm at first and then tuning magnetic properties of $Co_{40}Fe_{40}B_{20}$ films at higher thicknesses by utilizing multilayer structure of [CoFeB (*y* nm)/ Ta (*z*)]$_n$/ CoFeB (*y* nm) with

a careful variation of thickness of CoFeB and Ta layers. The temperature dependent magnetic properties of CoFeB thin films in the temperature range between 30 and 650 K at different thicknesses are also examined in this chapter. **Chapter 5** focuses on the systematic investigations of the effects of number of spacer layers (n), spacer layer thickness (z) and measurement temperature (T) on the interlayer coupling between the CoFeB layers, exhibiting stripe domain magnetic structure, and their influences on the magnetic properties at room temperature and at the low temperature region (30 K – 300 K) in the stack structured [CoFeB (100 nm)/Ta (z nm)]$_n$/CoFeB (100 nm films with z = 0 - 1.5 and n = 0 - 4. In order to understand the modification in the magnetic properties of stack structured films, single-layer CoFeB films of nearly equivalent thickness are prepared and characterized for comparison. **Chapter 6** is meant for studying thickness dependent surface topography, magnetic properties and magnetic domain structures of single-layer amorphous $Fe_{80}Ta_8C_{12}$ (x nm) films with x = 5 – 100 nm and systematic investigations on the effect of number of SiO_2 spacer layers (n), thickness of SiO_2 spacer layer (z), magnetic domains of FeTaC layers on the temperature dependent magnetization reversal behavior in multilayer films and their influences on the magnetic properties at room temperature and at lower temperatures (30 K – 300 K). The summary of conclusions drawn from the thesis work along with a brief write-up about the future scope of research in these types of materials is presented in **Chapter 7**. References and list of publications, originated out of this thesis work and the publications from other collaborative research works, are listed at the end of the thesis.

भारतीय प्रौद्योगिकी संस्थान गुवाहाटी
Indian Institute of Technology Guwahati

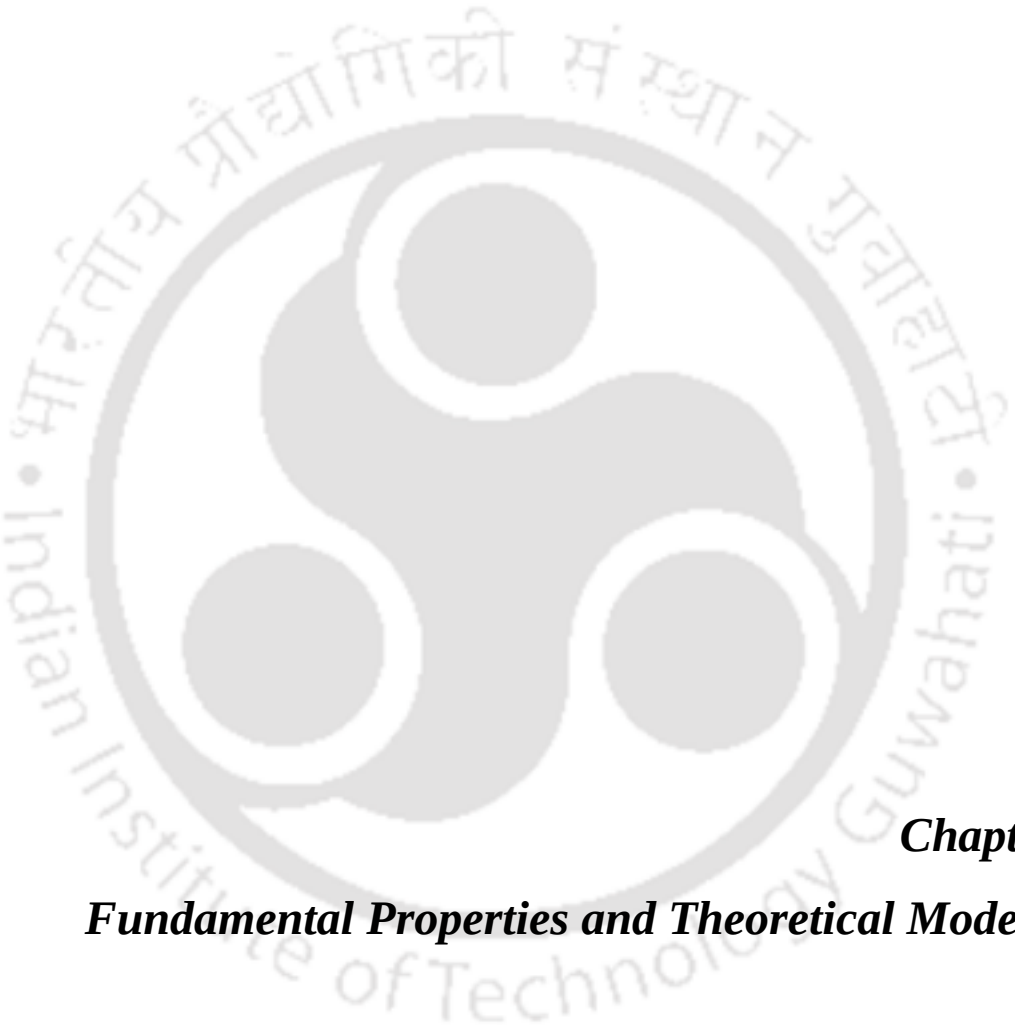

Chapter 2

Fundamental Properties and Theoretical Modeling

भारतीय प्रौद्योगिकी संस्थान गुवाहाटी
Indian Institute of Technology Guwahati

2.1. Introduction

Magnetism is the kind of phenomenon by which materials establish an attractive or repulsive force. Although the history of magnetism is known for thousands of years and coeval with the history of science, the underlying principles and mechanisms that explain the magnetic properties of the materials are still complex and mysterious. It is well-known that most of the modern technological devices such as flexible electronics, magnetic passives, energy transferring devices, magnetic flux amplifiers, magnetic recording heads, microwave integrated circuits, cores in high-frequency inductors, wireless inductors, microwave noise filters, electromagnetic wave absorbers, transformer, magnetic spin based devices, computers, and components of sound and video reproduction system rely on magnetism and magnetic materials. Recent endeavours to miniaturize magneto-electronic devices in order to reduce energy consumption and achieve higher speeds have generated a demand for new materials and methods for their production. Therefore, the understanding of development of magnetic properties in new materials, tuning their magnetic properties by thickness, composition and layered structure and optimization of the magnetic properties for different applications are very much essential. This chapter covers the fundamental properties of magnetism including basics of magnetism, intrinsic properties of magnetic materials, magnetic anisotropy, magnetic domains and walls and interlayer coupling in multilayer thin films.

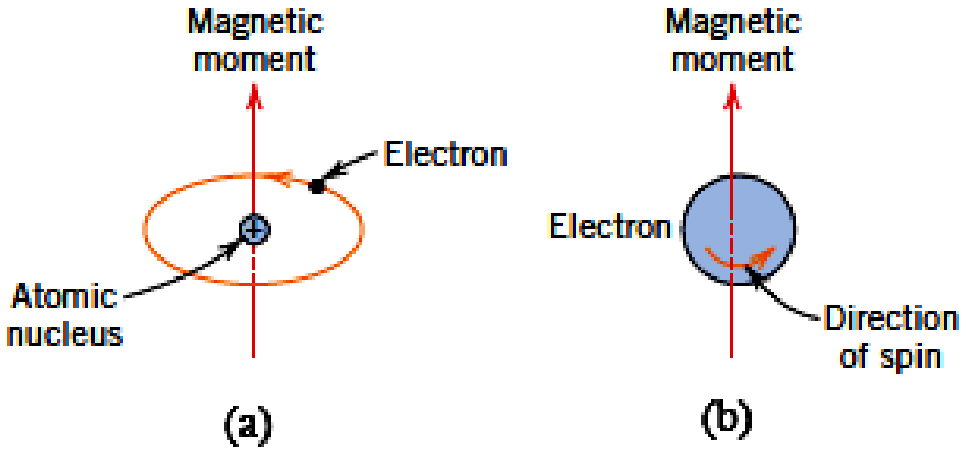

Figure 2.01: Demonstration of the magnetic moment associated with (a) an orbiting electron and (b) a spinning electron.

2.2. Origin of magnetism

The macroscopic magnetic properties of the materials are the consequences of magnetic moments associated with individual electrons [OHAN2000, KITT2004]. Each electron in an

atom has magnetic moments originating from two different sources as depicted in Figure 2.01: (a) One is orbital motion of the electron around the nucleus, which generates a magnetic field and having magnetic moment along the axis of rotation (see Figure 2.01a) and (b) Other magnetic moment originates from the electron spin, which is directed along the spin axis (see Figure 2.01b). This suggests that the each electron in an atom may be thought of as being a small magnet having permanent orbital and spin magnetic moments. It may be noted that the electrons in an atom are occupied according to the Pauli's exclusion principle and Hund's rule. Therefore, the net magnetic moment for an atom is the sum of the magnetic moments of each constituting electrons, including both orbital and spin contributions and taking into the account of moment cancellation. For an atom having completely filled electron shells or subshells, when all electrons are considered, there is a total cancellation of both the moments. Hence, the materials composed of atoms having completely filled electron shells are not capable of being permanently magnetized. Based on number of unpaired electrons in atom, their orientation in the orbitals and the spin-orbit interaction between the electron orbital angular momentum and spin angular momentum and their response in the external applied field, the materials are classified as diamagnetic, paramagnetic (PM), ferromagnetic (FM), antiferromagnetic (AFM) and ferrimagnetic (FiM) [KRON2003].

2.3. Diamagnetism

Diamagnetism is a fundamental property of the materials and it is a manifestation of Lenz's law, i.e., if one applies a field to a system of moving charges, then their motions change in such a way that they create a magnetization that opposes the original applied field [OHAN2000]. Such effect is present in all the materials, but is often masked by other types of magnetism. It generally occurs in materials having completely filled electronic configuration. The atoms and molecules of diamagnetic substances do not possess any net magnetic moments (i.e., all the orbital shells are filled and there is no unpaired electron). However, when exposed to a magnetic field, the electrons orient themselves such that they try to oppose the applied magnetic field and hence they register negative magnetization and negative susceptibility. Most of semiconducting material likes ZnO, SnO_2 *etc*. are diamagnetic in nature.

2.4. Paramagnetism

For some solid materials, each atom possesses a permanent dipole moment by virtue of incomplete cancellation of electron spin and/or orbital magnetic moments. The orientations of these atomic magnetic moments are random in the absence of an external magnetic field and

result no net macroscopic magnetization. However, these atomic dipoles are free to rotate and PM occurs when they preferentially align, by rotation, with an external field [KITT2004]. Some of the atoms or ions have a net magnetic moment due to unpaired electrons in partially filled orbital. However, the individual magnetic moments do not interact electrons magnetically. In the presence of an applied magnetic field, there is a partial alignment of atomic magnetic moments in the direction of the applied field. This leads to a net positive magnetization and hence positive susceptibility. Both diamagnetic and PM materials are generally considered to be non-magnetic because they exhibit magnetization only under the application of an external field. The tendency of alignment of magnetic moments along the field direction is opposed by the thermal energy, which tries to randomize the spin orientation. So they exhibit a temperature (T) dependent susceptibility, χ known as the Curie Law,

$$\chi = \frac{C}{T} \tag{2.01}$$

with a Curie constant C [BLUN2003]. In classical theory, each atomic moment is considered as magnetic dipole alignment in a particular direction with an angle θ with respect to applied field and average magnetic moment along the field direction, z is written as

$$< \mu^z > = \mu L(y) \tag{2.02}$$

Here, μ is the magnetic moment of each dipole and $L(y)$ is the Langevin function, $L(y)=\mathrm{Coth}(y)-1/y$ and $y = \mu_B/(k_B T)$. This function explains the magnetization of small particles made up of atomic clusters. For low applied field or at high temperature, such that y is small, $L(y)$ tends to $y/3$. So

$$< \mu^z > = \frac{\mu y}{3} = \frac{\mu^2 B}{3k_B T} \tag{2.03}$$

or the magnetization

$$M = N < \mu^z > = \frac{N\mu^2 B}{3k_B T} \tag{2.04}$$

So, the susceptibility

$$\chi = \frac{M}{H} = \frac{\mu^2 N \mu_0}{3k_B T} = \frac{C}{T} \tag{2.05}$$

and the Curie law is obtained by the classical theory. According to quantum mechanical treatment and by considering the quantization of total angular momentum of each atom, the average magnetic moment per atom aligned along the magnetic field direction (i.e., z direction) of any PM sample can be written as [JILE1997, BLUN2003].

$$< \mu_J{}^z > = g\mu_B J B_J(x) \qquad (2.06)$$

Here g is Landgé g-factor and it depends on spin-orbit coupling of electrons in each atom. J is the total angular momentum quantum number. $\mu_B = 9.27\times10^{-24}$ J/T is Bohr magnetron. $B_J(x)$ is Brillouin function, which can be written as,

$$B_J(x) = \frac{1}{J}\left[\left(J+\frac{1}{2}\right)Coth\left(J+\frac{1}{2}\right)x - \frac{1}{2}Coth\frac{x}{2}\right] \qquad (2.07)$$

Here, the variable $x = (g\mu_B B)/(k_B T)$, where k_B is the Boltzmann constant and T is the temperature. If N is the number of atoms per unit volume, the volume magnetization M can be written as,

$$M = N < \mu_J{}^z > = Ng\mu_B J B_J(x) \qquad (2.08)$$

For the selection of B and T such that x is small, $B_J(x) \sim [J(J+1)/3]x$. Such assumption holds true for PM sample in a wide temperature region and for low applied field. So

$$< \mu^z > = Ng\mu_B J\frac{(J+1)}{3}x = \frac{Ng^2\mu_B^2 B}{3kT}J(J+1) \qquad (2.09)$$

Or the susceptibility

$$\chi = \frac{\mu_0 N g^2 \mu_B^2}{3kT}J(J+1) \qquad (2.10)$$

It is in the form of Curie law, C/T. Thus the magnetic susceptibility based on Brillouin function expression reduces to Curie-law. The examples of PM materials are W, Ce, Al, Li, Mg, *etc.* with typical χ value of 6.8×10^{-5}, 5.1×10^{-5}, 2.2×10^{-5},1.4×10^{-5},1.2×10^{-5} respectively in SI units [BLUN2003].

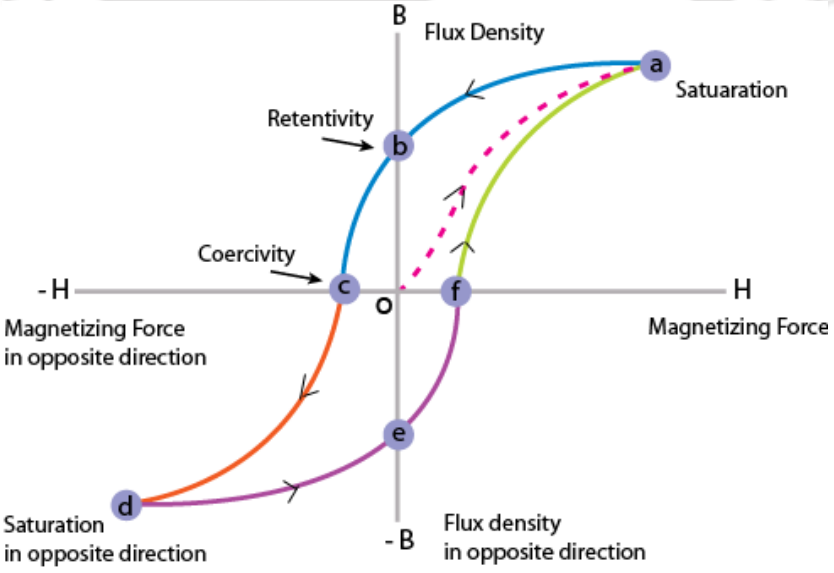

Figure 2.02: Magnetic hysteresis loop of a ferromagnetic material.

2.5. Ferromagnetism

Certain materials possess a permanent magnetic moment resulting from strong interaction between the magnetic moments even in the absence of an external field. This dominates over the thermal energy and reveals an alignment of magnetization in a particular direction. Such behaviors are displayed by the transition metals and some of the rare earth metals. In FM material, there are two distinct characteristics: (1) their spontaneous magnetization and (2) existence of magnetic ordering temperature. Spontaneous magnetization is the net magnetization that exists inside a uniformly magnetized microscopic volume even in the absence of external magnetic field. The atomic moments in FM materials align either a parallel or an antiparallel arrangement showing very strong interactions, which are produced by electronic exchange forces. As a result, a large net magnetization even after removing the external applied magnetic field exists in FM materials.

All FM materials exhibit magnetic hysteresis loop (*M-H* loop) under the application of magnetic field as displayed in Figure 2.02. By studying its hysteresis loop we can get information about the magnetic properties of a FM material. The loop is generated by measuring the magnetic flux of a FM material while the magnetizing field is changed continuously. FM materials in virgin states follow the dashed line (starting from the origin '*o*') as applied field is increased and reach the point '*a*' where almost all of the magnetic domains are aligned to field direction and an additional increase in the magnetizing field produces a very little or no increase in magnetic flux. The magnetization obtained at this point is called saturation magnetization (M_S). When the field is reduced to zero, the curve moves from point '*a*' to '*b*'. At this point, some magnetic flux remains in the material even at zero magnetic field. This is called as retentivity and indicates the remanence or level of residual magnetism in the material. As the magnetic field is reversed, the curve moves to point '*c*', where the magnetization reaches to zero. This point is called as coercivity (H_C) or coercive force. On further increasing the field in the negative direction, materials become magnetically saturated but in the opposite direction (point '*d*'). Reducing the field to zero brings the curve to point '*e*'. At this point, the level of residual magnetism is almost equal to that achieved in the other direction (point '*b*'). Increasing the field back in the positive direction returns the magnetization to zero. Subsequently, the curve takes a different path from point '*f*' back to the saturation point (point '*a*') and thereby completing the loop. From the *M-H* loop, the following magnetic parameters can be determined: (i) Retentivity: the material's ability to retain a certain amount of magnetization when the magnetizing field is removed after achieving saturation, (ii) Residual magnetism or Residual flux: The magnetic flux density that remains in a material

when the magnetic field is zero. Note that residual magnetism and retentivity are the same when the material has been magnetized to the saturation point. However, the level of residual magnetism may be lower than the retentivity value if the magnetic field did not reach the saturation level, (iii) Coercivity: The magnitude of reverse magnetic field required to make the magnetization zero; (iv) Permeability: A property of a material that describes the ease with which a magnetic flux is established in the component. These hysteresis parameters are not solely intrinsic properties but dependent on various parameters such as grain size, domain state, internal stresses and temperature. Since the hysteresis parameters are dependent on grain size, they are useful for magnetic grain sizing of natural samples. The elements Fe, Ni, and Co and their alloys are typical examples of FM materials. FM materials are mainly divided into two groups (see Figure 2.03): (a) hard FM materials exhibiting very high H_C (> 80 kA/m) are mainly used as permanent magnets and media for data storage and (b) soft FM materials with low H_C (< 8 kA/m) are used for transformer core, read head and magnetic sensor applications.

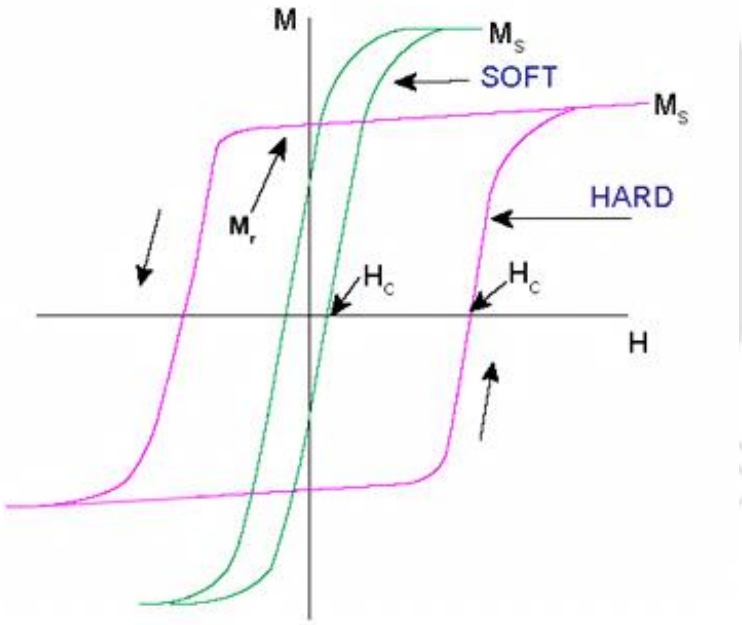

Figure 2.03: Typical magnetic hysteresis loops of soft and hard ferromagnetic materials.

Another important parameter is the magnetic induction [$B = \mu_0 (H + M)$, where μ_0 is the permeability of free space], which is the total flux of magnetic field lines through a unit cross sectional area of the material. From the initial magnetization curve, the initial magnetic permeability μ_I (= B/H), for very small applied magnetic field and maximum permeability μ_{max} [= $(B/H)_{max}$] can be obtained. These parameters indicate the amount of induction generated by the material in a given magnetic field and are useful in characterizing magnetic materials. μ_I

and H_C have a reciprocal relationship. So, materials exhibiting low H_C necessarily have a high μ_I. When increasing temperature, a transition from FM state to PM state occurs at a temperature called Curie temperature (T_C) that is due to thermal energy eventually overcomes the exchange energy and produces a randomizing effect leading to PM. The phenomenon of FM can often be described by mean field or molecular field model. The molecular field model simply assumes that all the interactions from the neighboring magnetic species can be described in terms of an effective internal or molecular field B_m, which is proportional to magnetization ($B_m = \lambda M$, where λ is Weiss molecular field constant). So total magnetic field experienced by each dipole is sum of B and B_m. Therefore, the expression for magnetization can be re-written by following eqn.(2.08) as

$$M = \frac{Ng^2\mu_B^2 J(J+1)}{3kT}(B_a + \lambda M) \qquad (2.11)$$

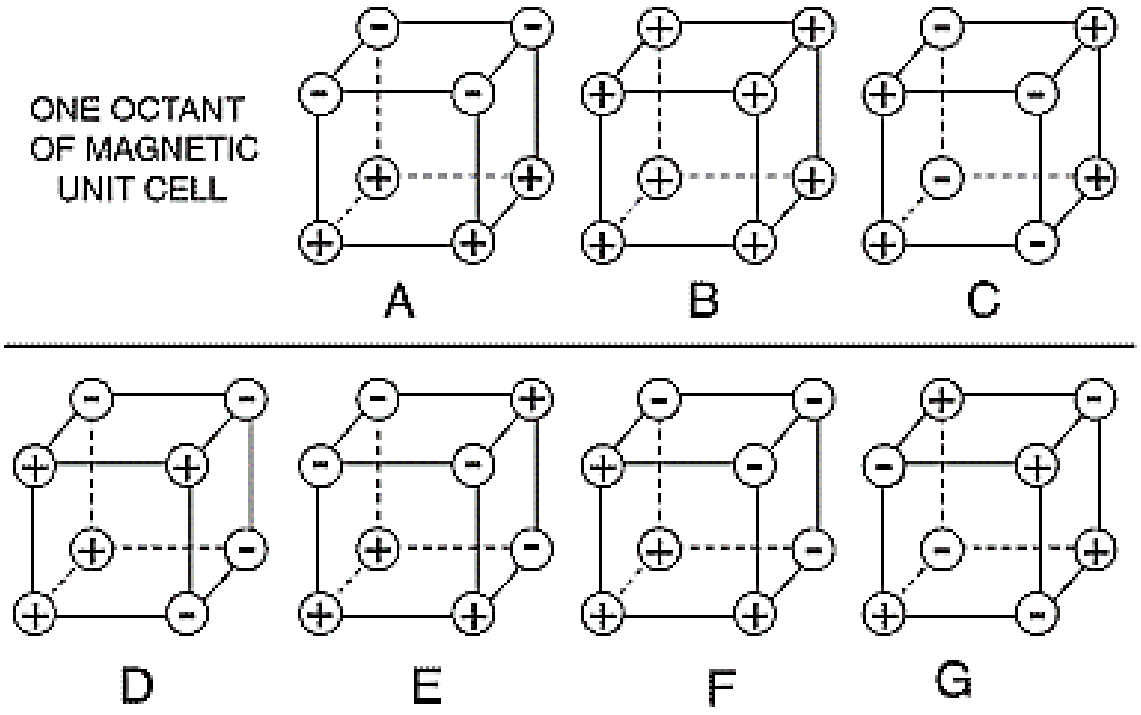

Figure 2.04: Different types of antiferromagnetic arrangement in a unit cell.

2.6. Antiferromagnetism

In AFM materials, the spins of electrons align in a regular pattern with neighboring spins pointing in opposite directions, below a certain temperature called Néel temperature (T_N). Above T_N, the material is typically PM. The magnetic susceptibility of AFM material will appear to go through a maximum as the temperature is lowered. The AFM ordering is possible

based on different type of magnetic unit cell structure as shown in Figure 2.04 except for *B* type, which is a FM one. In *A* type structure, the magnetic ions are coupled ferromagnetically in each (001) plane but with alternate planes aligned in opposite spin orientation such that they exhibit net AFM interaction. *B* type structure is a FM one with all six nearest neighbor magnetic ions coupled ferromagnetically. In *C* type structure, the atoms in (101) and (110) planes are ferromagnetically aligned. Each atom has two ferro and four AFM nearest neighbors such that there is net AFM unit cell. In *G* type structure, each ion is coupled antiferromagnetically to all its six nearest neighbors. Hence the atoms of positive and negative number of FM and AFM bonds are shown in Figure 2.04. Some of the materials follow a structure which is a result of coupling of two types of magnetic structures. One such example is *CE* type, where there is coherent stacking of octants of *C* and *E* type structures. The examples of AFM materials are MnF_2, MnO, CoO, FeO, Cr_2O_3 and α-Fe_2O_3 with T_N of 67 K, 116 K, 292 K, 116 K, 307 K, and 950 K with T_C of -80 K, -510 K, -330 K, -610 K, -485 K and -2000 K respectively [BLUN2003].

2.7. Intrinsic properties of magnetic materials

Intrinsic properties of FM materials are M_S, T_C and magnetocrystalline anisotropy (MCA). These properties describe the equilibrium properties of the material on the atomic scale.

2.7.1. Exchange Interaction

Weiss (1907) reported that in addition to any externally applied field *H*, there is an internal molecular field or exchange field in a FM proportional to its magnetization.

$$\overrightarrow{B_E} = \lambda \vec{M} \qquad (2.12)$$

where, λ is a temperature independent constant. According to eqn.(2.12), each spin sees the average magnetization of all the other spins. This molecular field is not really a magnetic field and therefore does not enter into the Maxwell equations. For example, there is no current density $\vec{j}$ related to $\overrightarrow{B_E}$ by $\vec{\nabla} \times \vec{H} = 4\pi\vec{j}/c$. The magnitude of the molecular field may be as high as 1000 Tesla. Now the question is what is the origin of such huge internal molecular field? For instance, the magnetic field at distance *r* due to a magnetic dipole of dipole moment *m* is [KITT2004],

$$\overrightarrow{B_{dip}} = \left(\frac{\mu_0 M}{4\pi r^3}\right)[2cos\theta\overrightarrow{e_r} + sin\theta\overrightarrow{e_\theta}] \qquad (2.13)$$

The order of magnitude of B_{dip} (= $\mu_0 H_{dip}$) is $\mu_0 M/4\pi r^3$ and taking m = 1 μ_B and r = 0.1 nm provides $B_{dip} \approx$ 1 Tesla or 10 kG only. This reveals that the huge molecular field is not due to the magnetic dipole interaction. This lingered as a mystery until Heisenberg introduced the concept of exchange interaction in 1928 [HEIS1928]. The origin of the Heisenberg exchange interaction is electrostatic, but the explanation involves quantum mechanics. The charge distribution of a system of two spins depends on whether the spins are parallel or antiparallel. Pauli's exclusion principle dismisses that no two identical electrons occupy the same quantum state simultaneously. However, it does not exclude two electrons of opposite spin. Therefore, the electrostatic energy of a system depends on the relative orientation of the spins: the difference in energy defines the exchange energy. The energy of interaction between the atoms i and j bearing electron spins S_i and S_j is defined from the Heisenberg model as [OHAN2000],

$$E_{exch} = -2\sum_{i<j} J_{ij} S_i . S_j \qquad (2.14)$$

where, J_{ij} is the exchange integral and is related to the overlap of the charge distribution of the atoms i and j. Assuming that the exchange interaction is the same for each nearest-neighbor pair, eqn.(2.14) turns out to be

$$E_{exch} = -2J\sum_{i<j}^{nn} S_i . S_j \qquad (2.15)$$

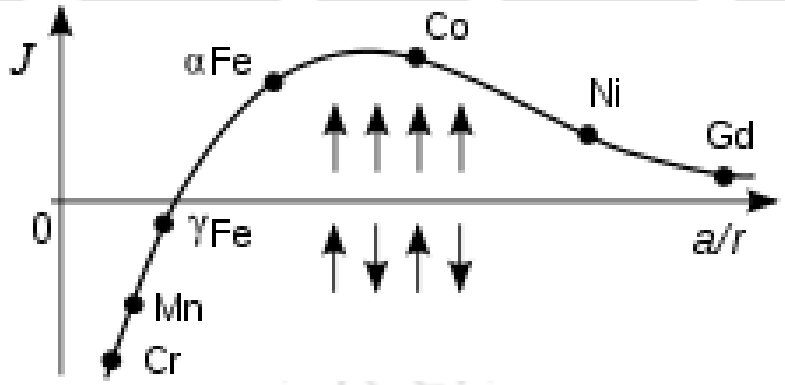

Figure 2.05: Bethe-Slater curve: Elements above (below) the horizontal axis are ferromagnetic (antiferromagnetic).

For parallel orientation of the magnetization (ferromagnet), J should be positive and for antiparallel alignment of spins, J should be negative. The variation of J as a function of the ratio of inter-atomic distance 'a' to the radius of 3d orbital 'r' is shown in Figure 2.05. This curve is also known as the Bethe-Slater curve. It is clear from the Figure 2.05 that the value of J and hence the short-range exchange interaction depends strongly on the inter-atomic distance.

The eqn.(2.15) can further be simplified by considering the energy of a particular atom *i* interacting with its *j* nearest neighbor:

$$E_{exch}^{i} = -2JS_i \sum_j S_j \tag{2.16}$$

while for the entire material,

$$E_{exch} = -\frac{1}{2}\sum_j E_{exch}^{i} \tag{2.17}$$

Thus, the discrete, pairwise interaction can be replaced by assuming that the magnetic moment $\mu_m^i = g\mu_B S_i$ at site *i* interacts with a molecular field. H_{eff} given by the net effect of the *z* nearest neighbor spins:

$$E_{exch}^{i} = -\mu_0 \mu_m^i H_{eff} = -g\mu_0\mu_B S_i H_{eff} \tag{2.18}$$

where, μ_0 is the permeability of the free space (= $4\pi\times10^{-7}$ H/m or 1.256×10^{-6} H/m). Comparing eqn.(2.18) with eqn.(2.16) provides the effective field as,

$$H_{eff} = \frac{2J}{g\mu_0\mu_B}\sum_j S_j \cong \frac{2zJ}{g\mu_0\mu_B}\langle S_j\rangle \tag{2.19}$$

Here, the sum over *z* neighboring spins has been replaced by *z* times the average spin value $\langle Sj\rangle$. Using $M = N_v g\mu_B\langle S_j\rangle$, eqn.(2.19) gives,

$$H_{eff} \cong \frac{2zJ}{N_v g^2 {\mu_B}^2 \mu_0} M \tag{2.20}$$

From eqn.(2.20), it can be seen that H_{eff} is the Weiss molecular field defined as $H_{mol} = \lambda$M, provided

$$\lambda = \frac{2zJ}{N_v g^2 {\mu_B}^2 \mu_0} \tag{2.21}$$

Using the value of molecular field coefficient λ as 10^3, *J* is calculated to be 2×10^{-21} J or 0.01 eV/atom. Exchange interactions are weaker than the Coulomb interactions that distinguish levels of different principal and orbital quantum numbers, but stronger than spin-orbit interaction. Following the treatment of Weiss molecular field that $T_C = \lambda C$ with $C = N_v {\mu_m}^2 \mu_0 / 3k_B$, the expression for T_C can be obtained from eqn.(2.21) as

$$T_C = \frac{2zJ{\mu_m}^2}{g^2{\mu_B}^2 3k_B} = \frac{2zJs(s+1)}{3k_B} \tag{2.22}$$

where, $\mu_m = \sqrt{g\mu_B s(s+1)}$. Another important relation between exchange energy and the magnetization is defined as,

$$\frac{E_{exch}^{ij}}{V} = \frac{s^2 a^2 J N_v'}{2}\left(\frac{\nabla M}{M}\right)^2 = A\left(\frac{\nabla M}{M}\right)^2 \qquad (2.23)$$

where, a is the distance between the spins, A is called the exchange stiffness constant having 10 - 20×10^{-12} J/m for most FMs, and N_v' is number of nearest neighbor atoms per unit volume. Therefore, it is clear from the above equations that the exchange energy or the Heisenberg exchange interaction depends strongly on temperature due to the dependence of interatomic distance on temperature. In particular, the disorder FM system is the subject of low T_C due to the low value of J.

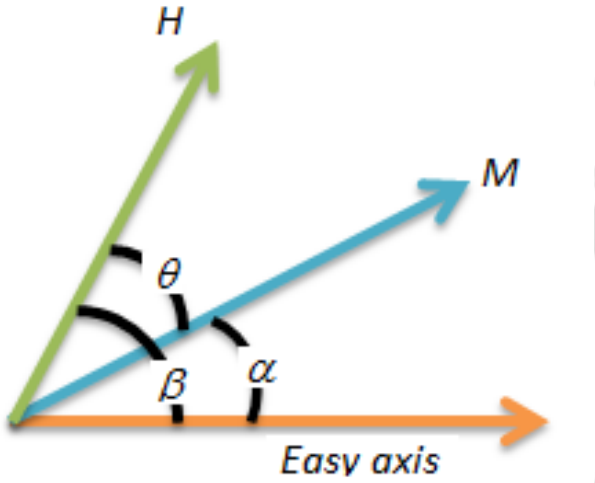

Figure 2.06: Schematic diagram of magnetization, applied field, and easy axis for a given material.

2.8. Anisotropy

When a physical property of a materials depends on the measurement direction of the samples that property is said to exhibit anisotropy. In magnetism, the preference of magnetization to lie in a particular direction of the sample is called as magnetic anisotropy. As anisotropy plays an important role in tuning the nature of *M–H* loop, it is much essential to understand the various possible sources of the magnetic anisotropy and its influence on the control of the magnetic properties. Figure 2.06 displays a typical situation where for zero applied field, the magnetization would point along the easy axis shown (α = 0). When a field is applied, the magnetization is pulled towards the field direction and approaches closer to the field direction with increasing the applied field. For any intermediate values of α, the magnetization is being attracted in opposite directions, i.e., up by the field and down by the anisotropy.

Let us assume that all the magnetization is pointing in the same direction in a magnetic material and the material exhibits an easy axis of magnetization. In such scenario, we can describe the energy per unit volume of the magnetization of this material by

$$E = K\,sin^2\alpha \tag{2.24}$$

where, K is called anisotropy constant with the units of energy per unit volume (J/m^3). Hence, the energy term, E, is also energy per unit volume. In general, the magnitude of uniaxial anisotropy is described in terms of the anisotropy field, which is defined as the field needed to saturate the magnetization of a uniaxial crystal in the hard axis direction, as given in eqn.(2.25)

$$H_k = \frac{2K}{\mu_0 M} \tag{2.25}$$

In general, the energy of the magnetization is given by,

$$E = K\,sin^2\alpha - \mu_0 MH\,cos(\beta - \alpha) \tag{2.26}$$

where, the first term is anisotropy energy. The second term is due to the magnetic field and the difference in the angle (β - α) is the angle between ***H*** and ***M***. In order to get equilibrium, we required first derivative to be zero.

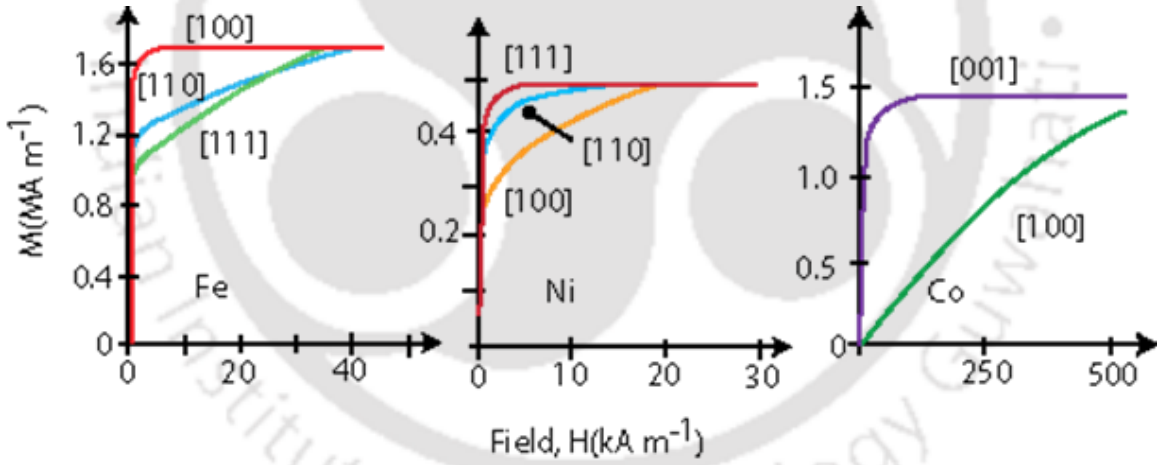

Figure 2.07: Magnetization of single crystals of Iron, Nickel and Cobalt.

Therefore, taking derivative of eqn.(2.26) with respect to the angle results,

$$\frac{dE}{d\alpha} = 2K \sin\alpha \cos\alpha - \mu_0 MH\,sin(\beta - \alpha) = 0 \tag{2.27}$$

Taking the value of β as 90^o for the equilibrium angle for the magnetization relative to the easy axis and considering the eqn.(2.25) gives

$$\sin\alpha = \frac{H}{H_k} \tag{2.28}$$

The above eqn. indicates that when field is zero, the magnetization points along the easy axis and when the field is equal to H_k, the magnetization points along the direction of field. For any intermediate value of the applied field, the magnetization points at a value of angle given by eqn.(2.28) rotating smoothly between the easy axis and the applied field.

2.8.1. Magnetocrystalline anisotropy

Figure 2.07 depicts initial magnetization curves of single crystals of different 3*d* FM elements. It is seen that the materials approach to saturation in different ways when magnetized in different directions. For example, iron displays a ⟨100⟩ as easy directions and ⟨111⟩ as hard directions, while nickel exhibits ⟨111⟩ as easy axis and ⟨100⟩ as hard directions. This behaviour can be understood by analyzing the development of anisotropy energy in different symmetries as given below:

For Hexagonal:

$$E_a = K_1 \sin^2\theta + K_2 \sin^4\theta + K_3 \sin^6\theta + K_3' \sin^6\theta \sin 6\phi \tag{2.29}$$

For Tetragonal:

$$E_a = K_1 \sin^2\theta + K_2 \sin^4\theta + K_2' \sin^4\theta \cos 4\phi + K_3 \sin^6\theta + K_3' \sin^6\theta \sin 6\phi \tag{2.30}$$

For Cubic:

$$E_a = K_{1c}(\alpha_1^2\alpha_2^2 + \alpha_2^2\alpha_3^2 + \alpha_3^2\alpha_1^2) + K_{2c}(\alpha_1^2\alpha_2^2\alpha_3^2) \tag{2.31}$$

where, α_i are the direction cosines of the magnetization. K_{1c} term is equivalent to $K_{1c}(\sin^2\theta\, cos^2\phi \sin^2\phi + \cos^2\theta \sin^2\theta)$. When, $\theta = 0$, $\phi = 0$, this term reduces to eqn.(2.24) [COEY2010].

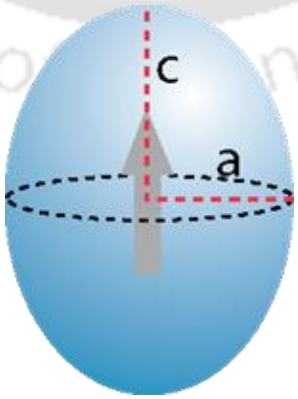

Figure 2.09: Magnetization of a prolate ellipsoid of revolution with $c > a$ and no magnetocrystalline anisotropy. *c*-axis is the easy direction of magnetization.

2.8.2. Shape anisotropy

Shape anisotropy arising due to the asymmetric shape of the material is important for thin films where one dimension is limited as compared to other two dimensions. The demagnetization field inside the material or the stray field outside the magnetic material depends on the magnetization and shape of the material [JILE1997, OHAN2000, BLUN2001]. The magnetostatic energy of a FM ellipsoid (see Figure 2.08) with magnetization M_S is given as

$$E_m = \frac{1}{2}\mu_0 V N M_S^2 \tag{2.32}$$

The anisotropy energy is related to the difference in energy ΔE when the ellipsoid is magnetized along its hard and easy directions. N is the demagnetization factor tensor for the easy direction. $N'=(1/2)(1-N)$ is the demagnetization factor tensor for the hard directions. Hence,

$$\Delta E_m = \frac{1}{2}\mu_0 V M_S^2 \left[\frac{1}{2}(1-N) - N\right]$$

$$\Delta E_m = \frac{1}{4}\mu_0 V M_S^2 [1-3N]$$

$$K_{sh} = \frac{1}{4}\mu_0 M_S^2 [1-3N] \tag{2.33}$$

In addition, the demagnetization factor tensor that relates the demagnetization field with a specimen magnetization as a function of position is given by [NEAL1994]

$$N(r) = -\frac{1}{4\pi}\iiint d^3r' \nabla' \left(\nabla' \left(\frac{1}{r-r'}\right)\right) \tag{2.34}$$

Table 2.01: Demagnetization factors (in Gaussian units) of selected shapes:

Shape	N_1	N_2	N_3
*Sphere	4π/3	4π/3	4π/3
Long Cylinder along z-axis	2π	2π	0
Infinite plate normal to *z*-axis	0	0	4π
Strip film normal to *z*-axis	0	8*t*/*W*	4π
(with *t* – thickness, *W* – Width, *L* – Length; $t \le W \le L$)			

*The shape anisotropy is zero for a sphere, as $N = 1/3$. Shape anisotropy is fully effective in samples which are so small that they do not break up into domains [COEY2010].

This tensor is given by an integral over the object volume and can be evaluated either inside or exterior to the body. The value of tensor *N* significantly depends on the specimen shape, which is difficult to obtain in closed-form. It may be calculated exactly for an ellipsoidal shape only. In many symmetrical objects such as any ellipsoids of revolution, the demagnetization factor tensor only has three principal components, i.e.,

$$\begin{pmatrix} H_1 \\ H_2 \\ H_3 \end{pmatrix} = -\begin{pmatrix} N_1 & 0 & 0 \\ 0 & N_2 & 0 \\ 0 & 0 & N_3 \end{pmatrix}\begin{pmatrix} M_1 \\ M_2 \\ M_3 \end{pmatrix} \qquad (2.35)$$

where, $N_1 + N_2 + N_3 = 1$ (in SI) and $N_1 + N_2 + N_3 = 4\pi$ (Gaussian). The demagnetization factors for the selected shapes are summarized in Table 2.01. A detailed calculation of demagnetization factor for various objects can be found in [NEAL1994].

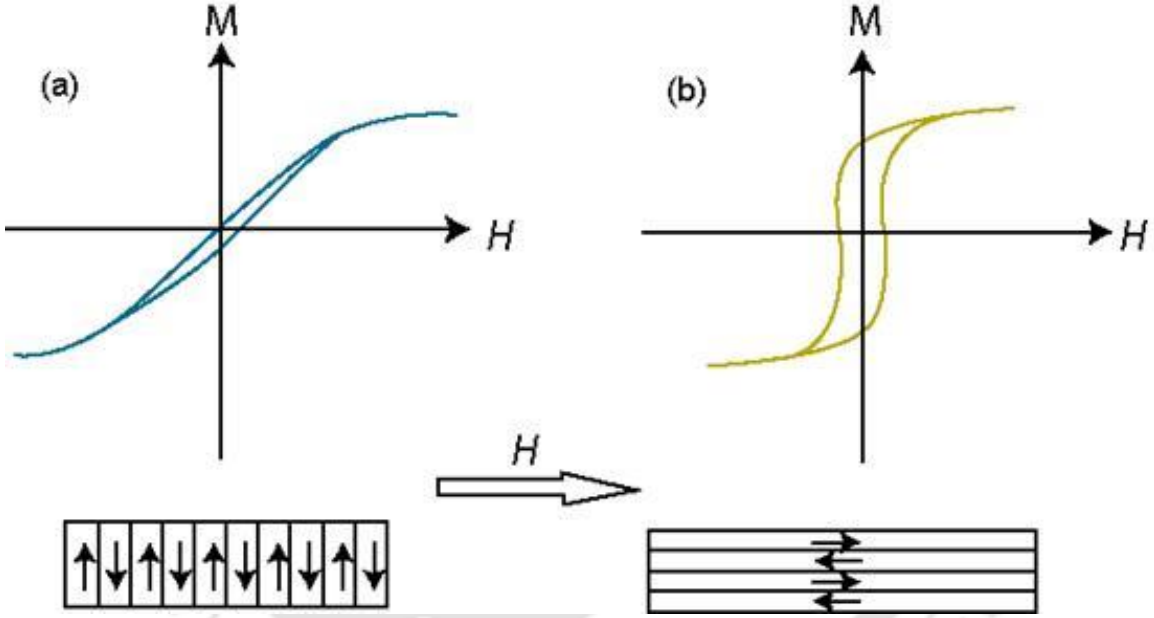

Figure 2.09: Magnetization of a thin film with induced anisotropy created by annealing in a magnetic field. The sheared (open) loop in a (b) is observed when the measuring field *H* is applied perpendicular (parallel) to the annealing field direction.

2.8.3. Induced anisotropy

In some materials, the magnetic anisotropy can be induced by many ways: (i) fabricating a film in the presence of a magnetic field, (ii) post annealing the materials in the presence of external applied magnetic field and (iii) apply uniaxial stress. In the first two cases, after such treatment, the material may exhibit an easy axis of magnetization that points in the direction of the magnetic field. This induced anisotropy is certainly independent of any crystalline anisotropy

or any other form of anisotropy that might be present. Figure 2.09 shows the typical example of inducing the anisotropy in FM materials by field annealing.

In the last case, the uniaxial anisotropy is induced by applying uniaxial stress (σ) in a FM solid [KRON2003]. The magnitude of the stress-induced anisotropy is

$$K_{u\sigma} = \frac{3}{2}\sigma\lambda_S \tag{2.36}$$

where, λ_S is the saturation magnetostriction. Both the single-ion and two-ion anisotropy contribute to the stress induced anisotropy. The highest values of uniaxial anisotropy are found in hexagonal and other uniaxial crystals. Smallest values are found in cubic alloys and amorphous FMs.

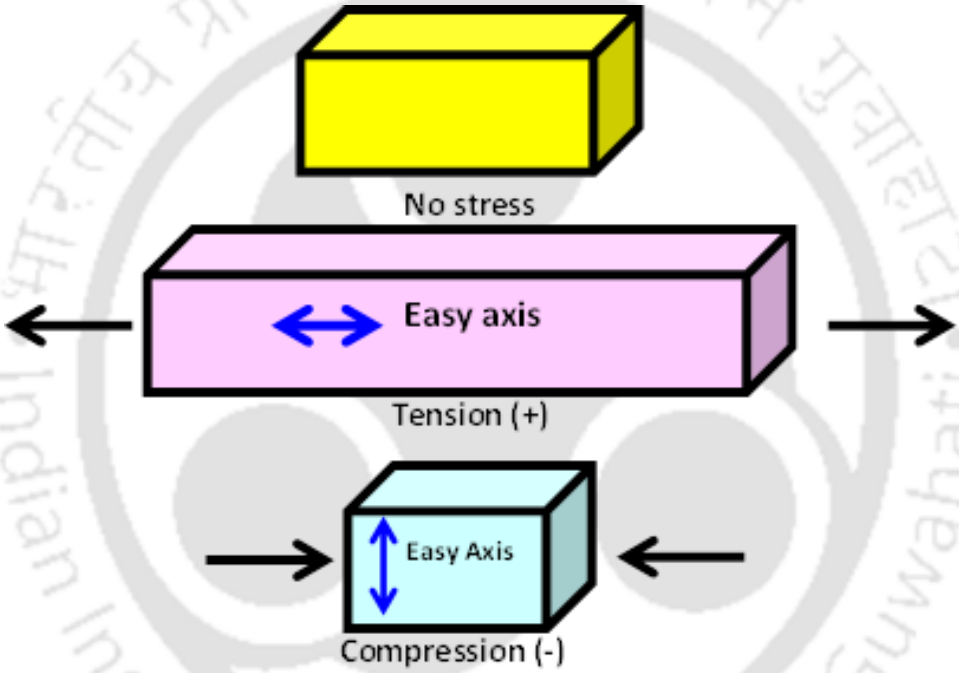

Figure 2.10: Schematic drawing of bars to demonstrate inducing an easy-axis in a material with the positive magnetostriction.

2.8.4. Magnetostrictive anisotropy

Another important form of anisotropy in magnetic materials is due to magnetostriction, a change of volume of an isotropic crystal due to magnetic order. Magnetostriction relates the stress in a magnetic material to an anisotropy created by that stress. Figure 2.10 shows schematic views of bars with different applied stress conditions. If λ is positive, then application of a tensile stress to the bar creates an easy axis in the direction of the applied stress. If a compressive stress is applied, then the direction of the easy axis created will be perpendicular to the stress direction. On the other hand, if the magnetostriction constant for the

material is negative, then the above phenomena would be reversed: a tensile stress will create an easy axis perpendicular to the stress direction and a compressive stress will create an easy axis in the direction of the applied stress.

2.8.5. Magnetic surface anisotropy

The orientation of magnetic moments in the ultrathin film strongly affects the magnetic properties and hence attracts enormous interest in magnetic based random access memory and recording industry since past decades [PAND2016, IKHT2018]. It has been reported that in ultrathin films, magnetic moments orient along perpendicular direction of the film plane up to certain critical thickness due to the magnetic surface anisotropy, which has the following origins: a) the lack of the neighbours or reduced symmetry at the interface gives rise to magnetocrystalline surface anisotropy [NEEL1954], b) strain at the interface due to the lattice mismatch between the substrate and the film and c) the interface roughness. The direction of magnetization in the ultrathin films is determined by the competition between shape (or dipolar anisotropy) and the magnetic surface anisotropy, i.e., when the thickness of the films is below the critical thickness, the surface anisotropy dominates over the shape anisotropy. On the other hand, the shape anisotropy dominates over the surface anisotropy above critical thickness resulting in an in-plane orientation of the magnetization [PESC1987, GARR2005, YILD20091, YILD20092, HIND2011]. Critical thickness and the easy direction of uniaxial surface anisotropy depend strongly on the deposition conditions, nature of substrate, temperature, materials and microstructure of the film [BRUN1989]. For example, the magnetization of Ni [111] ultrathin films deposited in Au/Ni/Au [111] multilayers always lies within the plane of films [BRUN1989]. On the other hand, the easy axis of magnetic surface anisotropy of *bcc* Fe [100] grown on Ag [100] is normal to the film plane [HEIN1987, KOON1987]. Hexagonal closed packed (HCP) Co deposited at room temperature on atomically flat polycrystalline Au [111] and covered by Au exhibits perpendicular magnetization for thicknesses less than 12 Å (6 ML) [CHAP1988]. Recently, CoFeB films show strong thickness dependent magnetic properties due to various anisotropy contributions including surface and interfacial anisotropies [NAIK2012, LIUT2012].

2.9. Magnetic domains and domain walls

Magnetic domains are the regions inside a FM material that are magnetized in different directions so that the net magnetization is nearly zero. The walls separating one domain from another are called as domain walls. There are different types of domain walls, i.e., 90°, 180°,

and 360° domain walls [ZHAN2016] as shown in Figure 2.11. The main cause of formation of magnetic domains and domain walls is to reduce the magnetostatic energy of a finite and uniformly magnetized sample.

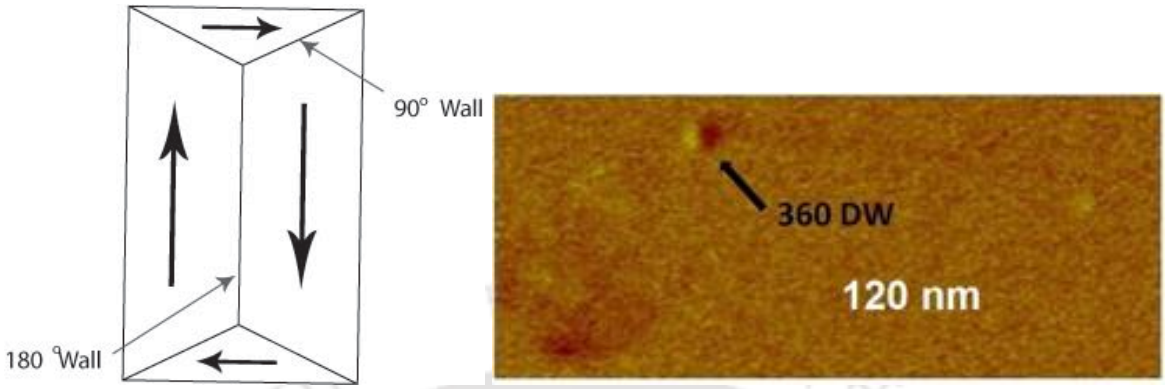

Figure 2.11: Schematic of 90°, 180° domain walls inside any FM material and simulation of a 360° [ZHAN2016] domain walls inside a Co arc of 10 nm thick and 120 nm wide.

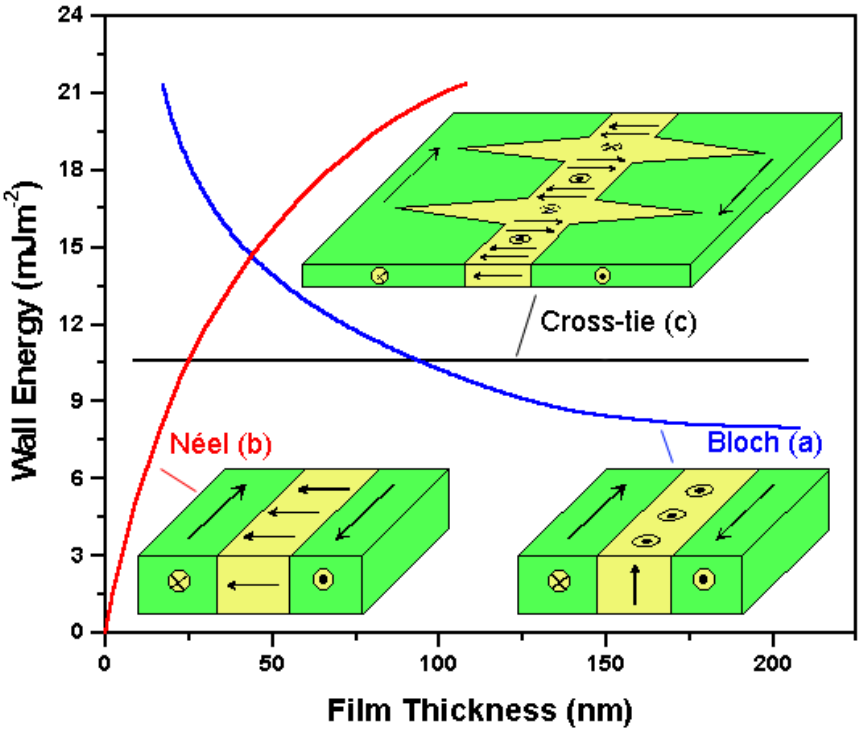

Figure 2.12: Comparison of domain wall energies for a (a) Bloch, (b) Néel and (c) Cross-tie wall for a permalloy film as a function of film thickness [PRUT1964] and illustrative diagrams of the respective domain wall spin configuration.

The size of the domain and domain wall, and orientation of magnetization within the domain and domain walls are determined by the minimization of the total energy of the system. This energy includes exchange anisotropy, magnetocrystalline anisotropy, magnetostatic energy,

magnetoelastic energy and domain wall energy [OHAN2000]. The width of a domain wall is dependent upon the exchange energy which prefers the magnetization to rotate slowly from one orientation to the other leading to wide walls, whereas the anisotropy and demagnetizing energies prefer the magnetization to switch immediately to the opposite direction and therefore result narrow walls. The thickness of the domain wall is determined by the equilibrium between these energies. There are three types of domain walls exist in thin films as shown in Figure 2.12: Bloch walls, Néel wall, and Cross-tie wall. As shown in Figure 2.12(a), magnetization rotates about an axis perpendicular to the wall in Bloch wall. Hence, for thin films, the magnetization rotation would be perpendicular to the film plane, which results in a high stray field on the surface. Similarly, Néel wall is defined by the magnetization rotating in the plane of the film which reduces the magnetostatic energy of the wall (see Figure 2.12b). A cross-tie wall is defined by a mixture of spins pointing out and in the plane, and is identifiable by spike walls which form to ensure flux closure (see Figure 2.12c) [CRAI1965]. It is found that in thin films, Néel walls have lower magnetostatic energy than Bloch walls and are therefore more energetically favorable. The variations of different types of wall energies in permalloy thin film are shown as a function of thickness in Figure 2.12. The cross-tie walls appear in between the transition region from Bloch wall to Néel wall. The widths of the domain walls also vary as a function of film thickness where Bloch walls become narrower and Néel walls become wider with decreasing film thickness [MIDD1963]. The typical length and energy scales related to different types of domain walls are defined as [OHAN2000],

Wall Type	Length scale	Energy Density
Bloch wall	$\delta_{Bw} = \pi\sqrt{\frac{A}{K}}$	$\sigma_{Bw} = 4\sqrt{AK}$
Néel wall	$\delta_{Nw} = \pi\sqrt{\frac{2A}{\mu_0 M_S^2}}$	$\sigma_{Nw} = 2\pi\sqrt{AK}$

where K is anisotropy constant, A is exchange stiffness constant ranging between 5×10^{-12} - 30×10^{-12} J/m for most FMs and M_S is saturation magnetization. There are several types of domains observed both in bulk materials and in thin films: (a) star like domain patterns observed in $Fe_{40}Ni_{40}P_{14}B_6$ (metglass), (b) the laminar domain structure observed in the $Fe_{40}Ni_{40}B_{20}$ alloys and (c) the stripe domain structure observed in thin films above certain critical thickness [KRON2003]. The development of anisotropy perpendicular to the film plane

arising due to the stress accumulated during the deposition of the film aligns the magnetization perpendicular to the film plane with stripe domain patterns [MURA1966, PRAD1997, CRAU2002]. The equation for the critical thickness above which the strip domain appears was derived from the micromagnetic equation with suitable approximations and the boundary conditions [HUBE2014] and given by,

$$x_{critical} = \frac{2\pi}{1 - \frac{\mu_0 M_S H_S}{2K}} \sqrt{\frac{A}{K}} \tag{2.37}$$

where, $x_{critical}$ is the critical thickness and H_S is the critical field beyond which the stripe domains are unstable. These stripe domains are periodical oscillations of the magnetization within a laminar conventional domain structure [CRAU2002, KRON2003, AMOS2008, HUBE2014], as shown in Figure 2.13. The advantage of such stripe domain structure along with the closer domains is the absence of stray field outside the specimen. The approximation for formation of the closer domains is given by [KRON2003],

$$Q = \frac{2K}{\mu_0 M_S^2} \ll 1 \tag{2.38}$$

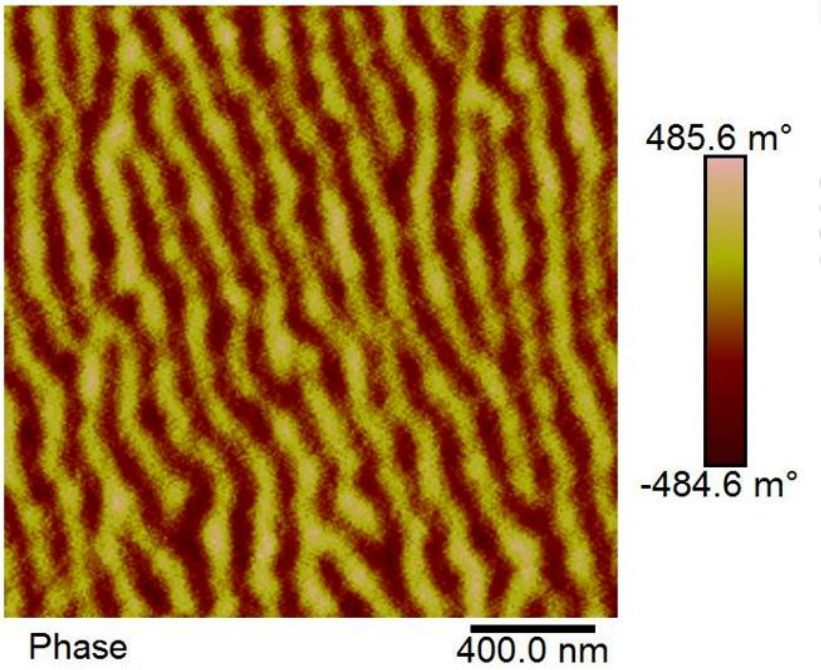

Figure 2.13: Stripe domain pattern observed in 100 nm FeTaC thin films [DASC2018].

It is clear from eqn.(2.38) that the formation of closer domains depends strongly on the anisotropy and M_S values. Soft magnetic materials in general exhibit a low anisotropy and

relatively high M_S. This favors the formation of closer domains for soft magnetic materials. For small Q (< 0.1), the critical thickness for the formation of stripe domains is approximately $x_{critical} = 2\pi\sqrt{A/K}$ in zero applied field. When Q approaches one, the critical thickness vanishes, i.e., stripe domains are expected even for ultrathin films and reported experimentally in ultrathin Co films [ALLE1990], where the surface anisotropy adds to the perpendicular anisotropy for ultra-thin films so that the effective value of Q becomes larger than unity.

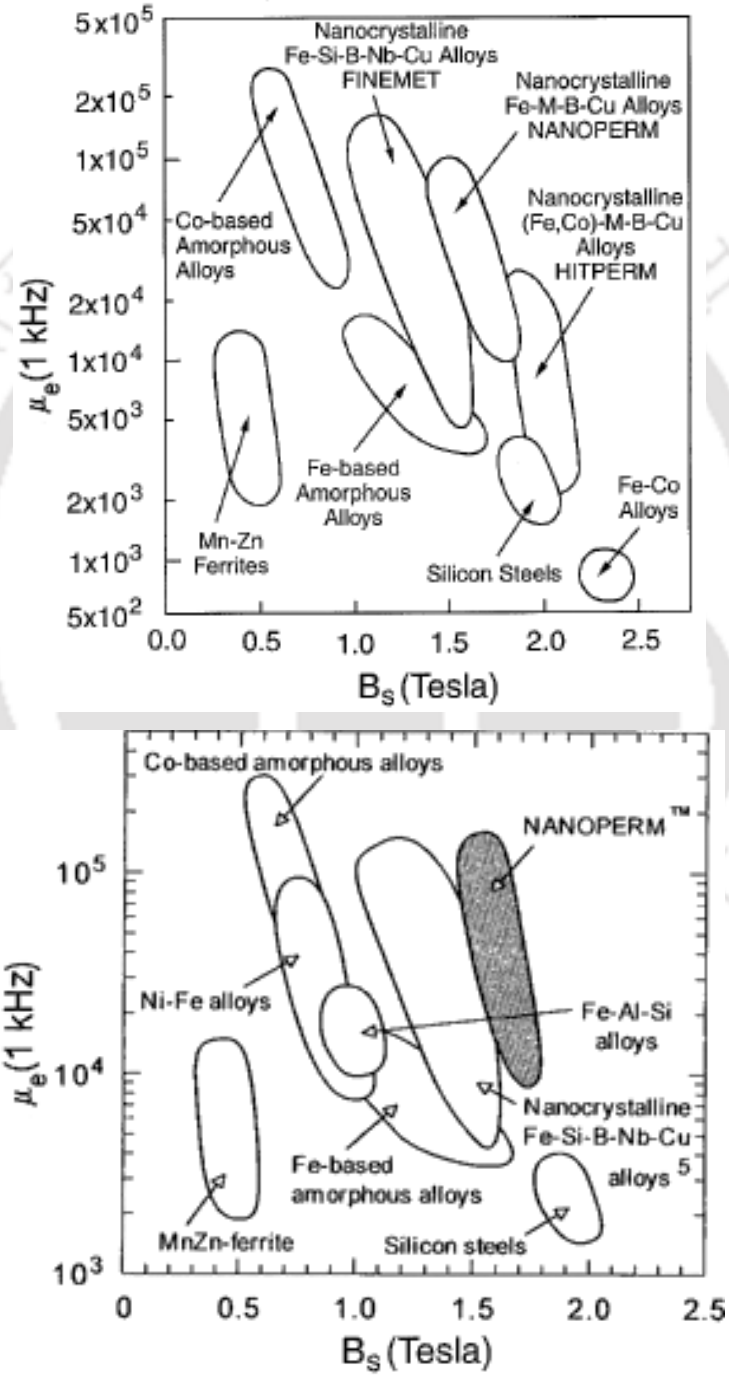

Figure 2.14: Relation between permeability (at 1 kHz) and saturation induction for soft magnetic materials (top) [MAKI1995] and (bottom) [YOSH1989].

2.10. Magnetic properties of amorphous and nanocrystalline materials

The reduction of structural correlation length of solids in to nanoscale results in a dramatic change in their physical properties, which are in general not predictable on the basis of their macroscopic properties. In particular, the enhancement of soft magnetic properties in Fe and Co based nanostructures is one of the examples of such size effects. After the development of $Fe_{74.5}Si_{13.5}B_9Nb_3Cu_1$ by Yoshizawa et al. [YOSH1988], the magnetic softening effect in nanostructures has opened the possibility of promising exploration for material developments in soft magnetic materials for magnetic cores for the purpose of magnetic flux multiplication. It has been reported that amorphous materials exhibit low H_C [KOBL1978, INOU1997] and high permeability. While the permeability of Co based amorphous materials is high as compared to Fe based amorphous alloys, M_S of Co based alloys is considerably lower than the Fe based amorphous alloys. In addition, the magnetostriction of Fe based amorphous alloys is quite high [ITOS1980, INOU1997] as compared to Co based alloys [OHAN1987, MCHE1999]. However, FeCo based amorphous alloys exhibit low value of permeability but relatively high M_S as compared to any other Fe based or Co based alloys.

Figure 2.14 summarizes the relation between the permeability and saturation induction for various soft magnetic materials. The advantage of amorphous materials is high electrical resistivity due to absence of long rang atomic ordering and makes them suitable for high frequency device applications. In case of thin films, they produce smooth surface for making devices without any pinning centers. However, they exhibit low T_C due to absence of long range FM ordering and weak FM exchange interaction.

2.11. Interlayer coupling in multilayer thin films

The study of magnetic properties of thin films composed of alternating magnetic and non-magnetic layers has recently attracted much attention, as the interplay between electron transport properties and magnetic behavior results in a variety of fascinating phenomena such as Anisotropic magnetoresistance, Giant magnetoresistance and Tunneling magnetoresistance [REIG2013, INOU2014, TSYM2016, ZHOU2017, IKHT2018]. These artificial structures are promising as potential memory elements, magnetic sensors and magnetic tunneling junctions, *etc*. One of the technological hurdles is to understand and control the interlayer magnetic coupling between the magnetic layers through non-magnetic films. It has been shown that two separate effects such as magnetostatic coupling due to uncompensated poles near the edges and the magnetostatic coupling between the stray fields of domain walls, and Néel coupling due to interface roughness tend to produce extraneous magnetic fields in the plane of the free layer.

In addition, the interlayer coupling originates from two different types of interactions such as short-range exchange interaction and long-range exchange interaction.

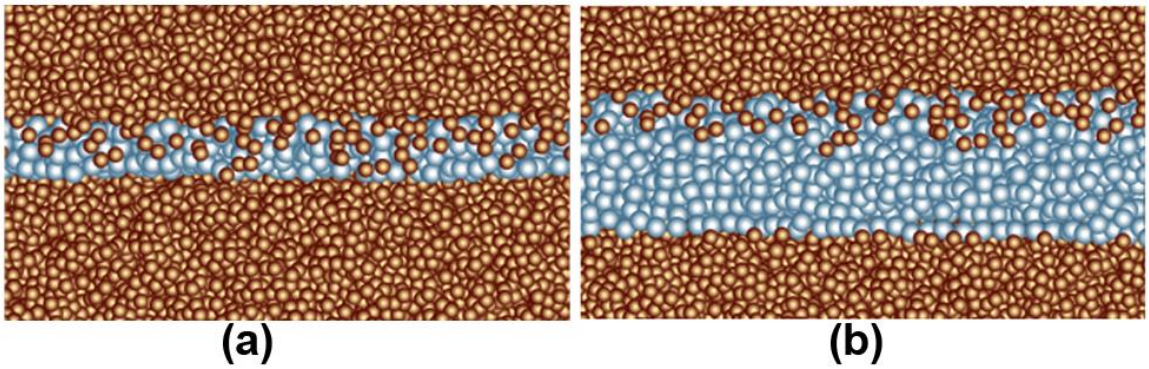

Figure 2.15: Schematic representation of multilayer films with thin and thick interlayers.

2.11.1. Exchange coupling

2.11.1.1. Direct exchange coupling

Two magnetic layers separated by a thin non-magnetic insulating or metallic spacer layer are directly coupled through pinholes present in the thin spacer layer as shown in Figure 2.15a. Since the pinhole appears mainly due to the formation of non-continuous spacer layer at very low thickness films, number of pinholes, which control the strength of the coupling depends on the thickness of the spacer layer, growth conditions, atomic size of the elements present in the spacer and magnetic layers [SAIT2002, STIL2005, PONG2008, SING2015]. Multilayer films having the direct exchange coupling through the pinholes exhibit strong temperature dependent magnetic properties due to the temperature dependent magnetic properties of diffused magnetic atoms into the non-magnetic layers [OLIV1999, SING2013].

2.11.1.2. Indirect exchange coupling

The increase in the spacer layer thickness between the magnetic layers results in the interlayer coupling between FM layers through conduction electrons of the non-magnetic metallic spacer layer (see Figure 2.15b). This is called as indirect exchange interaction or Ruderman-Kittel-Kasuya-Yosida (RKKY) interaction. Theory of indirect exchange interaction was first predicted by Ruderman and Kittel [RUDE1954] and later extended by Tadao Kasuya [KASU1956] and Kei Yosida [YOSI1957]. RKKY interaction was implemented in multilayer structured thin films to understand the magnetization orientation and the giant magnetoresistance of multilayer structured ultra-thin films. It was observed that RKKY coupling aligns the magnetization of adjacent FM layers to be either FM (parallel alignment) or AFM (antiparallel alignment). Hence, the magnetoresistance of the multilayer films exhibits

a strong dependence on the spacer layer thickness and shows an oscillating nature with spacer layer thickness. The amplitude of oscillation decreases with increasing spacer layer thickness [BAIB1988, PARK1990, BRUN1991, BRUN1992]. In addition, the coupling also depends on the roughness at the interfaces.

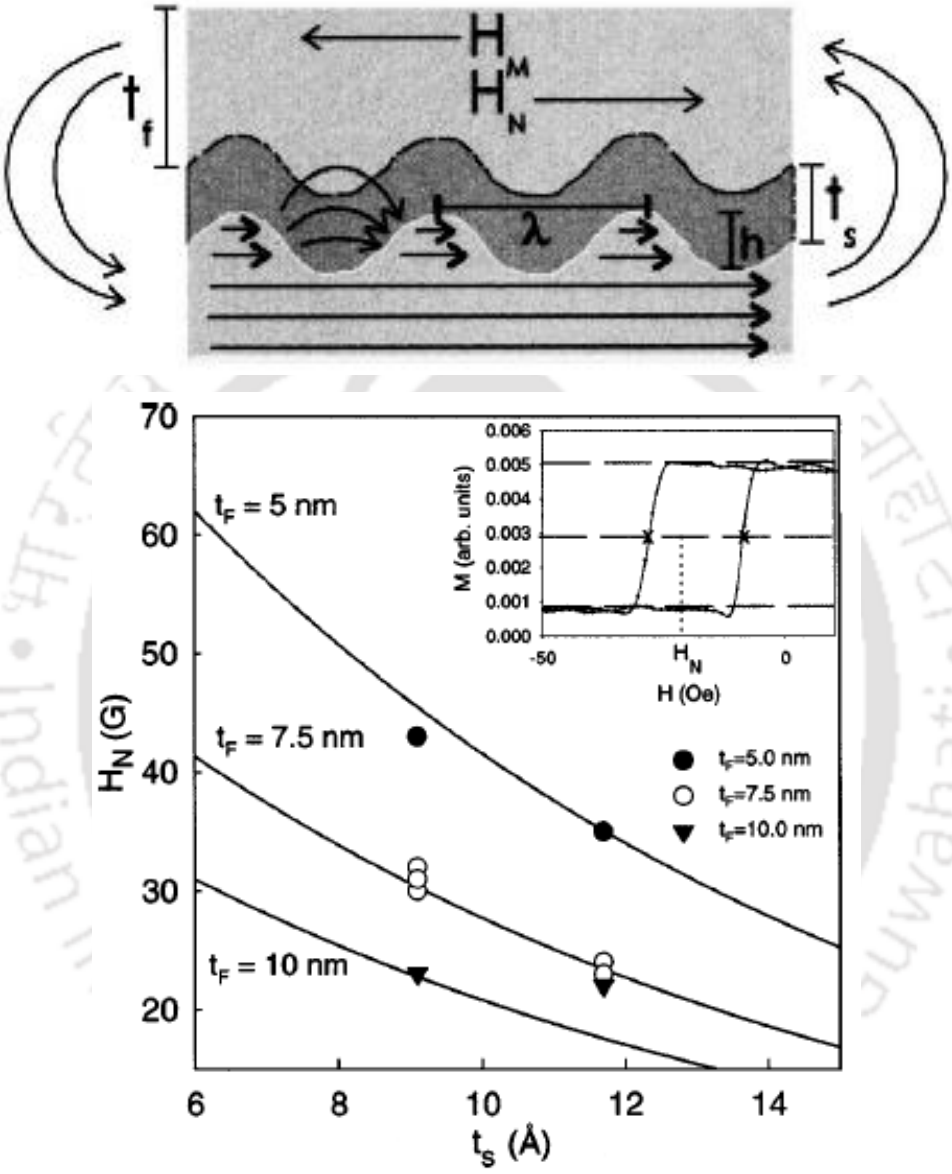

Figure 2.16: (top) Schematic drawing of two dominant interlayer coupling mechanisms, and (bottom) variation of Néel coupling with spacer layer thickness for different multilayer films [SCHR2000].

2.11.2. Magnetostatic coupling

2.11.2.1. Topological coupling

The topological coupling also known as Néel's orange peel coupling or the dipolar coupling is the magnetostatic interaction induced by the magnetic poles at the interface. These magnetic

poles are generated by the interface roughness. Néel carried out the first calculation of topological coupling for semi-infinite magnetic layers with a correlated sinusoidal interface roughness [NEEL1962]. Later, the model was extended by other researchers for the roughness of arbitrary phase and finite magnetic film thickness [ZHAN19961, ZHAN19962, KOOL1999]. The coupling strength depends on the thickness of magnetic layers and spacer layers, magnetization of magnetic layers, roughness amplitude at the interface and wavelength of the roughness profile. Néel coupling between two FM layers is defined as [SCHR2000],

$$H_N = \frac{\pi^2}{\sqrt{2}}\left(\frac{h^2}{\lambda t_F}\right) M_S exp\left(-\frac{2\pi\sqrt{2}t_s}{\lambda}\right) \tag{2.39}$$

where, t_F and t_s are the thickness of the magnetic layer and spacer layers respectively, h and λ are amplitude and wavelength of the roughness, respectively as demonstrated in the Figure 2.16(top). The coupling field strongly depends not only on the spacer layer thickness, but also depends on the FM layer thickness (see Figure 2.16(bottom)).

2.11.2.2. Stray field coupling

Magnetostatic coupling arises due to the magnetic poles at the edges of the film, is stray field coupling. Stray field generated from the edges of one magnetic layer magnetostatically coupled other layers as shown in the Figure 2.16 (top). Since the coupling is magnetostatic in nature, it depends strongly on the films' dimension and provides a significant interlayer coupling for thicker films [ANGU2000]. The variation of stray field coupling on the films' dimension can be described as [ANGU2000],

$$H_M = A\frac{W^\alpha}{L} \tag{2.40}$$

where, W and L are the width and length of the sample in micron, respectively, A and α (= 0.22) are constants. The value of α varies with the sample dimension, i.e., when the separation between the free layers and the relevant pinned layer is much larger than its width, α approaches to one, whereas in the opposite limit, the value of α should be nearly zero [ANGU2000].

2.11.2.3. Domain wall stray field coupling

Stray fields emanating from domain walls of a given FM layer magnetostatically lock in with the stray fields from walls in adjacent layers as shown in Figure 2.17. [CHOP2000, CHOP2005]. The rotation of magnetization within a Néel wall is denoted by the double arrows.

The stray field emanating out of the Néel walls, denoted by curved arrows, causes a magnetization fluctuation in the adjacent layers above and below it, giving rise to quasi-Néel walls. This stray field emanating from each domain wall is able to close its flux by magnetostatic locking-in with the stray fields from domain wall in adjacent layers.

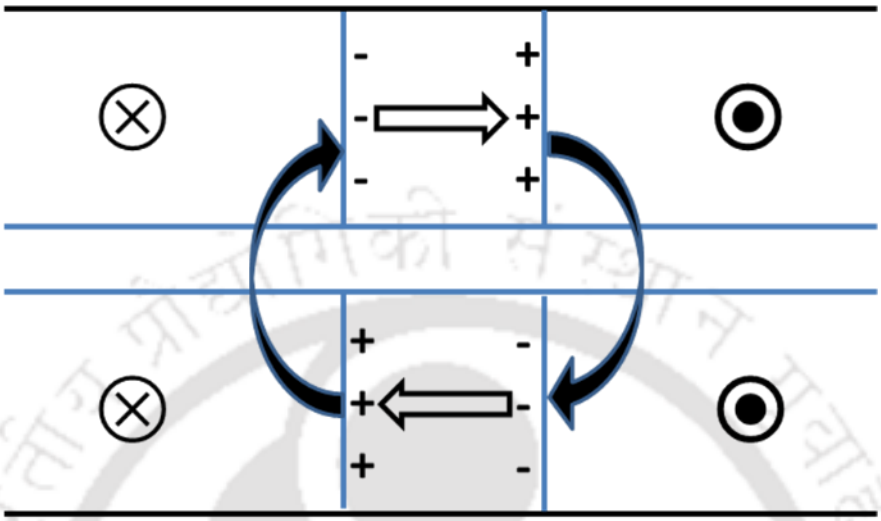

Figure 2.17: Schematic of Néel wall pair separating parallel domains. Superimposed Néel walls are energetically favorable entities due to a more complete flux closure associated with them [CHOP2000].

This leads to an overall reduction in the wall energy and hence the coercivity. Magnetic thin films reveal strong thickness dependent magnetic properties. Particularly, ultrathin films having in-plane magnetic anisotropy exhibits in-plane magnetization with large sized domains and Néel wall [OHAN2000]. Similarly, the multilayer thin films with thin FM layers also show in-plane magnetization with large sized domains and Néel wall, which results in minimum or zero stray field coupling. On the other hand, the development of multidomain patterns above the critical thickness depends on the net magnetization of the FM layers, anisotropy of the films, substrate nature, microstructure of the film and the growth conditions of the thin films [FELD1971, OEPE1990, ALLE1994]. Therefore, at larger thicknesses, the multidomain pattern with Bloch wall is energetically more favorable. This reveals that the domain wall stray field provides a significant coupling among the FM layers ensuing a strong variation in the magnetic properties of the multilayer structured films measured at different temperatures.

Chapter 3

Experimental Methods

भारतीय प्रौद्योगिकी संस्थान गुवाहाटी
Indian Institute of Technology Guwahati

3.1. Introduction

In the course of the present investigations, several experimental techniques were used for the fabrication and characterization of single-layer and multilayer thin films. This chapter provides a concise description of those experimental techniques.

3.2. Techniques used for sample preparation

3.2.1. Sputtering technique

The ejection of atoms from the cathode surface by impinging of energetic positive ions of noble gases such as helium, argon, neon and krypton, at a reduced gas pressure under high direct current (DC) voltage [OHRI1992, WAGE1994, SESH2002] is called as sputtering. In 1852, Sir W. R. Grove coincidencely discovered surface coatings generated in the valve under a glow discharge. This phenomenon was called as spluttering by Sir W. Thomson and later it was espoused as sputtering. This sputtering process involves a momentum transfer between the impinging positive inert gas ions and the cathode surface atoms as displayed in Figure 3.01 and as a result of which a physical removal of atoms takes place.

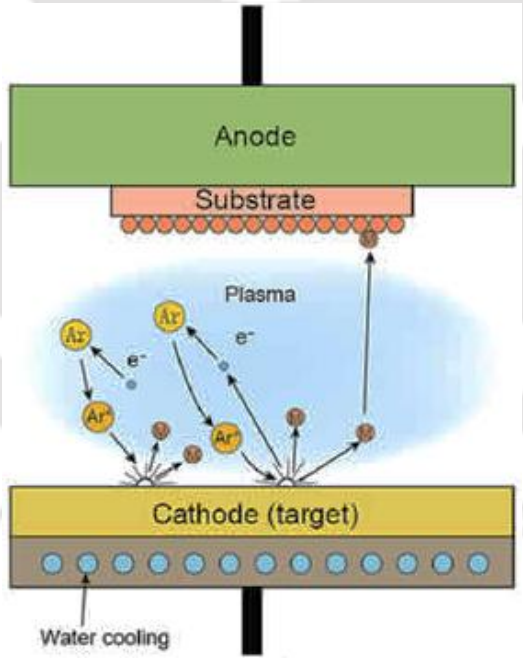

Figure 3.01: Schematic diagram of the sputtering process.

The yield of sputtering is defined as ratio between the average numbers of emitted atoms to number of incident ions on the surface of target.

- The sputtering yield increases with a) energy, b) mass of the bombarding atoms and c) decrease of angle of incidence to the target.

- A minimum energy is required to initiate the sputtering process.
- The sputter atoms are ejected along the crystallographic directions of the cathode metal lattices.
- Sputtering yield decreases with larger increase of the ion-energy because of the deeper penetration of ions inside the lattice.
- Sputtering is also accompanied by the emission of secondary electrons from the cathode surface.
- The sputtering yield is insensitive to the cathode temperature.
- If the sputtering process does not involve any of the chemical reaction between bombarding gas ions and the cathode, it is known as physical sputtering.
- If some reactions are involved then it is named as reactive sputtering.

The physical deposition process consists of three steps

1. Emission of the atoms from the target source,
2. Their transport to the substrate, and
3. Condensation on the substrate.

There are four different types of sputtering process [direct current (DC), Radio-frequency (RF), Magnetron and Reactive sputtering] used for thin film deposition. We have used DC and RF magnetron sputtering for depositing the films of present investigation.

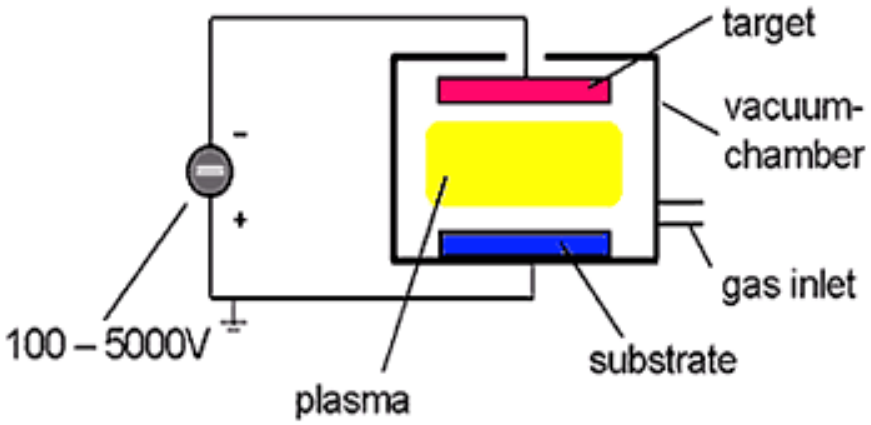

Figure 3.02: Schematic arrangement of DC sputtering technique.

3.2.1.1. DC sputtering technique

Figure 3.02 displays a typical arrangement used for DC sputtering. The target and substrate oppose each other in the vacuum chamber having a distance of few centimeters to few tens

of centimeters. The target is connected to a negative output of a DC power supply and hence acted as the cathode. The substrate and chamber walls act as anode. After the creation of required argon atmosphere with a pressure of about 0.13 Pa – 1.33 Pa, the gas discharge is ignited by applying a DC voltage. The created Ar^+ ions are now accelerated toward the target and eject atoms from the target. These atoms subsequently are deposited on the substrate. At low pressures, the mean free path between collisions is large, the ionization efficiency is low and self-sustained discharges cannot be maintained below few 0.13 Pa. As the pressure increases at a fixed voltage, the electron mean free path is decreased, more ions are generated and large current will flow. If the pressure is too high, the sputtered atoms undergo increased collisional scattering resulting a low deposition process. The deposition rate is proportional to (a) power consumed, (b) square of current density and (c) 1/(electrode spacing). DC sputtering works with all types of target materials which are conductive in nature.

However, DC sputtering suffers from two major drawbacks as compared to conventional evaporation: (i) low deposition rates and (ii) high thermal load of the substrate due to bombardment of secondary electrons. In order to increase the deposition rate and to control the thermal load, magnetron sputtering is utilized for the fabrication of the films.

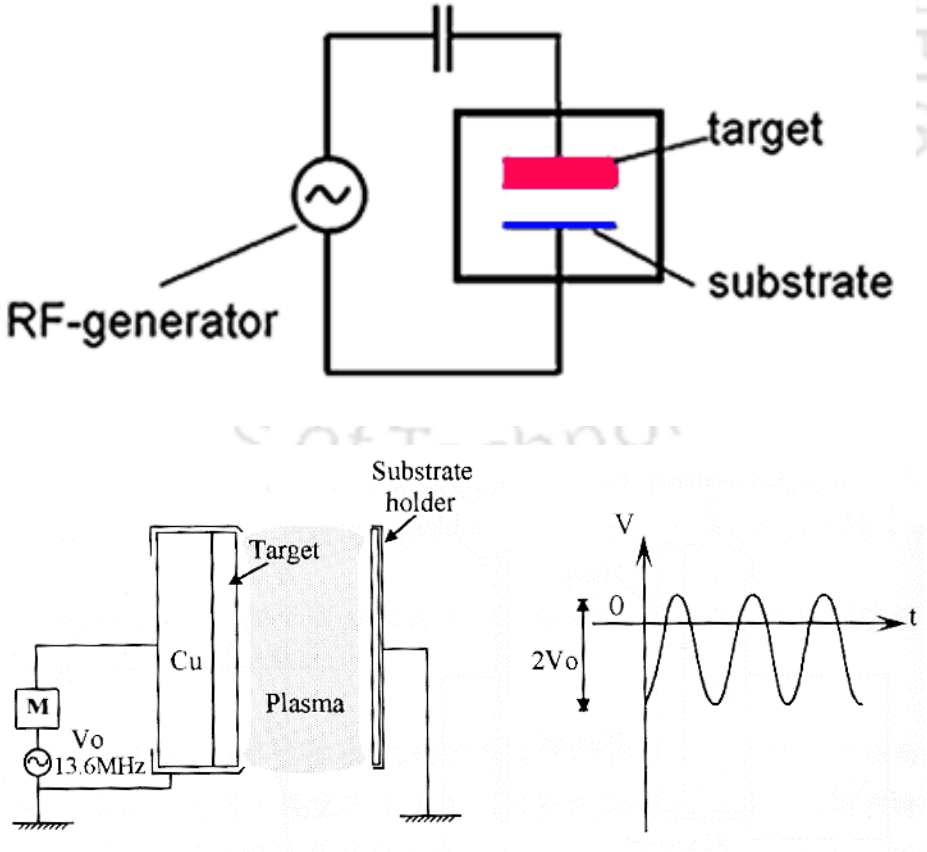

Figure 3.03: Schematic presentation of RF magnetron sputtering assembly.

3.2.1.2. RF sputtering technique

Figure 3.03 displays a typical arrangement of RF sputtering. Materials such as oxides, nitrides or ceramics have very high DC impedance and hence require prohibitively high voltages to ignite and maintain a plasma. This prevents neutralizing of the positive charge accumulation on the surface during ion bombardment. Thus the deposition of such insulating materials cannot be carried out by DC sputtering. However, the impedance of such materials changes with the frequency of the applied power. Hence, it can be overcome by applying a high frequency potential to a metal electrode behind the insulator. Using power delivered at radio frequencies typically at 13.56 MHz and an automatic impedance matching network, the total impedance of the circuit can be regulated to 50 Ω which is suitable for plasma ignition in typical sputtering environments. Since, the insulator now be alternately bombarded by ion and electron, the positive charge which accumulates on the surface during the negative or sputter portion of each cycle will be neutralized by electrons during the positive part of the cycle [DAVI1967]. Wehnerl in his review article on sputtering by ion bombardment proposed the principle of RF sputtering [WEHN1955]. Subsequently, Davidse and Maissel further developed RF sputtering for the deposition of thin insulator films at high rates [DAVI1966]. In the present thesis, the sputtering of SiO_2 target is carried out by RF magnetron sputtering.

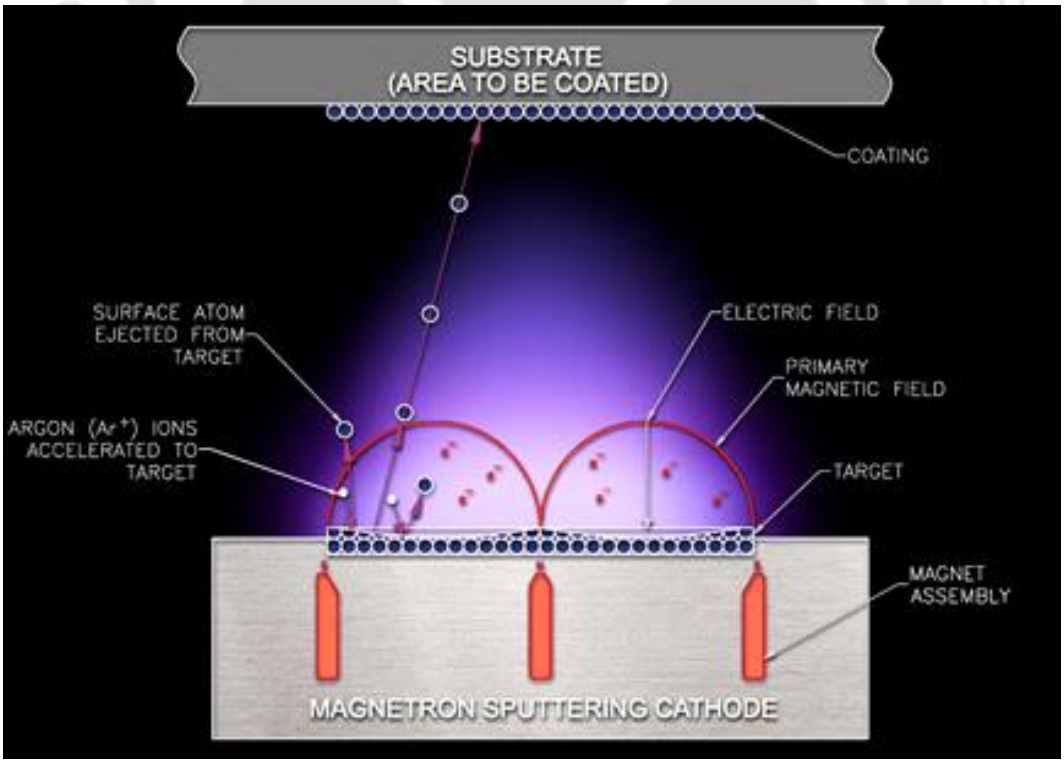

Figure 3.04: Schematic presentation of magnetron sputtering gun assembly.

3.2.1.3. Magnetron sputtering technique

In magnetron sputtering, electrons ideally do not reach the anode but are trapped near the target by magnetic field and thereby enhancing the ionization efficiency. This is accomplished by employing magnetic field oriented parallel to the target and perpendicular to the electric field. Practically, this is achieved by placing bar magnets behind the target as shown in Figure 3.04. The magnetic field lines emanate first normal to the target and then bend with a component parallel to the target surface and finally return to magnet completing the magnetic circuit. Electrons emitted from cathode are initially accelerated toward the anode, but undergo a helical motion when they encounter the region of the parallel magnetic field. Therefore, the path of the electron bent in an orbit back to the target. The chief reasons of its success are (1) increased sputtering rates (~ 5 - 10 times) due to high plasma density around target, (2) low discharge voltages of 300 to 1000 V due to the reduced plasma impendence resulting from high plasma density and (3) low thermal load of the substrate due to deflection of secondary electrons by the magnetic field.

Figure 3.05: Photograph of magnetron sputtering system used in the present work.

Figure 3.05 depicts the typical set up of magnetron sputtering used in the present thesis work for fabricating single and multilayer structured thin films using DC/RF magnetron sputtering technqiues. The chamber is equipped with four different guns for making multilayer films. The substrate was loaded on a rotating substrate holder. Subsequently, the chamber was pumped to high vacuum (< 10^{-4} Pa) using diffusion pump and rotary pump combination. Argon gas of fixed pressure was permitted into chamber continuously using mass flow controller (MFC) and the argon gas pressure in the chamber was maintained by adjusting the MFC and processing valve. The optimized sputtering Ar gas pressure for the deposition of CoFeB, FeTaC, Ta and SiO_2 films is fixed at 1.33 Pa. After stabilizing the constant argon gas pressure in the chamber, a constant DC power was applied to commence the sputtering process. The deposition of the films was carried out after stabilizing the plasma and completing the pre-sputtering process. The deposition rate for the films was calibrated by using an ex-situ surface profilometer (Veeco, Dektak-150) as described in the next section.

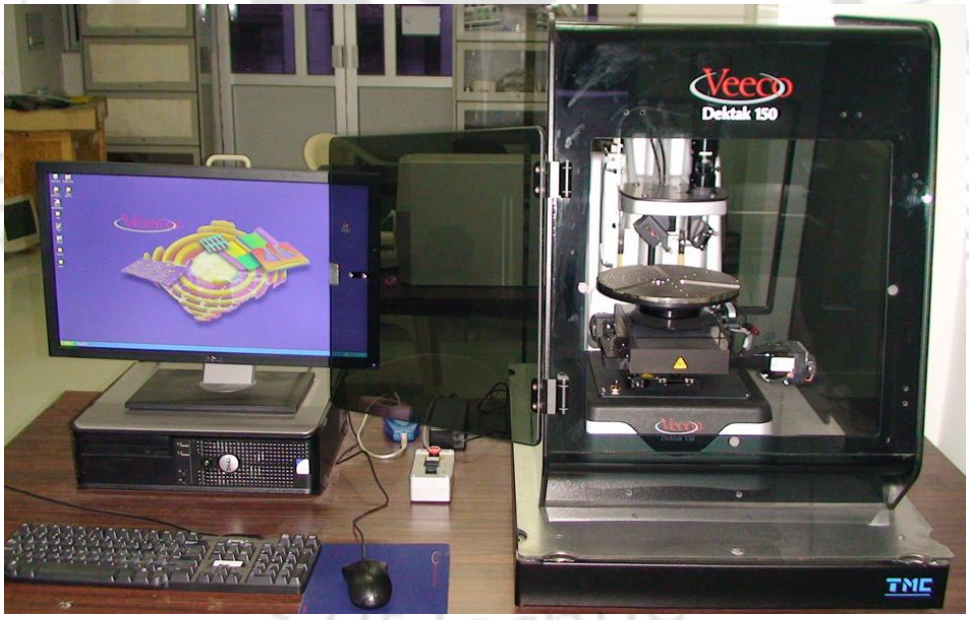

Figure 3.06: Photographic view of Veeco, Dektak-150 surface profilometer.

3.2.2. Calibration of deposition rate

As the properties of the thin films change with thickness, the pre-calibration of thickness under the particular preparation is ~~quite~~ crucial. To optimize the properties of the films at different thicknesses, it is ~~very much~~ essential to control the thickness of the film deposited under controlled sputtering conditions. Deposition rate of the films studied in the present investigations was calibrated with surface profilometer (Veeco, Dektak-150), as illustrated

in Figure 3.06. Stylus profilers are versatile measurement tools for studying surface topography. Their primary function is to measure film thickness by scanning step heights and trench depths. The stylus profilers typically rely on a small-diameter stylus moving along a surface either by movement of the stylus or movement of the surface of interest. A true stylus profiler moves linearly to obtain the measurement. As the stylus encounters surface features, the stylus moves vertically to measure various surface features, such as deposited film and irregularities. The stylus profiler used in the present work was sponsored by Defence Research & Development Organisation (DRDO), New Delhi [ERIP/ER/0900363/M/01/1185 Dated 16 November 2009]. To monitor the thickness of the deposited films, a proper marking using permanent marker was made on top of the cleaned substrate. Subsequently, the deposition was done under controlled sputtering environment (constant Ar gas pressure, DC power and target to substrate distance, *etc*.) for a given time at ambient temperature. After the completion of the deposition, the film was cleaned through sonication in acetone. As a result, the film deposited on the substrate reveals a clear step.

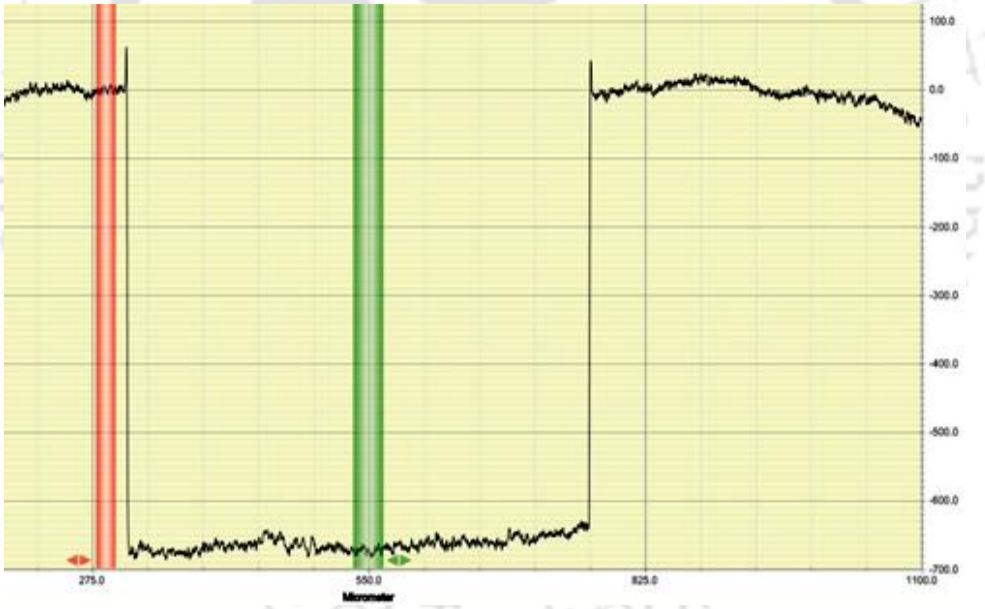

Figure 3.07: A typical scan profile of the Dektak surface profilometer.

The step size was evaluated using surface profiler as displayed in Figure 3.07 and the average deposition rate was eventually calculated by dividing the average thickness measured at various locations on the substrate with deposition time. In order to confirm the reproducibility, more films were subsequently made under the same sputtering conditions and analyzed using surface profilometer. Similar procedures were followed for all the films

prepared under different sputtering conditions. The thickness of the films is also monitored using X-ray reflectivity technique discussed later in this chapter.

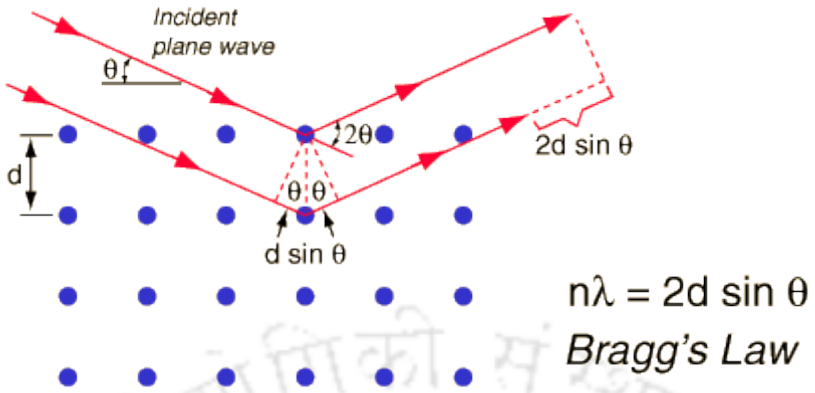

Figure 3.08: Schematic ray diagram of diffraction of X-rays by a crystal.

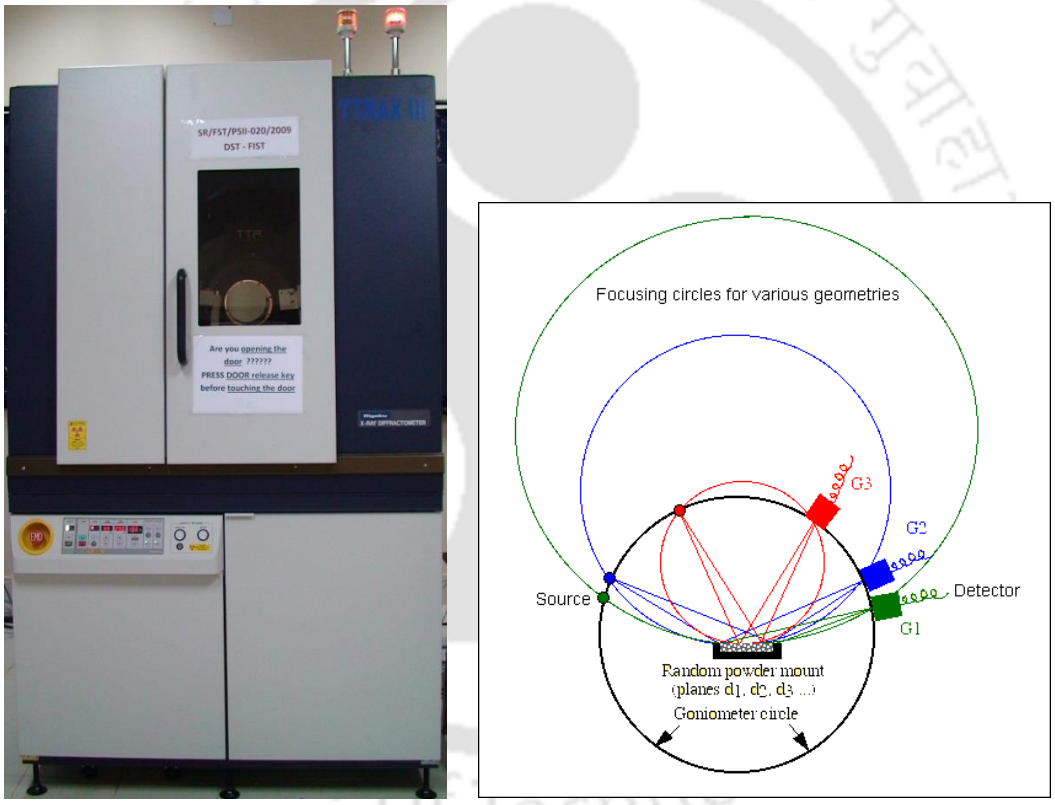

(a) (b)

Figure 3.09: (a) Photographic view of Rigaku TTRAX III 18 kW X-ray diffractometer and (b) Bragg-Brentano diffraction geometry of a powder X-ray diffractometer.

3.3. Structural property characterization

3.3.1. X-ray diffraction

X-ray diffraction (XRD) technique is useful to identify the existence of various phases, degree of crystalline order and quantitative analysis of secondary phases present in a two-

phase system. An ideal crystal has a periodic arrangement of atoms. Diffraction of X-rays occurs through constructive interference of X-rays scattered from atoms of a set of parallel planes in crystal lattice at particular angular positions of the incident wave known as Bragg angles. This condition for obtaining constructive interference is known as Bragg's law and given by the relation

$$2d_{hkl} \sin\theta = n\lambda \qquad (3.01)$$

where, d_{hkl} is inter-planer spacing, θ is glancing angle, λ is wavelength of the X-ray and n is order of diffraction. A sequence of these angles can be used to determine the Miller indices (*hkl*) values and the crystal structure can be identified from the systematic behavior of these indices. Figure 3.08 shows the diffraction of X-rays from crystal lattice planes illustrating Bragg's law. The structural parameters such as the average size of the crystallites, *d*-spacing, lattice constant and strain present inside the crystallites, *etc.* can be determined by a careful analysis of the XRD patterns using various models [CULL2001]. For the present work, Rigaku TTRAX III 18 kW (see Figure 3.09a) is used. Cu-K_α X-ray radiation with wavelength 1.541 Å was used in all the cases. The theta-theta (θ–θ) goniometer was used in the reflection (Bragg-Brentano) geometry (see Figure 3.09b) [CULL2001].

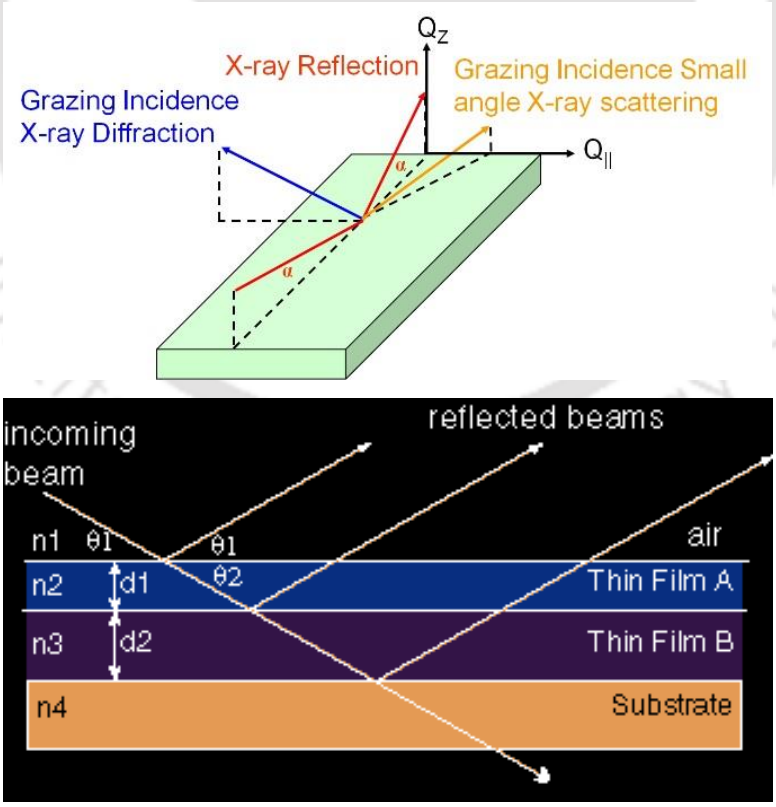

Figure 3.10: Schematic diagram of X-ray reflectivity arrangement.

3.3.2. X-ray reflectivity

Most of the recent technological applications require thin films of definite thickness and the literature review suggests that most properties of thin films are thickness dependent. Therefore, the determination of film thickness (x) with high precision is very crucial for these technologies. X-ray reflectivity (XRR) is a non-destructive and non-contact technique for studying the detailed surface properties and thickness determination of materials (between 2 nm and 100 nm with a precision of about 1 -3 Å). In addition, this technique is also employed for the determination of density and roughness of films and also multilayers with a high precision. The basic principle of the XRR method involves monitoring the intensity of the X-ray beam reflected by a sample at grazing angles. A monochromatic X-ray beam of wavelength (λ) irradiates a sample at a grazing angle ω and the reflected intensity at an angle 2θ is recorded by detector, as shown in Figure 3.10. The reflection at the surface and interfaces is due to the different electron densities in the different layers of films, which corresponds to different reflective indexes (in the classical optics). For incident angles θ below a critical angle θ_C, total external reflection occurs. The critical angle for most materials is less than 0.3°. The density of the material is determined from the critical angle. Above θ_C the reflection from the different interfaces interfere and give rise to interference fringes. The period of the interference fringes and the fall in the intensity are related to the thickness and the roughness of the layer(s). The reflection obtained in the typical range between 0° and 5° can be analyzed using the classical theory (Fresnel equation).

For incident angles greater than θ_C, ($\theta > \theta_C$) the X-ray beam penetrates inside the film and therefore reflection occurs at the top and the bottom surfaces of the film. The interference between the rays reflected from the top and the bottom of the film surfaces results in interference fringes. Due to the low amplitude reflection coefficient of interface between adjacent layers, contributions of multiply reflected beams can be neglected. The n^{th} interference maximum for a path difference $\Delta = n\lambda$, is located at

$$n\lambda = \Delta = 2x\tilde{N}_{X,1}(\theta_n) \tag{3.02}$$

$$n\lambda = \Delta \approx 2x\sqrt{\theta_n^2 - 2\delta}$$

$$\theta_n^2 = n^2\frac{\lambda^2}{4x^2} + 2\delta$$

$$\theta_n^2 = n^2\frac{\lambda^2}{4x^2} + \theta_C^2 \tag{3.03}$$

The plot of θ_n^2 versus n^2 yields a straight line and fitting the experimental data to linear fit provides thickness of the films from the slope and critical angle from the intercept. The thickness is often determined with a precision better than 1 Å for measurements exhibiting interference fringes in a bigger angular range. Another important quantity determined from XRR measurements is the surface and interface roughness. Roughness gives rise to diffuse scattering and results in less intensity in the specularly reflected beam. General scattering formalism has been developed that calculate the scattered fields for both specular and non-specular scattering. In one formalism, roughness is considered as non-homogeneous thickness. It is assumed that the thickness has a Gaussian distribution with a mean *x* and a standard deviation σ. With this assumption, the corrected Fresnel coefficients of reflection is given as $\rho exp(-x/(2\sigma^2))$.

3.3.3. Transmission electron microscope

Transmission electron microscopy (TEM, TECNAI G2 F30; JEOL 2100) was used to study the amorphous nature of the films. Figure 3.11 depicts the cut view of TEM (Figure 3.11a) and schematic ray diagrams for imaging (Figure 3.11b) and diffraction (Figure 3.11c) modes. Electrons emitted from the gun are accelerated to 200 keV or higher and first projected onto a thin specimen by means of the condenser lens system. The scattering processes experienced by electrons during their passage through the specimen determine the kind of information obtained. Elastic scattering, involving no energy loss when electrons interact with the potential field of the ion cores, gives rise to diffraction patterns. Inelastic interactions between beam and matrix electrons at heterogeneities such as grain boundaries, dislocations, second-phase particles, defects, density variations, *etc*., cause complex absorption and scattering effects, leading to a spatial variation in the intensity of the transmitted beam. The transmitted beams are further magnified by a set of intermediate lens and projector lens and finally projected on a fluorescent screen.

Microstructural images are obtained in a number of ways. The bright-field image is obtained by intentionally excluding all the diffracted beams and only allowing the central beam passing through the specimen. This is done by placing suitably sized apertures in the back focal plane of the objective lens. Dark-field images are also formed by magnifying a single beam of one of the diffracted beams by means of an aperture that blocks the central beam and the other diffracted beams. In a third method of imaging, the primary transmitted and one or more of the diffracted beams are made to recombine, thus preserving both their

amplitudes and phases. This is the technique employed in high-resolution lattice imaging, enabling diffracting planes and arrays of individual atoms to be distinguished. From the high-resolution TEM (HR-TEM) micrograph, average grain size and dislocations can be evaluated.

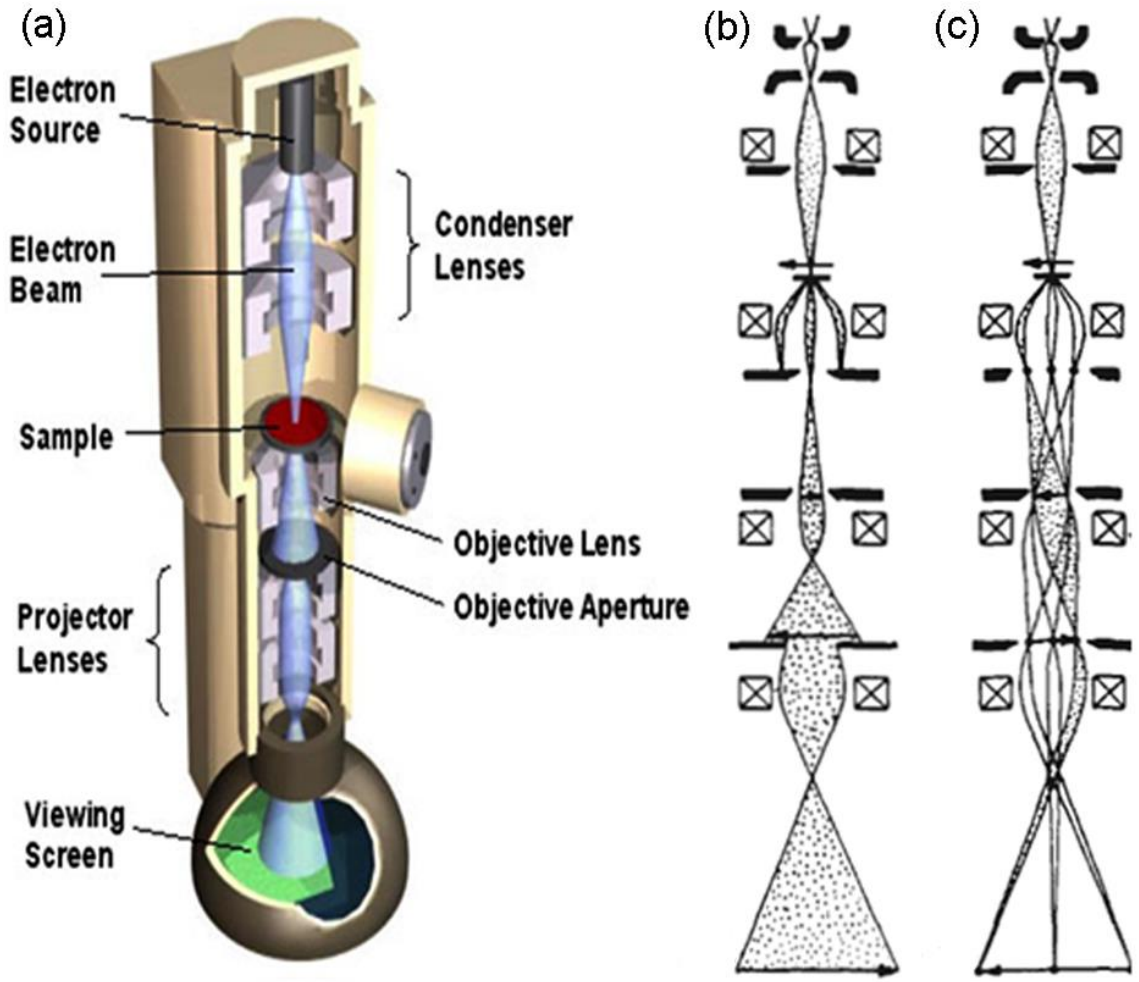

Figure 3.11: (a) Cut view of transmission electron microscope, (b) Schematic ray diagrams of image mode and (c) diffraction mode of TEM.

On the other hand, the selected area electron diffraction is done by intentionally excluding the central beam by beam blocker and collecting all the diffracted beams to form the diffraction patterns. The composition analysis of the samples can also be analyzed using X-ray energy dispersive analysis interfaced to TEM. Electrons emitted from the filament (cathode) are accelerated to high energies where they strike the specimen target (anode). In the process, X-rays characteristic of atoms in the irradiated area are emitted. The atoms can be identified by analyzing their energies and the concentration of atoms in the specimen can be determined by counting the number of X-rays emitted. In the present study, as-deposited

films were polished mechanically from substrate side using Gatan Disc grinder to reduce the thickness down to 10 μm and subsequently thinned down using precision ion polishing system (PIPS) to suitable thickness for the TEM observation.

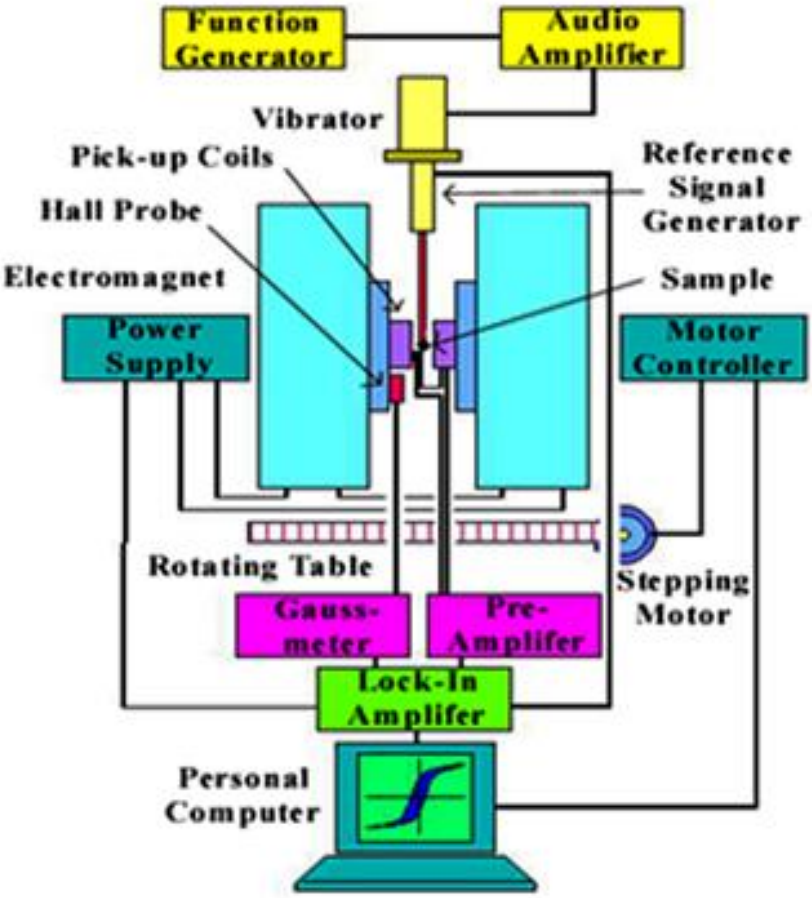

Figure 3.12: Schematic diagram of a vibrating sample magnetometer.

3.4. Magnetic property characterization

Magnetic properties of the magnetic materials can be characterized with various experimental techniques. One of the major techniques is based on the induction methods and have sensitivity of at least 10^{-6} emu. Similarly, the magnetic domain structure of the materials can be imaged using magnetic Kerr microscope and magnetic force microscope (MFM). In this section, a brief description of the principle involved in various magnetic measurement and domain imaging techniques employed in the present work is outlined.

3.4.1. Vibrating sample magnetometer

Vibrating sample magnetometer (VSM, Lakeshore 7410, USA) was used to characterize room temperature and temperature dependent magnetic properties in the temperature range

of 30 K – 300 K and 300 K – 700 K. VSM measures net dipole moment when material is exposed to magnetic field [SVOB2004, CZIC2006]. The magnetic moment of the material can be obtained either as a function of field called magnetic hysteresis (*M-H*) loop to investigate the evolution of magnetic properties with field or as a function of temperature (*M-T*) to understand the magnetic phase transition of the material. Figures 3.12 and 3.13 display schematic diagram of VSM and a photographic view of VSM used in the present study, respectively.

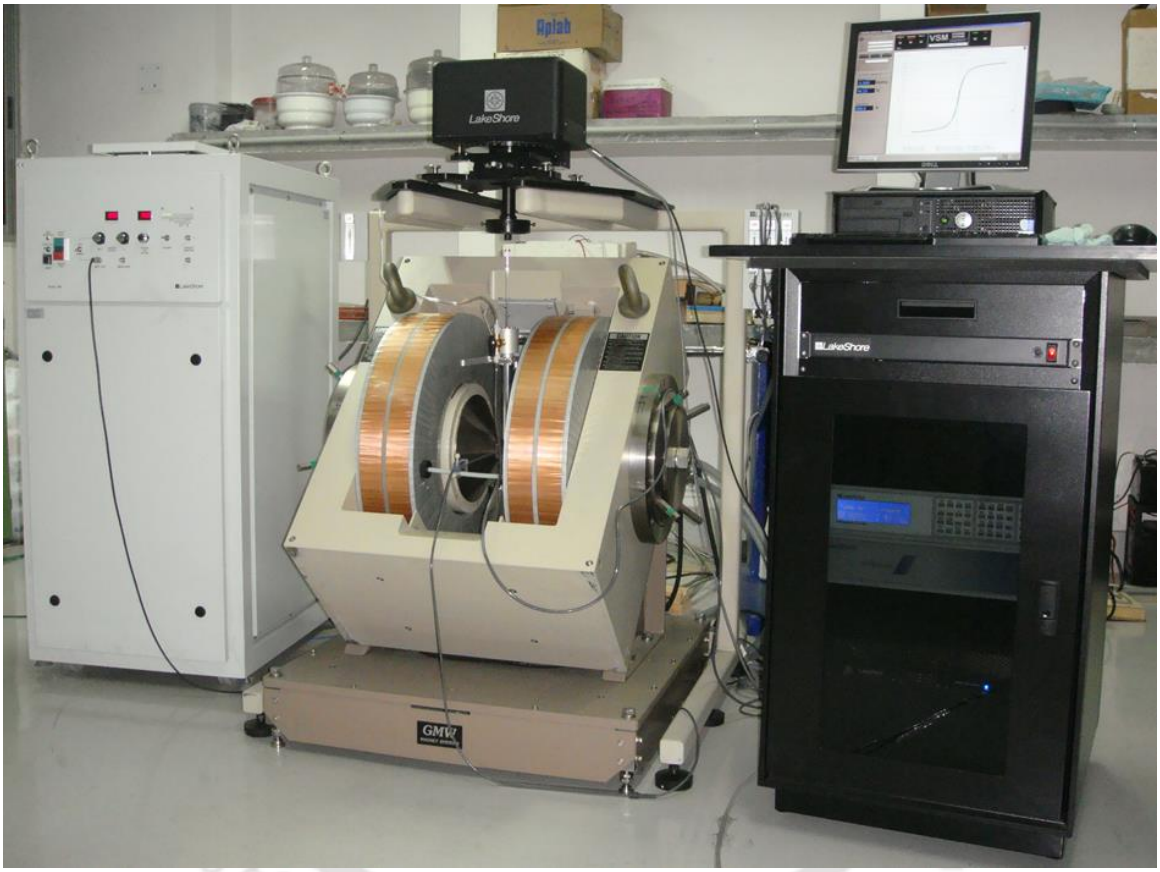

Figure 3.13: Photographic view of vibrating sample magnetometer (Model: Lakeshore 7410, USA) used in the present investigation.

When a sample is placed in a uniform magnetic field, a dipole moment proportional to the product of the sample susceptibility and the applied field is induced in the sample. If the sample is made to undergo sinusoidal motion, an electrical signal can be induced in suitably located stationary pickup coils (see Figure. 3.12). This signal has amplitude proportional to the magnetic moment of the sample, the vibrating amplitude and the vibration frequency. Through the use of lock-in-amplifier and feedback techniques, only that portion of the signal arising from the magnetic moment is picked up and is converted into direct read-out in the units of magnetization (e.g. emu) on a digital panel meter. As

shown in Figure 3.12, VSM consists of the following major parts: a) Vibration exciter and sample holder, b) Water cooled electromagnet and power supply, c) Hall probe, d) pick-up coils, e) Amplifier, f) Control panel system, g) Lock-in amplifier and h) Computer interface.

The thin film sample was fixed at the lower end of the sample rod aligning either in-plane or out-of-plane direction with respect to applied field. Prior to the magnetic measurements, the calibration procedure was carried out using standard Ni sphere sample. The measurement sequence is programmed as per the user's choice using the software (IDEASVSM) provided with the instrument such that the program starts either from the maximum field or from zero applied field. The sequence is made to collect more number of data, which helps to extract the magnetic parameters (saturation magnetization, remenance magnetization, coercivity, *etc*.) more accurately. The exciter is vibrated at a frequency of 72 Hz (Lakeshore model 7410) and the signal received from the hall probe and the pick-up coils is converted into the magnetic moment of the sample. The magnetic field is increased automatically in user-defined steps for measuring *M-H* loops. Similarly, for high temperature *M–T* measurements, a high temperature oven attachment capable of providing a controlled heating/cooling of the sample from room temperature to 700 K was used. For *M–T* measurements, the film was loaded on a high temperature sustainable holder (ceramic holder or quartz rod) after the calibration using standard Ni sample. The oven was purged with nitrogen gas to avoid oxidization of the sample at high temperature. Magnetization was recorded at different temperatures at a constant in-plane applied magnetic field. The heating rate and *M–T* sequences were programmed using the IDEASVSM software.

3.5. Magnetic domain structure analysis

3.5.1. MOKE microscope

The magneto-optical Kerr effect (MOKE) represents a change in the intensity or polarization state of the light reflected from a magnetic material. Figure 3.14 depicts a schematic view of conventional MOKE set up. The light beam from a laser is polarized using a linear polarizer, while a photo elastic modulator superimposes periodic quarter-wave retardation ($\pm \lambda/4$) to this beam before it reaches the sample. After the beam is reflected from the sample, the light beam is again made to pass through a linear analyzer and then the signal is collected at the detector. In principle, there are three different optical and magnetic geometries of the Kerr effect: (a) Longitudinal MOKE provides a signal proportional to the component of magnetization that is parallel to the film plane and the plane of incidence of the light. (b) In transverse MOKE, the signal is proportional to the component of magnetization that is

parallel to the film plane but perpendicular to the plane of incidence of the light. (c) Polar MOKE, in which a signal proportional to the component of magnetization that is perpendicular to the film plane is measured and often performed at normal incidence. There are three important properties to be noted that (i) the Kerr signal is a linear function of the Kerr amplitude *K* and therefore of the respective magnetization components, (ii) the Kerr signal can be enhanced by increasing the analyzer angle allowing to increase the signal-to-noise ratio and to adjust to the sensitivity of the detector and (iii) the visibility of domains is determined by the Kerr amplitude and not by the Kerr rotation.

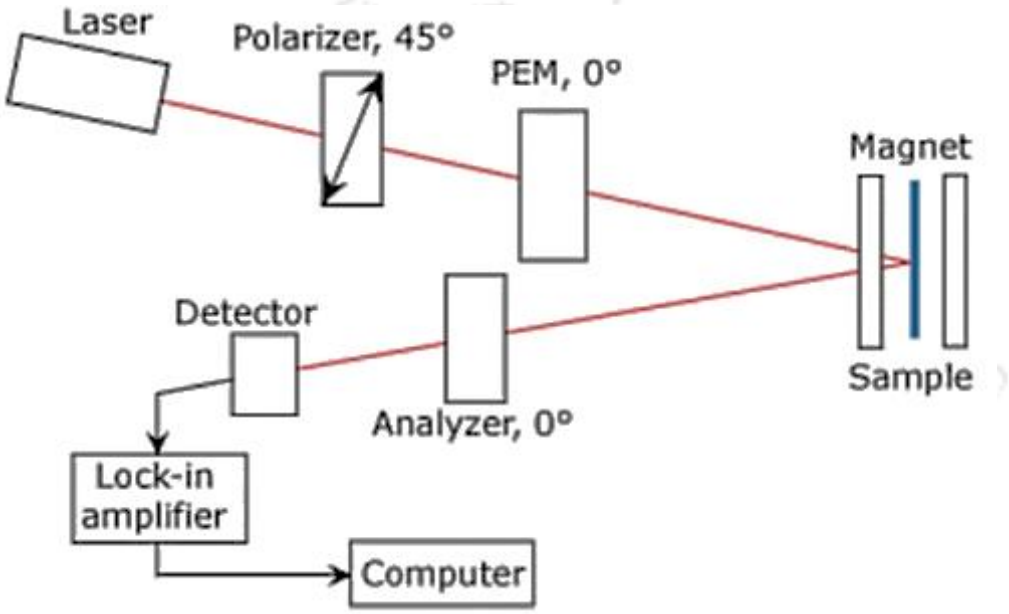

Figure 3.14: Schematic drawing of MOKE set up.

To produce a Lorentz movement that leads to detectable Kerr rotation, an appropriate direction of light incidence and polarization has to be selected for a given magnetization direction. As a simple rule, the Kerr rotation is proportional to the magnetization component parallel to the reflected beam of light. This rule implies that domains that are magnetized parallel to the sample surface require oblique light incidence and that for maximum rotation the plane of incidence must be parallel to the axis of magnetization with the polarizer set either parallel or orthogonal to the incidence plane (longitudinal Kerr effect, $\vartheta \neq 0$). The Kerr amplitude is then proportional to the sine of the angle of incidence ϑ, and therefore disappears for perpendicular incidence. In this case, maximum rotation is exhibited by domains that are magnetized perpendicularly to the sample surface (polar Kerr effect, $\vartheta = 0$), while in-plane domains do not cause a Kerr amplitude. At oblique incidence, both in-plane and out-of-plane magnetization components

generate a superimposed Kerr contrast. The separation of the two components is possible by proper difference images that are obtained at different microscope settings. Also, the transverse Kerr effect leads to in-plane magnetization sensitivity. Here, the in-plane *m* vector is normal to the plane of (oblique) incidence. Light with *E* parallel to this plane generates Kerr amplitude, but its polarization direction is the same as that of the normally reflected beam. The transverse Kerr effect thus causes an amplitude variation, which can be used for measuring purposes. A rotation that is detectable by an analyzer is obtained when the incident light is polarized at 45^{o} to the plane of incidence. Here, the *E* component perpendicular to the incidence plane is not affected, while the parallel component is modulated in its amplitude on reflection, leading to polarization rotation by superposition [SCHA2007, HUBE2014].

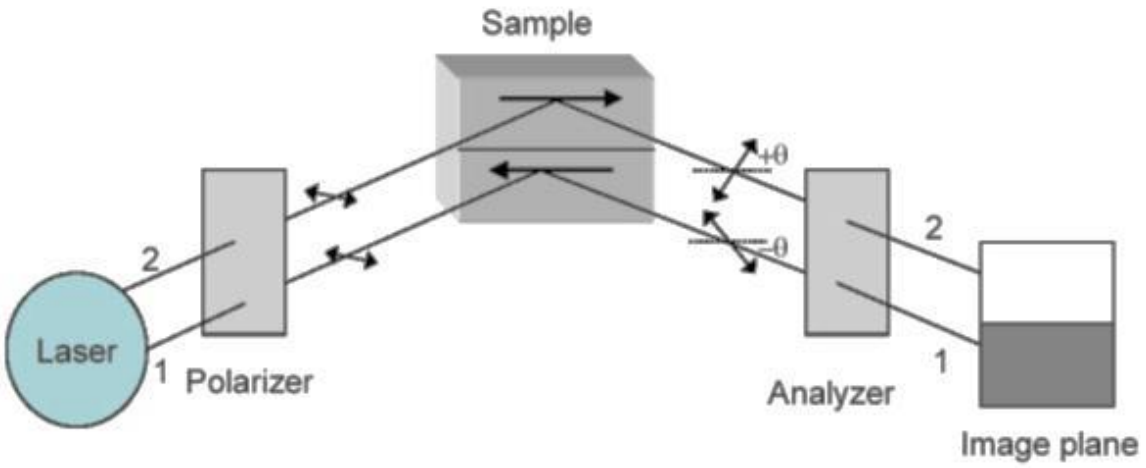

Figure 3.15: Schematic drawing of Kerr microscope.

Kerr microscopy allows the imaging of magnetic domain and magnetization processes in an optical polarization microscope. This is also based on the MOKE, but only with the difference that the domains are directly imaged. A schematic picture of the setup is shown in Figure 3.15. In this set up, the light from a source passes through a polarizer which transmits only plane polarized light. This polarized light is then allowed to fall on the sample. The resulting light in the image plane strongly depends on the magnetization of the sample. For example, let us consider a simple case of two domain states which are antiparallel to each other as indicated by arrows in Figure 3.15. After reflection from the sample, the plane of polarization of beam 1 is rotated one way by certain angle $-\theta$ and that of beam 2 is rotated by angle $+\theta$, as they encountered oppositely magnetized domains. The light then passes through an analyzer and into a camera to make images. Here, the analyzer

is rotated until it is crossed with respect to the reflected beam 1 and the beam is therefore extinguished and the lower domain appears dark. At the same time, the analyzer is not crossed with respect to beam 2 and thus beam 2 is not extinguished, resulting the upper domain as light one. This is the mechanism to find a contrast between two different domains.

Figure 3.16: Photograph-of the Kerr microscope (Evico Magnetics Ltd. Germany) used in the present study.

In the present study, magnetic domain images and Kerr loops were obtained using a MOKE microscope (Evico Magnetics Ltd., Germany) as shown in Figure 3.16. Imaging was performed using linearly polarized light with white LED as source. Magnetic domain images were observed in both branches of hysteresis loop in longitudinal MOKE mode. Hysteresis accompanied by simultaneous imaging has been performed for magnetic fields applied along various in-plane directions (easy and hard axes).

3.5.2. Magnetic force microscope

The magnetic force microscope (MFM) is a special mode of operation of the atomic force microscope (AFM). In this technique, a sharp magnetized tip is brought close to a sample and interacts with the magnetic stray fields near the surface, as shown in Figure 3.17. The tip-sample magnetic interactions are detected and used to reconstruct the magnetic structure of the sample surface. Many kinds of magnetic interactions are measured by MFM, including magnetic dipole–dipole interaction. MFM scanning often uses non-contact AFM

mode. MFM was introduced shortly after the invention of the AFM [MART1987]. This technique became popular as a technique that offers high imaging resolution without a special need for sample preparation or environmental conditions. The operating principle of an MFM is similar to that of an AFM. Both static and dynamic detection modes can be applied.

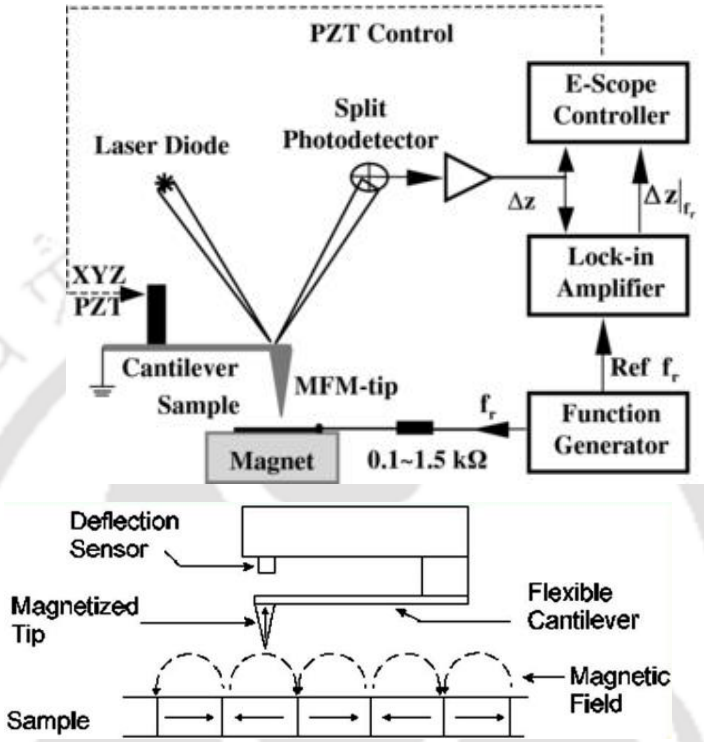

Figure 3.17: Schematic drawing of an MFM set up and field lines realized by the tip from the sample surface.

The cantilever is excited to vibrate close to its resonance frequency, with a certain amplitude and a phase shift with respect to the drive signal. The deflection sensor of the microscope monitors the motion of the tip. Under the influence of a probe-sample interaction, the cantilever behaves as if it had a modified spring constant, $c_F = c - \partial F/\partial z$. An attractive interaction with $\partial F/\partial z > 0$ makes the cantilever spring softer such that the resonance frequency decreases. This leads to a change of the oscillation amplitude of the probe and of its phase, which can be measured to map by the lateral variation of $\partial F/\partial z$. The force derivative $\partial F/\partial z$ originates from a wide range of sources, including electrostatic probe-sample interactions, van der Waals forces, damping, or capillary forces [PORT1998]. However, MFM relies on those forces that arise from a long-range magnetostatic coupling between probe and sample. This coupling depends on the internal magnetic structure of the probe, which greatly complicates the mechanism of contrast formation.

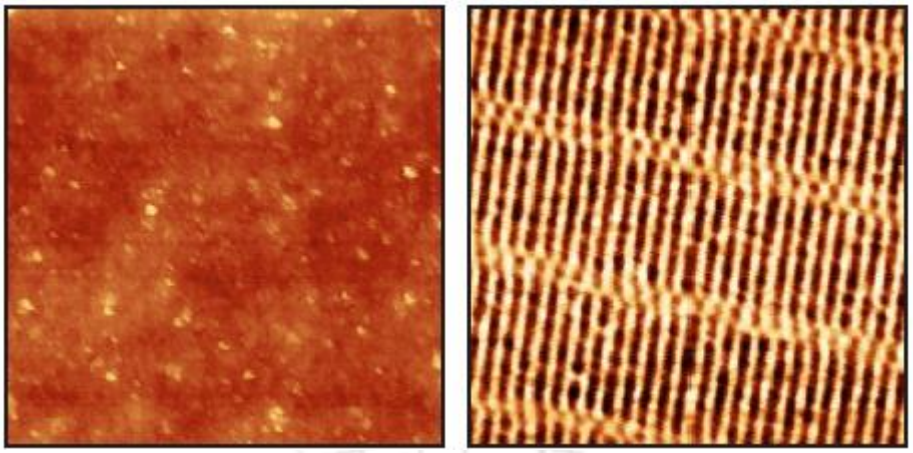

Figure 3.18: Typical AFM and MFM images (40×40 μm^2) of zip disk.

The cantilever/tip assembly is obviously the critical element of a magnetic force microscope [RUGA1998]. In addition, the tip shape is important due to the long-range nature of magnetic forces. Originally, electrochemically etched wires of cobalt or nickel were used as cantilevers [MART1987]. Recently, cantilevers with integrated sharp tips are fabricated in large numbers out of silicon-based materials. These tips can be coated with a thin layer of magnetic material for the purpose of MFM observations. A lot of effort has been spent on the optimization of magnetic tips in order to get quantitative information from MFM data [RUGA1998, HART1999]. However, the major problem with the coated conventional tips is that the magnetic domain pattern reduces the effective magnetic moment of the tip. As a result, the exact domain structure is unknown and can even change during MFM operation. The spatial resolution in MFM imaging is related to the tip-sample distance, but also to the magnetized part of the tip that is actually exposed to the sample stray field. To improve lateral resolution, it is beneficial to restrict the magnetically sensitive region to the smallest possible size. In ideal case, the effective volume of the probe would consist of a small single-domain ferromagnetic particle located at the probe apex. However, there is a physical lower limit for the dimensions because an ultra-small particle becomes superparamagnetic. The demand for a strong signal, produced by a small sensitive volume, indicates the need to maximize the magnetic moment in the tip. Hence, recently, the tips coated with 10 -150 nm of CoCr alloy are used as standard probes for an MFM. The typical AFM and MFM images of a zip disk are shown in Figure 3.18.

Chapter 4

Magnetic properties of single-layer and multilayer structured CoFeB thin films

भारतीय प्रौद्योगिकी संस्थान गुवाहाटी
Indian Institute of Technology Guwahati

4.1. Introduction

Recently, CoFeB based alloy thin film is found to be one of the pioneering materials for various applications [IKED2008, KODZ2012, KIMJ2013, TORR2014] such as magnetic tunnel junctions (MTJ) [IKED2010], magnetic random access memory [NAIK2012] and spin-logic based devices [SULI2015], as they exhibit extremely large tunnelling magnetoresistance (TMR) at room temperature in a stack structure of CoFeB/MgO(001)/ CoFeB. Hence, extensive studies have been carried out on CoFeB films to understand magnetic domain structure [YAMA2011], spin polarization [PALU2006], ferromagnetic resonance and damping properties [LIUX20111] and corrosion properties [PARK2011]. However, it is revealed from literature that most of the reported works on CoFeB films have focused mainly on tuning the magnetic properties of ultrathin films from application point of view and there are only a few reports available on the thickness dependent magnetic properties of CoFeB films from the fundamental point of view [KIPG2012, CHEN2013].

For instance, Kipgen et al. [KIPG2012] reported the structural and magnetic properties of $Co_{20}Fe_{60}B_{20}$ films in the thickness range of 5 - 50 nm prepared by ion-beam sputtering. Chen et al. [CHEN2013] presented the electric, magnetic, thermal and adhesive properties of amorphous $Co_{60}Fe_{20}B_{20}$ thin films over the thickness range of 100 - 500 nm prepared on glass substrates using DC magnetron sputtering technique. Thicker CoFeB based films were also grown on flexible substrates to investigate the influence of strain on the magnetic anisotropy of CoFeB films with applications in flexible electronics in mind [YANG2013, TANG2014, QIAO2016]. In addition, thick CoFeB based films with high in-plane magnetic anisotropy field as well as high saturation magnetization have been used as soft magnetic underlayers for obtaining high signal to noise ratio in perpendicular magnetic recording media [ITOS2005, PIRA2007]. The above studies reveal that most of the earlier reported works have been focused for studying the magnetic properties of the films at random thicknesses using different fabrication processes. However, no systematic study has been carried out to understand the thickness dependent magnetic properties of CoFeB alloy films over a wide range of thickness prepared by a single preparation technique. Naik et al. [NAIK2012] recently reported the effect of an ultra-thin Ta layer insertion in the CoFeB films on the magnetic and TMR properties of CoFeB-MgO system and showed that the effective magnetic anisotropy can be doubled and thermal stability is enhanced by a factor of 2.5 with Ta insertion. Sato et al. [SATO2012] have also reported the increase of thermal stability factor of MTJ by the insertion of Ta in CoFeB films. Nevertheless, the systematic investigation of effects of number of multilayers and thickness of spacer layer and CoFeB

layer on the magnetic properties and interlayer coupling between the CoFeB layers of the multilayer films have not been well addressed so far.

Hence, in this study, we report (i) thickness dependent magnetic properties of single-layer $Co_{40}Fe_{40}B_{20}$ (x nm) films in amorphous form over a wide range of thickness from 10 to 200 nm at first and then (ii) tuning the magnetic properties of $Co_{40}Fe_{40}B_{20}$ films at higher thicknesses by utilizing multilayer structure of [CoFeB (y nm)/ Ta (z nm)]$_n$/ CoFeB (y nm), as presented in literature [NAKA1997, NAOE1998, HUAN2001, NAKA2001, MISH2011], with a careful variation of thickness of CoFeB and Ta layers.

4.2. Experimental details

Amorphous $Co_{40}Fe_{40}B_{20}$ (CoFeB) single-layer films with different thicknesses (x = 10 to 200 nm) and the multilayer [CoFeB (y nm)/Ta (z nm)]$_n$/ CoFeB (y nm) films with different thicknesses of Ta spacer layer and CoFeB ferromagnetic layer are deposited using DC magnetron sputtering technique. All the films are deposited at ambient temperature directly on thermally oxidized Si substrate. The base pressure of the chamber is maintained to be better than 1×10^{-4} Pa. The sputtering Ar gas pressure for CoFeB and Ta layers is optimized at 1.33 Pa. The optimization of Ar gas pressure is done mainly by analysing the structural and variation in the magnetic properties of the single-layer and multilayer films. The distance between the target and the substrate is optimized at 0.1 m and the substrate is rotated uniformly for obtaining homogeneous films. The deposition rate is pre-calibrated using ex-situ surface profilometer (Veeco, Dektak 150 model) and found to be 1.2 Å/s and 0.5 Å/s for the deposition of CoFeB and Ta layers, respectively. The thickness of the individual CoFeB layer in multilayer films is controlled using the relation (as demonstrated in literature [NAKA1997, NAOE1998, HUAN2001, NAKA2001, MISH2011]): $y = 200/(n+1)$, where n is the number of multilayers varied between 0 and 3, and z is the spacer layer thickness controlled between 0 and 2 nm.

Amorphous nature of the films is confirmed by X-ray diffraction (XRD) recorded using a high-power X-ray diffractometer (Rigaku TTRAX III, 18 kW) with Cu-K_α radiation (λ = 1.541 Å) and transmission electron microscopy (TEM, Jeol 2100 and Technai G2 F20) techniques. X-ray reflectivity (XRR) technique is used to reconfirm the estimated film thickness from ex-situ surface profilometer. Surface topography of the films is analysed using atomic force microscopy technique. Magnetic properties of the films are analysed using vibrating sample magnetometer (VSM, LakeShore Model 7410) by performing (i)

magnetic hysteresis loops (*M-H*) at room temperature, (ii) thermomagnetization (*M-T*) measurements at a constant field over a temperature range of 300 K to 650 K and (iii) temperature dependent *M-H* loop between the temperature range of 30 K and 300 K. Magnetic domain images and Kerr loops are obtained using a magneto-optic Kerr effect (MOKE) microscope (Evico Magnetics Ltd, Germany). Imaging was performed using linearly polarized light with a white LED source. Magnetic domain images are observed in both branches of hysteresis cycle in the longitudinal MOKE mode. Both hysteresis loops and domain images are simultaneously recorded for magnetic fields applied along in-plane directions [easy (0°) and hard (90°) axes].

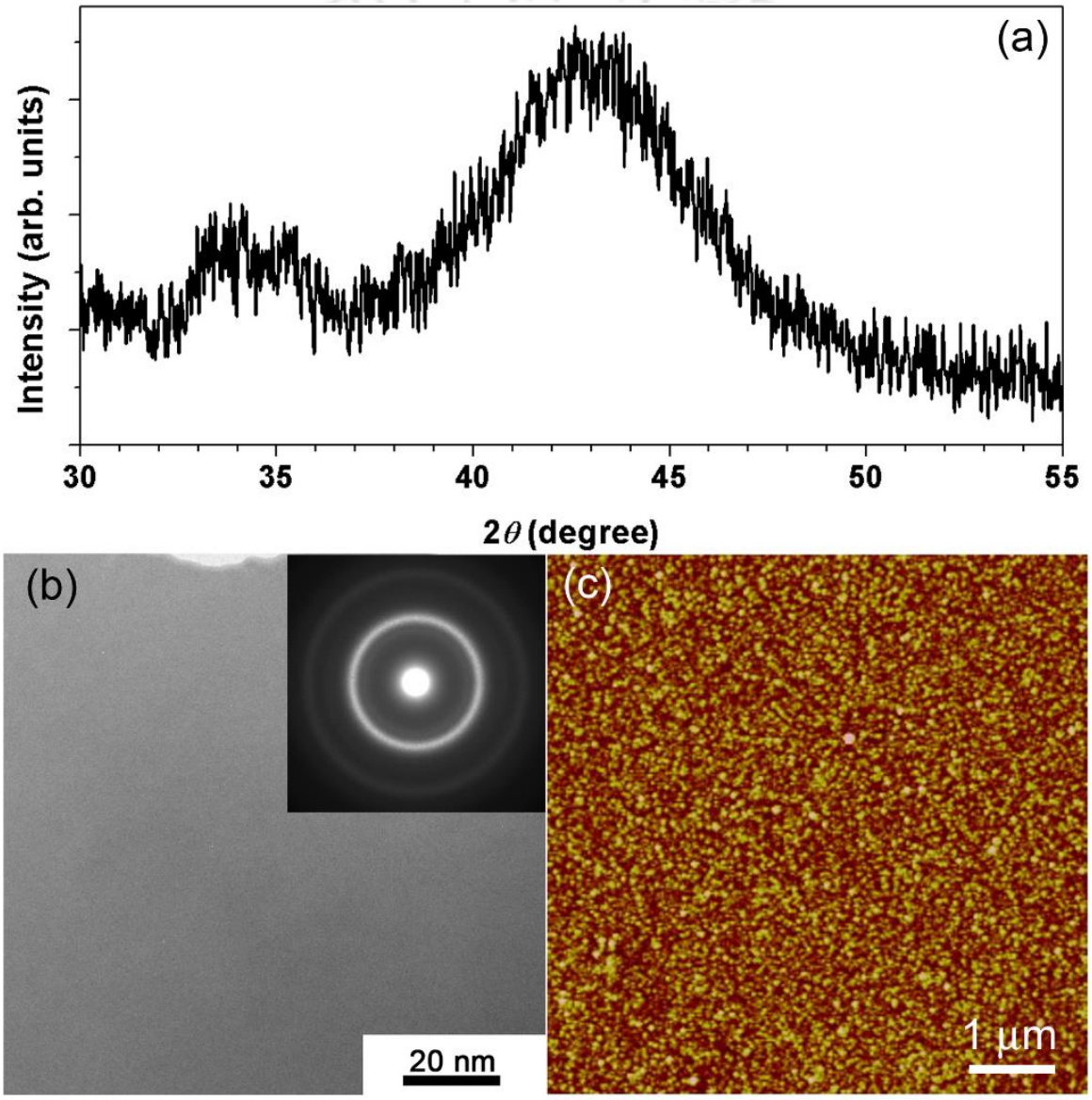

Figure 4.01: Room temperature (a) XRD pattern, (b) bright field TEM image and selected area electron diffraction pattern and (c) AFM image for CoFeB (200 nm) film.

4.3. Results and discussion

4.3.1. Properties of single-layer CoFeB thin films

4.3.1.1. Structural properties

Figure 4.01 displays typical XRD pattern, bright-field TEM image and selected area electron diffraction (SAED) pattern, and AFM image of the as-deposited single-layer CoFeB (200 nm) film. It is clearly seen that as-deposited film exhibits only a broad peak at around $2\theta =$ 44° without any other peaks corresponding to other crystalline phases. It may be noted that the XRD peak observed at 2θ = 33.05° represents Si(200) peak emanating from the Si substrate [CHOM2001]. The bright-field TEM image and the SAED pattern reveal the plain and even contrast microstructure, devoid of any local lattice fringes and halo diffraction rings, respectively. These results confirm that the as-deposited CoFeB films exhibit amorphous structure. The observed results are in good agreement with the earlier reports on similar systems [YOUC2008, DEMA2016]. AFM topography image shows the existence of very fine and sparsely dispersed nanosized grains of size ranging between 10 and 15 nm in the as-deposited films. In addition, the film exhibits a very clear uniform surface and the average roughness of the surface is found to be in the range of 0.4 -0.7 nm for CoFeB (200 nm) films.

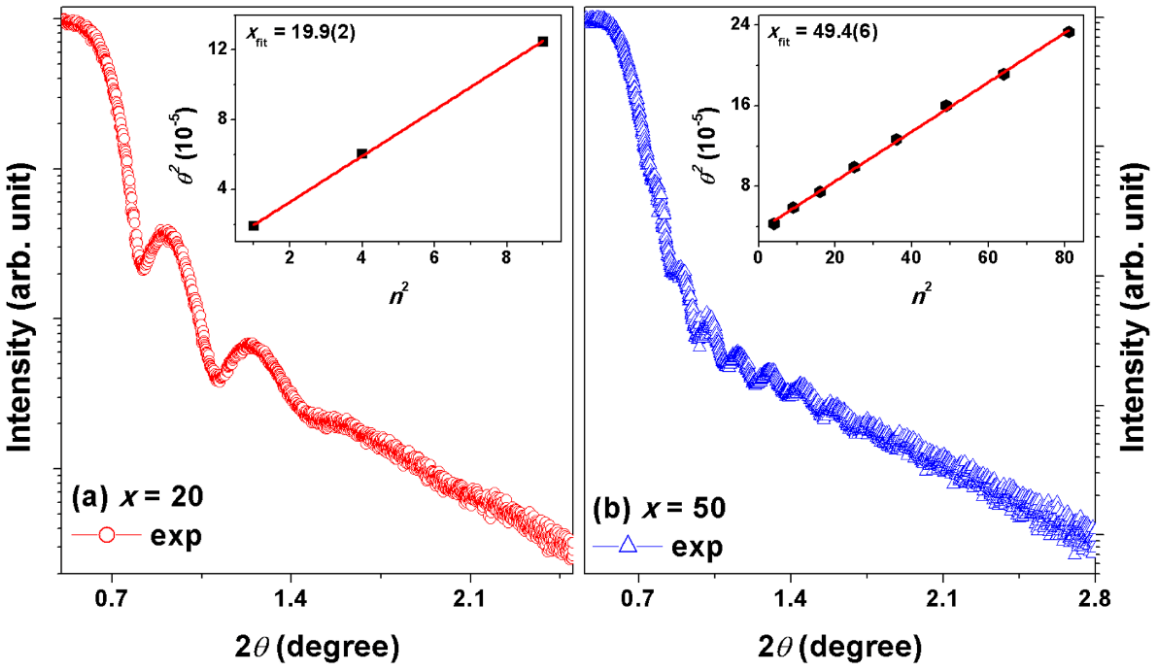

Figure 4.02: Room temperature XRR pattern for CoFeB (x nm) films with (a) x = 20 and (b) x = 50. Insets: plot of θ^2 versus n^2 for films with (a) x = 20 and (b) x = 50.

It is well known that XRR is a non-destructive and non-contact technique for studying the detailed surface properties and thickness determination of films (between 2 nm and 100 nm with a precision of about 1 -3 Å). Hence, to ensure pre-calibrated film thickness from the ex-situ surface profilometer, XRR curves are recorded for as-deposited CoFeB films and the typical curves are presented in Figure 4.02 for selected thicknesses (x = 20 and 50). The interference pattern (open symbol) with clear oscillation peaks is observed for all the as-deposited films. With increasing 2θ, the oscillation intensity decreases and attains the same level as the noise in the higher angle region. With increasing x, the number of oscillation peaks increases and peak width decreases systematically. The experimental film thickness is verified analytically by using Savitzky–Golay (SG) algorithm as described in eqn.(4.01) [SERA2011].

$$\theta^2 = \frac{\lambda^2}{4x^2} n^2 + 2\delta \qquad (4.01)$$

where θ is the Bragg angle, λ is the X-ray wavelength of the Cu-K$_\alpha$ radiation, x is the thickness of the film, n is the number of XRR maxima and δ is the dispersion factor of X-ray beam. The values of θ and n are extracted from the XRR curves and plotted as θ^2 *vs* n^2 typically for CoFeB films with x = 20 and 50 nm in the insets of Figure 4.02. The experimental data show almost linear behaviour and the fit to the data using eqn.(4.01) provides the values of 2δ from the intercept and $\lambda^2/(4x^2)$ from the slope. Subsequently, x is determined from the slope and found to be 19.9±0.2 nm and 49.4±0.6 nm for x = 20 and 50, respectively. Since the resolution of this method depends on the accuracy of position determination of the maxima of the diffraction peaks, thickness calculated from the SG algorithm is slightly different from estimated thickness, but lies within the error values. Nevertheless, the values of x determined from SG algorithm are in close agreement with the predicted thickness using pre-calibrated deposition rate.

4.3.1.2. Room temperature magnetic properties

Figure 4.03 depicts the room temperature normalized in-plane *M-H* loops of the CoFeB (x = 10 – 200 nm) films. It is observed that (i) CoFeB films with x < 30 nm exhibit either a rectangular shaped loop with remanence ratio (M_R/M_S, M_R – remanent magnetization and M_S – saturation magnetization) of more than 75 % or a flat type loop. In addition, the loops saturate at lower applied magnetic fields. (ii) Upon increasing $x \geq 67$ nm, the loop shape changes into different nature, i.e., the *M-H* loops are constituted by two distinct

magnetization phases: (a) in-plane magnetic component, which reverses quickly at fields close to H_C and (b) perpendicular component, which rotates progressively under the application of magnetic field and results in an almost linear approach to saturation. Therefore, the value of saturation field (H_S) increases largely (> 16 kA/m) [CRAU2002, YUJU2002, HUBE2014].

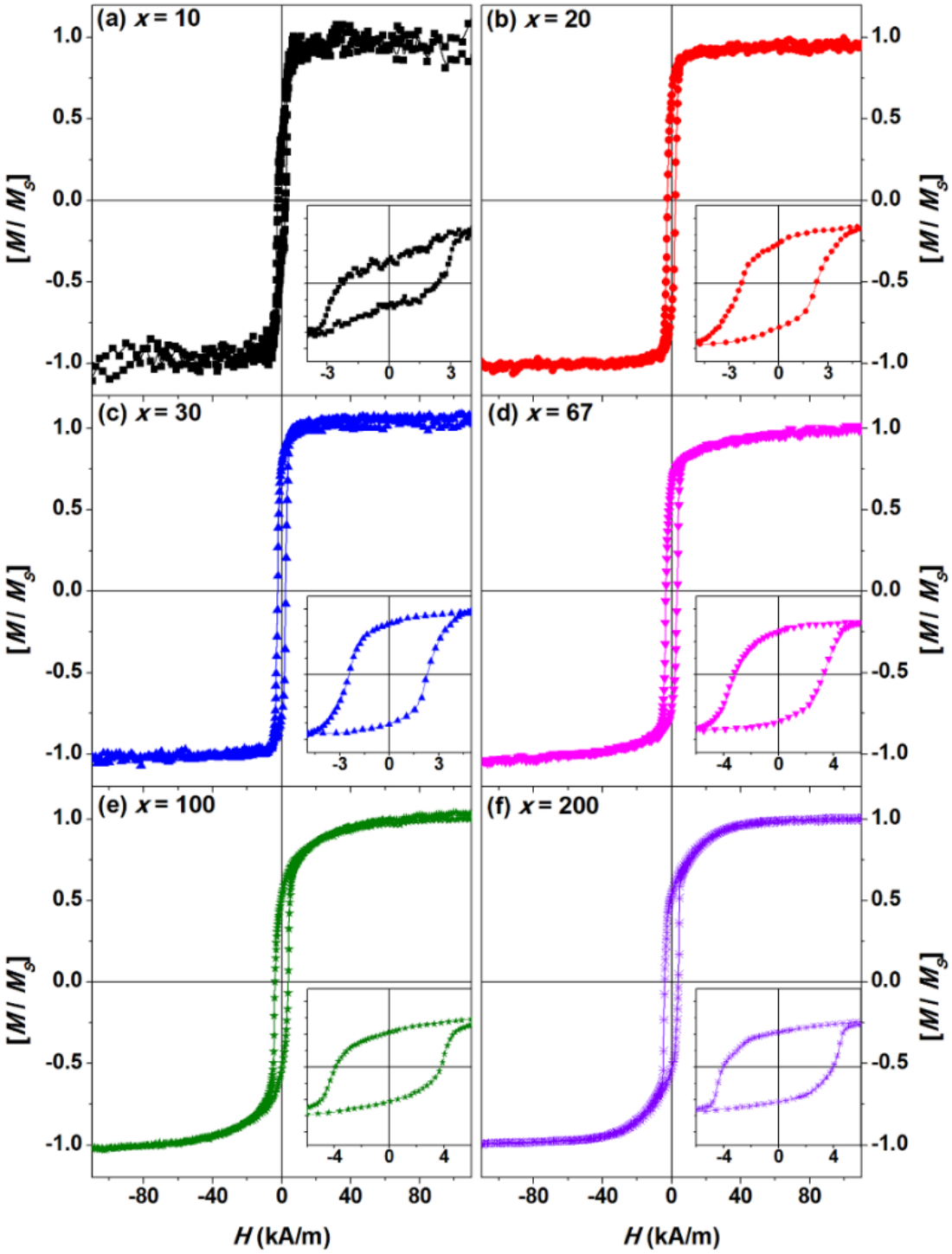

Figure 4.03: Room temperature normalized *M-H* loops measured along the film plane for CoFeB (*x* nm) films with different thicknesses (*x* = 10 – 200).

This particular hysteresis loop shape has been referred to as a transcritical loop and correlated to the development of effective magnetic anisotropy caused by the stress induced during the deposition of the films at a higher deposition rate to form amorphous nature [MURA1966, CRAU2002, PRAD2004, SHAR2006, COIS2009, MISH2011]. This leads to the formation of stripe domain patterns ($x \geq 67$ nm) in the as-deposited films. It may be noted that this type of effective magnetic anisotropy is different from the perpendicular magnetic anisotropy reported for ultrathin (< 2 nm) CoFeB films originating mainly due to the interfacial nature. (iii) The relative magnitude of in-plane components decreases with increasing CoFeB film thickness. As a result, the magnitude of magnetization reversing close to H_C decreases with increasing the thickness of CoFeB film.

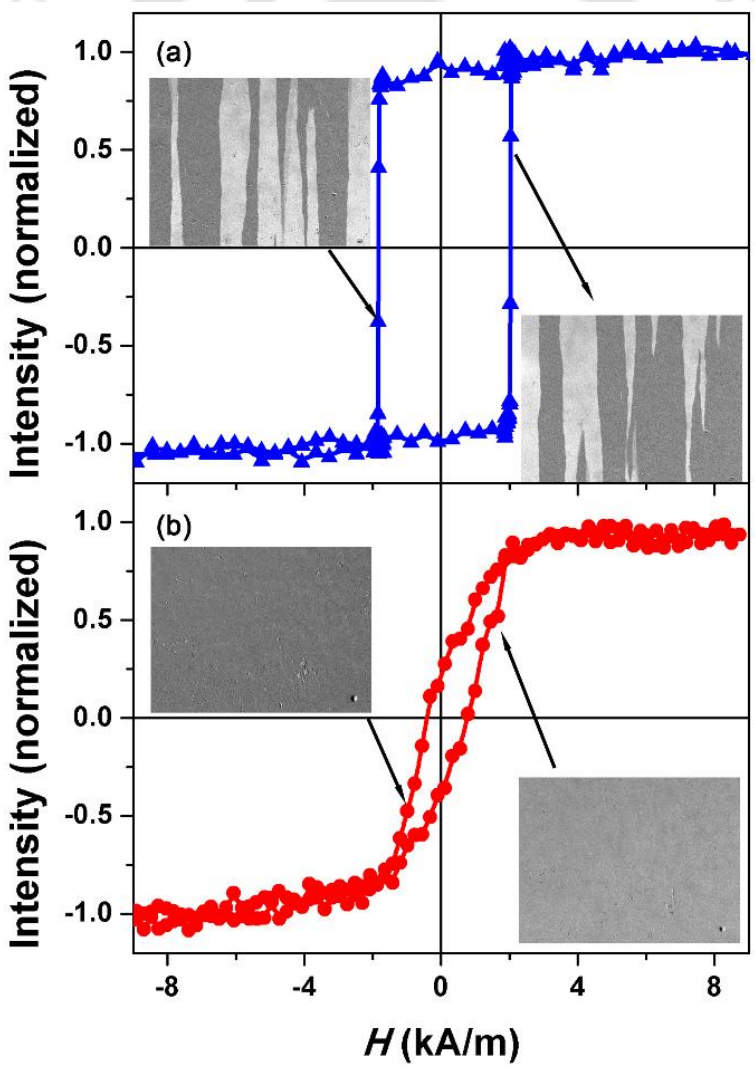

Figure 4.04: Room temperature normalized Kerr loops and magnetic domain images for CoFeB (20 nm) film measured along (a) easy-axis (H = 0°) and (b) hard-axis (H = 90°) in the film plane.

These results suggest that CoFeB films with $x < 30$ nm exhibit in-plane anisotropy, which is caused by the formation of aligned ferromagnetic atom pairs due to their strong magnetic exchange coupling during deposition process. It is parallel to the in-plane axis and resulting in the domains with magnetization parallel to the film plane. Such arrangement of in-plane orientation of magnetization provides either rectangular shaped loops when the loops are recorded along the easy-axis or flat type loops when the loops are recorded along the hard-axis of magnetization, which leads to a symmetrical structure of transverse domains in the plane.

In order to confirm the nature of magnetic domain structure for the CoFeB films with $x < 30$ nm, magnetic domain images and Kerr loops were obtained using the MOKE microscope with the applied field along the film plane and depicted in Figure 4.04 for CoFeB (20 nm) film. It is clearly evident that the film exhibits a rectangular hysteresis in one direction (easy-axis, see Figure 4.04a) and flat type loop characterized by a central range of constant slope combined with a low remanence and a loop around the origin in another direction (hard-axis, see Figure 4.04b). In the easy-axis direction, the domain images show a rapid switching of large sized domains with the applied field, while the domain images along the hard-axis reveal typical magnetization reversal through coherent rotation process. These results support the existence of in-plane uniaxial anisotropy in CoFeB films with $x <$ 30 nm. It may be noted that all the films are deposited at high deposition rates to form amorphous nature. Hence, they are expected to have stress quenched during the deposition and result in the development of degree of local magnetic disorder in the easy-axis. However, the observed results confirm that the magnetization lies mainly within the plane of the films. Accordingly, uniaxial anisotropy (K_U) is calculated using equation (4.02).

$$K_U = \frac{M_S H_K}{2} \qquad (4.02)$$

where H_K is the anisotropy field. The determined values of K_U listed in Table 4.01 show a continuous increase up to $x = 20$ nm and then decrease slightly for $x = 30$ nm. This reveals that the stress induced local magnetic disorder in these thin CoFeB films is not sufficient to overcome the in-plane anisotropy. Upon increasing the film thickness continuously beyond critical thickness (≥ 67 nm), the stress induced effective magnetic anisotropy overcomes in-plane anisotropy and increases the degree of local magnetic disorder in the easy-axis. This results in two different magnetic components and exhibits two distinct magnetization reversal processes.

Table 4.01: The thickness dependent H_K, H_S, K_U, $\mu_0 M_S$, K_{eff}, δ and θ_1 for CoFeB films.

CoFeB thickness (x nm)	H_K (or) H_S (kA/m)	K_U (kJ/m^3)	$\mu_0 M_S$ (mT)	K_{eff} (kJ/m^3)	δ (nm)	θ_1 (°)
10	6.36(4)	2.25(6)	708(2)	-	-	-
20	7.24(5)	3.46(2)	830(3)	-	-	-
30	8.12(6)	3.18(7)	785(4)	-	-	-
67	15.09(5)	-	760(3)	143(2)	74.1(3)	28.1(3)
100	30.33(6)	-	770(2)	154(3)	88.8(1)	41.9(2)
200	38.28(8)	-	857(2)	163(2)	123.9(2)	47.1(4)

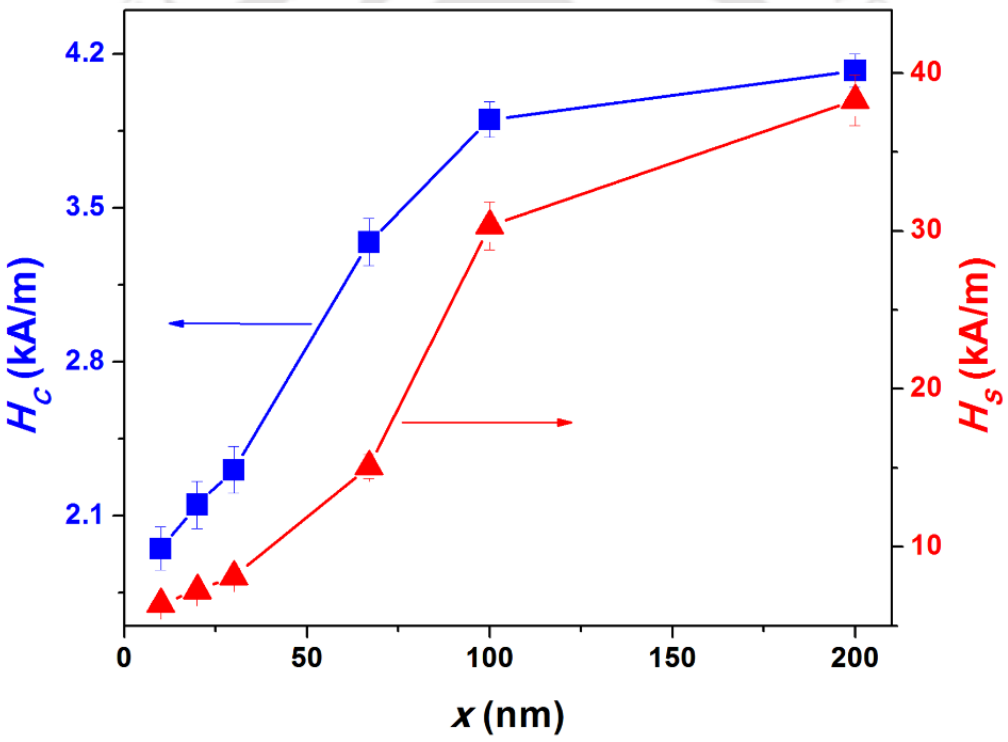

Figure 4.05: The variations of H_C and H_S as a function of CoFeB film thickness.

To understand thickness dependent magnetic properties, the values of H_C and H_S are extracted from *M-H* loops and shown in Figure 4.05. H_C increases gradually from about 1.99 kA/m to 2.30 kA/m with increasing x from 10 to 30 nm, respectively, followed by a rapid increase to nearly 3.98 kA/m for 100 nm thick CoFeB film. On further increasing x to 200 nm, H_C tends to saturate (~ 4.14 kA/m). Similarly, H_S increases weakly with increasing x up to 30 nm and then increases largely for higher values of x. As discussed earlier, the slow increase in H_C for lower thickness CoFeB films is mainly due to the in-plane

orientation of magnetization, while the rapid increase in H_C for $x \geq 67$ nm could be correlated to the development of effective magnetic anisotropy, resulting in two magnetic components and forming dense stripe domain in the as-deposited films. These results clearly state that room temperature soft magnetic properties of amorphous CoFeB films are degraded noticeably at larger thicknesses due to the change in the domain structure [MURA1966, PRAD2004, SHAR2006, COIS2009]. Sharma et al. [SHAR2006] and Coisson et al. [COIS2009] demonstrated that the transcritical loop is more pronounced in the films deposited at ambient temperature than the films deposited at elevated substrate temperatures. The development of dense stripe domain for higher thickness CoFeB films can be explained using the model proposed by Craus et al. [CRAU2002] following the original model proposed by Murayama [MURA1966] and Alvarez-Prado et al. [PRAD2004].

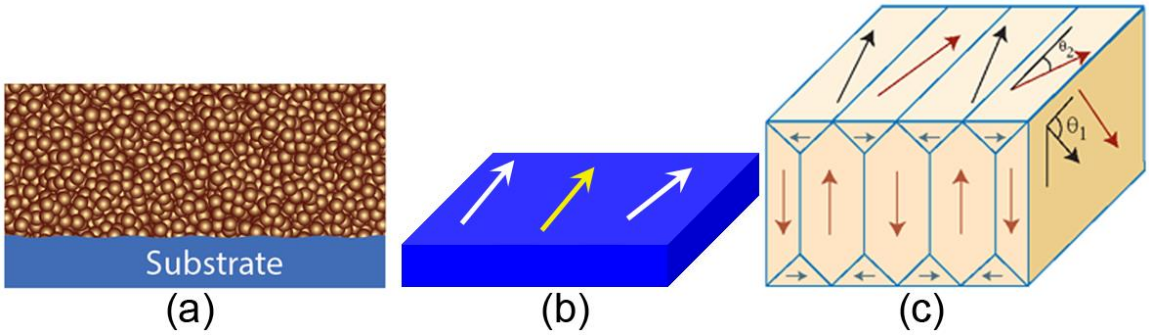

Figure 4.06: Schematic diagram of (a) amorphous nature of the film, (b) film having in-plane magnetization ($x \leq 67$ nm) and (c) dense stipe domain for thicker film ($x \geq 67$ nm) for CoFeB (x nm) film.

According to the model, the bulk domains, making an angle θ_1 with the surface domains (see Figure 4.06c), play a crucial role on the resulting magnetic properties of the thicker films. The angle θ_1 can be determined either from Mössbauer data [CRAU2002] or from the remanent magnetization (M_R) data measured using the VSM under the condition that the magnetization in the closure domains remains perpendicular to the direction of the applied magnetic field such that $\theta_2 = 90°$. The value of θ_1 can vary between 0 and 90° depending on the value of fractional change in the M_R with respect to M_S [CRAU2003]. By accounting into the continuous development of stress in the as-deposited films with increasing film thickness, there exists a critical thickness above which the presence of dense stripe domains strongly depends on the values of M_S and effective magnetic anisotropy constant (K_{eff}) as described in eqn.(4.03). Subsequently, the domain wall width (δ) can be

calculated using eqn.(4.04) and by assuming Landau domain structure [HUBE2014], which is compatible when the film thickness is larger than the value of $\sqrt{A/K_{eff}}$.

$$x_{critical} = \frac{2\pi}{\left(1-\frac{\mu_0 M_S H_S}{2K_{eff}}\right)}\sqrt{\frac{A}{K_{eff}}} \tag{4.03}$$

$$\delta = 2\sqrt{2x\sqrt{\frac{A}{K_{eff}}}} \tag{4.04}$$

where $x_{critical}$ is critical thickness (= 67 nm for the presently investigated films) above which the stripe domain appears depending on the values of M_S and K_{eff}, μ_0 is the absolute permeability, A is exchange stiffness constant taken as 15×10^{-12} J/m [CONC2013] and x is the thickness of the CoFeB film. The determined values of K_{eff}, δ and θ_1 are listed in Table 4.01 for CoFeB films with different thicknesses for $x \geq 67$ nm. The values of K_{eff} are found to be of the order of 10^5 J/m^3, but increase slightly with increasing film thickness from 67 to 200 nm. It is well known that the magnetic anisotropy in these films arises from magnetocrystalline anisotropy, shape anisotropy and magnetoelastic anisotropy [WANG1999]. As the as-deposited films are amorphous in nature and considering thick CoFeB films, the magnetic anisotropy is expected to be majorly due to magnetoelastic effects caused by the stress induced during the deposition. While the obtained value of K_{eff} in the presently investigated films is somewhat higher than the value reported in Fe based amorphous system [YUJU2002, COIS2008], a strong perpendicular magnetic anisotropy ranging between 0.5×10^6 J/m^3 and 2×10^6 J/m^3 has been reported for ultrathin (< 2 nm) CoFeB films [YAMA2011, MANT2013]. The first one could predominantly be related to the stress induced in higher thickness films with different magnetic metallic elements [HERZ1996, PLAT2001] and the latter one is mainly originated at the interfaces between CoFeB and other stacking films, which was further supported through micromagnetic modelling [WANG2014].

4.3.1.3. High temperature magnetic properties

To understand the stability of the ferromagnetic nature and magnetic phase transition behaviour of CoFeB films, high temperature *M-T* data were recorded at a constant applied field of 39.8 kA/m for all CoFeB film. Figure 4.07 displays the normalized *M-T* data with respect to room temperature magnetization for CoFeB (20 nm) film. It is clear from the figure that CoFeB film exhibits a large decrease in magnetization with increasing

temperature up to 550 K and then remains nearly constant until 650 K. This confirms the magnetic phase transition of the amorphous structure from ferromagnetic state and paramagnetic state. Curie temperature (T_C), determined from the thermal derivative of the magnetization data as a function of temperature, is found to be about 512 K. The obtained value of T_C is found to be significantly lower than those reported in literature for similar alloys [YAMA2011, PELL2015].

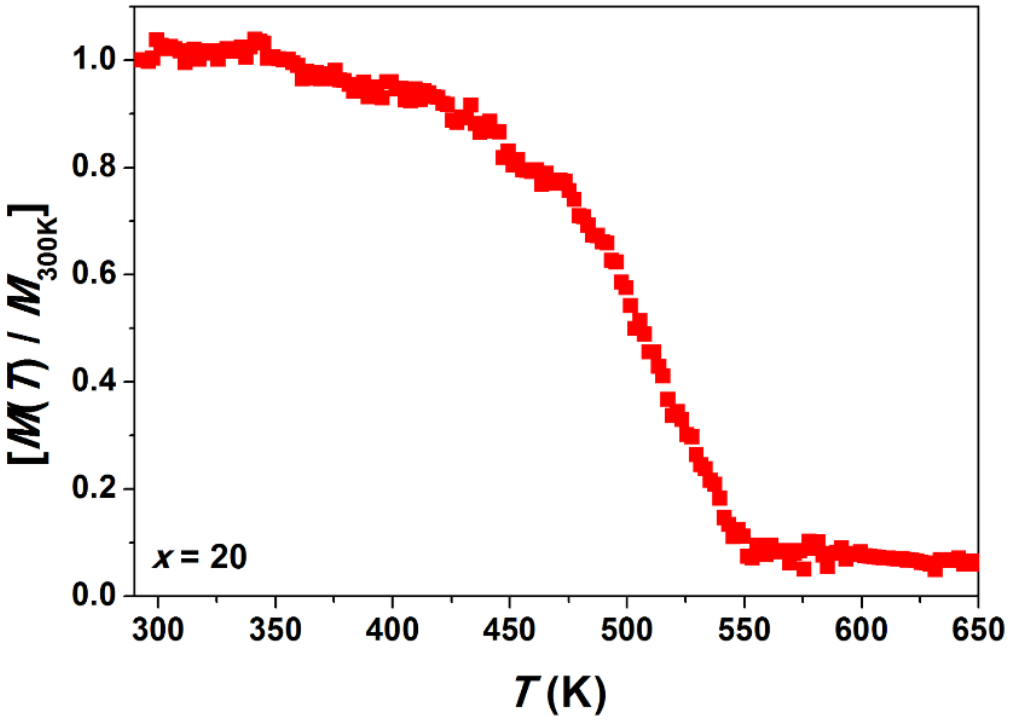

Figure 4.07: High-temperature thermomagnetization (*M-T*) data of CoFeB (20 nm) film recorded under 39.8 kA/m applied field along the film plane.

For instance, Yamanouchi et al. [YAMA2011] have reported T_C value of 728 K and 1026 K for as-deposited and annealed $Co_{20}Fe_{60}B_{20}$ films, respectively. However, they determine T_C by extrapolating temperature dependent domain wall surface energy. These results suggest that the low value of T_C in the presently investigated films could be correlated to the complete amorphous form of the films [LIUY2008, SAKU2013].

4.3.2. Properties of multilayer [CoFeB (*y* nm)/Ta (*z* nm)]$_n$/CoFeB (*y* nm) thin films

4.3.2.1. Room temperature magnetic properties

Figure 4.08 displays the schematic diagram of multilayer thin films. In these multilayer films, the total thickness of the CoFeB layer (*x*) is kept constant at *x* nm and the individual thickness of the CoFeB (*y*) layers in multilayer films is segmented typically by using the

formula, $y = x/(n+1)$, where n is the number of Ta spacer layers. For instance, if one considers x as 200 nm for single-layer film, then y in the multilayer films segmented to 100, 66.67 and 50 by taking n as 1, 2 and 3, respectively.

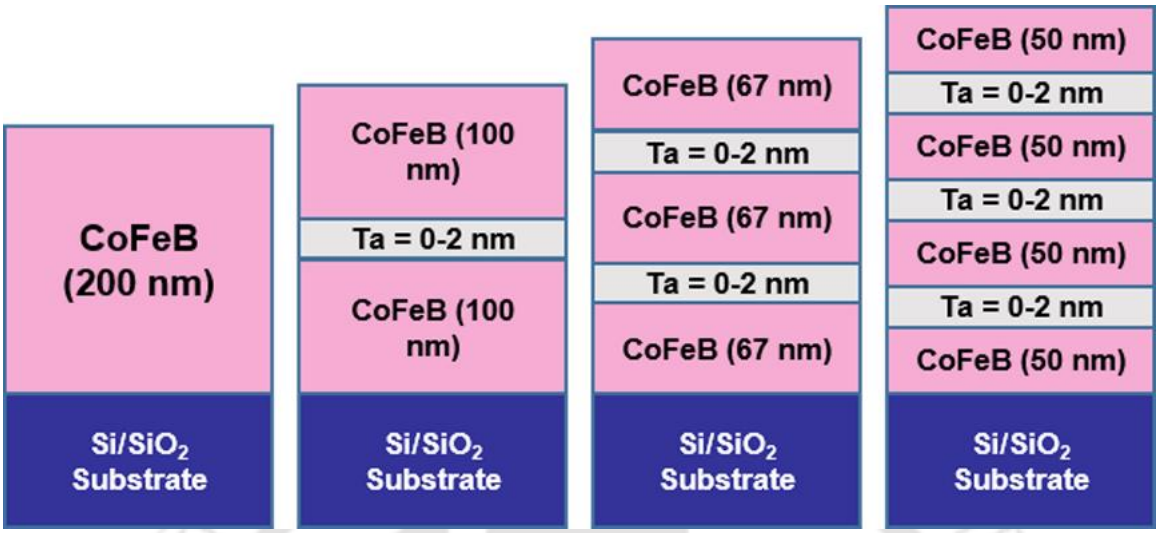

Figure 4.08: Schematic representation of multilayer [CoFeB (y nm)/Ta (z nm)]$_{n=1\text{-}3}$/CoFeB (y nm) thin film.

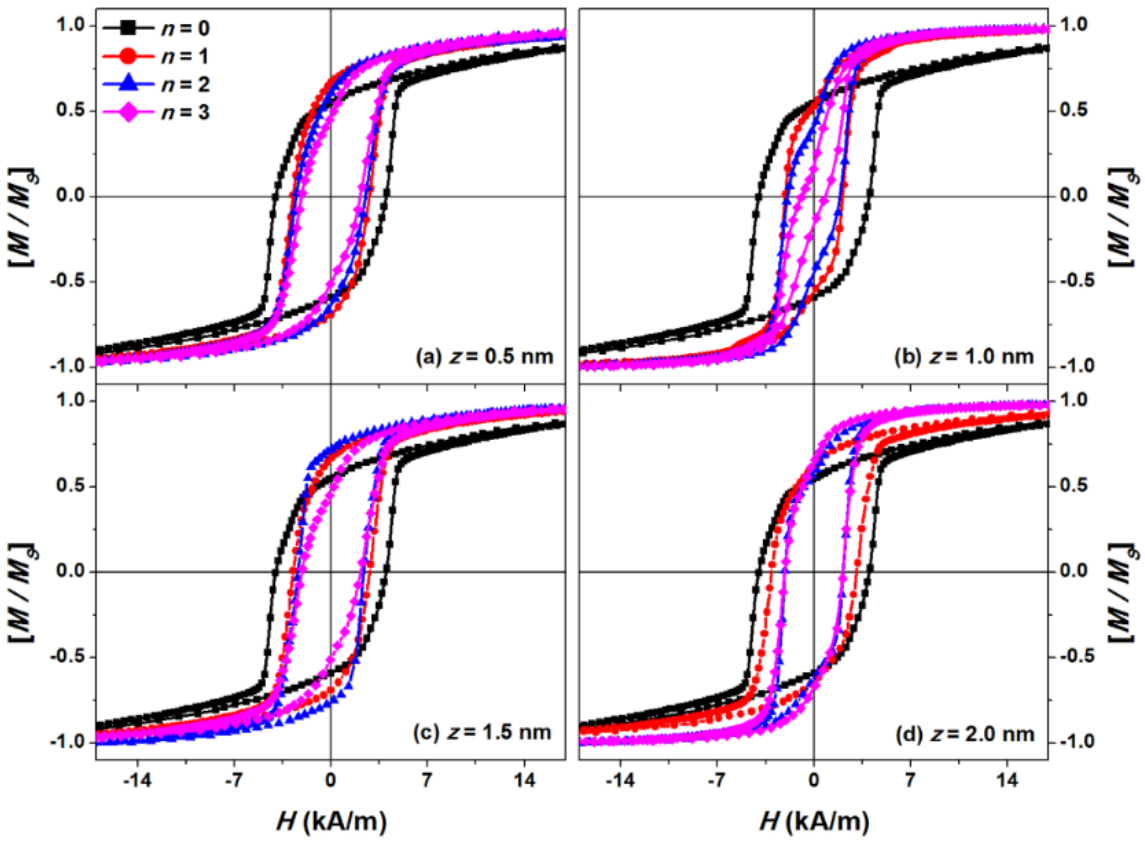

Figure 4.09: Room temperature normalized M-H loops measured along the film plane for [CoFeB (y nm)/Ta (z nm)]$_{n=0\text{-}3}$/CoFeB (y nm) films. The data are plotted by fixing the spacer layer thickness for different number of multilayers.

In order to tune the magnetic properties of CoFeB films at higher thicknesses, we have prepared multilayer films and studied the effects of number of multilayers and spacer layer thickness systematically. Figures 4.09 and 4.10 display expanded version of room temperature normalized *M-H* loops with respect to the magnetization at 39.8 kA/m (M_S) measured along the film plane for [CoFeB (*y* nm)/Ta (*z* nm)]$_{n=1\text{-}3}$/CoFeB (*y* nm) multilayer films with different values of *z* and *n*, respectively.

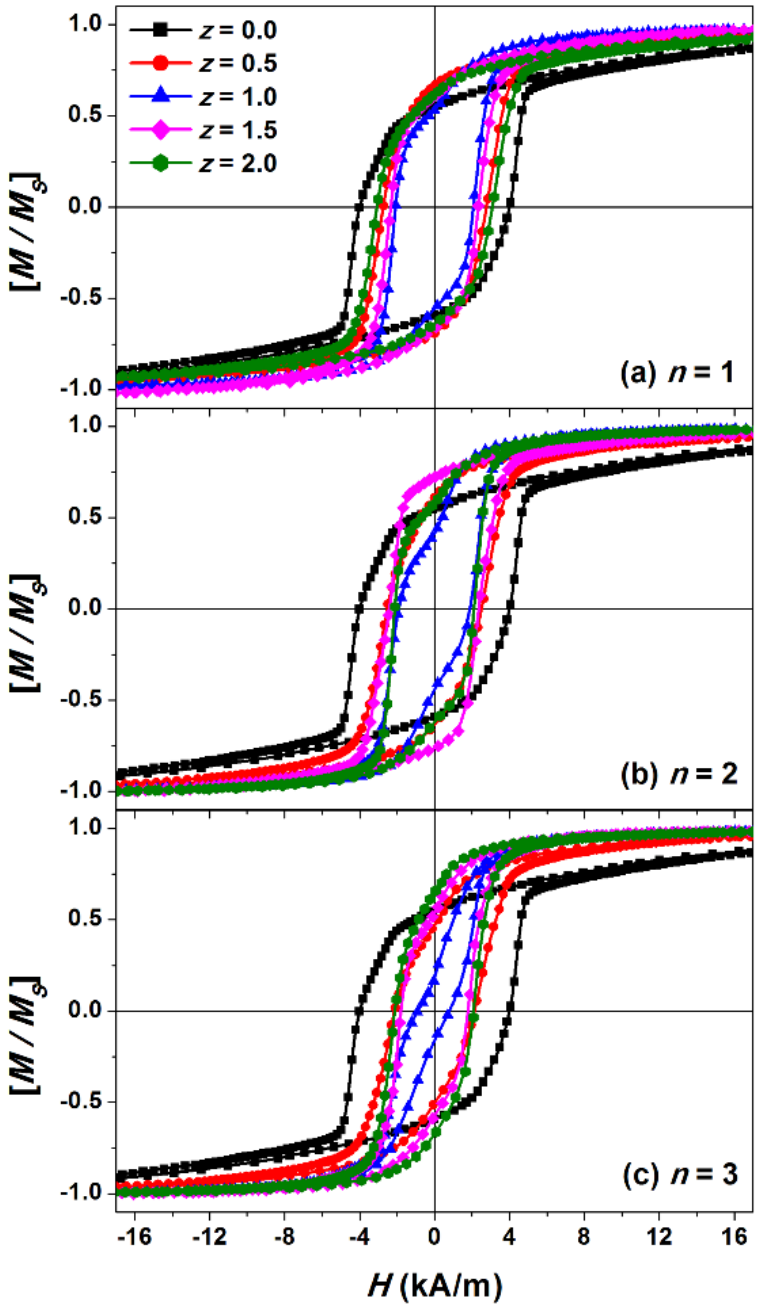

Figure 4.10:.Room temperature normalized *M-H* loops measured along the film plane for [CoFeB (*y* nm)/Ta (*z* nm)]$_{n=0\text{-}3}$/CoFeB (*y* nm) films. The data are plotted by fixing the number of multilayers for different spacer layer thicknesses.

To correlate the changes in the magnetic properties clearly, the loops are plotted either by fixing *z* for different *n* values (see Figure 4.09) or by fixing *n* for different values of *z* (see Figure 4.10). It is clear from the figures that (i) with increasing *n*, the shape of the loops transforms from transcritical one to rectangular loop and the value of H_S decreases. (ii) However, the transformation substantially depends on the value of *z*, i.e., for the films with $z \leq 1$, the loop shape changes quickly even for bilayer films, while for the films with $z > 1$, the transformation is observed to be gradual one with increasing *n*. (iii) Similarly, for the multilayer films with $n = 1$, the change in the loop shape occurs progressively with increasing *z* up to 1, but reverses towards the transcritical one on further increasing *z* (> 1). (iv) Interestingly, such reversibility process fades out with increasing $n > 1$. In addition, the transformation is observed only from transcritical one to rectangular loop or flat type loop.

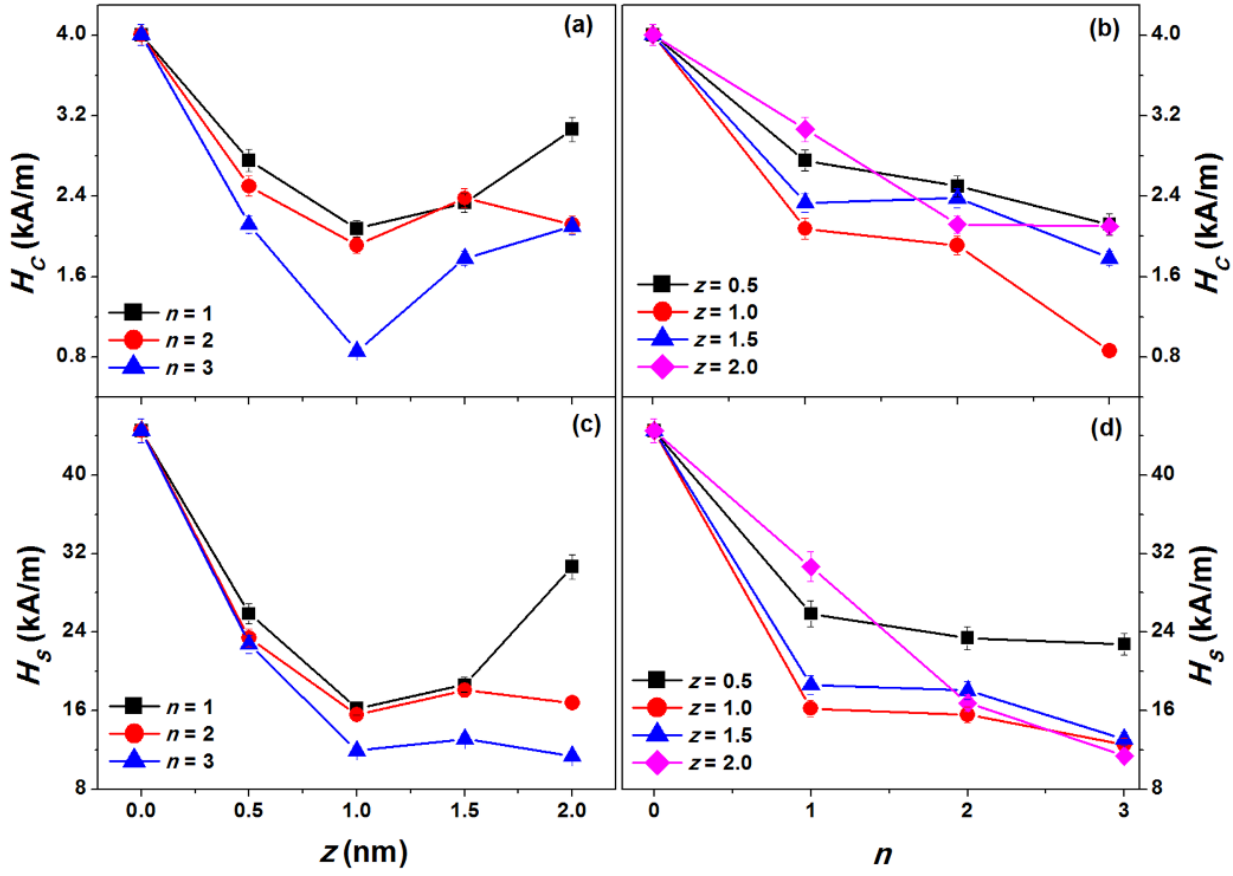

Figure 4.11: The variation of H_C and H_S as a function of spacer layer thickness (*z*) for different multilayers (a,c) and as a function of number of multilayers for different spacer layer thicknesses (b,d) for [CoFeB (*y* nm)/Ta (*z* nm)]$_{n=0\text{-}3}$/CoFeB (*y* nm) films.

To understand the effects of multilayers and spacer layer thickness on the magnetic properties more in detail, the magnetic parameters such as H_C and H_S are extracted from *M*-

H loops and plotted as functions of *z* and *n* in Figure 4.11. H_C decreases initially for all the multilayer films with increasing *z* up to 1 and then increases significantly with increasing *z* > 1. In addition, H_C decreases with increasing *n* for all the films having a fixed value of *z*. On the other hand, H_S decreases initially for all the multilayer films with increasing *z* up to 1 nm and the subsequent variation of H_S depends on the values of *n*. However, the variation of H_S with *n* shows almost similar behaviour of H_C versus *n*. These results confirm that the magnetic properties of multilayer films are strongly depending on the values of *n* and *z*. The observed results can be explained using change in the magnetic domain structure with increasing *n* and spacer layer dependent interlayer coupling in multilayer thin films. It is understood that the interlayer coupling between the ferromagnetic layers originates from the following different sources: (i) direct exchange coupling between ferromagnetic layers through pinholes present in the thin spacer layer [BOBO1999], (ii) the Ruderman-Kittel-Kasuya-Yosida (RKKY) interaction due to the conduction electrons through metallic spacer layer [KUDR1997, NIST2010], (iii) Orange peel or topological coupling induced by the interface roughness [NEEL1962, ZHAN1996, KOOL1999, CHOP2000, SCHR2000], (iv) magnetostatic coupling either through stray fields of domain walls [ANGU2000, CHOP2000, THOM2000, YUL2000, CHOP2005] or (v) through magnetic poles at edges of the films [MOON1999, LIUX2012]. It is illustrious that based on the results from Figures 4.09 and 4.10, and considering large resistivity of Ta spacer layer [NARA2006, NAIK2012] as compared to Cu and Ag [MURA1997, LIUD2001, CHIL2014], the interlayer coupling due to direct ferromagnetic coupling through pinhole and the indirect exchange coupling through RKKY interaction are negligible. Moreover, the stray field coupling, which plays a significant role on the interlayer coupling in the micron sized film dimension [ANGU2000, LIUX2012], is negligible for the current investigation as sample dimensions used for all the measurements are in millimetre range. Hence, the magnetostatic coupling, induced by correlated interface roughness [NEEL1962, KOOL1999] and by the stray field of domain walls [CHOP2005, NIST2010], is majorly responsible for the change in the magnetic reversal process. The coupling field between ferromagnetic layers is defined as [CHOP2000],

$$H_{CF} = \frac{\pi^2}{\sqrt{2}}\left(\frac{l^2}{\lambda\, y}\right) M_S \exp\left(\frac{-2\pi\sqrt{2}z}{\lambda}\right) \qquad (4.05)$$

where *l* and λ are the amplitude and wavelength of the roughness at the interfaces, and *y* and *z* are the thicknesses of CoFeB and Ta layers, respectively. It is clear from eq. (4.05) that

coupling field (H_{CF}) depends on the magnetization, roughness parameters, *y* and *z*. Upon increasing *n*, the thickness of individual CoFeB layer in multilayer films decreases. This leads to a transition from dense stripe domains to in-plane orientation of magnetization. Therefore, the magnetostatic coupling between the stray fields of the domain walls is also expected to vary with *n*. In general, the transcritical loop observed at higher film thickness is correlated to the development of effective magnetic anisotropy [MURA1966, CRAU2002, PRAD2004, SHAR2006, COIS2009, MISH2011]. The introduction of thin spacer layers in multilayer films revealed a considerable change in the loop shape from transcritical to rectangular loop or flat type loop, which strongly depends on the values of *n* and *z*. For example, the multilayer film with $n = 1$ has two numbers of CoFeB (100 nm) layers with each one exhibiting transcritical loop, as shown in Figure 4.03, due to the existence of stripe domain patterns. Considering the interaction between CoFeB (100 nm) layers through Ta spacer layer is magnetostatic one [NAOE1998, TANA20032], the interlayer coupling [SCHR2000] helps switching them together. Therefore, H_C and H_S decrease ascetically as compared to single-layer CoFeB (200 nm) film. With increasing *z* above a critical value ($z = 1$ nm), the interlayer coupling between CoFeB layers decreases and hence reveals collective magnetic properties of single-layer CoFeB (100 nm). This is responsible for the marginal increase in both H_C and H_S of bilayer films in Figures 4.11a and 4.11c. On further increasing the number of multilayers ($n > 1$), the thickness of individual CoFeB layer in multilayer films decreases and therefore the magnetic domain structure changes from stripe domains to in-plane orientation of magnetization. Therefore, the interlayer coupling reduces H_C largely up to certain value of *z* (≤ 1 nm) and then increases significantly at higher *z* values due to the reduction in the interlayer coupling. Nevertheless, H_S does not change at higher spacer layer thickness for the films having $n \geq 2$ because of the in-plane orientation of magnetization in multilayer films.

4.3.2.2. Temperature dependent magnetic properties

To understand the effect of temperature on the magnetization reversal of multilayer thin films in detail and to study the effect of temperature on various magnetic parameters, temperature dependent *M-H* loops are measured using VSM over a wide range of temperature from 30 K to 300 K for all the multilayer films. Figure 4.12 illustrates the temperature dependent *M-H* loops measured along the film plane for the multilayer films with different *n* and *z*. It is clear from the Figure 4.12 that (i) film with $z = 0$, $n = 0$, actually

single-layer CoFeB (200 nm) films, does not show any change in the transcritical loop shape with decreasing temperature down to 30 K.

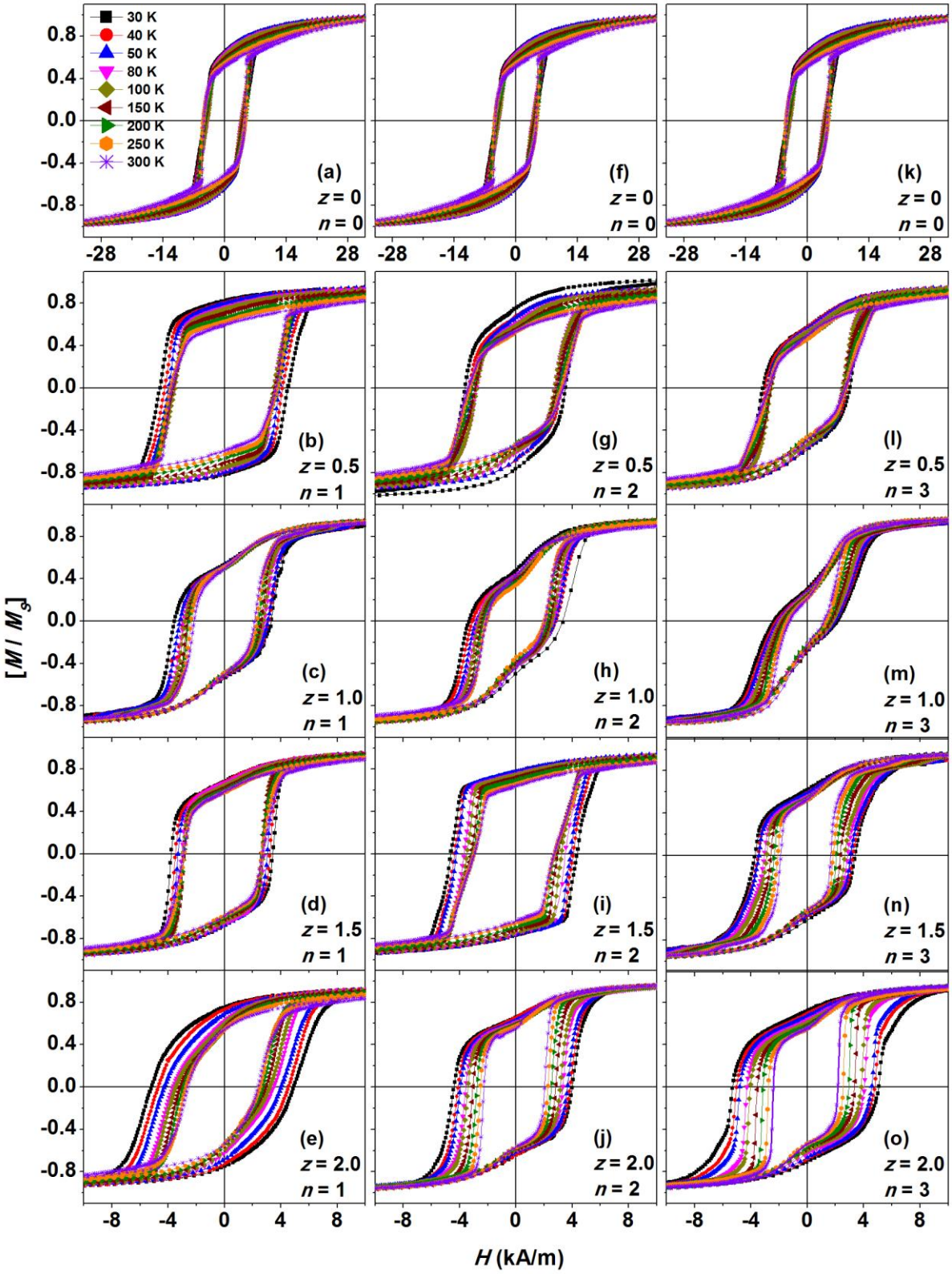

Figure 4.12: Temperature dependent *M-H* loops measured along the film plane for [CoFeB (*y* nm)/Ta (*z* nm)]$_{n=1-3}$/CoFeB (*y* nm) films with different values of *z* and *n*.

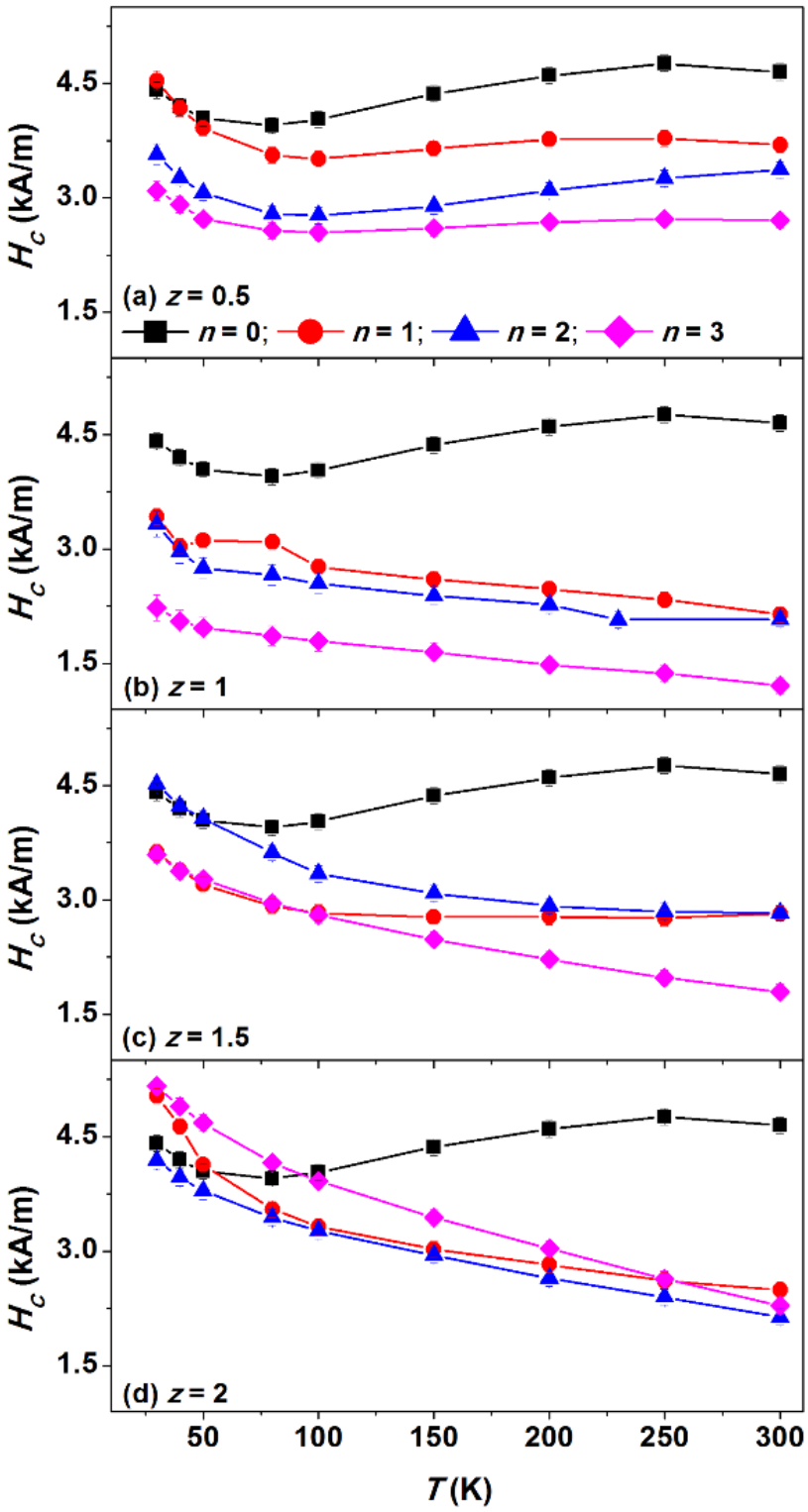

Figure 4.13: Variation of H_C as a function of temperature for [CoFeB (y nm)/Ta (z nm)]$_{n=0-3}$/CoFeB (y nm) films. The data are plotted by fixing the spacer layer thickness for different number of multilayers.

(ii) With increasing *z* to 0.5 for all *n* (Figures 4.12b, 4.12g, 4.12i), temperature dependent loops show only collective switching of all the CoFeB layers down to 30 K. (iii) With increasing *n* for a particular *z* (= 1), the area under the loop reduces progressively due to strongly interlayer coupling between CoFeB layers.

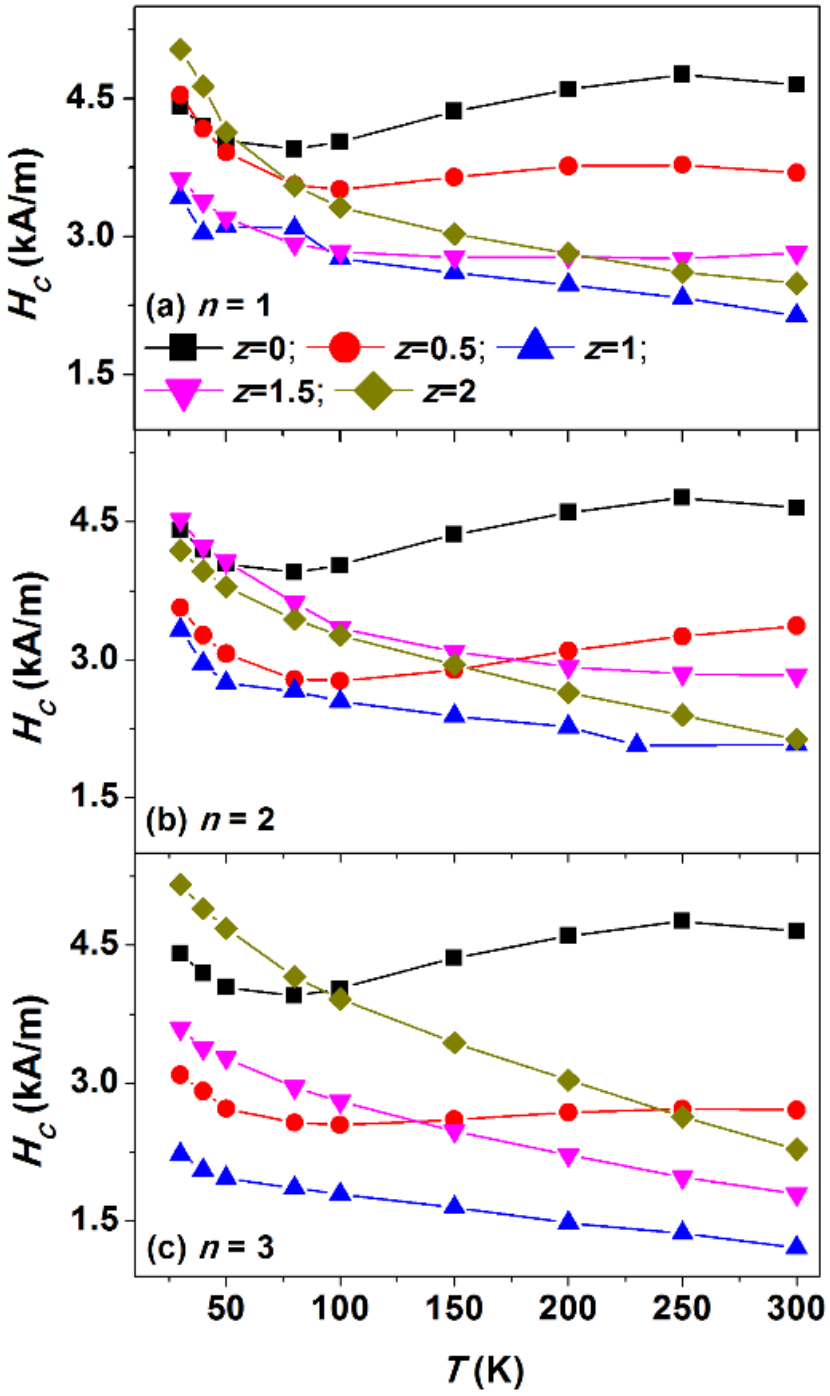

Figure 4.14: Variation of H_C as a function of temperature for [CoFeB (*y* nm)/Ta (*z* nm)]$_{n=0-3}$/CoFeB (*y* nm) films. The data are plotted by fixing the number of multilayers for different spacer layer thickness.

(iv) On further increasing $z > 1$ nm, the hysteresis behaviour increases and no change in the loop shape is observed with decreasing temperature. This could be related to the reduced interlayer coupling between CoFeB layers with increasing spacer layer thickness.

The extracted values of H_C from temperature dependent *M-H* loops for different *n* and *z* are plotted as a function of temperature in Figures 4.13 and 4.14 for a fixed *z* with different *n* and for a fixed *n* with different *z*, respectively. H_C of the single-layer CoFeB films ($n = 0$) shows unusual variation with decreasing temperature, i.e., H_C increases slightly down to 250 K and then decreases with decreasing temperature to 75 K. On further decreasing temperature, H_C increases progressively down to 30 K. Such behaviour is completely different from the typical ferromagnetic material and could be attributed to dense stripe domain caused by the stress induced effective magnetic anisotropy, which changes significantly with decreasing temperature. Similarly, H_C of multilayer films with $z = 0.5$ nm also shows similar behaviour, but the amount of variation in H_C depends on *n* (Figure 4.13a). This is mainly due to fact that the thin Ta spacer layer of 0.5 nm thick may not be sufficient to separate the CoFeB layers in multilayer films and hence there exists a direct ferromagnetic coupling between CoFeB layers through pinholes, which helps them to switch collectively. Therefore, the multilayer films with $z = 0.5$ nm show almost similar variation of H_C. The increase of *z* to 1 nm forms a stable spacer layer between CoFeB layers and hence the interaction between CoFeB layers is merely due to magnetostatic coupling or indirect exchange coupling, which decreases with increasing *z*. As a result, H_C increases progressively with decreasing temperature for the whole temperature range, which is similar to the typical ferromagnetic materials (Figure 4.13b-4.13d). Interestingly, the magnitude of increase in H_C strongly depends on the values of *n* and *z* in multilayer films (Figure 4.14). These results clearly demonstrate that the stacks of thin CoFeB films decoupled by optimum Ta spacer layers ($z = 1$) are promising to improve the soft magnetic properties and their suitability for the selective application in magneto-electronic devices.

4.4. Summary

A systematic investigation of thickness dependent structural and magnetic properties of $Co_{40}Fe_{40}B_{20}$ (*x* nm) single-layer films and effects of number of multilayers and thickness of spacer layer on the magnetic properties of multilayer [$Co_{40}Fe_{40}B_{20}$ (*y* nm)/Ta (*z* nm)]$_{n=1-3}$/ $Co_{40}Fe_{40}B_{20}$ (*y* nm) films has been carried in this chapter. The salient features of $Co_{40}Fe_{40}B_{20}$ ($x = 10 – 200$ nm) single-layer films and multilayer [CoFeB (*y* nm)/Ta (*z* nm)]$_n$/ CoFeB (*y* nm) films from the current investigations are as follows:

- $Co_{40}Fe_{40}B_{20}$ (x = 10 – 200 nm) single-layer films and multilayer [CoFeB (y nm)/Ta (z nm)]$_n$/ CoFeB (y nm) films could be prepared directly on thermally oxidized Si substrate at ambient temperature using DC magnetron sputtering system.
- Structural studies reveal that as-deposited CoFeB films exhibit amorphous structure. The average surface roughness is found to be in the range of 0.4-0.7 nm for CoFeB (200 nm) film. The results of thickness determination from XRR analysis and surface profilometer are in close agreement with each other.
- CoFeB (x < 67) films reveal soft magnetic nature with rectangular or flat-type loops due to in-plane magnetization with uniaxial anisotropy, as confirmed using MOKE microscopy. With increasing film thickness above critical thickness (~ 67 nm), the soft magnetic properties are degraded due to the transition of in-plane magnetization to dense stripe domain. Coercivity and saturation field increase from 1.99 kA/m to 4.14 kA/m and 7.16 kA/m to 38.2 kA/m, respectively with increasing CoFeB film thickness from 10 nm to 200 nm.
- High temperature thermomagnetization data reveal Curie temperature of CoFeB (20 nm) film to be around 512 K.
- The room temperature magnetic properties at higher film thickness could be improved by introducing optimum Ta spacer layer in multilayer films.
- However, the decrease of room temperature coercivity and saturation field with increasing the number of multilayers depends on the Ta spacer layer thickness. Room temperature coercivity of as-deposited multilayer films with n = 3 and z = 1 decreases to the lowest value of 0.8 kA/m.
- The improvement in magnetic properties of multilayer films strongly dependent on the number of multilayers and optimum spacer layer thickness.
- Temperature dependent *M-H* loops of single-layer CoFeB (200 nm) films do not show any change in the transcritical loop shape with decreasing temperature down to 30 K. The magnitude of increase in coercivity strongly depends on the values of n and z in multilayer films.
- The observed results are discussed on the basis of change in the magnetic domain structure and spacer layer thickness dependent interlayer coupling between CoFeB layers in multilayer films.

Chapter 5

Tuning the magnetic properties of stripe domain structured CoFeB films using stack structure with spacer layer thickness dependent interlayer coupling

Indian Institute of Technology Guwahati

5.1. Introduction

CoFeB based thin films are found to be one of the promising materials suitable for various applications in modern magneto-electronic devices due to their tunable magnetic properties [ZABE2013, TSYM2016]. The detailed investigation of CoFeB based thin films in Chapter 4 suggests that the magnetic properties of the films are strongly dependent on film thickness, i.e., in-plane magnetization with uniaxial magnetic anisotropy transformed into dense stripe domain with increasing thickness above 67 nm. Therefore, thicker CoFeB films become magnetically hard and display transcritical loop. Yet, thicker CoFeB based films exhibiting high resistivity, high permeability and high saturation magnetization were explored for the applications in magnetic flux amplifiers, soft magnetic underlayers in perpendicular magnetic recording media, flexible electronics, *etc* [ITOS2005, MUNA2005, PIRA2007, KAZI2013, YANG2013, TANG2014, QIAO2016]. However, only a few reports are available in the literature related to tuning of the magnetic properties of thick CoFeB films [ITOS2005, SHAR2006, CHEN2013, GUPT2013, TANG2014] despite their vast applicability. Chen et al. [CHEN2013] reported tuning of thermal, magnetic, electric and adhesive properties of as-deposited amorphous $Co_{60}Fe_{20}B_{20}$ (x = 100-500 nm) thin films by post annealing at different temperatures. However, the amorphous nature of the as-deposited films changed into nanocrystalline with increasing annealing temperature. Sharma et al. [SHAR2006] showed that the transcritical loops are more pronounced in the films deposited at ambient temperatures, as compared to the films deposited at elevated substrate temperature. In addition, they also demonstrated that a spin reorientation transition from in-plane single domain state to perpendicular multi-domain state, and perpendicular to in-plane occurred with increasing film thickness and substrate temperature, respectively. The other method of improving the magnetic properties of thick amorphous films was to make stack structure having ferromagnetic (FM) layers separated by thin non-magnetic (NM) layers, i.e., $[FM(y\text{ nm})/NM(z\text{ nm})]_n/FM(y\text{ nm})$ [NAOE1998, HUAN2001, NAIK2012, SING2013] where, total thickness of the ferromagnetic layer (x) was kept constant and thickness of the individual ferromagnetic layer (y) in stack structured films was changed typically by the formula, $y = x/(n+1)$, where n is the number of non-magnetic layers. While these studies were carried out to understand the role of spacer layer thickness and number of ferromagnetic layers to control the soft magnetic properties, the reduction of ferromagnetic layer thickness in stack structured films changed the magnetic domain structure from stripe domains to in-plane orientation of magnetization, which in-turn modified the nature of

magnetic interaction between ferromagnetic layers in stack structured films depending on the spacer layer thickness.

The alternative method of making stack structure is to fix the thickness of the individual ferromagnetic layer at a constant value and vary both the values of *n* and *z*. Since the thickness of the individual ferromagnetic layer in stack structure is kept as constant, the magnetic domain structure in each ferromagnetic layer is not expected to change. Although the total thickness of the stack structured films changes with *n*, this method allows to study the magnetic interaction between the ferromagnetic layers systematically and the resulting magnetic properties as a function of *n* and *z*. Draaisma et al. [DRAA1987] reported that in stack structured films, there is an additional contribution to the magnetostatic energy of a magnetic film coming from the stray fields produced by other magnetic films, whose contribution has to be taken into account to predict the effect of film thickness and separation between the magnetic films on the domain size. Similarly, Janicka et al. [JANI2007] demonstrated using simple models for stripe domain structure that the formation of magnetic domains in exchange-coupled ferromagnetic films exhibiting perpendicular magnetic anisotropy is strongly affected by the nature of magnetostatic interlayer coupling . However, the systematic investigation on the magnetic properties of thick CoFeB films in stack structure as a function of spacer layer thickness, number of ferromagnetic layers and the measurement temperature have not been well addressed.

Therefore, in this chapter, we report systematic investigations of the effects of number of spacer layer (*n*), spacer layer thickness (*z*) and measurement temperature (*T*) on the interlayer coupling between the CoFeB layers, exhibiting stripe domain magnetic structure, and their influences on the magnetic properties at room temperature and in the low temperature region (30 K – 300 K) in the amorphous stack structured [$Co_{40}Fe_{40}B_{20}$ (100 nm)/Ta (*z* nm)]$_n$/$Co_{40}Fe_{40}B_{20}$ (100 nm) films with *z* = 0 - 1.5 and *n* = 0 - 4. The schematic of the stack structured films is shown in Figure 5.01. In order to understand the modification in the magnetic properties of stack structured films, we also prepared single-layer films of nearly equivalent thicknesses and characterized for comparison.

5.2. Experimental details

Amorphous $Co_{40}Fe_{40}B_{20}$ (CoFeB) alloy thin films are prepared both in the form of single-layers with *x* = 100 – 300 nm and stack structure of [CoFeB (100 nm)/Ta (*z* nm)]$_n$/CoFeB (100 nm) with *z* = 0 - 1.5 and *n* = 0 - 4 at ambient temperature directly on thermally oxidized Si substrate using DC magnetron sputtering technique. The thickness of CoFeB film in stack

structure is fixed at a thickness of 100 nm to attain the stripe domain. The base pressure of the chamber is maintained to be better than 1×10^{-4} Pa and the sputtering Ar gas pressure for CoFeB and Ta layers was optimized at 1.33 Pa. The deposition rate is pre-calibrated using ex-situ surface profilometer (Veeco, Dektak 150 model) and found to be 1.2 Å/s and 0.5 Å/s for the deposition of CoFeB and Ta layers, respectively.

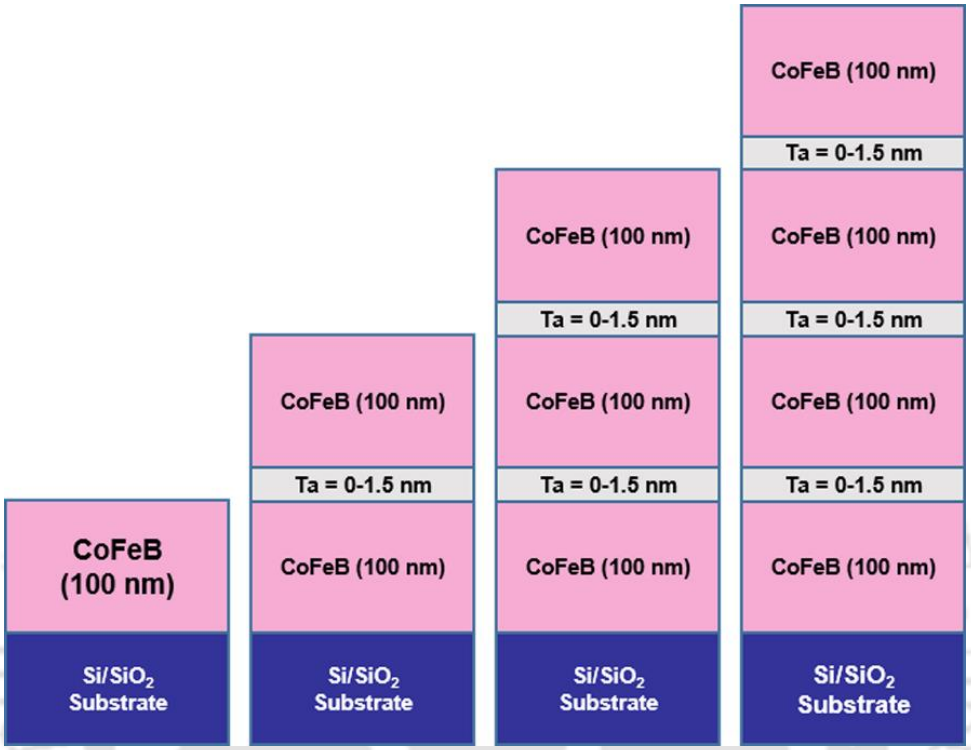

Figure 5.01: Schematic diagram of stack structure of [CoFeB (100 nm)/Ta (z nm)]$_n$/CoFeB (100 nm) film with z = 0 – 1.5 and n = 0 – 3.

Amorphous nature of the as-deposited CoFeB films is confirmed by X-ray diffraction (XRD) obtained using a high-power X-ray diffractometer (Rigaku TTRAX III, 18 kW) with Cu-K$_\alpha$ radiation (λ=1.54056 Å) and transmission electron microscopy (TEM, JEOL 2100 and Technai G2 F20) techniques. Magnetic properties of the single-layer and stack structured films are characterized using vibrating sample magnetometer (VSM, LakeShore Model 7410) by performing magnetic hysteresis loops (*M-H*) along the film plane both at room temperature and at low temperatures over a wide range of temperature from 30 K to 300 K. Simultaneous atomic force microscopy and magnetic force microscopy (MFM, Bruker Dimension Icon) characterizations are performed to study the topographic features and local magnetic domains. MFM is performed in dual-pass lifting mode with commercially available CoCr-coated tips, which are magnetized along the tip axis and therefore sensitive to stray field gradients from out-of-plane oriented domains or the out-of-

plane components of domains oblique to the surface. The domain images are acquired at the zero-field state.

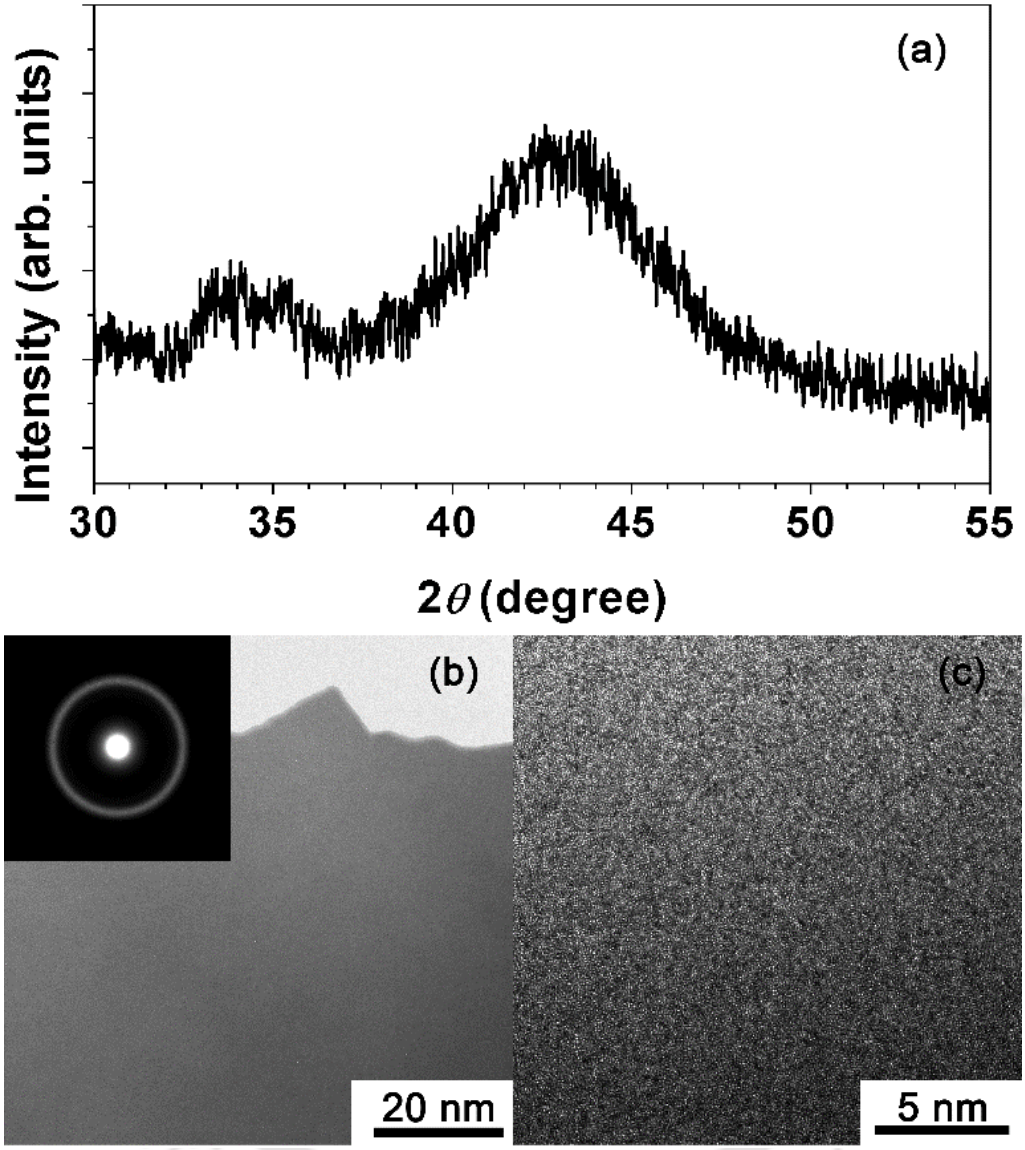

Figure 5.02: Room temperature (a) X-ray diffraction pattern, (b) bright-field TEM image and selected area electron diffraction pattern, and (c) high-resolution TEM image for as-deposited CoFeB (200 nm) film.

5.3. Results and discussion

5.3.1. Properties of stack structured thin films

5.3.1.1. Structural properties

Figure 5.02 displays typical XRD pattern, bright-field TEM image, selected area electron diffraction (SAED) pattern and high-resolution TEM (HRTEM) image of 200 nm thick as-deposited CoFeB film. It could be clearly seen that as-deposited film exhibits only a broad

peak at around $2\theta = 44°$ without any other sharp peaks corresponding to any crystalline phase. Note that the XRD peak observed at $2\theta = 33°$ represents Si(200) peak emanating from thermally oxidized Si substrate [CHOM2001].

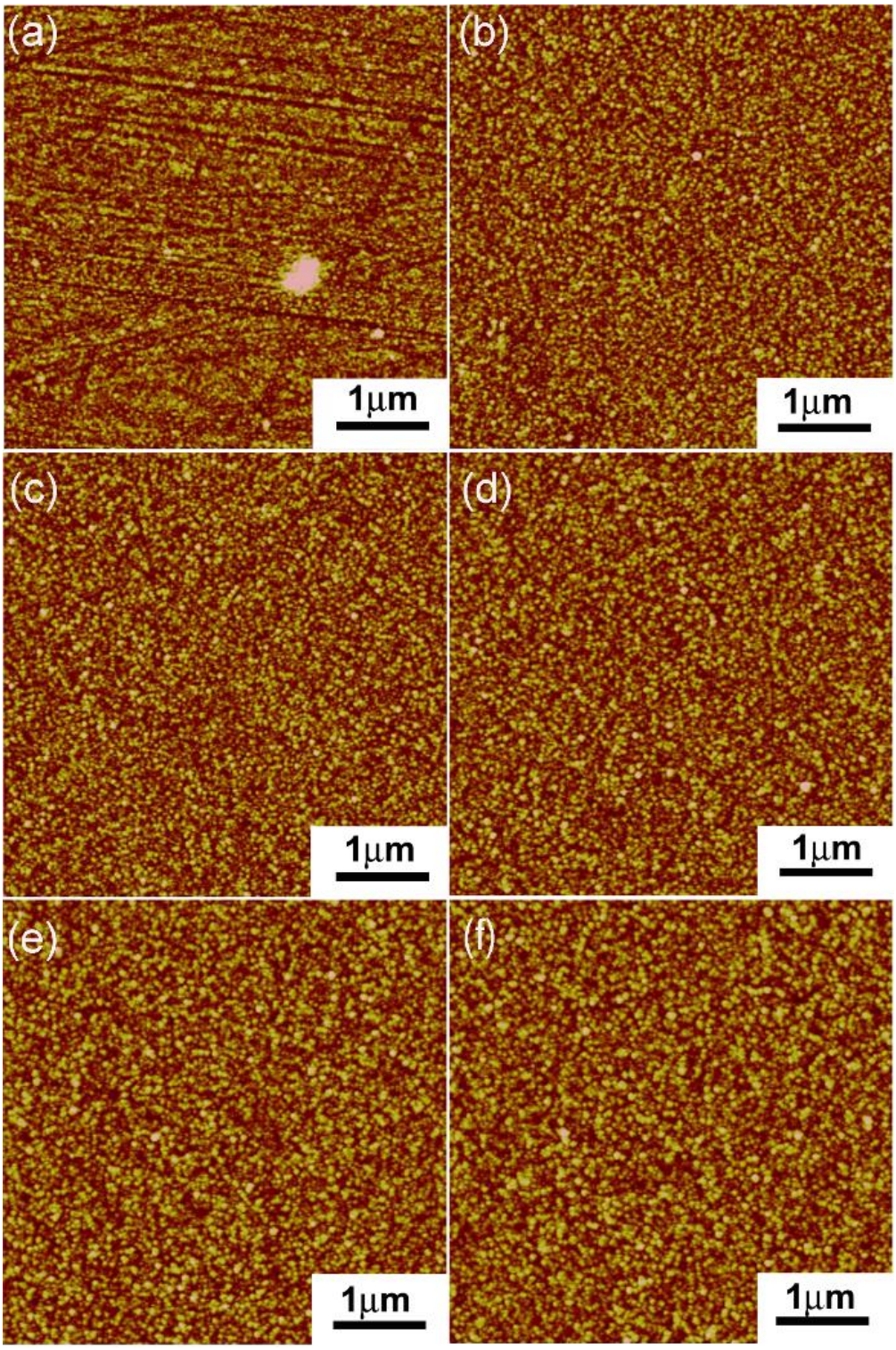

Figure 5.03: AFM images for CoFeB (x nm) single-layer film with (a) $x = 100$ and (b) $x = 200$ and stack structured [CoFeB (100 nm)/Ta (z nm)]$_n$/CoFeB (100 nm) films with (c) $z = 1$, $n = 2$; (d) $z = 1.5$, $n = 2$; (e) $z = 1$, $n = 4$; and (f) $z = 1.5$, $n = 4$.

The microstructural studies using bright-field TEM image, SAED pattern and HRTEM image reveal the existence of plain and even contrast microstructure without any local lattice fringes and halo diffraction ring, respectively. This confirms the existence of amorphous structure in as-deposited films. The observed results are in good agreement with the earlier reports on similar systems [YOUC2008, DEMA2016].

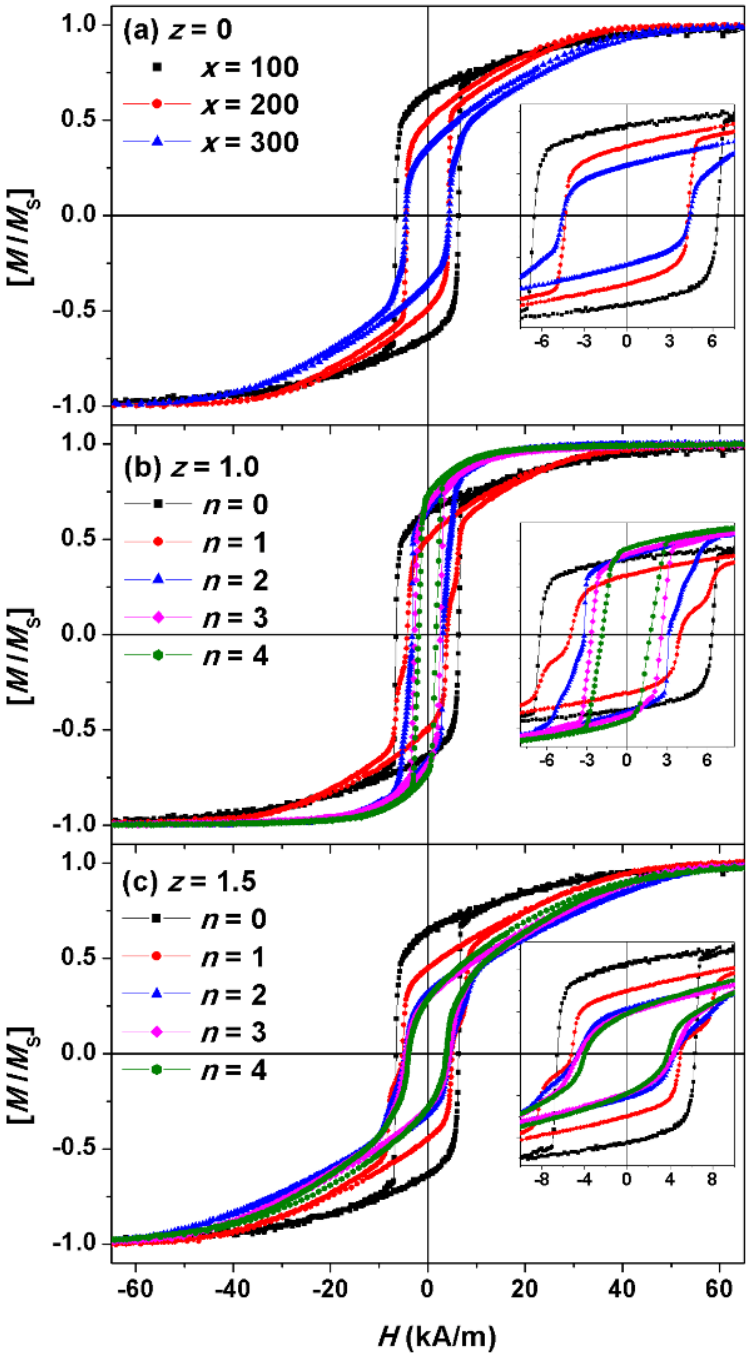

Figure 5.04: Room temperature normalized *M-H* loops of (a) single-layer CoFeB (*x* nm) films with different thicknesses and stack structure [CoFeB (100 nm)/Ta (*z* nm)]$_{n=0\text{-}4}$/CoFeB (100 nm) films with (b) *z* = 1 and (c) *z* = 1.5 for different values of *n*. Inset: Expanded view of *M-H* loops close to the origin.

To study the surface topography of the multilayer films with increasing *n* and *z*, we have investigated the topography of the films using AFM and shown in Figure 5.03. The existence of fine and nano-sized grain in the as-deposited films is directly observed by AFM. The films exhibit very clear surfaces and the average roughness of the films increases significantly from 0.4-0.65 nm for single-layer CoFeB films to 1.5-2 nm with increasing *n* =4 and *z* = 1.5 nm. High-resolution images showed the existence of very fine and sparsely distributed nano-sized grains with size of around 19 nm in single-layer CoFeB films. With increasing *n* and *z*, the grain density increases considerably along with the increase in average size of the grains to 40 nm.

5.3.1.2. Room temperature magnetic properties

Figure 5.04 displays the room temperature *M-H* loops measured along the film plane for amorphous CoFeB single-layer and stack structured films with different values of *z* and *n*. The expanded view of the *M-H* loops close to origin is presented in insets. To study the changes in the room temperature magnetic parameters, the extracted values of coercivity (H_C), field required for magnetization saturation (H_S), remanence ratio (M_R/M_S, M_R – remanent magnetization and M_S – saturation magnetization) from the *M-H* loops are plotted as a function of *n* for different *z* in Figure 5.05. It is clear from Figure 5.04a that all the single-layer CoFeB films exhibit transcritical like loops, i.e., the *M-H* loops constitute with two distinct magnetization phases: (a) an in-plane magnetic component, which reverses quickly as the applied magnetic field approaches to coercive field and (b) out-of-plane component, whose magnetization rotates progressively under the application of magnetic field and produces a linear variation of magnetization before saturation. Therefore, such loops require larger values of H_S (> 40 kA/m). With increasing *x*, the magnitude of magnetization reversing close to H_C decreases and thus reducing M_R/M_S from 67% to 34% and increasing H_S from 41.6 kA/m to 53.8 kA/m as *x* is increased from 100 to 300 nm, respectively. H_C decreases from 6.4 kA/m to 4.3 kA/m with increasing *x* from 100 to 200 nm and then increases slightly to 4.4 kA/m for the film with *x* = 300 nm.

On the other hand, the introduction of more number of CoFeB layers in stack structured films with different *z* changes the nature of the *M-H* loops substantially (see Figures 5.04b, 5.04c). For instance, the stack structured films with *z* = 1 exhibit the following features: (i) With increasing *n* to 1, the shape of the *M-H* loop changes into two-step magnetization reversal along with a considerable reduction in H_C, H_S and M_R/M_S. (ii) On further increasing *n* (> 1), the loop shape transforms progressively from two-step

magnetization reversal into simple hysteresis with a considerable increase in the magnitude of magnetization reversing close to H_C. (iii) While H_C decreases at a rate of 9.32 kA/m per n for $n > 1$, H_S decreases largely from 38 kA/m to 16 kA/m with increasing n from 1 to 2 and then varies linearly at a rate of 2.8 kA/m per n for higher n values. (iv) M_R/M_S is also found to increase from 51 % to 77 % with the increase in n from 1 to 4, respectively.

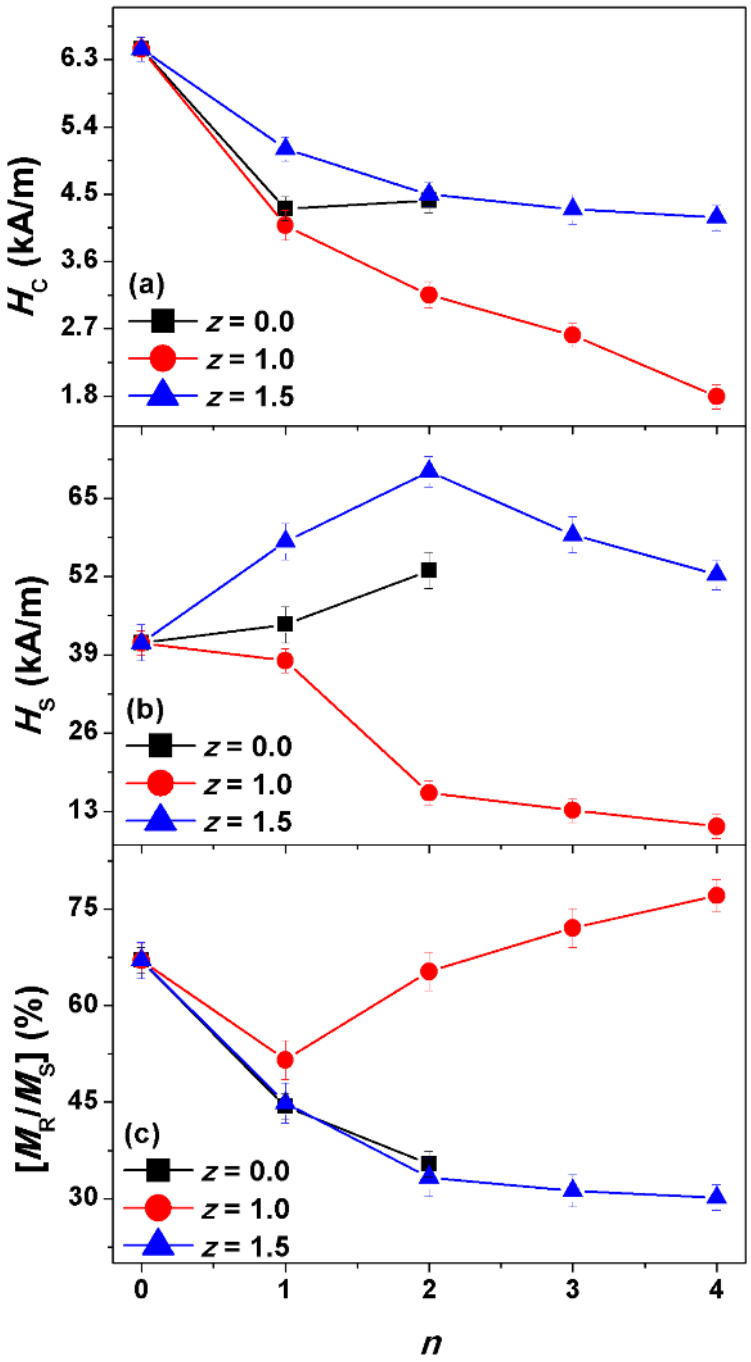

Figure 5.05: The variations of room temperature (a) coercivity (H_C), (b) field required for saturating the films' magnetization (H_S) and (c) remanence ratio (M_R/M_S) as a function of number of CoFeB layers (n) for different spacer layer thicknesses (z = 0 - 1.5).

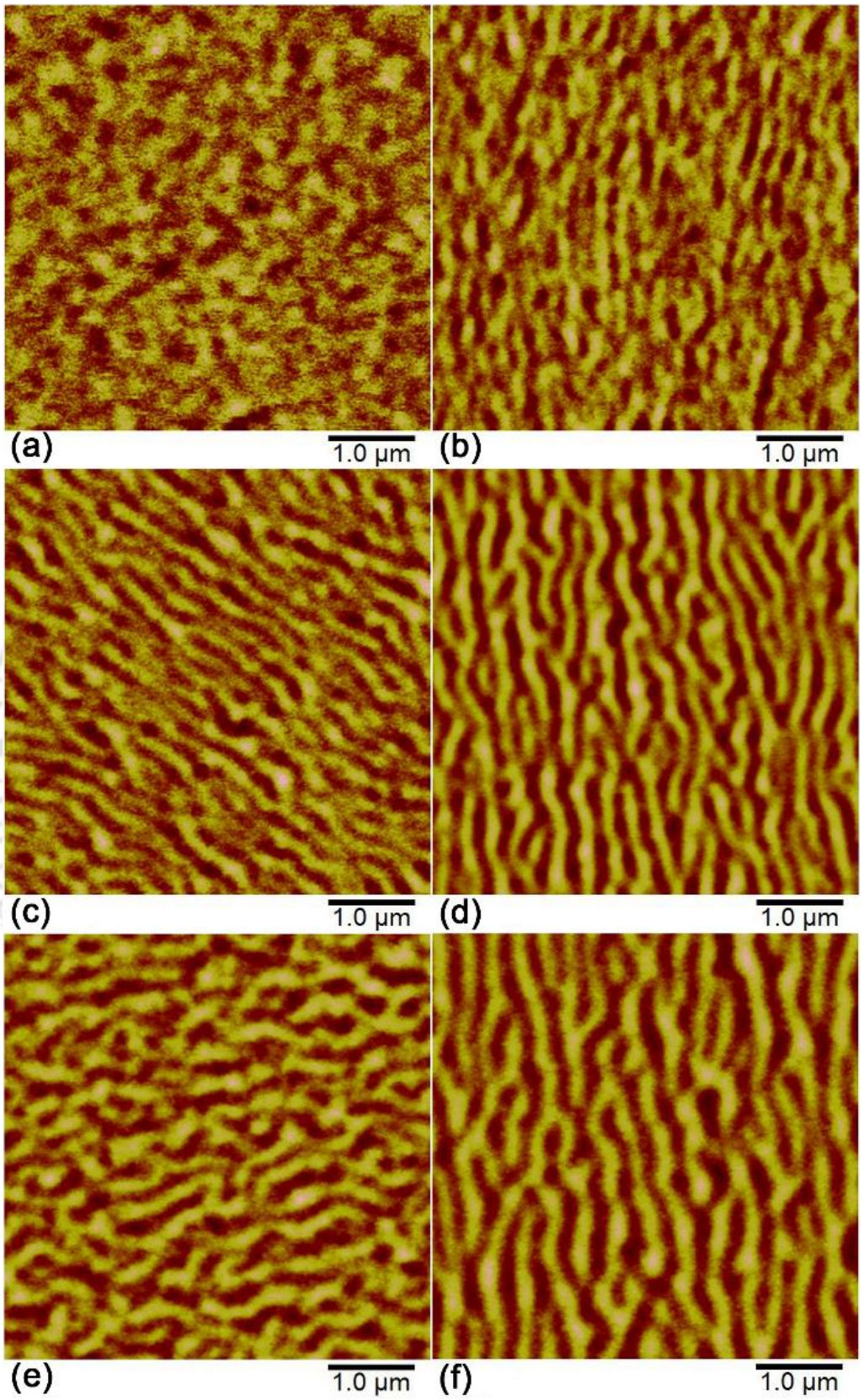

Figure 5.06: MFM images at the zero-field state for CoFeB (x nm) single-layer film with (a) x = 100 and (b) x = 200 and stack structured [CoFeB (100 nm)/Ta (z nm)]$_n$/CoFeB (100 nm) films with (c) z = 1, n = 2; (d) z = 1.5, n = 2; (e) z = 1, n = 4; and (f) z = 1.5, n = 4.

(v) Nevertheless, the *M-H* loop of stack structured film with z = 1 and n = 4 still shows a weak linear region before saturation (inset of Figure 5.04b). In contrast, the *M-H* loops of stack structure films with z = 1.5 exhibit different natures, i.e., With increasing n, the magnitude of magnetization reversing close to H_C decreases up to n = 2 and then remains almost constant. This reduces M_R/M_S from 67% for film with n = 0 to 33% for film with n = 2 and increases H_S initially from 41.6 to 69.4 kA/m for n up to 2 and then decreases to 52.3 kA/m for n = 4. However, H_C decreases slowly from 6.4 kA/m to about 4.4 kA/m with increasing n up to 2 and then remains almost constant.

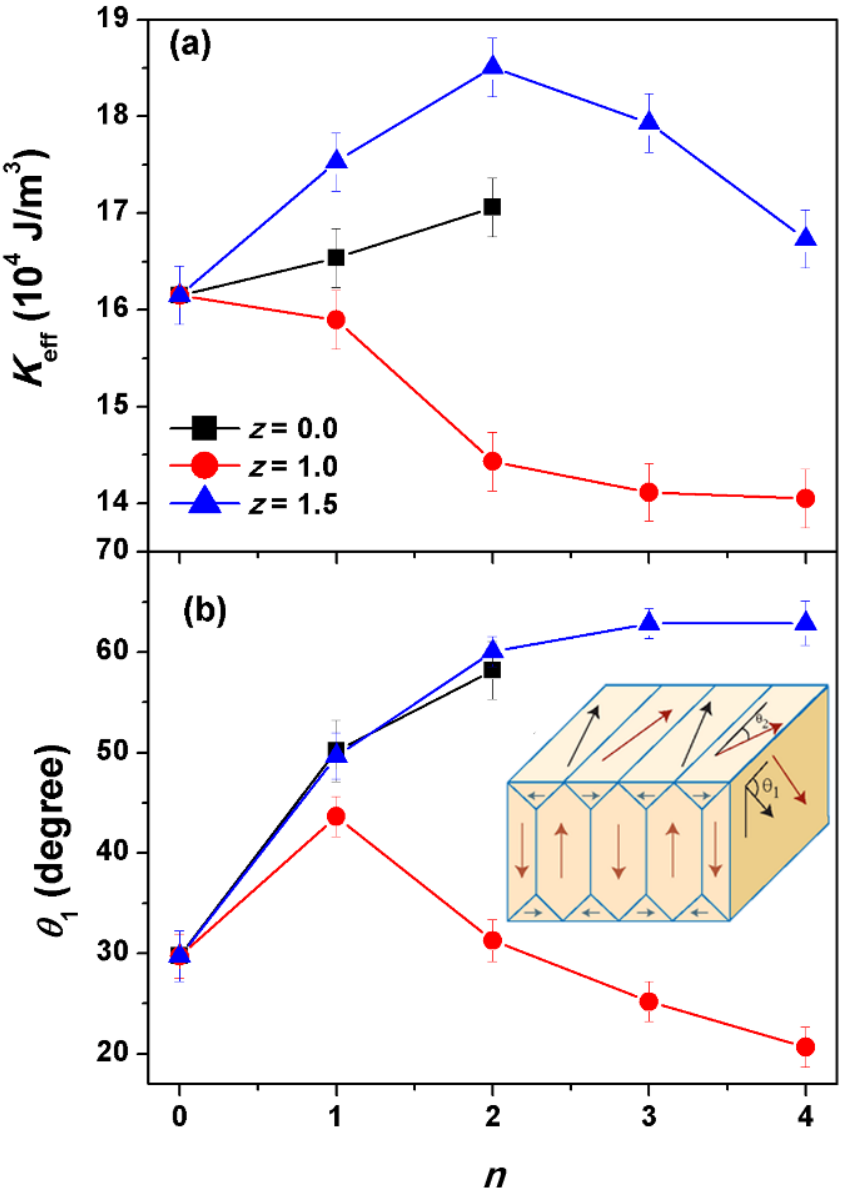

Figure 5.07: The variations of K_{eff} (a) and θ_1 (b) as a function of number of CoFeB layers (n) for different spacer layer thicknesses (z = 0 - 1.5). Inset: Schematic representation of stripe domain magnetic structure.

The observed results suggest that single-layer CoFeB films exhibit transcritical loops with high H_C and H_S mainly due to the formation of stripe domains originated from the development of effective magnetic anisotropy induced by the stress quenched during the preparation of the films at a high deposition rate to form amorphous structure. In order to study the nature of domain structure in both single-layer and stack structured CoFeB films, MFM images were obtained in zero-field state and shown in Figure 5.06. CoFeB (100 nm) film shows weak stripe domains with low magnetic signal in out-of-plane direction due to the existence of local disorder in the easy-axis of magnetization of the as-deposited films [SUNZ2004, HUBE2014, WUDO2015, GAYE2017]. With increasing x to 200 nm, the magnetic signal is increased significantly and tends to form dense stripe domains. The stripe domain pattern is typical for materials with out-of-plane magnetic components induced by the stress [SHAR2006]. This is in good agreement with the results of *M-H* loops presented in Figure 5.04a for single-layer films. On the other hand, the magnetic domain structure of the stack structured films varies strongly with z and n. For instance, the stack structured films with z = 1.5 showed dense stripe domains as compared to the stack structured films with z = 1 at different values of n. The stripe width of the domains is found to vary between 120 nm and 200 nm, which is in close agreement with the other similar soft magnetic thin films [SUNZ2004, COIS2009, WUDO2015].

To understand the magnetic domain structure, we have used the stripe domain model proposed by Craus et al. [CRAU2002] following the original model proposed by Murayama [MURA1966] and Alvarez-Prado et al. [PRAD2004], which allows to determine the effective magnetic anisotropy. According to the model, the spins within the bulk domains make an angle θ_1 with the surface (see inset of Figure 5.07b) and the closure domain spins make an angle θ_2 with the long axis of the stripes. The value of θ_1 can be calculated from the remanent magnetization data measured using VSM under the assumption that the magnetization in the closure domains remains perpendicular to the direction of the applied field such that $\theta_2=\pi/2$ [CRAU2002]. The value of θ_1 can vary between 0 and 90° depending on the fractional change in M_R with respect to M_S. In addition, there exists a critical thickness, as defined in eqn.(4.03), above which the existence of stripe domains is strongly dependent on the values of M_S and K_{eff} [PRAD1997, CRAU2002]. The determined values of K_{eff} and θ_1 are plotted as function of n for different z in Figure 5.07. The typical values of H_S, $\mu_0 M_S$, K_{eff} and θ_1 for CoFeB (x nm) single-layer films with different thicknesses are summarized in Table 5.01. K_{eff} is found to be of the order of 10^5 J/m^3. K_{eff} and θ_1 increases

with increasing x indicating that the degree of local disorder in the as-deposited films increases, which in-turn enhances the out-of-plane component of magnetization in the stripe domains.

Table 5.01: The values of H_S, $\mu_0 M_S$, K_{eff} and θ_1 for CoFeB (x nm) films.

CoFeB thickness (x nm)	H_S (kA/m)	$\mu_0 M_S$ (mT)	K_{eff} (J/m^3)	θ_1 (°)
100 ± 0.4	41.59 ± 0.04	750 ± 4	(1.61 ± 0.02)×10^5	29.7 ± 0.2
200 ± 0.4	44.60 ± 0.07	795 ± 3	(1.65 ± 0.03)×10^5	50.1 ± 0.3
300 ± 0.4	53.75 ± 0.06	768 ± 4	(1.70 ± 0.02)×10^5	58.1 ± 0.2

This is further supported from the MFM images and the reduction in the magnetization component reversing close to coercive field. Upon introducing n, H_C decreases considerably depending on the values of z. This suggests that the ferromagnetic layers in stack structure possibly interact and couple to exhibit a collective behaviour. It is well described [CHEL2003] that the interlayer coupling between ferromagnetic layers in stack structure originates from different sources. The stray field coupling from the magnetic poles at the edges is negligible due to the use of millimetre size samples for the measurements. Similarly, the direct and indirect exchange coupling between ferromagnetic layers is also negligible, as the spacer layer of Ta with $z \geq 1$ deposited at room temperature is expected to form a continuous layer with large resistivity [SING2013]. Hence, the spacer layer dependent magnetostatic coupling between ferromagnetic layers induced by interface roughness and stray fields of domain walls is majorly responsible for the change in the M-H loop [CHOP2000, SCHR2000, SING20161]. This interlayer coupling between the ferromagnetic layers helps them to couple and reverse collectively leading to an overall decrease in H_C. This is evident from the change in the loop shape with increasing n, i.e., the stack structured films with n =1 and z = 1 show two-step reversal behaviour due to non-closure of flux as effectively as the stack structure with more number of ferromagnetic layers. With increasing n, the number of ferromagnetic layer increases providing a better flux closure, which leads to a substantial drop in H_C and changes in the loop shape away from transcritical to soft magnetic type with reduced H_S and increased M_R/M_S. A similar trend of reduction in H_C has been reported by Chopra et al. in exchange-spring stack structures [CHOP2005]. On further increasing z in stack structured films, the interlayer

coupling between ferromagnetic layers reduces notably and thus exhibits a collective behaviour of dense stripe domain patterns. As a result, H_C and M_R/M_S reduce sluggishly and tends to saturate at higher n. Since stack structured films also exhibit transcriticality, we have extended the calculation of K_{eff} and θ_1 and shown in Figure 5.07. The variations of K_{eff} and θ_1 strongly depend on the spacer layer thickness, i.e., (i) for stack structured films with $z = 1$, both K_{eff} and θ_1 decreases with increasing $n > 1$ mainly due to the enhanced coupling between ferromagnetic layers, which improves the soft magnetic nature along the in-plane direction in stack structured films, and (ii) with increasing z to 1.5, K_{eff} and θ_1 increase due to the reduction in the interlayer coupling, which results in a collective behaviour with reduced components of in-plane magnetization, as evidenced from dense stripe domain patterns.

5.3.1.3. Temperature dependent magnetic properties

As the values of M_S and interfacial strain arising from the different thermal expansion coefficients of the materials at the interfaces vary with temperature, they play a vital role in modifying the interlayer coupling as a function of temperature. To investigate the effect of temperature on the nature of interlayer coupling and the resulting magnetic properties, *M-H* loops were obtained at different temperatures between 30 K and 300 K and depicted in Figures 5.08 and 5.09 for stack structures with $z = 1$ and 1.5, respectively. The expanded view of the loops close to the origin is shown in inset for each stack structure. H_C as a function of temperature for different values of n and z is extracted from *M-H* loops. Considering a large difference in the absolute values of H_C and to monitor the relative change in temperature dependent H_C, the normalized coercivity, i.e., $H_C(T)/H_{C@300K}$ is plotted as a function of temperature for different values of n and z in Figure 5.10. It is observed from Figure 5.08 that (i) the stack structure films with $n = 1$ exhibit two step magnetization reversal behaviour from 300 K to 150 K. On further reducing the temperature below 150 K, *M-H* loops exhibit only simple hysteresis without any steps. This can be attributed to enhanced interlayer coupling with decreasing temperature caused by the increase in M_S. As a result, the variation of $H_C(T)$ shows different nature as compared to single-layer film, i.e., $H_C(T)$ increases almost linearly down to 150 K like in single-layer film, but stagnates around 100 K followed by a larger increase at lower temperature below 50 K. (ii) A similar variation of hysteresis was observed for $n = 2$ films as well. However, a close observation of the loops suggests that $H_C(T)$ increases with decreasing temperature

down to 150 K and then decreases slightly down to 80 K. On further reducing the temperature below 80 K, H_C again increases. This leads to a minimum in $H_C(T)$ curve.

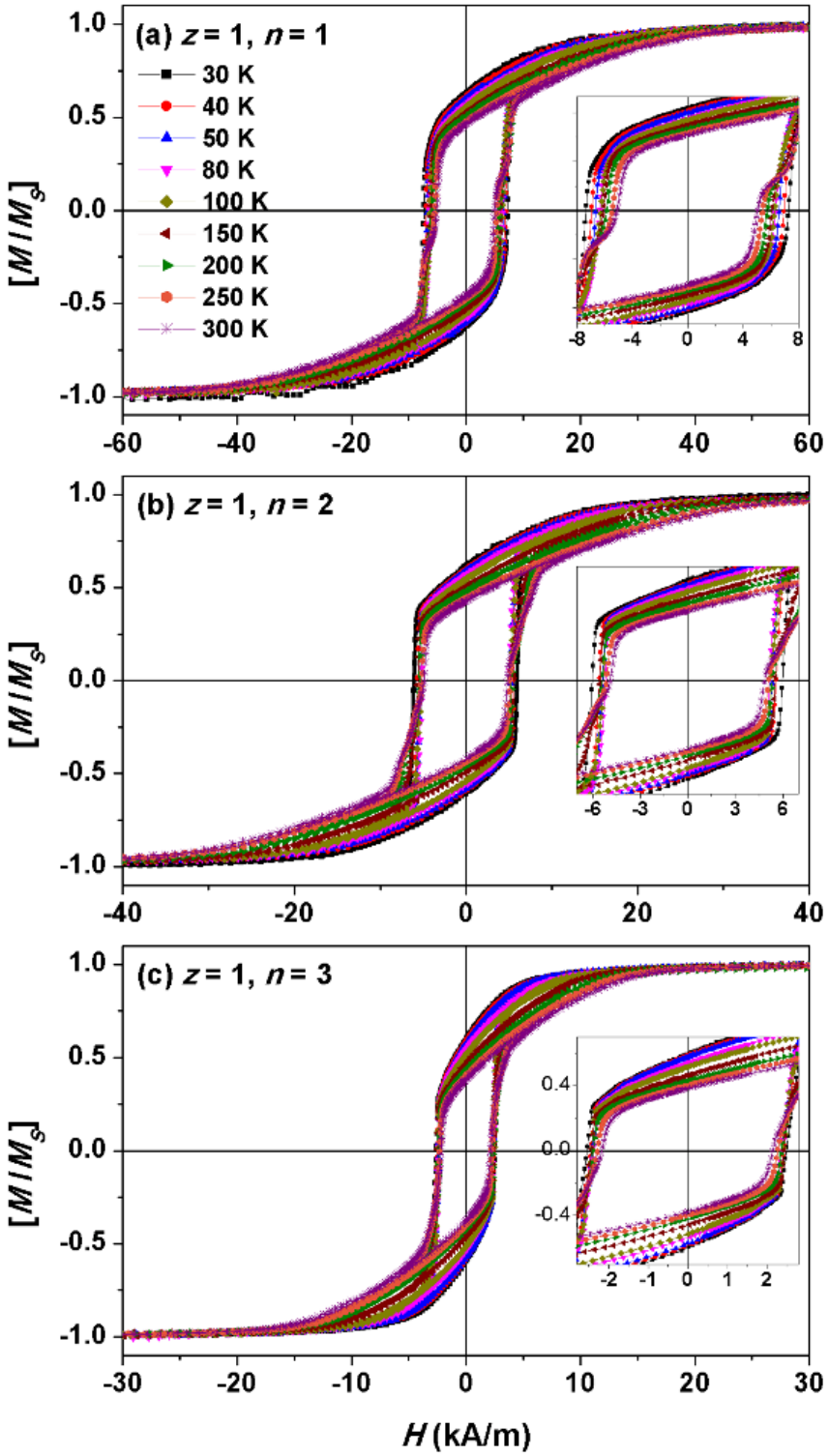

Figure 5.08: Temperature dependent normalized *M-H* loops of stack structure [CoFeB (100 nm)/Ta (1 nm)]$_n$/CoFeB (100 nm) films with n = 1 (a), 2 (b) and 3 (c). Inset: Expanded view of *M-H* loops close to the origin.

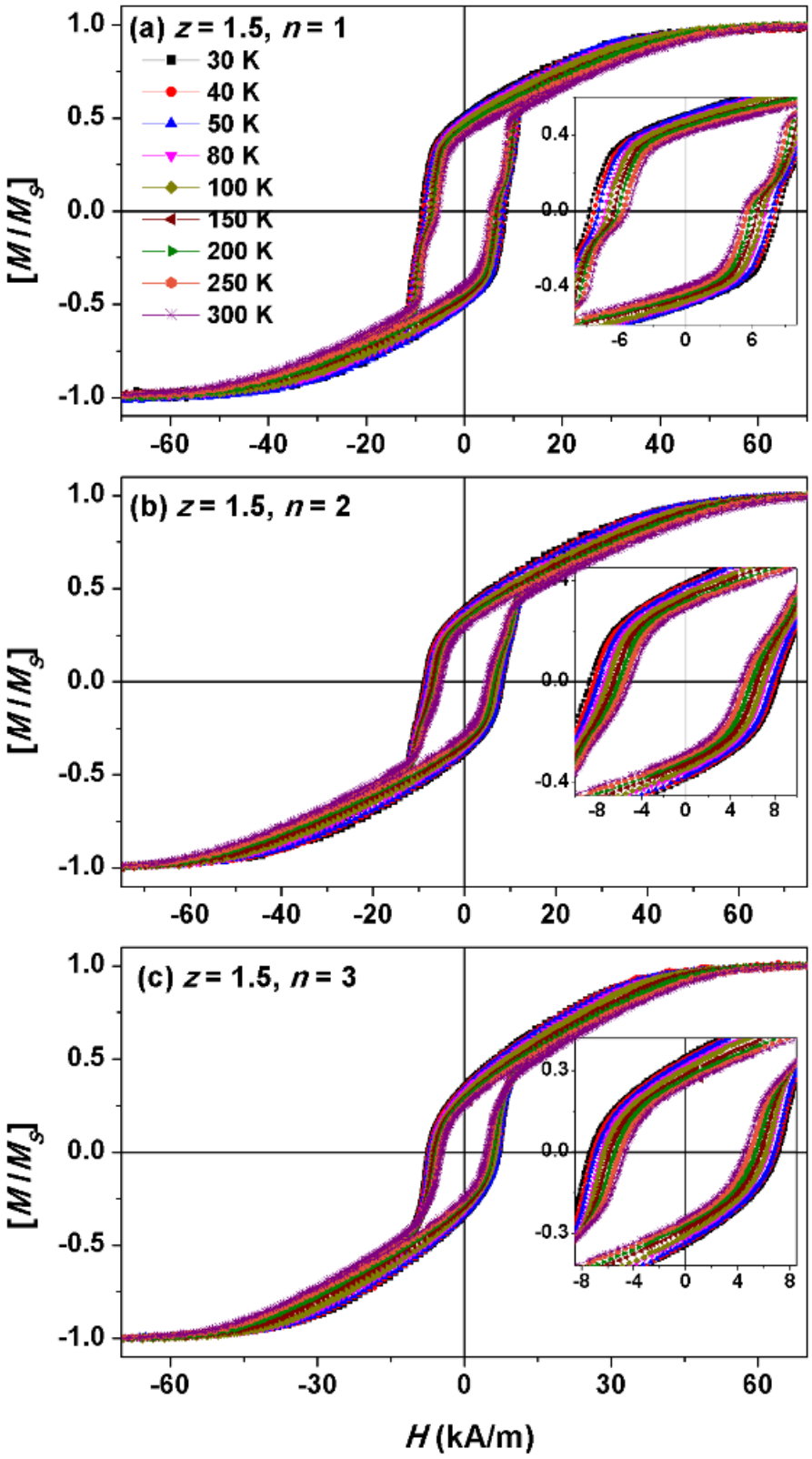

Figure 5.09: Temperature dependent normalized *M-H* loops of stack structure [CoFeB (100 nm)/Ta (1.5 nm)]$_n$/CoFeB (100 nm) films with n = 1 (a), 2 (b) and 3 (c). Inset: Expanded view of *M-H* loops close to the origin.

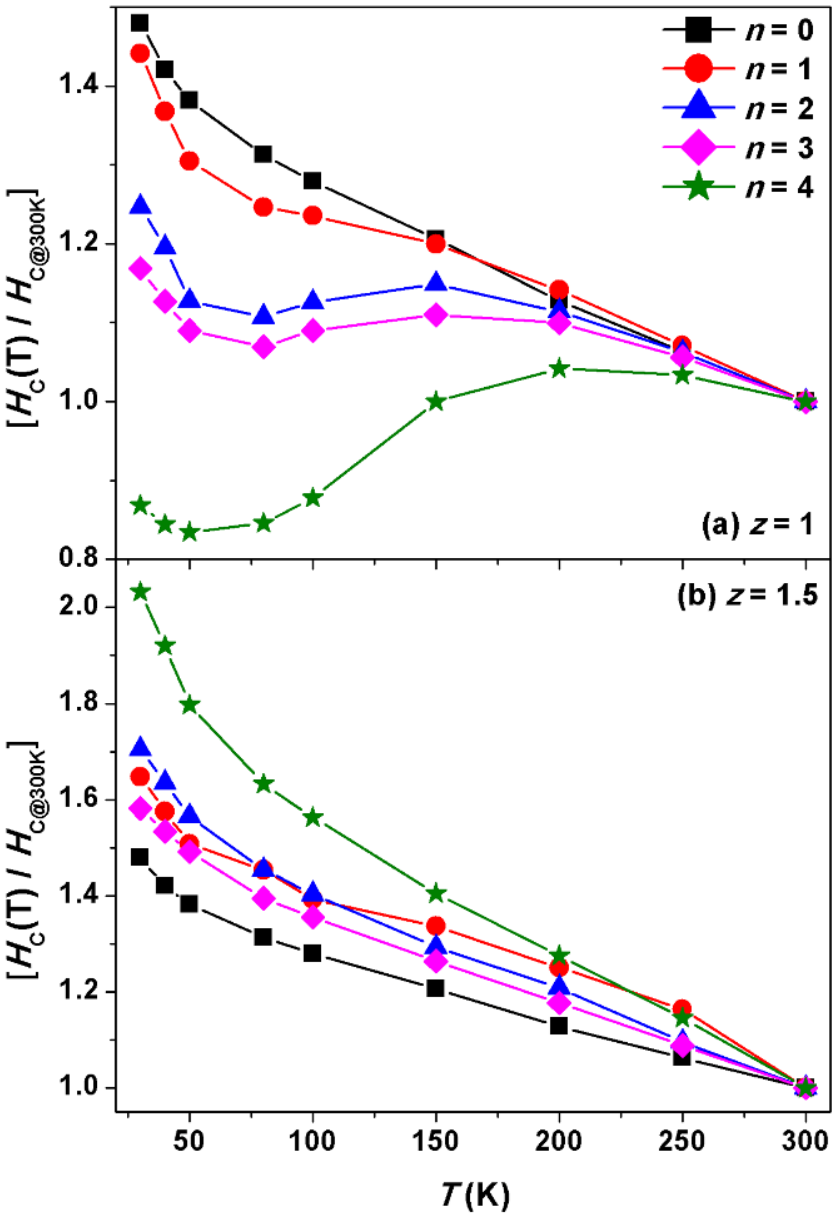

Figure 5.10: The variations of normalized coercivity, $H_C(T)/H_{C@300K}$ plotted as a function of temperature for stack structure [CoFeB (100 nm)/Ta (z nm)]$_n$/CoFeB (100 nm) films with different spacer layer thicknesses [z = 1 (a) and 1.5 (b)].

(iii) With increasing $n > 2$, the shape of the *M-H* loops does not change significantly with decreasing temperature. But, the point of minimum in $H_C(T)$ curve shifts to lower temperature significantly with increasing n. This can be understood from the competition between interlayer coupling and interfacial strain, i.e., with decreasing temperature, M_S increases significantly and improves the coupling between ferromagnetic layers, thereby leading to a decrease in H_C. At the same time, the interfacial strain increases with decreasing temperature. Hence, when the interfacial strain dominates over the magnetostatic coupling,

H_C is expected to increase at low temperature. These observations are in good agreement with the earlier reports on similar stack structured thin films [SING20162]. On the other hand, for the stack structure films with z = 1.5, two step magnetization reversal, observed for n = 1 and 2 films as similar to z = 1 films, changes into simple hysteresis at low temperature. However, the transformation is quite sluggish, which could be attributed to the reduced interlayer coupling between the CoFeB layers and collective behaviour of dense stripe domains with increasing z. On further increasing n > 2, the shape of the *M-H* loops does not change with temperature. As a result, the variations of $H_C(T)$ in these films are almost linear down to 100 K and then increase slightly at a faster rate at low temperature, a behaviour similar to single-layer CoFeB films. However, the magnitude of relative variation in $H_C(T)/H_{C@300K}$ strongly depends on the number of CoFeB layers. The observed results clearly demonstrate that the fabrication of stack of thick CoFeB films having stripe domain pattern and separated by optimum Ta spacer layers is an alternative and promising approach to improve the magnetic properties of the stack structured films with thick CoFeB ferromagnetic layers for the selective application in magneto-electronic devices.

5.4. Summary

A novel approach for tuning the magnetic properties of stripe domain structured amorphous $Co_{40}Fe_{40}B_{20}$ (CoFeB) films by using stack structured [CoFeB (100 nm)/Ta (z = 0-1.5 nm)]$_{n=0-4}$/CoFeB (100 nm) films with spacer layer thickness dependent interlayer coupling has been carried out in this chapter. The salient features of stack structured [CoFeB (y nm)/Ta (z nm)]$_n$/ CoFeB (y nm) films from the current investigations are as follows:

- All single-layer and stack structured [CoFeB (y nm)/Ta (z nm)]$_n$/ CoFeB (y nm) films could be prepared on thermally oxidized Si substrate at ambient temperature using DC magnetron sputtering system.
- Structural studies confirm the presence of amorphous structure in all the as-deposited CoFeB films. AFM analysis of film surface reveals a clear surfaces and the existence of fine and nano-sized grain in the as-deposited films. The average roughness increases significantly from 0.4-0.65 nm for single-layer CoFeB films to 1.5-2 nm with increasing n =4 and z = 1.5 nm.
- The single-layer CoFeB films exhibit transcritical loops due to the formation of stripe domains in the as-deposited films caused by the development of stress induced

effective magnetic anisotropy. Hence, they show high coercivity (> 4 kA/m) and require large applied magnetic field (> 40 kA/m) for magnetization saturation.

- Upon increasing number of stacks in stack structure, the interlayer coupling between CoFeB layers enhances and provides a better flux closure, which leads to a substantial drop in H_C and changes the hysteresis loop shape away from transcritical to soft magnetic type with high remanence ratio (> 75 %) and saturates considerably at lower applied magnetic field (~ 10 kA/m).
- The improvements in the magnetic properties of stack structured films as compared to thick single-layer films are found to be strongly dependent on thickness of spacer layer and number of spacer layers.
- The interlayer coupling between CoFeB layers in stack structure changes significantly with temperature caused mainly by the increase in M_S. In addition, temperature dependent *M-H* loops display that the competition between interlayer coupling and interfacial strain determines the nature of *M-H* loop and provides unusual variation of $H_C(T)$, i.e., minimum in $H_C(T)$ vs T curve, which shifts to lower temperature depending on spacer layer thickness and number of stacks.
- The variations in the magnetic properties of single-layer and stack structured films are explained on the basis of stress dependent stripe domain in single-layer films and number of CoFeB layers and spacer layer thickness dependent interlayer coupling in stack structured thin films.

Chapter 6

Temperature dependent magnetization reversal and enhanced magnetic properties in FeTaC/SiO_2 multilayer thin films

भारतीय प्रौद्योगिकी संस्थान गुवाहाटी
Indian Institute of Technology Guwahati

6.1. Introduction

The development of magnetic multilayer thin films with enhanced soft magnetic properties has revealed various fascinating phenomena and attracted enormous interest in recent eras due to their potential application in modern magnetoelectronic devices such as magnetic random access memory [TANG2010, IANN2014], soft magnetic underlayer in perpendicular magnetic recording media [KHIZ2004, SPAL2011], magnetoresistive read head [PIRA2011, MALL2012], *etc*. However, a careful review of the literature shows that the soft magnetic properties of different alloy thin films exhibit a strong dependence on the film thickness, growth conditions and constituent elements of the films [INGV2002, LIUZ2006, SHAR2006, IKED2010, KIMJ2013, SUNJ2015]. Thickness dependent study of various amorphous thin films unveils that soft magnetic properties are degraded at higher film thickness (> 100 nm) due to change in magnetic domains caused by the development of stress induced effective magnetic anisotropy [CRAU2002, SHAR2006, LIXW2007, IKED2010]. In addition, these type of films display spin reorientation transition from in-plane magnetization to out-of-plane orientation of magnetization or vice-versa [SHAR2006, LIXW2007, COIS2009], which induces additional noise and hence limits thicker magnetic films from selective applications [TANA20032, ITOS2005, PIRA2007]. Among various soft magnetic amorphous thin films, FeTaC based alloy thin film is considered to be one of the promising materials due to its tunable magnetic properties [WEIV2000, TANA2002, JIAN2005, PERU2009, PERU2010, MISH2011], high thermal stability [HASE1995] and reduced noise properties [TANA2002].

In order to obtain enhanced soft magnetic properties at higher film thickness, multilayer thin films having ferromagnetic layers separated by non-magnetic (metallic and non-metallic) layers were reported [NAOE1998, KATI2000, HUAN2001, NAKA2001, TANA2002, OKUM2003, OKUM2004, JICW2005, URSE2005, NAVA2009, PERU2009, SHAH2010, MISH2011, KORE2012, KRAV2012, GENG2013, DASC2016]. This opened up novel paths of studying magnetism and magnetic interactions between ferromagnetic layers in multilayer thin films from both theoretical and experimental points of view. As the magnetic thin films are deposited sequentially with a fine non-magnetic spacer layers, the magnetic interaction between ferromagnetic layers is unavoidable. One of the technological hurdles in multilayer films is to understand and control the interlayer magnetic coupling between ferromagnetic layers. For instance, Naoe et al. [NAOE1998] reported that the introduction of Al spacer layer between FeCuNbSiB layers in multilayer films reduces coercivity (H_C) largely (nearly two orders) for Al thickness of 2 nm and shows oscillatory

nature of H_C with increasing Al thickness up to 10 nm. Hence, FeCuNbSiB/Al multilayers revealed superior soft magnetic properties than thick FeCuNbSiB single-layer film due to the magnetostatic coupling between two FeCuNbSiB layers. Tanahashi et al. [TANA20032] reported that laminated type Fe(Ta,Ti,Nb)C/Ta nanocrystalline thin films display lower H_C as compared to single-layer thick films and attributed to magnetostatic interaction between adjacent nanocrystalline layers. Liu et al. [LIUX2012] investigated the interlayer coupling between continuous multilayer films and patterned one (nanowires) and proposed that the interlayer coupling in continuous $[CoPd]_4/Au/[CoPd]_2$ film is significantly weak as compared to that of nanowires due to additional magnetostatic interaction via stray field in nanowires. Huang et al. [HUAN2001] reported that the improvement of soft magnetic properties in HITPERM/SiO_2 multilayer thin films is very much dependent on the thicknesses of both ferromagnetic and spacer layers. Okamura et al. [OKUM2003, OKUM2004] reported that in HITPERM/SiO_2 multilayer films, neither thickness variation of each layer nor the number of stacking significantly affects the damping process in a range of film thicknesses of 50–150 nm, while coercivity (H_C) values strongly depend on the number of multilayers and spacer layer thickness. Furthermore, the laminated type HITPERM films with SiO_2 spacer layers exhibit stepped magnetization curves with multiple states associated with temperature dependent sequential switching of various layers [OKUM2004]. Urse et al. [URSE2005] reported the effect of number of multilayers, composition, and thermal treatment conditions on the structural, electrical and magnetic properties of $[FeNi/SiO_2]_n$ thin films and showed superior soft magnetic properties in multilayer films. Recently, Geng et al. demonstrated that multilayer thin films of $[FeNi\text{-}O/SiO_2]_n$ exhibit in-plane uniaxial magnetic anisotropy and show excellent high-frequency performances in GHz range [GENG2013].

While most of the earlier works on multilayer films have been focused from applications point of view, there are only limited reports or no systematic studies have been reported to understand (i) the effect of SiO_2 spacer layer on the improvement of soft magnetic properties of multilayer thin films and (ii) their stability against the spacer layer thickness, number of spacer layers and the individual thicknesses of ferromagnetic layers and (iii) the effect of temperature on various types of magnetic coupling between ferromagnetic layers. Therefore, in this chapter, we report systematic investigations on the effect of number of SiO_2 spacer layers (n), thickness of SiO_2 spacer layer (z), magnetic domains of FeTaC layers on the interlayer coupling between FeTaC layers and their influences on the magnetic properties at room temperature and at lower temperatures (30 K

– 300 K) in multilayer [FeTaC (y nm)/SiO_2 (z nm)]$_n$/FeTaC (y nm) films with y = 100/(n+1), n = 0 - 3 and z = 0 - 6. In order to understand the modification in the magnetic properties of multilayer films, single-layer FeTaC (x nm) films of varying thicknesses (x = 5 – 100 nm) are prepared and studied for comparison.

6.2. Experimental details

Amorphous $Fe_{80}Ta_8C_{12}$ (FeTaC) alloy based single-layer thin films with different thicknesses (x = 5 – 100 nm) and multilayer thin films of [FeTaC (y nm)/SiO_2 (z nm)]$_n$/FeTaC (y nm) are deposited directly on thermally oxidized Si substrate using DC/RF magnetron sputtering techniques at ambient temperature. The base pressure of the chamber is maintained to be better than 1×10^{-4} Pa. The sputtering Ar gas pressure for the deposition of FeTaC and SiO_2 layers is optimized at 1.33 Pa. The deposition rate is pre-calibrated using ex-situ surface profilometer (Veeco, Dektak 150 model) and found to be 2.46 nm/min and 0.21 nm/min for the deposition of FeTaC and SiO_2 layers, respectively. The total thickness of FeTaC film is fixed at 100 nm and the thickness of the individual FeTaC layer in multilayer films is controlled using the relation y = 100/(n+1) [NAOE1998, HUAN2001, TANA20032, MISH2011], where y is the individual thickness of FeTaC layer in multilayer films, n is the number of SiO_2 spacer layers varied between 0 and 3, and z is the thickness of spacer layer controlled between 0 and 6 nm. The total thickness of each film in multilayer films was controlled by monitoring the pre-calibrated deposition time during deposition.

Amorphous nature of as-deposited FeTaC films was confirmed by X-ray diffraction (XRD) recorded using a high-power X-ray diffractometer (Rigaku TTRAX III, 18 kW) with Cu-K_α radiation (λ = 1.541 Å) and transmission electron microscopy (TEM, Jeol 2100 and Technai G^2 F20) techniques. Thickness and surface roughness of the as-deposited films were also measured by X-ray reflectivity (XRR) technique. Simultaneous atomic force microscopy (AFM) and magnetic force microscopy (MFM) studies were performed to study the topographic feature and local magnetic domains (Bruker Dimension Icon). MFM was performed in dual-pass lifting mode with commercially available CoCr-coated tips, which were magnetized along the tip axis and therefore sensitive to stray field gradients from out-of-plane oriented domains or the out-of-plane components of domains oblique to the surface. The domain images were acquired at the zero-field state. Room temperature and temperature dependent magnetic properties of the films were analysed using vibrating sample magnetometer (VSM, LakeShore Model 7410) by performing magnetic hysteresis

loops (*M-H*) at room temperature and at low temperatures in the temperature range between 30 K and 300 K. Magnetic domain images and Kerr loops were obtained using magneto-optic Kerr effect (MOKE) microscopy (Evico Magnetics Ltd, Germany) technique. Imaging was performed using linearly polarized light with white LED source. Magnetic domain images were observed in both branches of hysteresis cycle in longitudinal MOKE mode. Hysteresis accompanied by simultaneous imaging has been performed for magnetic fields applied at different angles [0° - 180°; easy (0°) and hard (90°) axes] along the film plane.

6.3. Results and discussion

To understand the magnetic properties of FeTaC/SiO_2 multilayer films, we have first examined the structural and magnetic properties of single-layer FeTaC (*x* nm) films as a function of thickness.

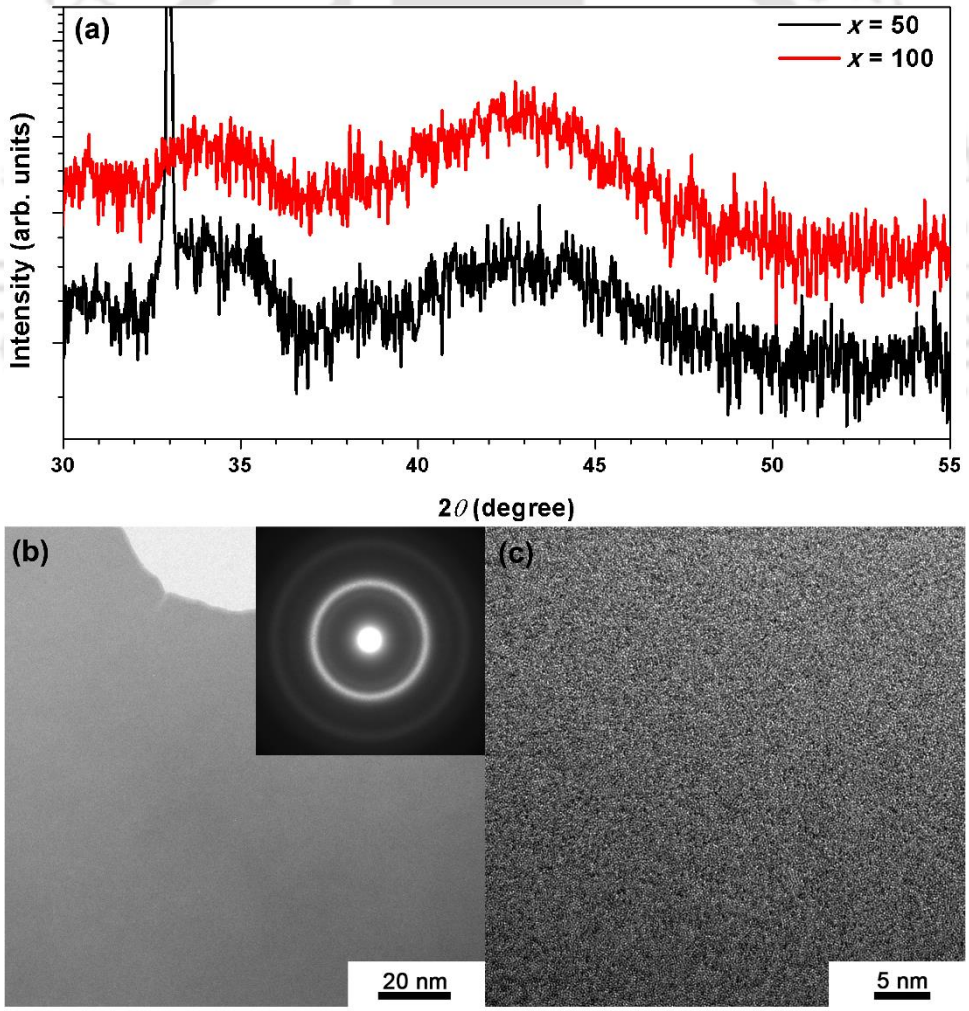

Figure 6.01: Room temperature (a) XRD patterns for FeTaC (*x* nm) films with *x* = 50 and 100, (b) bright-field TEM image and selected area electron diffraction pattern and (c) high-resolution TEM image of FeTaC (100 nm) film.

6.3.1. Properties of single-layer FeTaC thin films

6.3.1.1. Structural properties

Figure 6.01 shows typical XRD patterns of FeTaC films with x = 50 and 100 nm, bright-field plane-view TEM image, selected area electron diffraction (SAED) pattern and high-resolution TEM (HRTEM) image for FeTaC (100 nm) film. It is clearly seen that as-deposited films exhibit only broad peaks at around 2θ = 44° without any other peaks corresponding to other crystalline phases. The XRD peak observed at 2θ = 33° represents Si(200) peak emanating from thermally oxidized Si substrate [CHOM2001]. In addition, the microstructural studies using TEM reveal the existence of plain and even contrast microstructure without any local lattice fringes and halo diffraction ring. This confirms amorphous structure in as-deposited films.

Since the magnetic properties of the thin films strongly depend on the film thickness, it is very much essential to study the actual film thickness and associated roughness as a function of thickness. XRR is one of the non-destructive techniques widely used to evaluate various film parameters such as film thickness, film density, surface/interface roughness, *etc*. Hence, the XRR curves are recorded for the as-deposited FeTaC films and the typical curves are presented in Figure 6.02 for selected thicknesses. The interference pattern (open circles) with clear oscillation peaks is observed for all as-deposited films. With increasing 2θ, the oscillation intensity decreases and attains the same level as the noise in the higher angle region. With increasing thickness, the number of oscillation peaks increases and peak width decreases systematically. To understand the changes in the XRR curves with increasing x carefully, fitting of the XRR curves is preceded by a pattern fitting process between the measured and simulated XRR pattern using GlobalFit software offered by Rigaku. During the analysis, a layered sample model, consists of two simulated layers: (i) a thick SiO_2 layer (as substrate) and (ii) a layer of FeTaC film, is constructed to generate a simulated reflectivity curves. The thickness of the films, interfacial and surface roughnesses, and density of the materials are treated as free fitting parameters to obtain best fits using Globalfit software. As shown in Figure 6.02, the solid lines representing the simulated data using the layered sample model show decent fit to the experimental data and the extracted parameters from the fit are listed in the Table 6.01. While the thickness determined from the fit merely matches with the experimental value, the surface roughness of the FeTaC film does not show any good correlation with the thickness. Nevertheless, the surface roughness increases slightly with increasing x. This could be attributed to the stress, induced in the film

during the deposition at a faster deposition rate to form amorphous structure, which modifies the surface topography with increasing *x*.

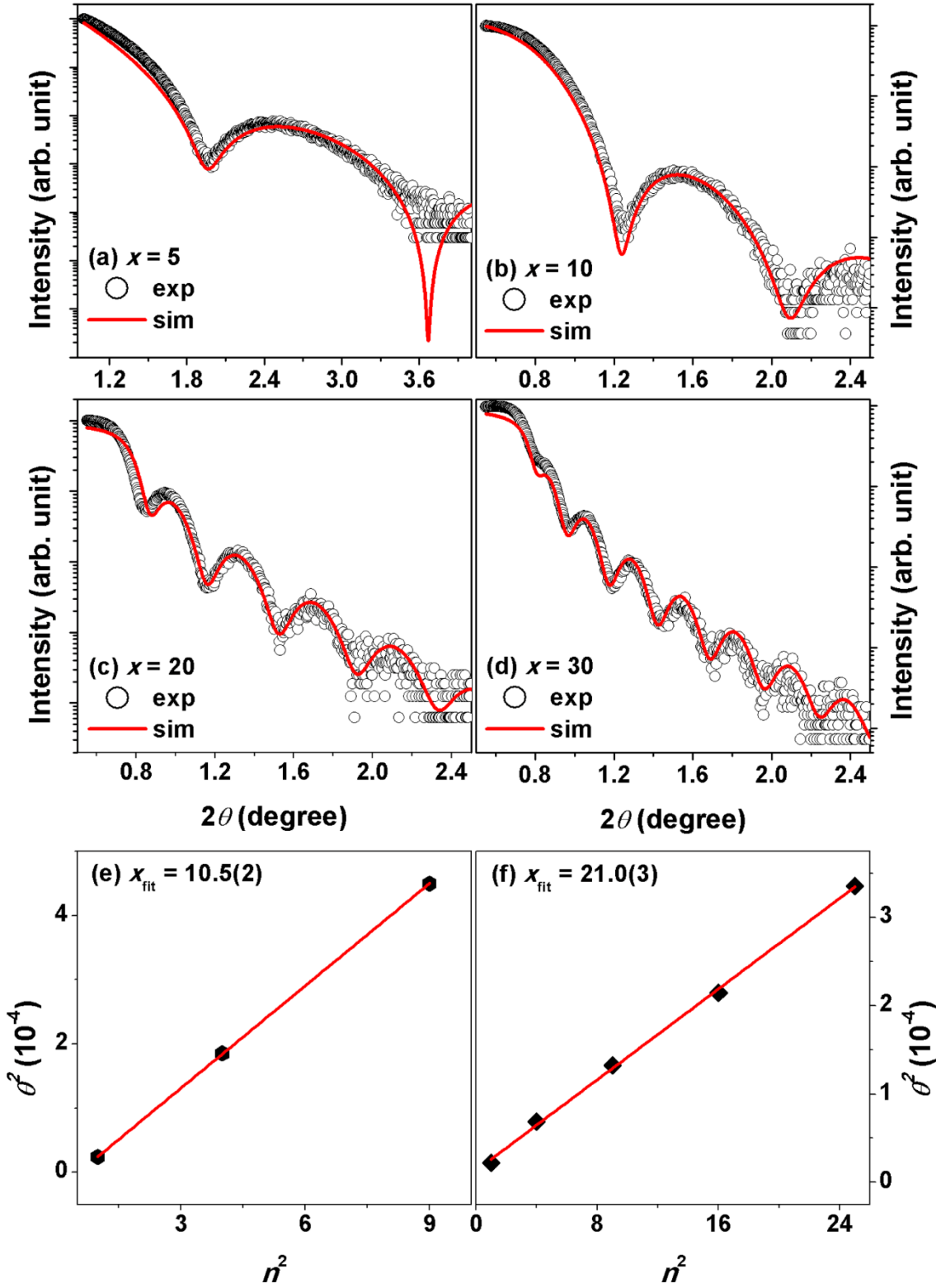

Figure 6.02: Room temperature XRR curves for FeTaC (*x* nm) films with (a) *x* = 5 (b) *x* = 10, (c) *x* = 20, (d) *x* = 30 and the plot of θ^2 versus n^2 for films with (e) *x* = 10 and (f) *x* = 20.

The simulated film thickness is further reconfirmed analytically by using Savitzky–Golay (SG) algorithm as described in eqn.(4.01) [SERA2011]. The values of θ and n are extracted from the XRR curves and plotted as θ^2 *vs* n^2 typically for FeTaC films with x = 10 and 20 nm in Figure 6.02e and 6.02f, respectively.

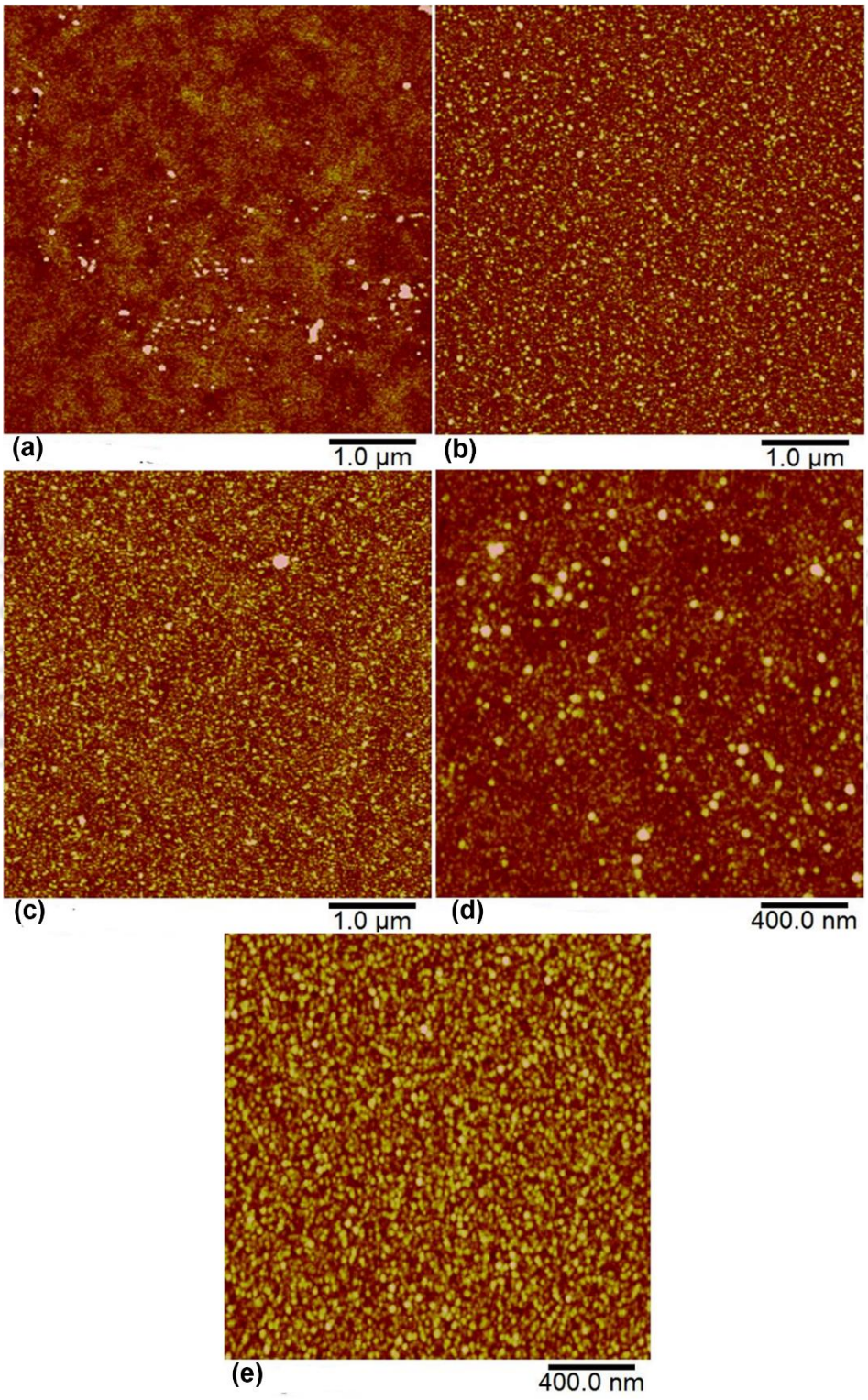

Figure 6.03: AFM images for FeTaC (x nm) films with (a) x = 5, (b) x = 20, (c) x = 30, (d) x = 50 and (e) x = 100.

The experimental data show almost linear behaviour and the fit to the data using eqn.(4.01) provides the values of 2δ from the intercept and $\lambda^2/(4x^2)$ from the slope. Subsequently, x is determined from the slope and listed in Table 6.01. The thickness calculated from the SG algorithm is found to be slightly higher than the estimated thickness, but within the error values. Nevertheless, the values of x determined from layered sample model using Globalfit and SG algorithm are in close agreement with the predicted thickness using pre-calibrated deposition rate. To study the effect of thickness on the surface topography of the films, we have investigated the topography of the films using AFM and shown in Figure 6.03. The following features are observed from the AFM images: (i) FeTaC film with x = 5 nm forms island-like structure along with the existence of very fine nanosized grains of less than 10 nm, which are sparsely distributed. Therefore, the resistance of the film is found to be very high in the range of 10^5 Ω. (ii) With increasing x > 5 nm, all the films display a very clear uniform surface with grain morphology and the grain density increases with increasing x. This reduces the resistance of the films largely down to below 100 Ω. (iii) The extracted values of average surface roughness, summarized in Table 6.01, suggest that although the surface roughness increases significantly with increasing thickness, it does not show any systematic dependency on thickness. These results are in good agreement with those results obtained from XRR analysis using Globalfit software.

Table 6.01: Comparisons of pre-calibrated thickness and thickness obtained from simulation and analytical results from XRR patterns of FeTaC (x = 5 – 100 nm) films. The average surface roughness estimated from both simulation and AFM topography is also included.

FeTaC film thickness (x nm)	Simulated XRR results		Analytical results thickness (x nm)	AFM surface roughness (nm)
	Thickness (x nm)	Surface roughness (nm)		
5	4.9(3)	0.45(2)	5.3(2)	0.38(3)
10	9.4(6)	0.47(3)	10.5(2)	0.53(2)
20	19.8(3)	0.55(2)	21.0(3)	0.60(2)
30	29.3(7)	0.61(2)	30.7(2)	0.53(1)
50	49.5(5)	0.72(3)	50.3(2)	0.69(3)
70	69.4(7)	0.69(3)	70.6(3)	0.74(3)
100	99.1(9)	0.75(2)	100.2(4)	0.80(2)

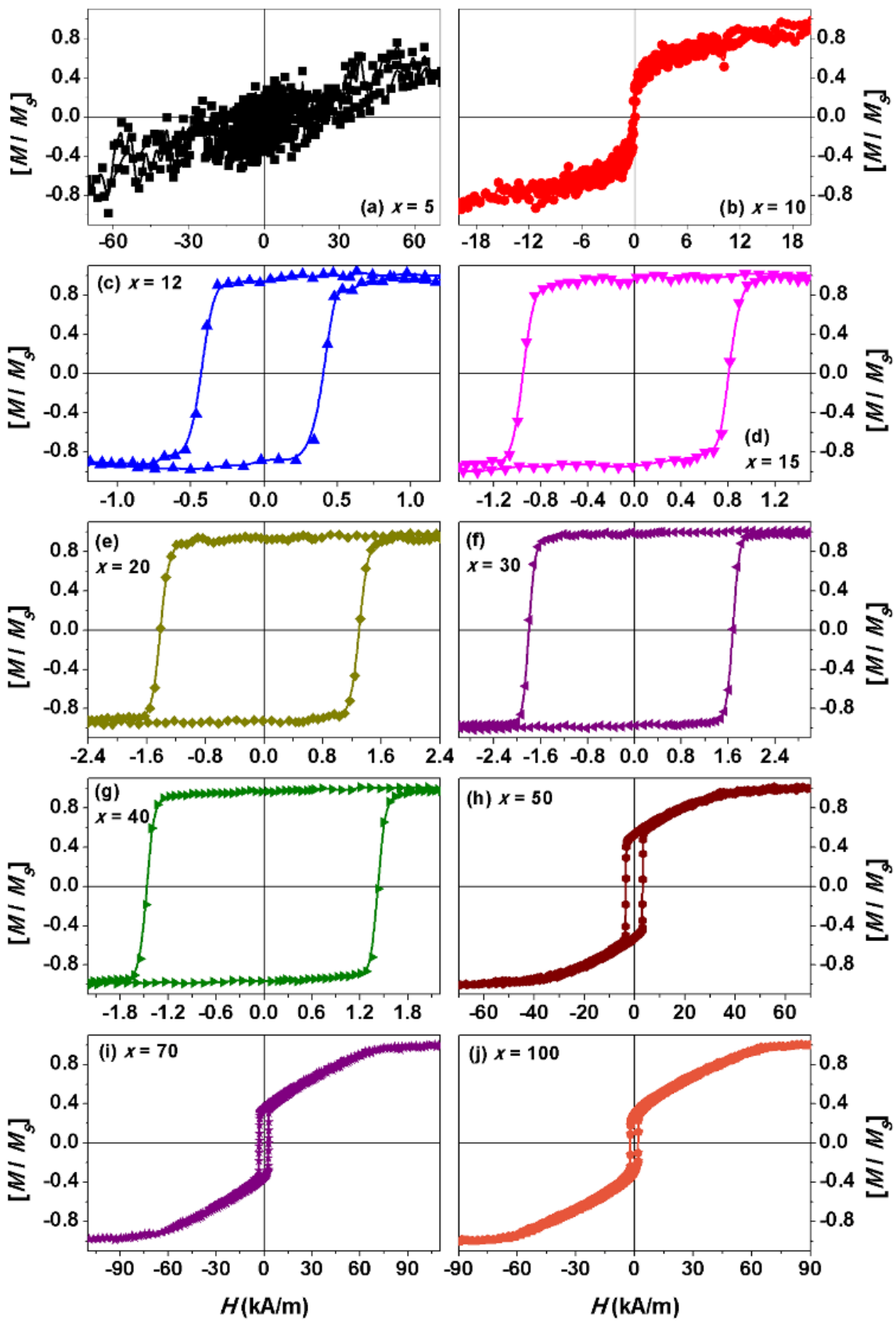

Figure 6.04: Room temperature normalized *M-H* loops measured along the film plane for FeTaC (*x* nm) films with different thicknesses.

6.3.1.2. Room temperature magnetic properties

Figure 6.04 depicts room temperature normalized *M-H* loops measured along the film plane for FeTaC (*x* nm) films with different thicknesses (*x* = 5–100 nm). The extracted magnetic parameters such as H_C, saturation field (H_S), nucleation field (H_N) and remanence ratio (M_R/M_S, where M_R is remanence magnetization) from the *M-H* loops are plotted as a function of thickness in Figure 6.05.

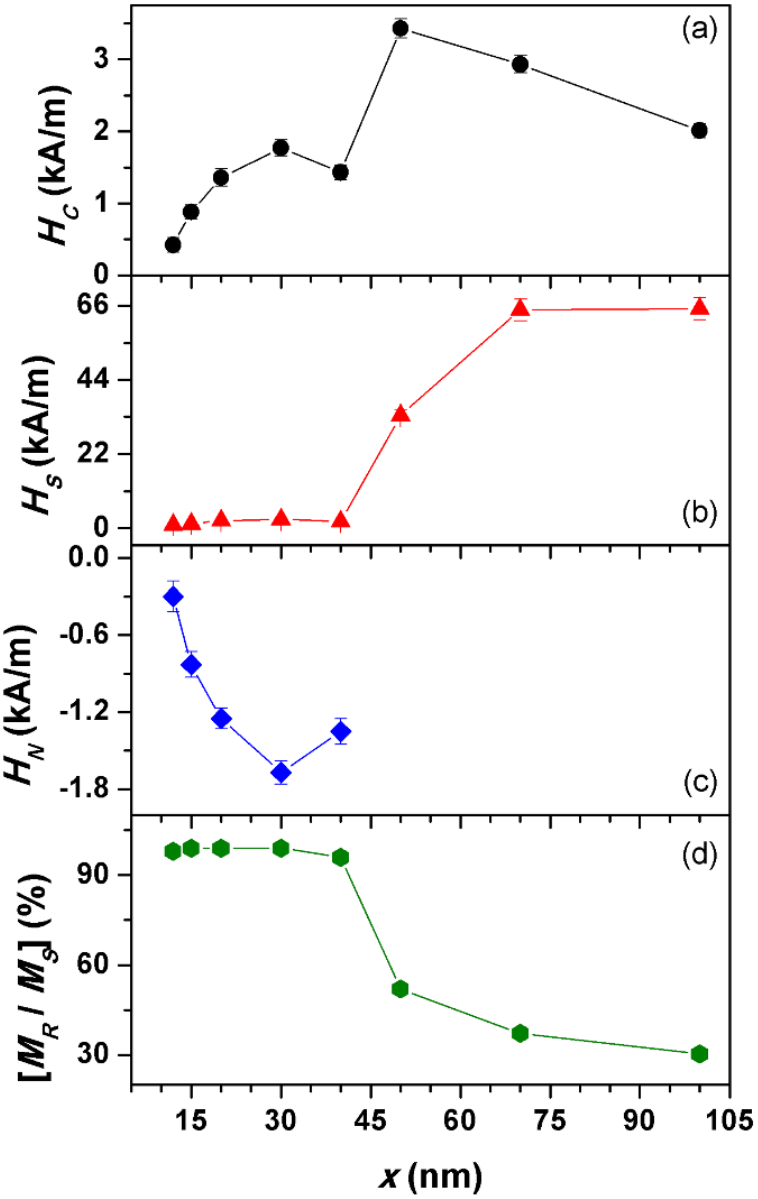

Figure 6.05: The variations of (a) H_C, (b) H_S, (c) H_N and (d) $[M_R/M_S]$ as a function of thickness of FeTaC (*x* nm) films.

It is observed that (i) FeTaC (5 nm) film shows a very weak magnetic signal (paramagnetic) with a noisy background. (ii) With increasing *x* to 10 nm, the film displays a clear hysteresis

behaviour, which needs significantly higher applied magnetic field to saturate the film's magnetization. (iii) On further increasing x up to 40 nm, all the films depict rectangular loops with high M_R/M_S of more than 98 % and lower H_S (< 2.2 kA/m). H_C and H_N increase progressively from 0.42 kA/m to 1.77 kA/m and from -0.3 kA/m to -1.67 kA/m with increasing x from 12 to 30 nm, respectively and then decreases slightly to 1.43 kA/m and -1.35 kA/m for x = 40 nm film. (iv) The loop shape changes drastically into different nature upon increasing $x \geq 50$ nm, i.e., into transcritical loop [MURA1966, PRAD2004, SHAR2006, LIXW2007, COIS2009]. As a result, a linear variation of magnetization before the saturation occurs and one needs considerably a large H_S to saturate film's magnetization (> 40 kA/m). (v) Therefore, H_C increases suddenly to 3.5 kA/m and then decreases almost linearly at a rate of 28.6 A/(m-nm) for x up to 100 nm. Similarly, H_S also increases rapidly to 64.7 kA/m with increasing x to 70 nm and then tends to saturate for x = 100 nm film with H_S of 65.13 kA/m. (vi) In addition, the magnitude of magnetization reversing close to H_C decreases significantly and the region of linear variation of magnetization increases largely with increasing thickness. This causes a large reduction in M_R/M_S down to 30% for FeTaC (100 nm) film. These results clearly suggest that the magnetic properties of FeTaC films at room temperature strongly depend on x, i.e., (i) FeTaC films with $x < 10$ nm show paramagnetic nature, (ii) a clear ferromagnetic behaviour with rectangular shaped loop is observed when 12 nm $\leq x \leq$ 40 nm, and (iii) the rectangular shaped loop transforms into transcritical one for $x \geq 50$ nm.

The observation of paramagnetic nature in ultra-thin films could be interpreted as the growth morphology of island-like structure during the initial growth stage of the films. With increasing x, the island-like structure turns out to be continuous and the average size of surface grains increases with increasing x. This develops in-plane anisotropy in the films caused by the formation of aligned ferromagnetic atom pairs due to their strong magnetic exchange coupling during deposition process. Since the films are deposited at a faster deposition rate to form amorphous structure, the stress quenched in the films during deposition increases progressively with increasing x [SHAR2006, COIS2009]. Hence, H_C, H_S and H_N increase gradually with increasing x up to 30 nm. Upon increasing x beyond critical value (50 nm in the presently investigated films), the spin-reorientation transition from in-plane magnetization to dense stripe domain occurs due to stress induced effective magnetic anisotropy (K_{eff}). In order to elucidate the nature of magnetic domains, the magnetic domain structure is investigated using MFM and depicted in Figure 6.06. The

films with $x \leq 40$ nm display almost no features visible through MFM, which is sensitive only to the magnetic field generated by the sample magnetization directed out-of-plane to the sample surface. This could be attributed to the existence of in-plane magnetic domains, which characterize soft magnetic behaviour in these films as evidenced from Figure 6.04.

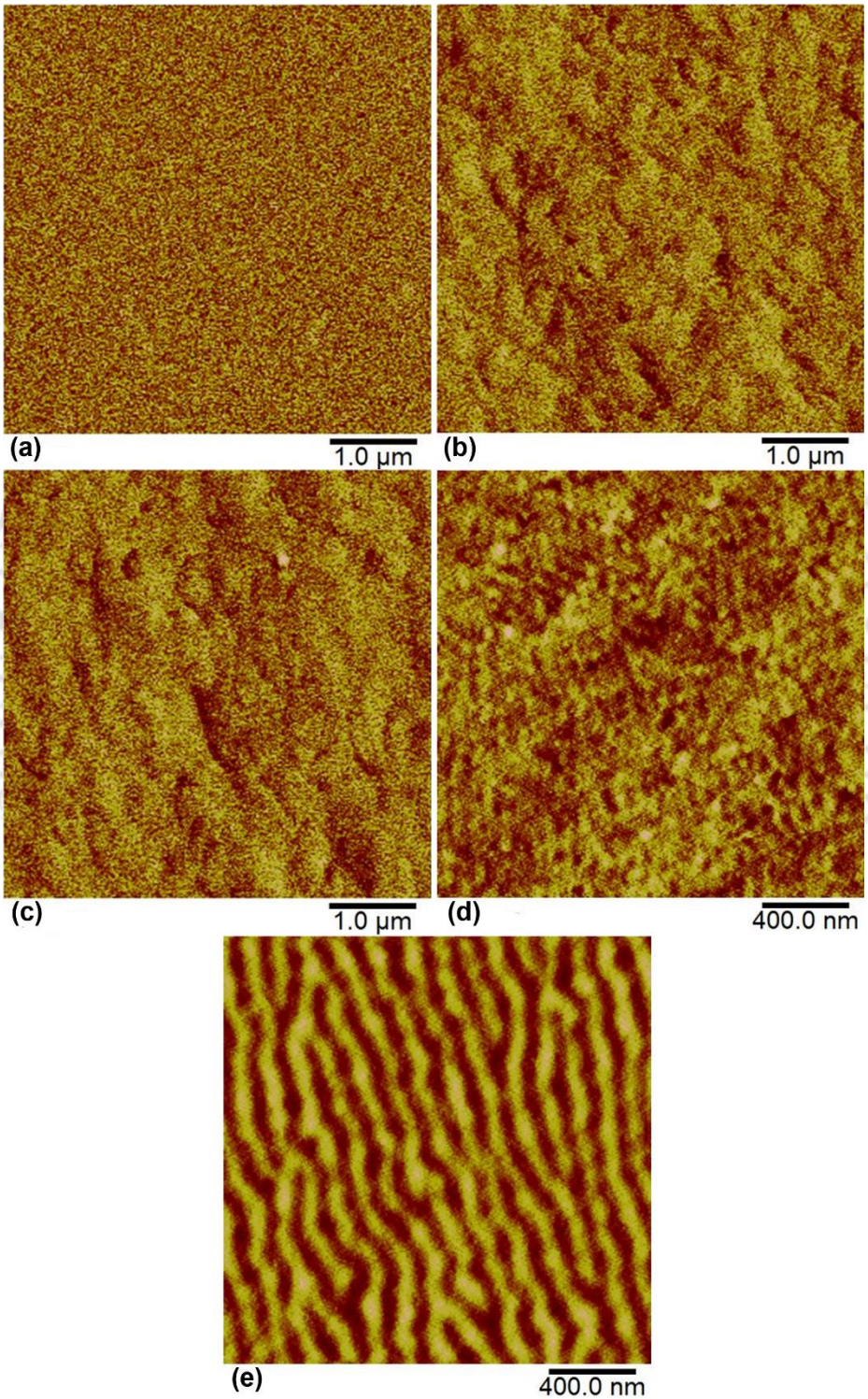

Figure 6.06: MFM images obtained at zero-field state for FeTaC (x nm) films with (a) x = 5, (b) x = 20, (c) x = 30, (d) x = 50 and (e) x = 100.

On the other hand, higher thickness FeTaC films (x > 50 nm) are elucidated by the presence of magnetic dense stripe domains with a component of the magnetization vector directed perpendicular to the film plane. Therefore, these films exhibit transcritical loop due to two distinct magnetization phases. The width of the stripe domains determined by fast Fourier transform analysis of the MFM image is found to be about 74 nm. This is in close agreement with the earlier reports on similar amorphous systems [CRAU2002, PORR2002, SHAR2006, COIS2009, CHEN2013, WUDO2015]. Although FeTaC (50 nm) film unveiled transcritical like loop [see Figure 6.04h], the MFM image depicts random nucleation of perpendicular magnetic component without a clear dense stripe domain pattern. This could be attributed to presence of large in-plane magnetic component and development of progressive perpendicular component in the film. These results confirm that the magnetic domains transform from in-plane orientation of magnetization to stripe domain at a critical thickness of 50 nm.

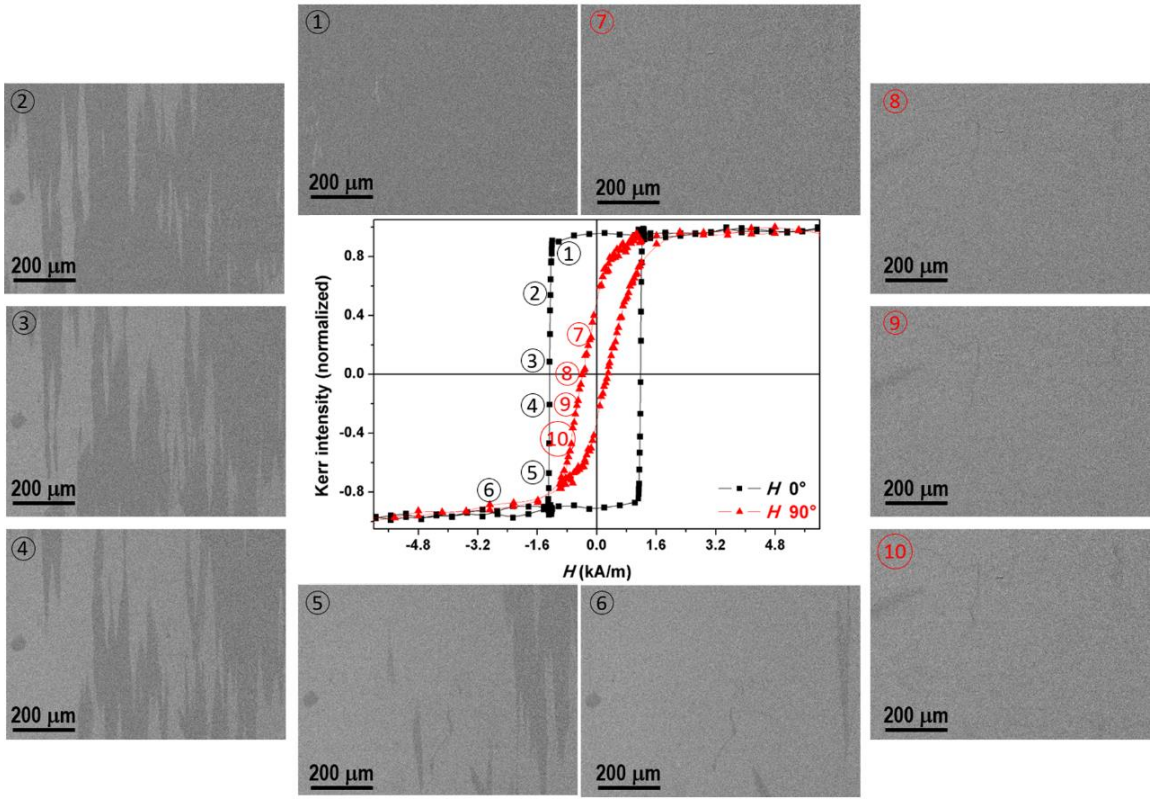

Figure 6.07: Kerr loops and magnetic domain images for FeTaC (20 nm) film measured along easy axis (H = 0°) and hard axis (H = 90°) in the plane.

To study the nature of in-plane magnetic domains in detail, we have simultaneously obtained Kerr loops and magnetic domain images along the film planes using MOKE microscopy. Figure 6.07 depicts the room temperature Kerr loops measured along the film

planes and magnetic domain images for FeTaC (20 nm) film. It is clearly evident that the film displays rectangular loop in one direction [easy-axis direction in the plane (0°)] and nearly flat type loop characterized by reduced remanence in another direction [hard-axis direction in the plane (90°)]. The values of H_S in both the measurement directions are found to be nearly the same. In addition, the magnetic field required to switch the magnetization along the easy-axis from one direction to another direction is observed to be quite low (< 0.25 kA/m). From the VSM results (Figure 6.04e), the magnetic field required to switch the magnetization from one direction to another direction is found to be about 0.4 kA/m, which is slightly larger than the one obtained from MOKE microscopy. This could be possibly related to the contribution from the finite edges of the sample used in VSM measurement. The magnetic domain images obtained along the easy-axis display a rapid switching of large-sized magnetic domains due to domain wall motion.

Table 6.02: The thickness dependent H_K, H_S, K_U, $\mu_0 M_S$, K_{eff}, δ and θ_1 for FeTaC films.

FeTaC thickness (x nm)	H_K (or) H_S (kA/m)	K_U (J/m^3)	$\mu_0 M_S$ (mT)	K_{eff} (J/m^3)	δ (nm)	θ_1 (°)
12	1.03(5)	147.7(3)	265(2)	-	-	-
20	2.31(7)	449.5(4)	389(3)	-	-	-
30	2.63(6)	646.8(5)	492(3)	-	-	-
40	1.99(4)	461.2(5)	463(4)	-	-	-
50	33.44(5)	-	594(3)	$1.77(2)\times10^5$	54.8(3)	43.2(3)
70	64.73(6)	-	415(2)	$1.83(3)\times10^5$	64.3(1)	56.6(4)
100	65.13(8)	-	501(2)	$1.89(2)\times10^5$	76.3(2)	62.7(2)

On the other hand, the magnetic domain images obtained along the hard-axis reveal no clear domain reversal process due to coherent like magnetization rotation process. This supports the existence of in-plane uniaxial magnetic anisotropy in the films. Accordingly, the value of K_U is determined using eqn.(4.02). The determined values of K_U listed in Table 6.02 show a continuous increase up to x = 30 nm and then decrease slightly for x = 40 nm. On further increasing x (≥ 50 nm), the stress induced magnetic disorder destabilizes the uniaxial anisotropy, which in turn enhances K_{eff} to develop magnetic dense stripe domain.

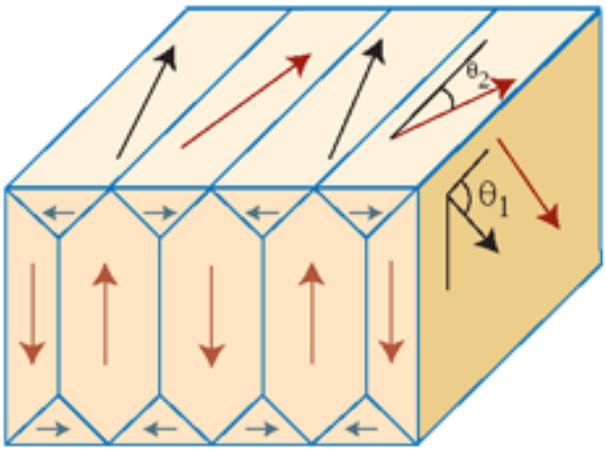

Figure 6.08: Schematic diagram of dense stripe domain for FeTaC (x nm) films with $x \geq 50$.

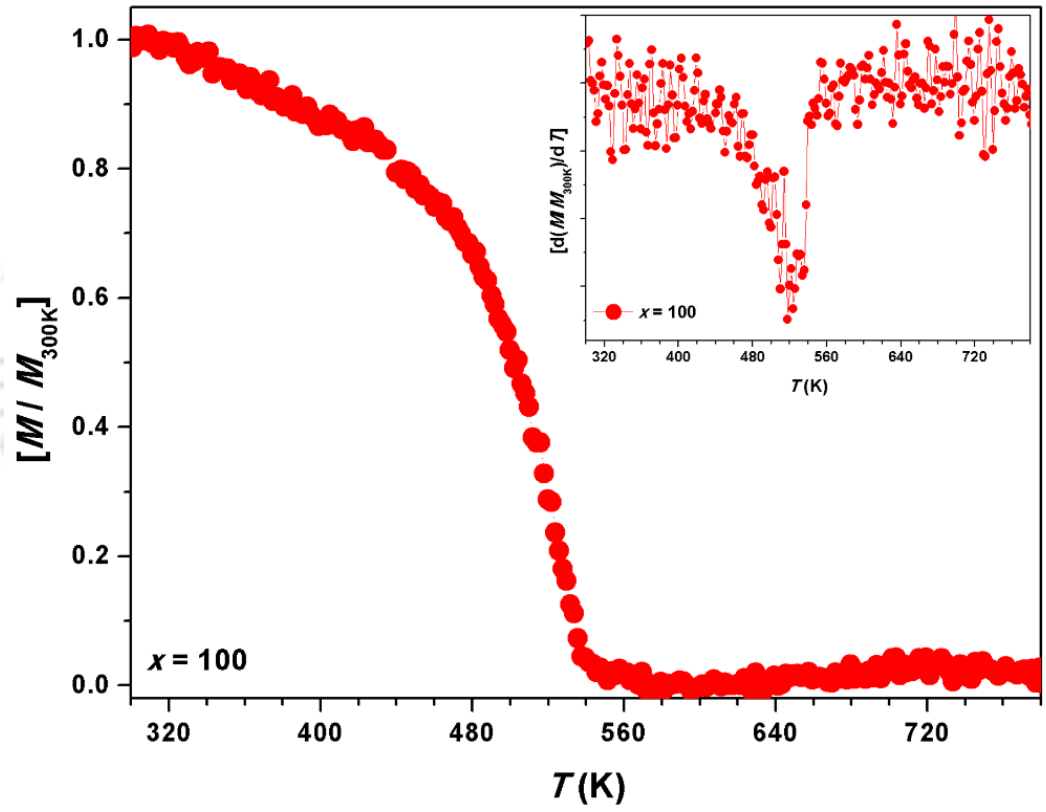

Figure 6.09: High temperature thermomagnetization (M-T) data for FeTaC (100 nm) film recorded under 39.8 kA/m applied field along the film direction.

To analyse the development of K_{eff} at higher x and the corresponding magnetic domain configuration, dense stripe domain model, as shown schematically in Figure 6.08, proposed by Craus et al. [CRAU2002, CRAU2003] following the original model proposed by Mayurama [MURA1966] and Alvarez-Padro [PRAD2004] is used to calculate K_{eff} by substituting the values of H_S, M_S, A and x_c in eqn.(4.03). The critical thickness (x_c) is taken

as 50 nm and *A* is exchange stiffness constant taken as 10×10^{-12} J/m [SING2013]. Similarly, the domain wall width (δ) is calculated by assuming a Landau domain structure [HUBE2014], which is compatible when the sample thickness is larger than $\sqrt{A/K_{eff}}$, as in the present case, using eqn.(4.04). The determined values of K_{eff}, θ_1 and δ are listed in Table 6.02 for $x \geq 50$ nm films. The domain wall width determined from this model and MFM image is in close agreement with each other. In addition, the obtained values of K_{eff} are in good agreement with those values reported for other similar amorphous systems [COIS2008].

6.3.1.3. High temperature magnetic properties

In order to understand the stability of ferromagnetic phase in FeTaC film, high temperature *M-T* data are recorded at a constant applied field of 39.8 kA/m. Figure 6.09 illustrates the normalized *M-T* data above room temperature for FeTaC (100 nm) film. It could be clearly seen from the figure that the film exhibits an incessant decrease in magnetization with increasing temperature up to 540 K and then nearly constant up to 720 K. This is correlated to the magnetic phase transition of the amorphous phase from ferromagnetic to paramagnetic state. Curie temperature (T_C) determined from the thermal derivative of *M-T* data is found to be about 525±3 K. This is almost similar to the one obtained for CoFeB alloys confirming thermally stable magnetic phase in amorphous FeTaC film [DASC2016]. The obtained results reveal that the magnetic properties of amorphous FeTaC (*x* nm) films depend strongly on thickness.

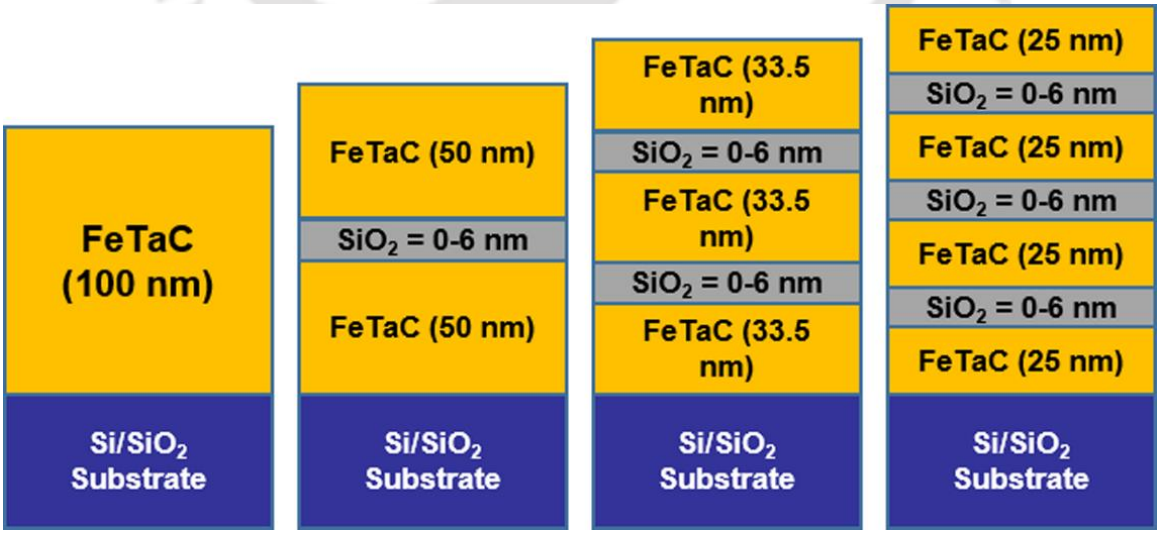

Figure 6.10: Schematic representation of single-layer FeTaC (100 nm) and multilayer structured thin [FeTaC (*y* nm)/SiO_2 (*z* nm)]$_{n=1\text{-}3}$/FeTaC (*y* nm)] films.

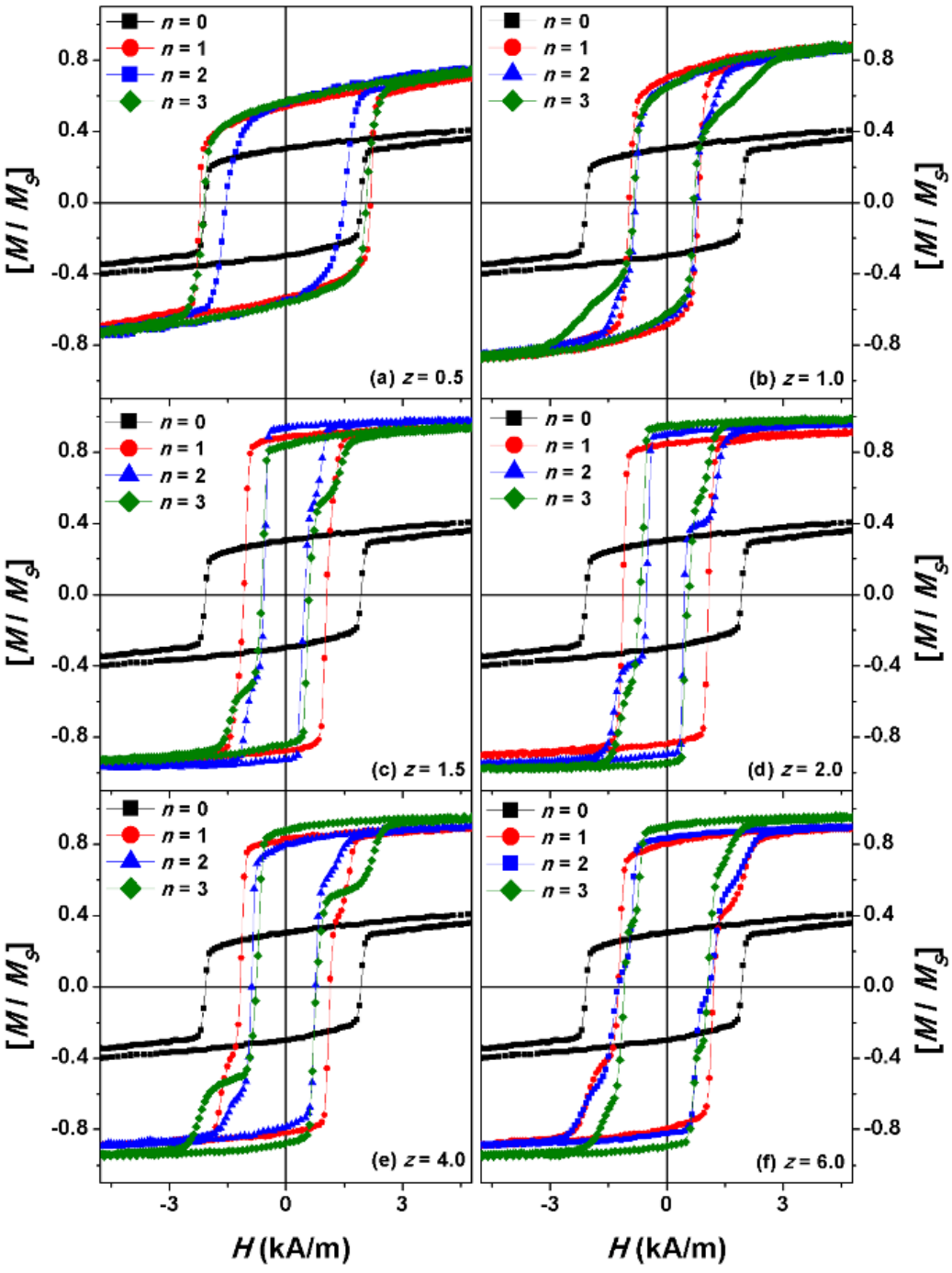

Figure 6.11: Room temperature normalized *M-H* loops for multilayer [FeTaC (*y* nm)/SiO_2 (*z* nm)]$_n$/FeTaC (*y* nm) films with different *z* and *n*.

6.3.2. Properties of multilayer [FeTaC (*y* nm)/SiO_2 (*z* nm)]$_n$/FeTaC (*y* nm) thin films

6.3.2.1. Room temperature magnetic properties

To tune the magnetic properties of thick FeTaC films, multilayer [FeTaC (*y* nm)/SiO_2 (*z* nm)]$_n$/FeTaC (*y* nm) films, as shown schematically in Figure 6.10, is employed in the

present study using SiO_2 spacer layer, as SiO_2 spacer layer plays an important role in controlling the magnetic properties of multilayer films [NAOE1998, HUAN2001, OKUM2003, OKUM2004, URSE2005, PERU2010].

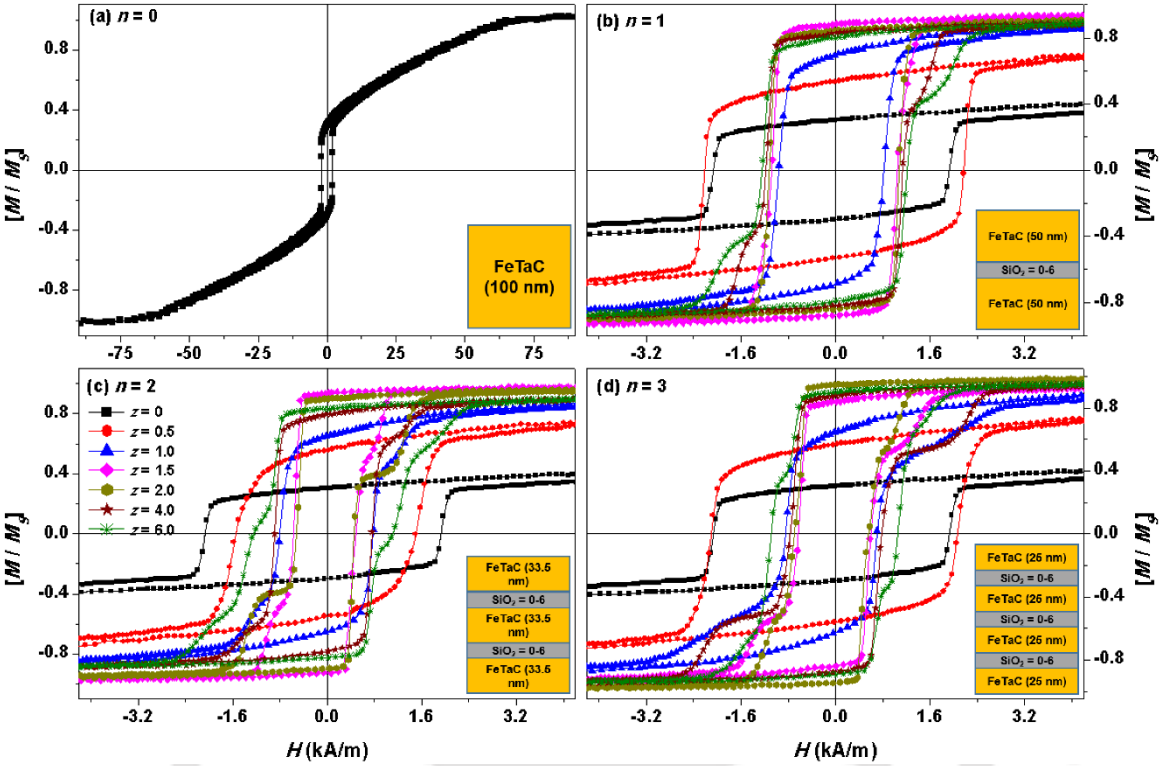

Figure 6.12: Room temperature normalized *M-H* loops for multilayer [FeTaC (*y* nm)/SiO_2 (*z* nm)]$_n$/FeTaC (*y* nm) films with different *n* and *z*.

Figures 6.11 and 6.12 display *M-H* loops measured along the film plane at room temperature for multilayer films. The loops are plotted as a function of *z* for different *n* values (Figure 6.11) and as a function of *n* for different *z* values (Figure 6.12), respectively. Accordingly, the extracted magnetic parameters such as H_C, H_S and M_R/M_S from the *M-H* loops are plotted in Figure 6.13. Room temperature *M-H* loops and extracted parameters reveal the following features: (i) The single-layer FeTaC (100 nm) film exhibits transcritical loop with reduced M_R/M_S of 0.3 and large H_S and H_C of 65.13 kA/m and 1.99 kA/m, respectively. (ii) The introduction of a thin SiO_2 layer (z = 0.5 nm) does not change the loop shape from transcritical nature (Figure 6.11a), but increases M_R/M_S significantly to 0.6 and reduces H_S largely to about 15 kA/m. H_C shows oscillatory behaviour with increasing *n*. (iii) As *z* is increased to 1 nm, the loop shape changes away from transcritical to rectangular one with a large increase in M_R/M_S to 0.75 and reduction in H_S and H_C to 4 kA/m and 0.77 kA/m, respectively. Multilayer film with z = 1 and n = 1 shows a simple magnetization reversal

behaviour, but the increase in n to 2 and 3 reveals a clear stepped magnetization curve (Figure 6.11b) and the formation of step is distinct with increasing n. (iv) On further increasing z up to 2 nm, the loop shape becomes nearly perfect rectangular with almost 100% M_R/M_S and a considerable reduction in H_C to 0.48 kA/m. (v) Multilayer films with $z \geq 4$ nm show stepped magnetization curves even for films with $n = 1$ and the number of such steps increases with increasing n (Figure 6.11f).

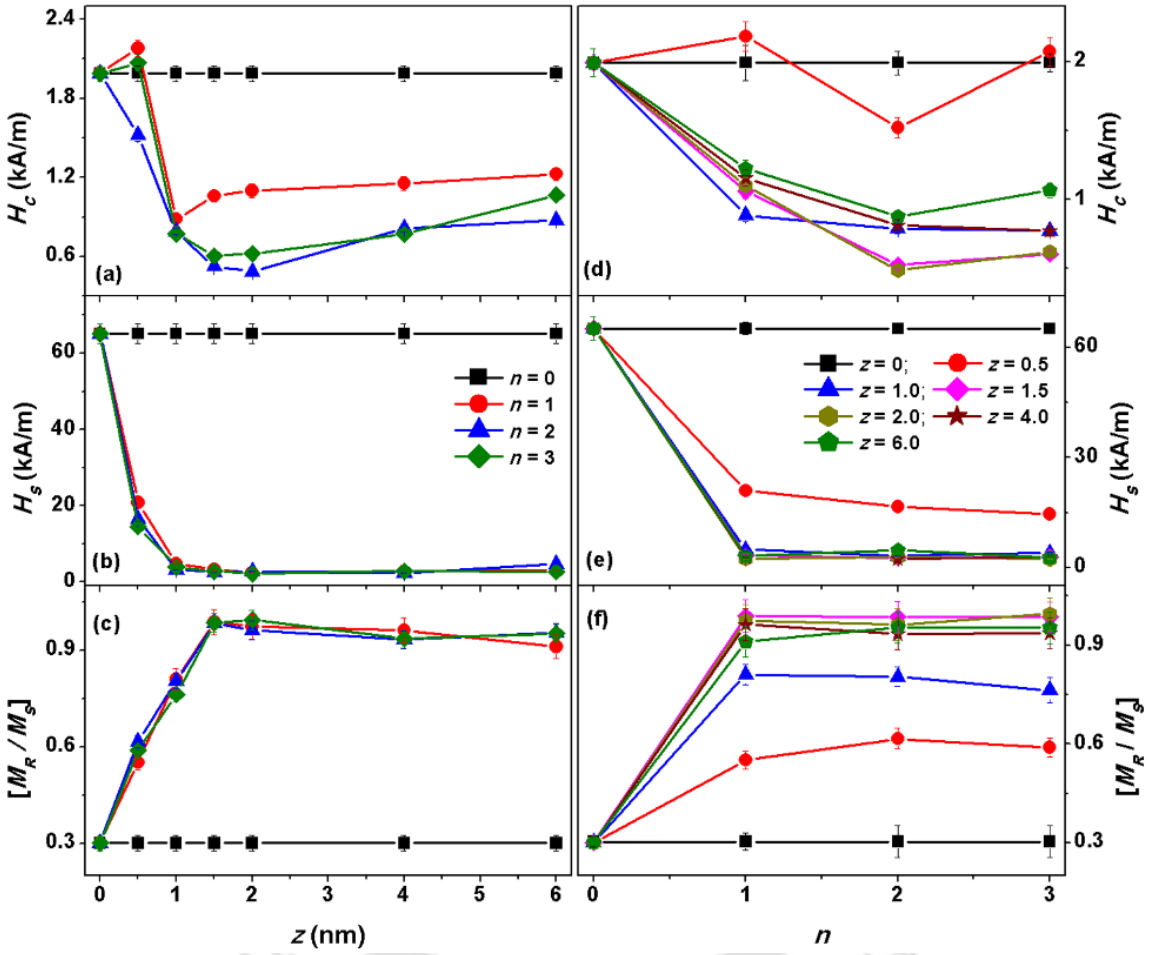

Figure 6.13: The variations of H_C, H_S and M_R/M_S as a function of spacer layer thickness (z) and number of multilayers (n).

On the other hand, the plot of M-H loops for different multilayers (Figure 6.12) reveals the following features: (i) For bilayer films (n = 1, Figure 6.12b), the loop shape changes progressively from transcritical to rectangular as z is increased from 0 to 2 nm. The formation of stepped magnetization curves is observed when z is above 2 nm. As compared to single-layer FeTaC(50 nm) film exhibiting transcritical loop (Figure 6.04h), the bilayer films with two FeTaC(50 nm) layers separated by SiO_2 spacer layer show tuneable magnetic properties depending on z. (ii) For trilayer films (n = 2, Figure 6.12c), the thickness of each

FeTaC layer turns out to be about 33.5 nm and therefore expected to show in-plane magnetization (Figure 6.04). The trilayer films with $z < 1$ exhibit simple magnetization curve. With increasing z up to 4 nm, two-step magnetization curves are observed, while the film with $z = 6$ nm displays three-step magnetization curve. (iii) Similar behaviours are observed for quaternary layer films ($n = 3$) with different z. These results confirm that the nature of magnetization reversal and enhancement in soft magnetic properties of multilayer films strongly depend on n and z.

The obtained results can be explained using change in magnetic domains with increasing n or decreasing y, interface roughness and spacer layer dependent interlayer coupling in multilayer thin films. The single-layer film of amorphous FeTaC (100 nm) showed transcritical loop due to existence of both in-plane and out-of-plane magnetic components, which formed dense stripe domain. Similarly, multilayer films with $z = 0.5$ nm and $n = 1$-3 still showed transcritical loops but with reduced H_S and enhanced M_R/M_S. These results and the surface roughness of the FeTaC layers suggest that the interlayer coupling between FeTaC layers due to direct ferromagnetic coupling through pinholes and the indirect exchange coupling depends strongly on z. Since the average surface roughness of FeTaC layers is varied between 0.55 nm and 0.75 nm, the growth of the SiO_2 spacer layer with $z = 0.5$ nm may not be continuous all the way and therefore the subsequent growth of FeTaC layers may not be well separated from the adjacent FeTaC layer. Therefore, there exists a direct exchange coupling between FeTaC layers through pinholes at random locations depending on the roughness. This arrangement helps to switch FeTaC layers collectively and displays similar transcritical loops, but with reduced H_S and enhanced M_R/M_S. As a result, H_C exhibits oscillatory behaviour with increasing n (Figure 6.13d). With increasing z from 0.5 nm to 4 nm, the spacer layer thickness overcomes the average roughness of FeTaC layers and forms a stable interface. This separates completely two adjacent FeTaC layers and prevents direct interaction through pinholes. Under this circumstance, the interaction between FeTaC layers is expected through either magnetostatic coupling or indirect exchange coupling, which decreases with increasing z [CHOP2000] as given in eqn.(4.05). According to the eqn.(4.05), coupling field (H_{CF}) depends on magnetization, roughness parameters, y and z. Therefore, H_C decreases considerably, but the maximum reduction in H_C depends not only on z, but also on n, i.e., H_C reduces to a minimum value at $z = 1$, 2 and 1.5 nm for $n = 1$, 2 and 3 films, respectively. On further increasing z, the interlayer coupling between FeTaC layers decreases due to larger interlayer thickness. In addition, the magnetic domain state and saturation

magnetization of the FeTaC layers in multilayer film changes due to the decrease in FeTaC thickness (< 50 nm) with increasing $n \geq 2$. This increases H_C significantly and the tendency to saturate H_C at higher z decreases with increasing n (Figures 6.13a and 6.13d). Furthermore, the number of steps in the magnetization curve increases with increasing n at larger z. For instance, the bilayer films ($n = 1$) exhibit single magnetization reversal for z up to 2 nm. With increasing $z > 2$ nm, two-step magnetization curve is observed due to non-collective switching of the bilayer films caused by the reduction in interlayer coupling between FeTaC layers. Similarly, for trilayer films, two-step magnetization curve is observed for z up to 4 nm. By considering the relative variation of magnetization with respect to saturation magnetization, it can be explained that the additional step in the *M-H* loops is mainly due to switching of bottom most FeTaC layer deposited directly on the substrate. On further increasing z to 6 nm in trilayer films, three-step magnetization curve due to individual switching of all three FeTaC layers is observed (Figures 6.11f and 6.12c). For quaternary films with $z = 6$, it is expected to have four-step magnetization curve, if each FeTaC layer switches independently. However, we observed only three-step magnetization reversal behaviour indicating different switching sequences described as follows: the switching of top FeTaC layer followed by the collective switching of next two FeTaC layers and finally bottom most FeTaC layer. This could be attributed to (i) two different interfaces for bottom FeTaC layer (Figure 6.14a) and (ii) strain induced by thick substrate on bottom FeTaC layer is more significant than interfacial strain arising from other materials at different interfaces [COIS2009, HUAN2001, SING2014].

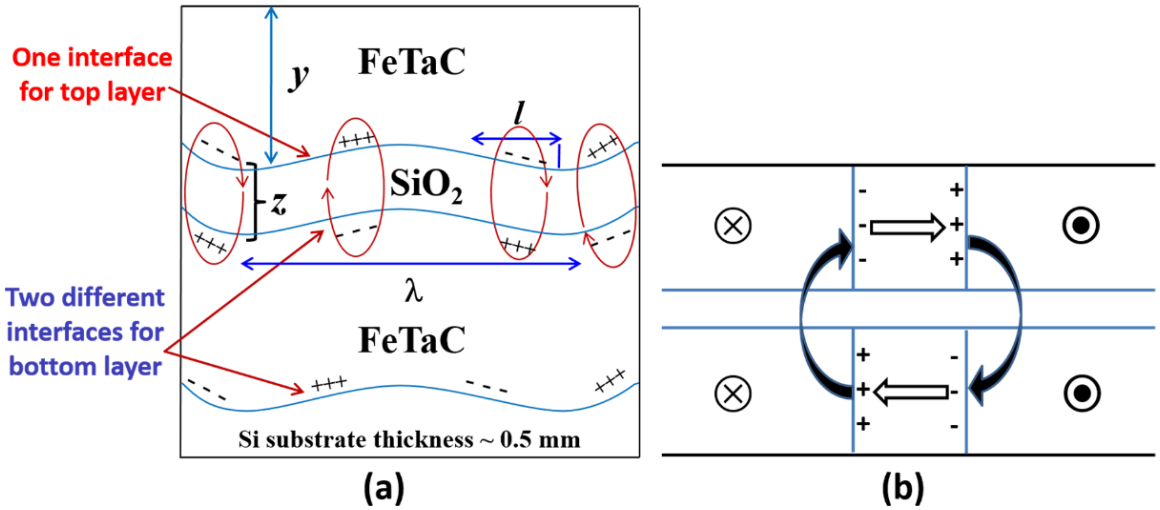

Figure 6.14: Schematic drawing of (a) Néel's orange peel coupling and (b) magnetostatic coupling between the stray fields of domain walls in multilayer thin films.

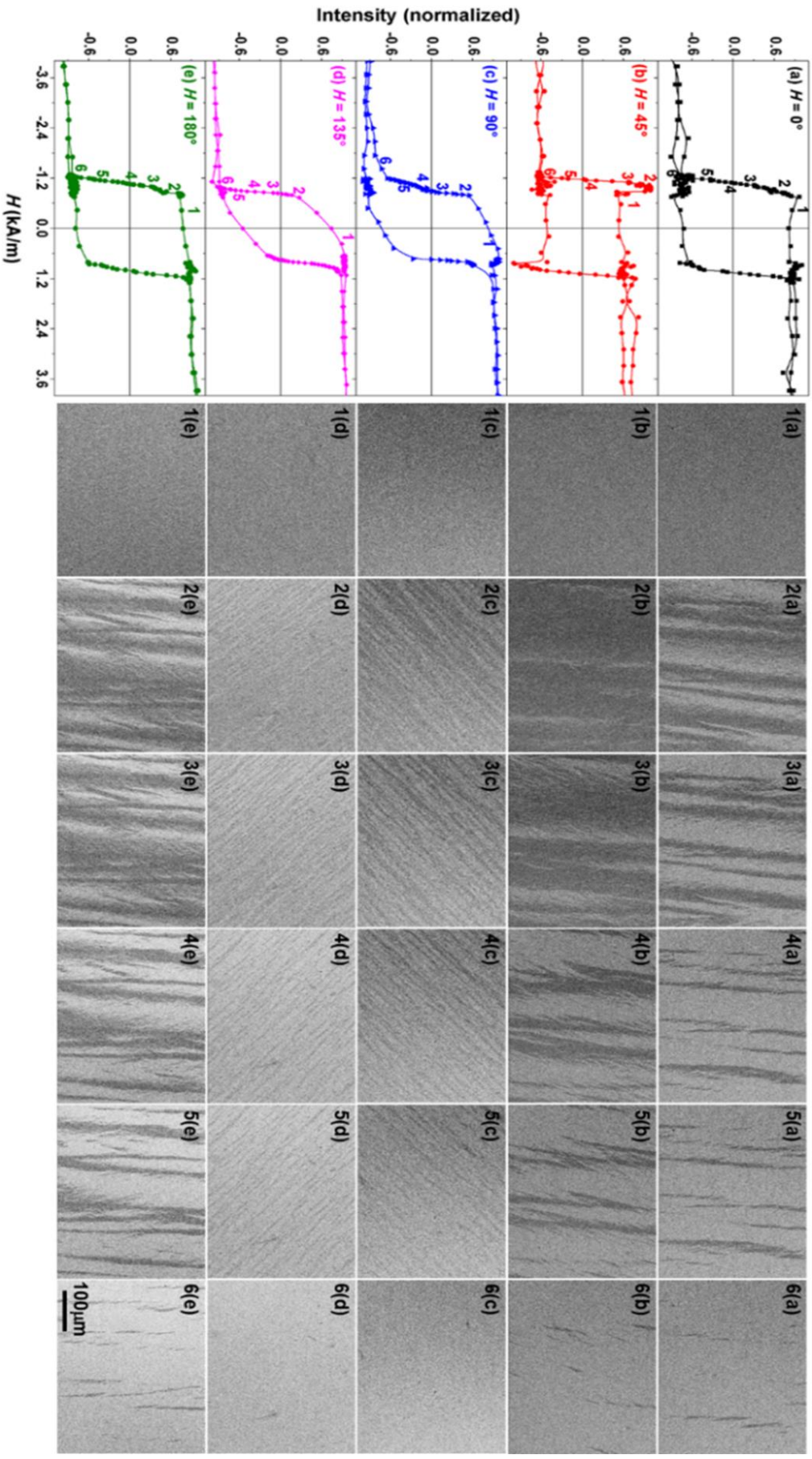

Figure 6.15: Kerr loops and magnetic domain images for multilayer [FeTaC (50 nm)/SiO_2 (z nm)/FeTaC (50 nm)] films with z = 1 obtained at different angles along the film plane. The scale bar is same for all the images.

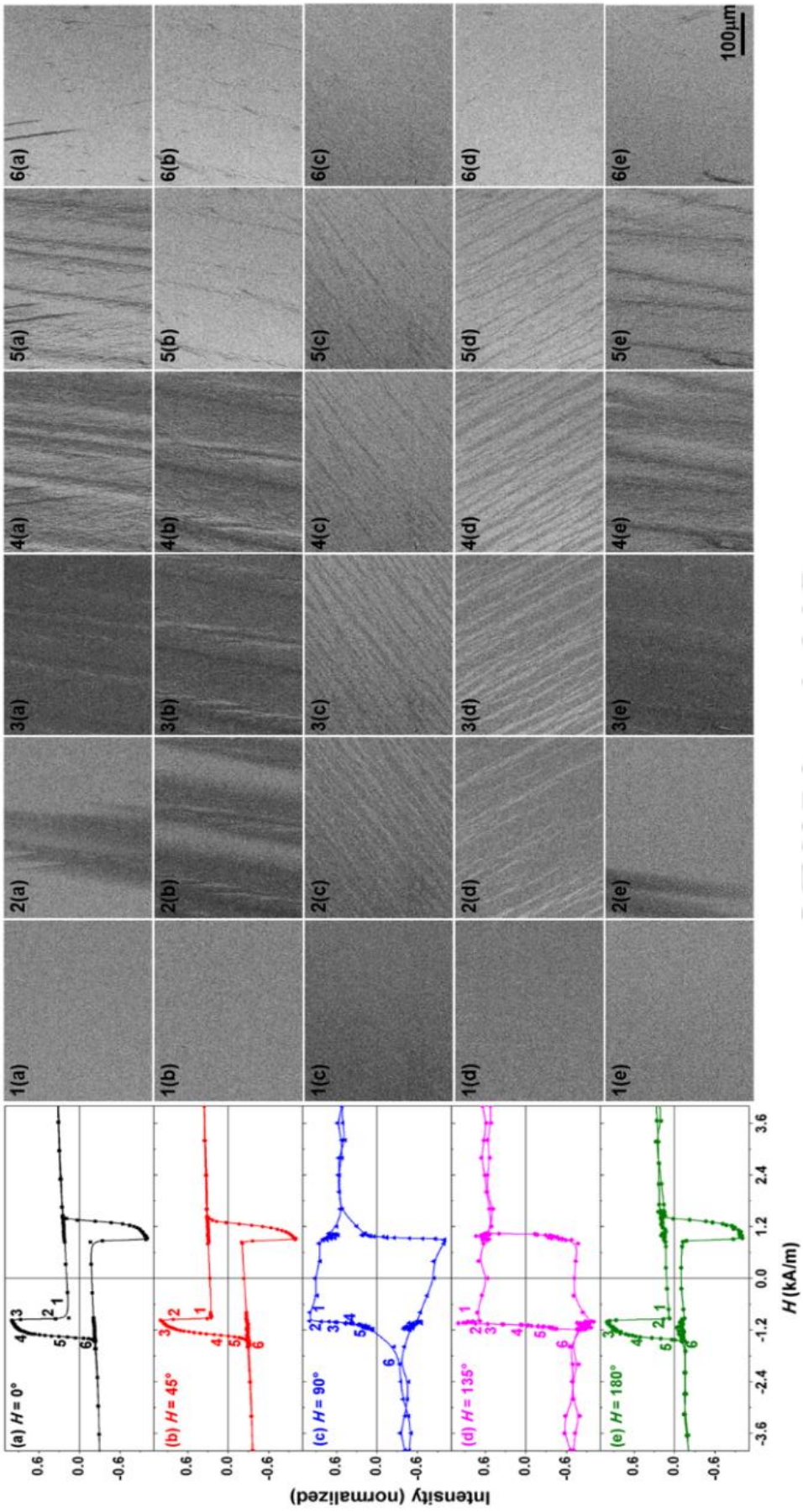

Figure 6.16: Kerr loops and magnetic domain images for multilayer [FeTaC (50 nm)/SiO_2 (z nm)/FeTaC (50 nm)] films with z = 4 obtained at different angles along the film plane. The scale bar is same for all the images.

The dominance of different strain effects could be clearly visualized at low temperatures due to temperature dependent interfacial strain arising from the different thermal expansion coefficients of the materials, which is discussed latter. Nevertheless, these results evidently suggest that the interlayer coupling between FeTaC layers in multilayer films not only reduces H_C markedly from 1.99 kA/m to 0.48 kA/m and reduces H_S rapidly from 65.13 kA/m to 2.2 kA/m, but also enhances M_R/M_S from 0.3 to more than 0.98. This confirms tuning of hard magnetic properties of thick FeTaC films into soft magnetic nature in multilayer thin films.

To study the magnetization reversal in detail, angle dependent magnetization reversal behaviours using longitudinal MOKE for bilayer films with different *z* values are investigated. Figures 6.15 and 6.16 display the Kerr loops and magnetic domain images recorded by longitudinal MOKE and obtained as a function of field applied at different angles along the film plane for $n = 1$ and $z = 1$, and $n = 1$ and $z = 4$ films, respectively. As discussed earlier, the bilayer films having two FeTaC (50 nm) layers exhibit rectangular shaped loop with single and two-step magnetization reversal behaviours for $z = 1$ and 4, respectively. This is completely different from the behaviour observed for single-layer FeTaC (50 nm) film (Figure 6.04h). Figure 6.15 displays the following features: (i) Hysteresis loop measured along the film plane at 0° angle shows rectangular loop and the magnetic domain images illustrate a rapid switching of large sized domains due to domain wall motion. (ii) Tilting the field angle to 45°, we observed a sudden increase of the MOKE intensity in both branches of the hysteresis as compared to saturation. This is due to the existence of transverse component of magnetization exhibiting an overshoot in Kerr intensity [MALL2018]. Such asymmetric loops may also arise due to the dominant contribution from the quadratic component of the magneto-optical effect over the linear one [OSGO1997, POST1997, BUCH2009]. (iii) With increasing applied field angle to 90°, we observed a flat like loop but characterized by switching of smaller sized domains. No coherent rotational process is observed. (iv) A similar behaviour has been observed but with further reduction in domain size when the field is applied along 135° and finally (v) rectangular loop is observed in 180°, a situation similar to the 0°. Although the bilayer films showed enhancement in the magnetic properties of FeTaC films due to interlayer coupling, the behaviour of magnetization reversal is not straightforward as in films with simple magnetic domain structure. With increasing *z* to 4 nm, the sharp increase in MOKE intensity

in both branches of the hysteresis is observed in almost all the angles and the amount of increase in MOKE intensity strongly depends on the applied field angle.

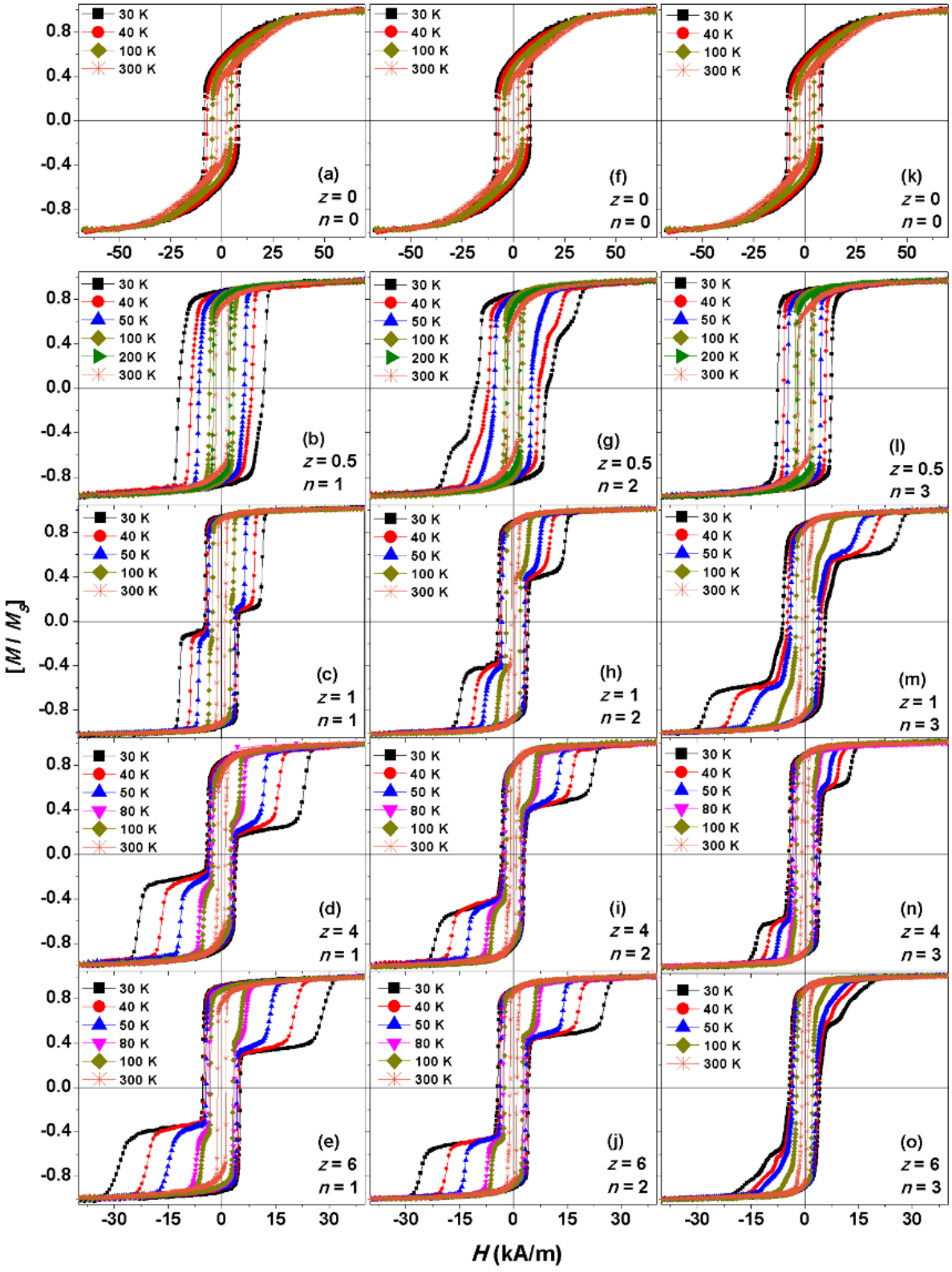

Figure 6.17: Temperature dependent normalized *M-H* loops measured along film plane for multilayer [FeTaC (*y* nm)/SiO_2 (*z* nm)]$_n$/FeTaC (*y* nm) films.

This suggests that the magnitude of transverse components is plausibly high, as compared to bilayer film with z = 1, due to reduced interlayer coupling between FeTaC layers at larger z, which does not help collective switching of FeTaC layers together and hence exhibiting stepped magnetization curve. The presence of any antiferromagnetic coupling between FeTaC layers could not be observed in bilayer films [OSGO1997, SEME2004, BUCH2009]. These results are in close agreement with the magnetization results shown in Figures 6.11 and 6.12.

6.3.2.2. Temperature dependent magnetic properties

To empathise the effect of temperature on the stepped magnetization curves with multiple states and sequential switching in multilayer thin films [HUAN2001, OKUM2004], temperature dependent *M-H* loops are measured along the film plane using VSM over a wide range of temperature 30 K -300 K for multilayer films with n = 1, 2 and 3, and z = 0, 0.5, 1, 4 and 6 and depicted in Figure 6.17. The extracted values of H_C from the *M-H* loops are plotted as a function of temperature in Figure 6.18. It is clear from Figure 6.17a, 6.17f and 6.17k that the single-layer FeTaC (100 nm) film (z = 0, n = 0) displays almost similar transcritical loops over the entire temperature range. However, the values of H_C, H_S and M_R/M_S increase significantly with decreasing temperature, as expected for a typical ferromagnetic material. Interestingly, the shape of *M-H* loops changes in multilayer films with decreasing temperature and hence we discuss the changes in the loop shape separately. For bilayer films (n = 1): (i) the loop shape changes progressively from weak transcritical to rectangular loop with high M_R/M_S of more than 90% (Figure 6.17b) as temperature is decreased from 300 K to 30 K for film with z = 0.5. This is due to the strong ferromagnetic coupling between FeTaC layers caused by the increase in magnetization with decreasing temperature. As a result, the maximum change in H_C between 30 K and 300 K increases largely at lower temperatures, as compared to single-layer film (Figure 6.18a). (ii) With increasing z to 1 nm, a clear change in the loop shape is observed with decreasing temperature, i.e., with decreasing temperature down to 100 K, the film exhibits only single magnetization reversal, but changes into two-step magnetization reversal for temperatures below 100 K. The step size and step nature become dominant at lower temperatures below 50 K. This is mainly due to thermally activated decoupling between FeTaC layers caused by temperature dependent interfacial strain from thick substrate on the bottom FeTaC layer and different thermal expansion coefficients of the films, interlayers and substrate [HUAN2001, OKUM2004, SING2014]. This does not allow bottom FeTaC layer to switch

collectively with the top one and hence produces stepped magnetization curve with multiple states. Therefore, the bottom FeTaC layer needs a considerably larger applied magnetic field to switch, which is again temperature dependent. (iii) Upon increasing z to 4 and 6 nm (Figures 6.17d and 6.17e), the step size becomes very clear at lower temperatures due to reduction in the interlayer coupling between FeTaC layers with increasing z [CHOP2000]. Therefore, the field required to switch the bottom FeTaC layer increases markedly not only with decreasing temperature but also with increasing z. Hence, the overall increase in $H_C(T)$ between 30 K and 300 K decreases for bilayer films with z up to 4 nm and increases slightly for z = 6 nm.

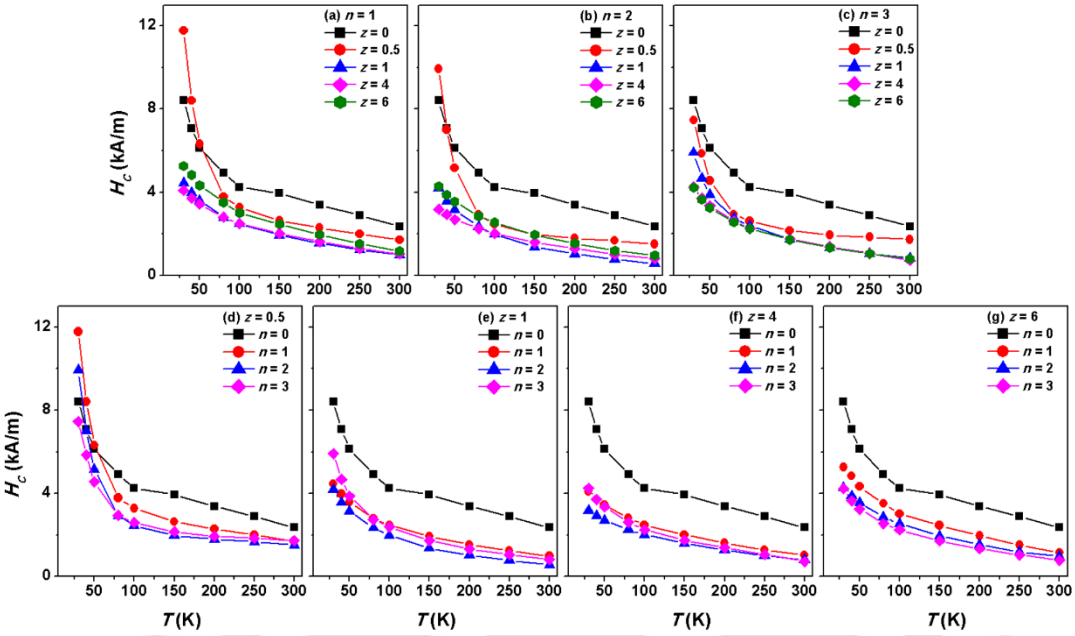

Figure 6.18: The variations of H_C as a function of temperature for multilayer [FeTaC (y nm)/SiO_2 (z nm)]$_n$/FeTaC (y nm) films.

For trilayer films (n = 2): (i) the weak transcritical loop observed at room temperature for film with z = 0.5 nm changes progressively with decreasing temperature, i.e., with decreasing temperature down to 100 K, the loop shape changes to rectangular type with increase in M_R/M_S due to collective switching of all three FeTaC layers. At 50 K, the loop exhibits a long tail nature before saturation due to difficulty in switching the bottom FeTaC layer. On further decreasing temperature below 50 K, a clear three-step magnetization reversal due to individual switching of three FeTaC layers is observed. This increases overall change in $H_C(T)$ between 30 K and 300 K as shown in Figure 6.18b. On the other hand, the increase in z between 1 and 6 nm in trilayer films shows only two-step magnetization reversal due to collective switching of top two FeTaC layers followed by the

bottom FeTaC layer. With decreasing temperature, the step size becomes more dominant due to temperature dependent interfacial strain from thick substrate on bottom FeTaC layer. As compared to bilayer films, the field required to switch the bottom most FeTaC layer in trilayer films decreases significantly due to the change in magnetic domains of the individual FeTaC layer from dense stripe domain to in-plane magnetization with increasing n. The change in $H_C(T)$ displays a behaviour almost similar to the bilayer films. For quaternary layer films (n = 3): (i) the introduction of thin SiO_2 layer (z = 0.5 nm) changes the loop shape from weak transcritical to rectangular at lower temperatures, indicating collective switching of all four FeTaC layers with in-plane magnetic domains due to strong coupling between them. With increasing z = 1 nm, three-step magnetization reversal is observed due to switching of top two FeTaC layers followed by third and fourth FeTaC layers separately. The switching of the bottom most FeTaC layers strongly depends on the measurement temperature for all z values. On further increasing z to 4 and 6 nm, the top three FeTaC layers switch together followed by the bottom most FeTaC layers. Hence, only two-step magnetization reversal is observed. The above results clearly state that the number of steps and nature of switching in the magnetization reversal strongly depend on z and n.

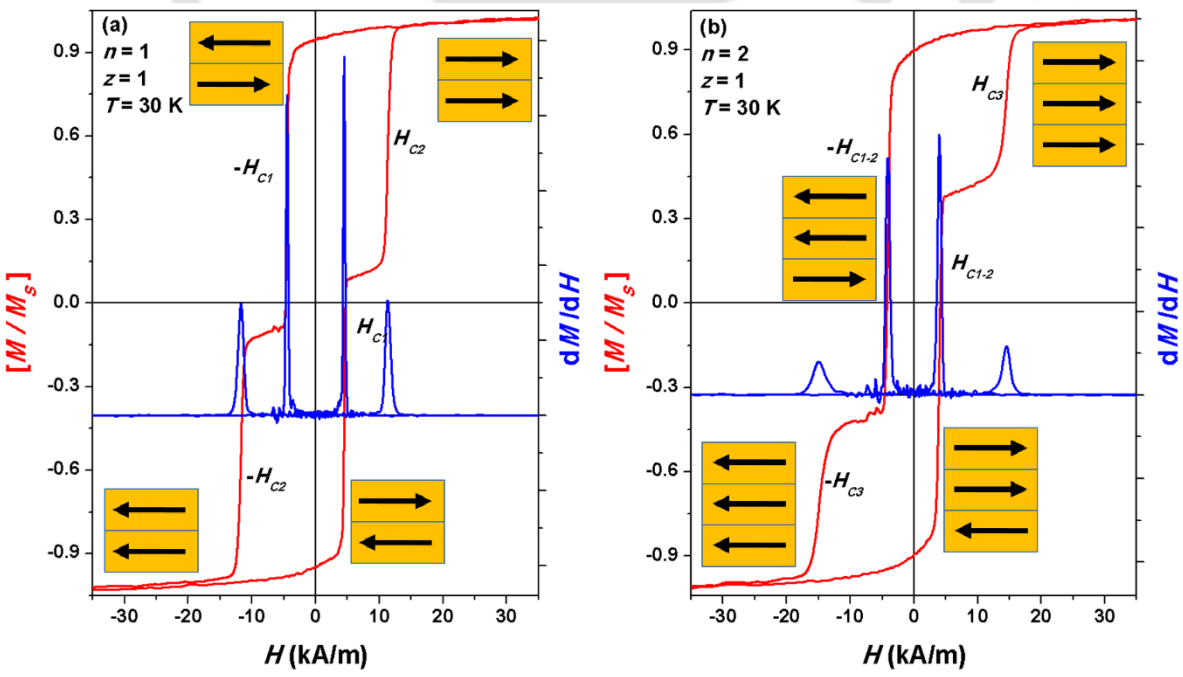

Figure 6.19: *M-H* loops measured at 30 K along with field derivative of magnetization for multilayer [FeTaC (y nm)/SiO_2 (z nm)]$_n$/FeTaC (y nm) films with (a) n = 1, z = 1 and (b) n = 2, z = 1.

To study individual or collective switching behaviours of FeTaC layers as a function of temperature and to understand relative switching between FeTaC layers in multilayer films in more details, *M-H* loops of multilayer films are carefully analysed by taking derivative of the *M-H* loops. The fundamental concept behind such magnetization reversal is that when the interlayer coupling is strong enough as compared to H_C of individual FeTaC layer then they switch all together leading to a simple hysteresis loop [NAOE1998, LIUX20112]. Otherwise, one would expect individual switching of FeTaC layers, which leads to a multi-step hysteresis loop [HUAN2001, OKUM2004]. Figure 6.19 demonstrates *M-H* loops of bilayer films (n = 1) and trilayer films (n = 2) with z = 1 nm measured at 30 K. H_C of individual or collective switching appeared in the *M-H* loop is defined as H_{Ci} or $H_{Ci\text{-}j}$ depending upon whether the switching occurs independently by a single FeTaC layer or collectively between two or more adjacent FeTaC layers.

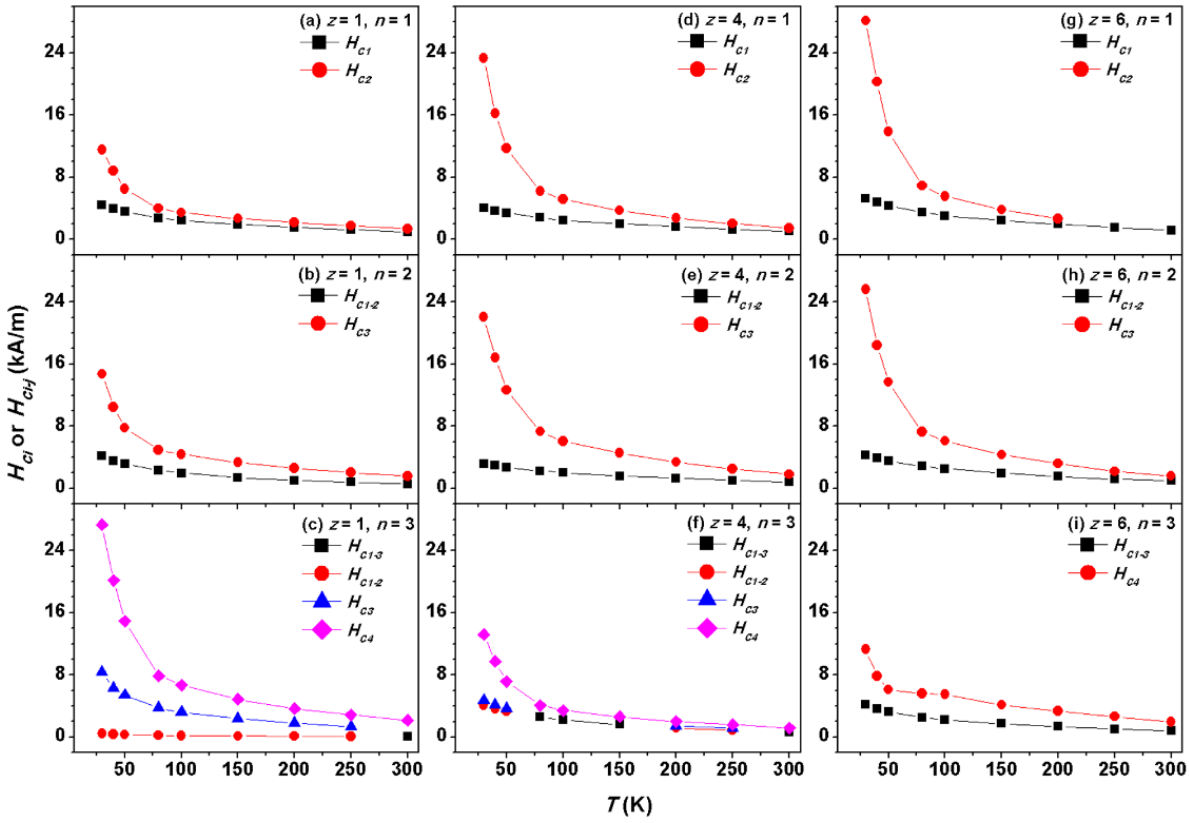

Figure 6.20: The variations of H_{Ci} (or $H_{Ci\text{-}j}$) for multilayer [FeTaC (y nm)/SiO_2 (z nm)]$_n$/FeTaC (y nm) films with different n and z.

The switching behaviour is approximately determined based on the relative variation of magnetization with respect to saturation magnetization using the schematic drawing illustrated in Figure 6.19. For instance, the bilayer film has two FeTaC (50 nm) layers

separated by a thin SiO_2 spacer layer. This film is expected to show either single magnetization reversal curve when both FeTaC layers switch together due to strong interlayer coupling or two-step magnetization reversal curve provided both FeTaC layers switch independently. It is clear from the Figure 6.19a that two-step magnetization reversal is observed due to individual switching of two FeTaC layers at two different fields. Hence, H_C of each FeTaC layer is defined as H_{C1} (= 4.6 kA/m) and H_{C2} (= 11.7 kA/m) representing H_C of top and bottom FeTaC layers in bilayer films, respectively. Similarly, the trilayer film has three FeTaC (33.5 nm) layers separated by two SiO_2 spacer layers. Therefore, this film would show single, two-step or three-step magnetization reversal curves depending on whether all three FeTaC layers switch together, collective switching of top-two FeTaC layers followed by bottom FeTaC layer and/or top FeTaC layer followed by bottom two FeTaC layers or individual switching of three FeTaC layers, respectively.

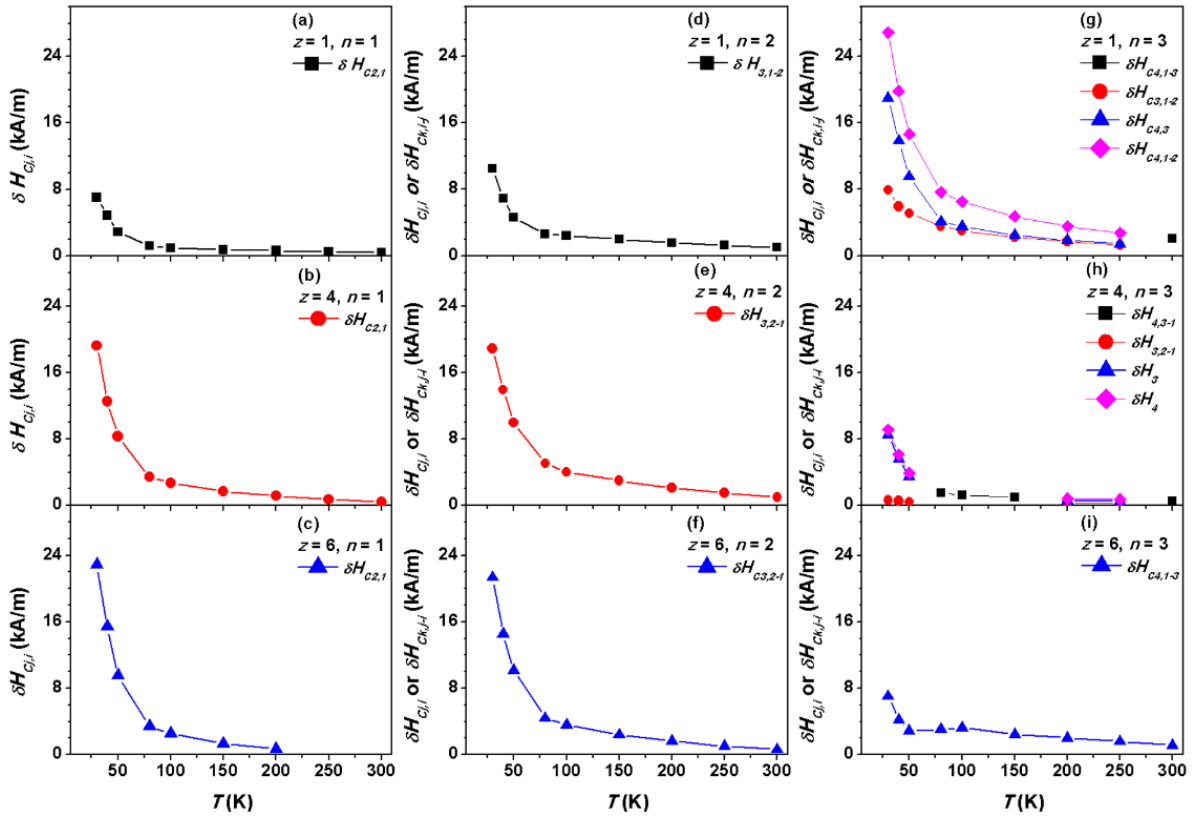

Figure 6.21: Variation of $\delta H_{Cj,i}$ (or $\delta H_{Ck,i-j}$) for multilayer [FeTaC (y nm)/SiO_2 (z nm)]$_n$/FeTaC (y nm) films with different n and z.

Figure 6.19b depicts only two-step magnetization curves mainly due to collective switching of top two FeTaC layers followed by bottom FeTaC layer. Hence, H_C is represented as $H_{C1\text{-}2}$ (= 4.1 kA/m) and H_{C3} (=14.5 kA/m) representing coercivity of top two FeTaC layers and

bottom FeTaC layer, respectively. Likewise, the relative switching between FeTaC layers in multilayer films is analysed by defining another set of parameters as $\delta H_{Cj,i}$ (= $H_{Cj} - H_{Ci}$) or $\delta H_{Ck,i-j}$ (= $H_{Ck} - H_{Ci-j}$) representing the difference in H_C of two individual switching of adjacent FeTaC layers or difference in H_C of one individual layer and collective switching of two or more adjacent FeTaC layers, respectively. For instance, the value of $\delta H_{C2,1}$ (= $H_{C2} - H_{C1}$ = 11.7 – 4.6 = 7.1 kA/m) and $\delta H_{C3,1-2}$ (= $H_{C3} - H_{C1-2}$ = 14.5 – 4.1 = 10.4 kA/m) can be determined from Figure 6.19 for bilayer and trilayer films, respectively. Following the above procedures carefully for all multilayer thin films, H_{Ci} (or H_{Ci-j}) and $\delta H_{Cj,i}$ (or $\delta H_{Ck,i-j}$) are determined and summarized as a function of temperature in Figures 6.20 and 6.21, respectively. The variations of H_{Ci} (or H_{Ci-j}) and $\delta H_{Cj,i}$ (or $\delta H_{Ck,i-j}$) reveal a strong dependence on temperature, particularly at temperatures below 100 K. For instance, H_{Ci} of bottom most FeTaC layer in multilayer films not only increases with increasing n for a given z (Figures 6.20a-c), but also increases largely with increasing z for a particular n [Figures 6.20a, 6.20d and 6.20g]. As a result, the rate of change of $\delta H_{Cj,i}$ (or $\delta H_{Ck,i-j}$) also increases largely in the low temperature region (< 100 K). This is majorly related to thermally activated switching and substrate induced strain on the reversal behaviour of bottom FeTaC layer in multilayer films [HUAN2001, OKUM2004]. However, with increasing n (> 1) and z (> 2 nm), H_{Ci} of the bottom most FeTaC layer decreases mainly due to change in the magnetic domain structure and reduced interlayer coupling between FeTaC layers with increasing z. The observed results reveal that the number and the nature of switching in multilayer films exhibit a strong dependence on temperature, number of SiO_2 spacer layer and spacer layer thickness. It also provides a comprehensive study on the temperature dependent magnetization reversal with respect to multilayers and helps to tune the hard magnetic properties of thick FeTaC films in to soft magnetic one using multilayer structure.

6.4. Summary

Thickness dependent structural and magnetic properties of single-layer amorphous $Fe_{80}Ta_8C_{12}$ (x nm) films and the temperature dependent magnetization reversal and enhancement in the magnetic properties of multilayer [$Fe_{80}Ta_8C_{12}$ (y nm)/SiO_2 (z nm)]$_n$/$Fe_{80}Ta_8C_{12}$ (y nm) films as a function of number of spacer layers, spacer layer thickness and measurement temperature have been systematically carried out in this chapter. The salient features of single-layer $Fe_{80}Ta_8C_{12}$ (x = 5 – 100 nm) films and multilayer [FeTaC (y nm)/ SiO_2 (z nm)]$_n$/ FeTaC (y nm) films from the current investigations are as follows:

- Single-layer $Fe_{80}Ta_8C_{12}$ (x = 5 – 100 nm) films and multilayer [FeTaC (y nm)/ SiO_2 (z nm)]$_n$/ FeTaC (y nm) films could be prepared directly on thermally oxidized Si substrate at ambient temperature using magnetron sputtering techniques.
- Structural studies display that as-deposited FeTaC films exhibit amorphous structure and a very clear uniform surface with grain morphology. The grain density increases with increasing thickness. XRR and AFM results suggest that the average surface roughness increased with increasing film thickness, but without any systematic dependency on thickness.
- Room temperature magnetic properties show that with increasing film thickness, the paramagnetic nature of the films for x < 10 nm changes into ferromagnetic one with simple magnetization reversal for x up to 40 nm and transforms into transcritical one for $x \geq$ 50 nm thickness.
- FeTaC(x < 50) films exhibit soft magnetic nature with rectangular or flat-type loops due to in-plane magnetization with uniaxial anisotropy, as confirmed using MOKE microscopy. With increasing film thickness above critical thickness (~ 50 nm), the soft magnetic properties are degraded due to the transition of in-plane magnetization to dense stripe domain.
- High temperature thermomagnetization data reveal the magnetic phase transition from ferromagnetic to paramagnetic state at relatively higher temperature of about 525 K.
- Interestingly, the transcritical loop observed in thick FeTaC film turns out to be rectangular loop with single or multistep magnetization curves depending on n and z. The interlayer coupling between FeTaC layers in multilayer films not only reduces H_C markedly from 1.99 kA/m to 0.48 kA/m and H_S rapidly from 65.13 kA/m to 2.2 kA/m, but enhances M_R/M_S from 0.3 to more than 0.98.
- Magnetic domain analysis using longitudinal MOKE microscopy reveals angle dependent hysteresis loops and contribution from transverse components in the loops depending on the strength of the interlayer coupling between FeTaC layers in multilayer films.
- Temperature dependent magnetic properties show that the number and the nature of switching in multilayer films exhibit a strong dependence on temperature. The overall increase in temperature dependent coercivity decreases with increasing number of SiO_2 layers and its thickness mainly due to the change in the magnetic

domain structure of the individual FeTaC layers and reduced interlayer coupling between FeTaC layers.

- The present study not only provides an understanding of temperature dependent magnetization reversal in multilayer films, but also confirms tuning of hard magnetic properties of thick FeTaC films into soft magnetic nature in multilayer thin films.

Indian Institute of Technology Guwahati

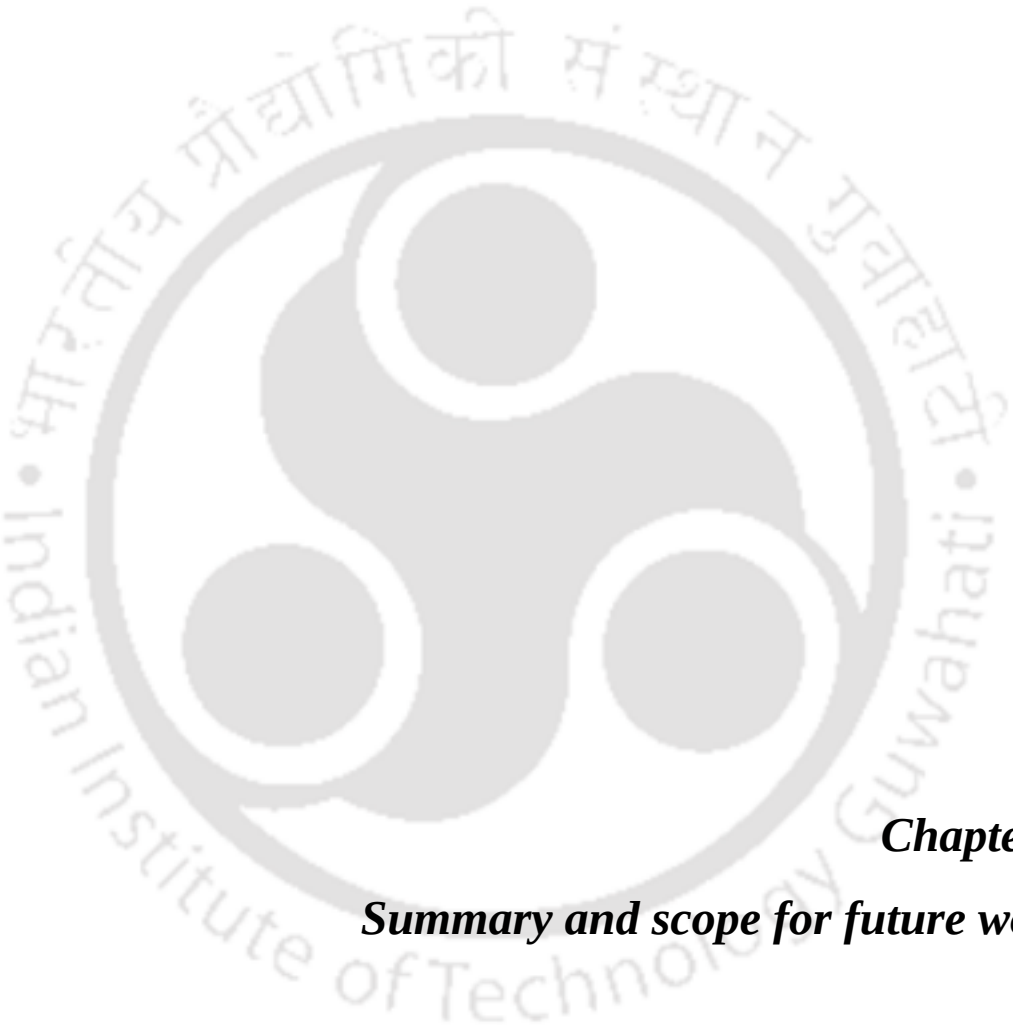

Chapter 7

Summary and scope for future work

भारतीय प्रौद्योगिकी संस्थान गुवाहाटी
Indian Institute of Technology Guwahati

The overall summary of the significant results obtained on the structural and magnetic properties of single-layer amorphous $Co_{40}Fe_{40}B_{20}$ (CoFeB) (x = 10 – 200 nm) and $Fe_{80}Ta_8C_{12}$ (FeTaC) (x = 5 – 100 nm) films, multilayer [CoFeB (y nm)/Ta (z nm)]$_{n=1\text{-}3}$/ CoFeB (y nm) and [FeTaC (y nm)/ SiO_2 (z nm)]$_n$/ FeTaC (y nm) films and stack structured [CoFeB (100 nm)/Ta (z=0-1.5 nm)]$_{n=0\text{-}4}$/CoFeB (100 nm) films is described in this chapter. Highlights of the current investigations and the possibilities for future work are also summarized below.

7.1. Summary of the results

Single-layer amorphous CoFeB (x = 10 – 200 nm) and FeTaC (x = 5 – 100 nm) films, multilayer [CoFeB (y nm)/Ta (z nm)]$_{n=1\text{-}3}$/ CoFeB (y nm) and [FeTaC (y nm)/ SiO_2 (z nm)]$_n$/ FeTaC (y nm) films and stack structured [CoFeB (100 nm)/Ta (z=0-1.5 nm)]$_{n=0\text{-}4}$/CoFeB (100 nm) films were prepared directly on the thermally oxidized Si substrates using DC/RF magnetron sputtering technique at ambient temperature.

Structural investigations using X-ray diffraction and transmission electron microscopy techniques confirmed the existence of amorphous structure in all the as-deposited CoFeB and FeTaC films. AFM topography images of CoFeB films showed that the existence of very fine and sparsely dispersed nanosized grains and the average surface roughness was found to be in the range of 0.4-0.7 nm for CoFeB (200 nm) films. The results of thickness determination from XRR analysis and surface profilometer were in close agreement with each other.

The magnetic properties of CoFeB (x nm) single-layer films revealed a strong thickness dependence in the thickness range between 10 nm and 200 nm. CoFeB (x < 67 nm) films exhibited soft magnetic nature with rectangular or flat-type loops due to in-plane magnetization with uniaxial anisotropy. With increasing x > 67 nm, the soft magnetic properties were degraded due to the transition of in-plane magnetization to dense stripe domain. This was attributed to the enhancement of effective magnetic anisotropy (K_{eff}) caused by the stress quenched in during deposition of the films at a faster deposition rate to form amorphous structure. Coercivity and saturation field increased from 1.99 kA/m to 4.14 kA/m and 7.16 kA/m to 38.2 kA/m, respectively with increasing CoFeB film thickness from 10 nm to 200 nm. High temperature thermomagnetization data revealed Curie temperature of CoFeB (20 nm) film to be around 512 K. In order to control the effective magnetic anisotropy and tune soft magnetic properties of CoFeB films at higher thicknesses, multilayer [CoFeB (y nm)/Ta (z nm)]$_{n=1\text{-}3}$/ CoFeB (y nm) films where each CoFeB layer

thickness is controlled by the relation: $y = 200/(n+1)$ were prepared with different number n (= 0 – 3) and different thickness z (= 0 - 2 nm) of Ta layer. The room temperature magnetic properties at higher film thickness could be improved by introducing optimum Ta spacer layer in multilayer films. However, the decrease of room temperature coercivity and saturation field with increasing the number of multilayers depends on the Ta spacer layer thickness. For as-deposited multilayer films with n = 3 and z = 1, room temperature coercivity decreased to the lowest value of 0.8 kA/m. The improvement in magnetic properties of multilayer films strongly dependent on the number of multilayers and optimum spacer layer thickness. Temperature dependent *M-H* loops of single-layer CoFeB (200 nm) films did not show any change in the transcritical loop shape with decreasing temperature down to 30 K. Interestingly, the magnitude of increase in coercivity strongly depend on the values of n and z in multilayer films. The observed results were discussed on the basis of change in the magnetic domain structure and spacer layer thickness dependent interlayer coupling between CoFeB layers in multilayer films.

To obtain enhanced magnetic properties in thick CoFeB films exhibiting stripe domain structure and their influence on the interlayer coupling as a function of number of stacks in stack structure, spacer layer thickness and measurement temperature, stack structured [CoFeB (100 nm)/Ta (z nm)]$_n$/CoFeB (100 nm) films with z = 0 - 1.5 and n = 0 – 4 were prepared. Structural studies confirmed the presence of amorphous structure in all the as-deposited CoFeB films. AFM analysis of the films revealed clear surfaces and the existence of fine and nano-sized grain in the as-deposited films. The average roughness increased significantly from 0.4-0.65 nm for single-layer CoFeB films to 1.5-2 nm with increasing n =4 and z = 1.5 nm in stack structured film. Single-layer CoFeB (x = 100 – 300 nm) films revealed transcritical loops due to the formation of stripe domains in the as-deposited films caused by the development of stress induced effective magnetic anisotropy. Hence, they showed high coercivity (> 4 kA/m) and required large applied magnetic field (> 40 kA/m) for magnetization saturation. Upon increasing number of stacks in stack structure, the interlayer coupling between CoFeB layers enhanced and provided a better flux closure, which led to a substantial drop in H_C and changed the hysteresis loop shape away from transcritical to soft magnetic type with high remanence ratio (> 75 %) and saturated considerably at lower applied magnetic field (~ 10 kA/m). The improvements in the magnetic properties of stack structured films as compared to thick single-layer films were found to be strongly dependent on thickness of spacer layer and number of spacer layers. The interlayer coupling between CoFeB layers in stack structure changed significantly with

temperature caused mainly by the increase in M_S. In addition, temperature dependent *M-H* loops revealed that the competition between interlayer coupling and interfacial strain determines the nature of *M-H* loop and provides unusual variation of $H_C(T)$, i.e., minimum in $H_C(T)$ vs T curve, which shifted to lower temperature depending on spacer layer thickness and number of stacks. The variations in the magnetic properties of single-layer and stack structured films were explained on the basis of stress dependent stripe domain in single-layer films and number of CoFeB layers and spacer layer thickness dependent interlayer coupling in stack structured thin films.

To study thickness dependent structural and magnetic properties of single-layer FeTaC (x nm) films and the temperature dependent magnetization reversal and enhancement in the magnetic properties of multilayer films as a function of number of spacer layers, spacer layer thickness and measurement temperature, single-layer FeTaC (x = 5 – 100 nm) films and multilayer [FeTaC (y nm)/ SiO_2 (z nm)]$_n$/ FeTaC (y nm) films were prepared directly on thermally oxidized Si substrate at ambient temperature using magnetron sputtering techniques. Each FeTaC layer thickness, in multilayer film was controlled by the relation: $y = 100/(n+1)$. Structural studies revealed that as-deposited FeTaC films exhibited amorphous structure and a very clear uniform surfaces with grain morphology. The grain density increased with increasing thickness. XRR and AFM results suggested that the average surface roughness increased with increasing film thickness, but without any systematic dependency on thickness. Room temperature magnetic properties showed that with increasing film thickness, the paramagnetic nature of the films for $x < 10$ nm changed into ferromagnetic one with simple magnetization reversal for x up to 40 nm and transformed into transcritical one for $x \geq 50$ nm thickness. FeTaC($x < 50$) films exhibited soft magnetic nature with rectangular or flat-type loops due to in-plane magnetization with uniaxial anisotropy and confirmed using MOKE microscopy. With increasing film thickness above critical thickness (~ 50 nm), the soft magnetic properties were degraded due to the transition of in-plane magnetization to dense stripe domain. High temperature thermomagnetization data revealed the magnetic phase transition from ferromagnetic to paramagnetic state at relatively higher temperature of about 525 K. Transcritical loop observed in thick FeTaC film turned out to be rectangular loop with single or multistep magnetization curves depending on n and z. The interlayer coupling between FeTaC layers in multilayer films not only reduced H_C markedly from 1.99 kA/m to 0.48 kA/m and H_S rapidly from 65.13 kA/m to 2.2 kA/m, but also enhanced M_R/M_S from 0.3 to more than 0.98. However, magnetic domain analysis using longitudinal MOKE microscopy revealed angle

dependent hysteresis loops and contribution from transverse components in the loops depending on the strength of the interlayer coupling between FeTaC layers in multilayer films. Temperature dependent magnetic properties showed that the number and the nature of switching in multilayer films exhibited a strong dependence on temperature. The overall increase in temperature dependent coercivity decreased with increasing number of SiO_2 layers and its thickness mainly due to the change in the magnetic domain structure of the individual FeTaC layers and reduced interlayer coupling between FeTaC layers. The observed results not only provided an understanding of temperature dependent magnetization reversal in multilayer films, but also confirmed tuning of hard magnetic properties of thick FeTaC films into soft magnetic nature in multilayer thin films.

7.2. Scope for future work

The current investigations have emphasized some new and interesting features and characteristics of single-layer and multilayer CoFeB and FeTaC based thin films. These observations have not only revealed the potential of this material and multilayer films for the selective applications in modern magneto-electronic devices, but also shown paths for future scope of work in single-layer and multilayer CoFeB and FeTaC films. Some of the prospects are briefly discussed below to serve as appropriate conclusion to the current thesis work.

Since the multilayer (CoFeB/FeTaC) thin films exhibit single and multistep magnetization reversal behavior depending on the spacer layer materials, its thickness, measurement temperature, and the change in the magnetic domains from dense stripe domain to in-plane magnetization in multilayer films, it would be interesting to measure the electrical transport properties in these films as a function of applied magnetic field (magnetoresistance), spacer layer thickness and at different temperatures. This would hopefully reveal a correlation between the magnetic and transport properties, provided the transport properties are affected by the change in the domain structure, spacer layer materials and its thickness. Furthermore, the nature of the interlayer coupling between the ferromagnetic layers in the multilayer films depends on the thickness of spacer and ferromagnetic layers. In the current investigation, we have analyzed the switching of magnetic domains at two different angles along the film plane in multilayer films only at room temperature. However, the nature of the magnetic hysteresis loops changes with temperature and hence a careful analysis of switching or rotation of magnetic domains as a function of different applied field angles along the film plane at different temperatures

would reveal the nature of magnetic interaction between CoFeB layers and FeTaC layers as a function of thickness of spacer and ferromagnetic layers.

Recently, nanocrystalline metallic materials, achieved by controlled annealing of amorphous precursors at different temperatures under different environment, attract much attention from a view point of industrial applications. The excellent soft magnetic properties in the nanocrystalline materials is due to their characteristic two phase microstructure in which nanosized (< 20 nm) crystals of soft ferromagnetic phase are embedded in sferromagnetic amorphous matrix. These nanocrystalline soft magnetic thin films shows M_S, low H_C, low anisotropy, high thermal stability and low noise characteristics. In addition, magnetic softness in nanocrystalline materials is related to the ratio of the exchange correlation length (or domain wall thickness) to the orientation of fluctuations of randomly distributed local easy axis. According to random anisotropy model, the coercivity of the nanocrystalline materials varies as the sixth power of the average grain size when the average size of the nanocrystal is less than the exchange correlation length. Hence, the formation of fine nanosized grains plays an important role in the improvement of the soft magnetic properties of the nanocrystalline materials. Therefore, it will be interesting to anneal the as-deposited amorphous single-layer films at different constant temperatures to investigate how the static and dynamic magnetic properties are altered with resulting crystallinity. In case of multilayer films, the crystallinity will modify the interlayer coupling and provide interesting magnetic properties and domain structure.

भारतीय प्रौद्योगिकी संस्थान गुवाहाटी
Indian Institute of Technology Guwahati

References

भारतीय प्रौद्योगिकी संस्थान गुवाहाटी
Indian Institute of Technology Guwahati

[ACHA2004] Acharya B.R, Zhou J.N, Zheng M, Choe G, Abarra E.N, Johnson K.E, IEEE Trans. Magn. 40 (2004) 2383.

[ALLE1990] Allenspach R, Stampanoni M, Bischof A, Phys. Rev. Lett. 65 (1990) 3344.

[ALLE1994] Allenspach R, J. Magn. Magn. Mater. 129 (1994) 160.

[AMOS2008] Amos N, Fernandez R, Ikkawi R, Lee B, Lavrenov A, Krichevsky A, Litvinov D, Khizroev S, J. Appl. Phys. 103 (2008) 07E732.

[ANGU2000] Anguelouch A, Schrag B.D, Xiao G, Trouilloud Y.L.P.L, Wanner R.A, Gallagher W.J, Parkin S.S.P, Appl. Phys. Lett. 76 (2000) 622.

[BAIB1988] Baibich M.N, Broto J.M, Fert A, Dau F.N.V, Petroff F, Eitenne P, Creuzet G, Friederich A, Chazelas J, Phys. Rev. Lett. 61 (1988) 2472.

[BALT2007] Baltz V, Marty A, Rodmacq B, Dieny B, Phys. Rev. B 75 (2007) 014406.

[BENN1994] Bennett L.H, Watson R.E, Magnetic Multilayers, World Scientific, Singapore (1994).

[BINA1989] Binasch G, Grunberg P, Saurenbach F, Zinn W, Phys. Rev. B 39 (1989) 4828.

[BLUN2001] Blundell S, Magnetism in Condensed Matter, Oxford University Press Inc., New York (2001).

[BLUN2003] Blundell S, Magnetism in Condensed Matter, Oxford University Press, Chapter 3 (2003).

[BOBO1999] Bobo J.F, Kikuchi H, Redon O, Snoeck E, Piecuch M, White R.L, Phys. Rev. B 60 (1999) 4131.

[BRAJ2010] Brajpuriya R, J. Appl. Phys. 107 (2010) 083914.

[BRUN1989] Bruno P, Renard J.P, Appl. Phys. A 49 (1989) 499.

[BRUN1991] Bruno P, Chappert C, Phys. Rev. Lett. 67 (1991) 1602.

[BRUN1992] Bruno P, Chappert C, Phys. Rev. B 46 (1992) 261.

[BUCH2009] Buchmeier M, Schreiber R, Bürgler D. E, Schneider C.M, Phys. Rev. B 79 (2009) 064402.

[CAST1997] Castano F.J, Stobiecki T, Gibbs M.R.J, Czapkiewicz M, Kopcewicz M, Gacem V, Speakman J, Cowlam N, Blythe H.J, J. Phys.: Condens. Matter 9 (1997) 10603.

[CHAP1988] Chappert C, Bruno P, J. Appl. Phys. 64 (1988) 5736.

[CHEL2003] Chelaru L.I, Microscopic studies of interlayer magnetic coupling across nonmagnetic and antiferromagnetic spacer layers, PhD Thesis, Chap 01, Universitat Halle-Wittenberg (2003).

[CHEN2013] Chen Y-T, Hsieh W.H, J. Alloys Compd. 552 (2013) 283.

[CHIL2014] Childress J.R, Read J.C, Smith N, CPP-GMR Sensor with Corrosion Resistant Spacer Layer and Higher Signal/Noise Ratio, US Patent 8,743,511 B2, June 3, (2014).

[CHOM2001] Cho M.-H, Ko D.-H, Choi Y.G, Jeong K, Lyo I.W, Noh D.Y, Kim H.J, Whang C.N, J. Vac. Sci. Technol. A 19 (2001) 192.

[CHOP2000] Chopra H.D, Yang D.X, Chen P.J, Parks D.C, Egelhoff W.F, Phys. Rev. B 61 (2000) 9642.

[CHOP2005] Chopra H.D, Sullivan M.R, Ludwig A, Quandt E, Phys. Rev. B 72 (2005) 054415.

[COEY2010] Coey J.M.D, Magnetism and Magnetic Materials, Cambridge university press, Cambridge (2010).

[COIS2008] Coisson M, Celegato F, Olivetti E, Tiberto P, Vinai F, Baricoo M, J. Appl. Phys. 104 (2008) 033902.

[COIS2009] Coisson M, Vinai F, Tiberto P, Celegato F, J. Magn. Magn. Mater. 321 (2009) 806.

[CONC2013] Conca A, Greser J, Sebastian T, Klingler S, Obry B, Leven B, Hillebrands B, J. Appl. Phys. 113 (2013) 213909.

[CRAI1965] Craik D.J, Tebble R.S, Ferromagnetism and Ferromagnetic Domains, North-Holland Publishing Company, New York (1965).

[CRAU2002] Craus C.B, Chezan A.R, Siekman M.H, Lodder J.C, Boerma D.O, Niesen L, J. Magn. Magn. Mater. 240 (2002) 423.

[CRAU2003] Craus C.B, Magnetic Properties of Nanocrystalline Materials for High Frequency Applications, Thesis (PhD), University of Groningen (2003).

[CUCH2016] Cuchet L, Rodmacq B, Auffret S, Sousa R C, Prejbeanu I.L, Dieny B, Sci. Rep. 6 (2016) 21246.

[CUIB2013] Cui B, Song C, Wang Y Y, Yan W S, Zeng F, Pan F, J. Phys. Condens. Matter 25 (2013) 106003.

[CULL2001] Cullity B.D, Stock S.R, Elements of X-ray diffraction, 3rd edn, Pearson Eduaction, Boston (2001).

[CZIC2006] Czichos H, Saito T, Smith L, Handbook of Materials Measurements methods, Springer, Berlin (2006).

[DASC2016] Das C, Mohapatra S, Vitthal G.A, Perumal. A, Thin Solid Films 616 (2016) 126.

[DASC2018] Das C, Das J, Vijayabhaskaran T, Bedanta S, Talapatra A, Mohanty J.R, Perumal Alagarsamy, J. NanoMater. (2018) (under submission).

[DAVI1966] Davidse P.D, Maissel L.I, J. Appl. Phys. 37 (1966) 574.

[DAVI1967] Davidse P.D, Vacuum 17 (1967) 139.

[DECH2012] Decher G, Schlenoff J.B, Multilayer Thin Films: Sequential Assembly of Nanocomposite Materials, Vol. 1, John Wiley & Sons, Germany (2012).

[DEMA2016] Demasius K.-U, Phung T, Zhang W, Hughes B.P, Yang S.-H, Kellock A, Han W, Pushp A, Parkin S.S.P, Nature Comm. 7 (2016) 10644.

[DIEN2016] Dieny B, Goldfarb R.B, Lee K-J, Introduction to Magnetic Random-Access Memory, John Wiley & Sons, New Jersy (2016).

[DIMO2004] Dimopoulos T, Gieres G, Wecker J, Wiese N, Sacher M.D, J. Appl. Phys. 96 (2004) 6382.

[DRAA1987] Draaisma H.J.G, Jonge W.J.M. de, J. Appl. Phys. 62 (1987) 3318.

[FELD1971] Feldtkeller E, J. De Physique 32 (1971) 452.

[FREI2016] Freitas P.P, Ferreira R, Cardoso S, Proc. of IEEE 104 (2016) 1894.

[FUJI2006] Fujii I, Shima T, Takanashi K, Mater. Trans. 47 (2006) 47.

[GARR2005] Garreau G, Hajjar S, Bubendorff J.L, Pirri C, Berling D, Mehdaoui A, Stephan R, Wetzel P, Zabrocki S, Gewinner G, Boukari S, Beaurepaire E, Phys. Rev. B 71 (2005) 094430.

[GAYE2017] Gayen A, Prasad G.K, Mallik S, Bedanta S, Perumal A, J. Alloys and Compounds 694 (2017) 823.

[GENG2013] Geng H, Wei J. Q, Nie S. J, Wang Y, Wang Z. W, Wang L. S, Chen Y, Peng D. L, Li F. S, Xue D. S, Mater. Lett. 92 (2013) 346.

[GUER2007] Guerrero M.G, Prieto J.L, Ciudad D, Sanchez P, Aroca C, Appl. Phys. Lett. 90 (2007) 162501.

[GUPT2013] Gupta R, Gupta A, Gupta M, Rajput P, Wildes A, J. Appl. Phys. 114 (2013) 63903.

[HADJ2013] Hadjipanayis G.C, Prinz G.A, Science and Technology of Nanostructured Magnetic Materials, Springer Science & Business Media, New York (2013).

[HART1999] Hartmann U, Annu Rev Mater Res 29 (1999) 53.

[HART2000] Hartman U, Magnetic Multilayers and Giant Magnetoresistance Fundamentals and Industrial Applications, Springer-Verlag Berlin Heidelberg (2000).

[HASE1995] Hasegawa N, Makino A, Kataoka N, Fujimori H, Tsai A.P, Inoue A, Masumoto T, Mater. Tran. JIM 6 (1995) 952.

[HASH2007] Hashimoto A, Nakagawa S, Yamaguchi M, IEEE Trans. Magn. 43 (2007) 2627.

[HEDI2013] Hedin E.R, Joe Y.S, Spintronics in Nanoscale Devices, CRC Press, USA (2013).

[HEIN1987] Heinrich B, Urquhart K.B, Arott A.S, Cochran J.F, Myrtle K, Purcell S.T, Phys. Rev. Lett. 59 (1987) 1756.

[HEIS1928] Heisenberg V.W, für. Z, Phys. 49 (1928) 619.

[HERN2008] Herndon N.B, Oh S.H, Abiade J.T, Pai D, Sankar J, Pennycook S.J, Kumar D, J. Appl. Phys. 103 (2008) 07D515.

[HERZ1996] Herzer G, Amorphous and Nanocrystalline Soft Magnets, in Proceedings of the NATO Advanced Study Institute on Magnetic Hysteresis in Novel Materials, Ed. George C. Hadjipanayis, Greece, (1996).

[HILL1993] Hill E.W, Tomlinson S.L, Li J.P, J. Appl. Phys.73 (1993) 5978.

[HIND2011] Hindmarch A T, Rushforth A W, Campion R P, Marrows C H, Gallagher B L, Phys. Rev. B 83 (2011) 212404.

[HIRA2000] Hirayama Y, Kikukawa A, Honda Y, Shimizu N, Futamoto M, IEEE Trans. Magn. 36 (2000) 2396.

[HIRO2013] Hirota E, Sakakima H, Inomata K, Giant Magneto-Resistance Devices, Springer Science & Business Media, UK (2013).

[HIRO2015] Hirohata A, Sukegawa H, Yanagihara H, Žutic I, Seki T, Mizukami S, Swaminathan R, IEEE Trans. Magn. 51 (2015) 0800511.

[HUAN2001] Huang M-Q, Hsu Y.N, McHenry E, Laughlin D.E, IEEE Trans. Magn. 37 (2001) 2239.

[HUBE2014] Hubert A, Schäfer R, Magnetic Domains: the Analysis of Magnetic Microstructures, Springer, New York (2014).

[IANN2014] Iannone E, Labs on Chip: Principles, Design and Technology, CRC Press, Florida (2014).

[IKED2008] Ikeda S, Hayakawa J, Ashizawa Y, Lee Y.M, Miura K, Hasegawa H, Tsunoda M, Matsukura F, Ohno H, Appl. Phys. Lett. 93 (2008) 082508.

[IKED2010] Ikeda S, Miura K, Yamamoto H, Mizunuma K, Gan H.D, Endo M, Kanai S, Hayakawa J, Matsukura F, Ohno H, Nat. Mater. 9 (2010) 721.

[IKHT2018] Ikhtiar, Sukegawa H, Xu X, Belmoubarik M, Lee H, Kasai S, Hono K, Appl. Phys. Lett. 112 (2018) 022408.

[INGV2002] Ingvarsson S, Xiao G, Parkin S.S.P, Gallagher W.J, J. Magn. Magn. Mater. 251 (2002) 202.

[INOU1997] Inoue A, Zhang T, Takeuchi A, Appl. Phys. Lett. 71 (1997) 464.

[INOU2014] Inoue J-I, Nanomagnetism and Spintronics: 2. GMR, TMR, BMR, and Related Phenomena, Elsevier Inc. USA (2014).

[ISHI2014] Ishikawa S, Sato H, Yamanouchi M, Ikeda S, Fukami S, Matsukura F, Ohno H, J. Appl. Phys. 115 (2014) 17C719.

[ITOS1980] Ito S, Aso K, Makino Y, Uedaira S, Appl. Phys. Lett. 37 (1980) 665.

[ITOS2005] Ito S, Okamoto T, Kong S.-H, Nakagawa S, J. Magn. Magn. Mater. 287 (2005) 281.

[JANI2007] Janicka K, Burton J.D, Tsymbal E.Y, J. Appl. Phys 101 (2007) 113921.

[JIAN2005] Jiang R.F, Lai C.H, J. Appl. Phys. 97 (2005) 10N302.

[JIAN2009] Jiang L, Naganuma H, Oogane M, Ando Y, Appl. Phys. Express. 2 (2009) 83002.

[JICW2005] C. W. Ji, S. H. Kim, I. Kim, K. H. Kim, and M. Yamaguchi, IEEE Trans. Magn. 41 (2005) 3277.

[JILE1997] Jiles. D, Introduction to Magnetism and Magnetic Materials, Chapman and Hall, Boca Raton (1997).

[JUNG2006] Jung H.S, Velu E.M.T, Malhotra S.S, Jiang W, Bertero G, J. Appl. Phys. 99 (2006) 08E702.

[KASU1956] Kasuya T, Progress of Theoretical Physics 16 (1956) 45.

[KATI2000] Katine J. A, Albert, F. J, Buhrman R. A, Myers E. B, Ralph D. C, Phys. Rev. Lett. 84 (2000) 3149.

[KAZI2013] Kazimierczuk M.K, High-frequency magnetic components, Second ed., Wiley-VCH, UK (2013).

[KHIZ2004] Khizroev S, and Litvinov D, J. Appl. Phys. 95 (2004) 4521.

[KIMJ2013] Kim J, Sinha J, Hayashi M, Yamanouchi M, Fukami S, Suzuki T, Mitani S, Ohno H, Nature Mater. 12 (2013) 240.

[KIPG2012] Kipgen L, Fulara H, Raju M, Chaudhary S, J. Magn. Magn. Mater. 324 (2012) 3118.

[KITT2004] Kittel C, Introduction to Solid state Physics, 7th edn Wiley, Singapore (2004).

[KOBL1978] Kobliska R.J, Aboaf J.A, Gangulee A, Cuomo J.J, Klokholm E Appl. Phys. Lett. 33 (1978) 473.

[KODZ2012] Kodzuka M, Ohkubo T, Hono K, Ikeda S, Gan H.D, Ohno H, J. Appl. Phys. 111 (2012) 043913.

[KOOL1999] Kools J.C.S, Kula W, Mauri D, Lin T, J. Appl. Phys. 85 (1999) 4466.

[KOON1987] Koon N.C, Jonker B.T, Volkening F.A, Krebs J.J, Prinz G.A, Phys. Rev. Lett. 59 (1987) 2463.

[KORE2012] Korelis P. T, Jonsson P. E, Liebig A, Wannberg H.-E, Nordblad P, Hjorvarsson B, Phys. Rev. B 85 (2012) 214430.

[KRAV2012] Kravets A.F, Timoshevskii A.N, Yanchitsky B.D, Bergmann M.A, Buhler J, Andersson S, Korenivski V, Phys. Rev. B 86 (2012) 214413.

[KRON2003] Kronmuller H, Fahnle M, Micromagnetism and the Microstructure of Ferromagnetic Solids, Cambridge University Press, New York (2003).

[KUDR1997] Kudrmovsky J, Drchal V, Bruno P, Turek I, Weinberger P, Phys. Rev. B 56 (1997) 8919.

[KURI2017] Kurinec S.K, Iniewski K, Nanoscale Semiconductor Memories: Technology and Applications, CRC Press, Florida (2017).

[LEED2006] Lee D.W, Wang S.X, J. Appl. Phys. 99 (2006) 08F109.

[LEES2017] Lee S-E, Baek J-U, Park J-G, Sci. Rep. 7 (2017) 11907.

[LEON2014] León J.C.-, Svendsen W.E, Lab-on-a-Chip Devices and Micro-Total Analysis Systems: A Practical Guide, Springer, UK (2014).

[LIUD2001] Liu H.-D, Zhao Y.-P, Ramanath G, Murarka S.P, Wang G.-C, Thin Solid Films 384 (2001) 151.

[LIUT2012] Liu T, Cai J.W, Sun L, AIP Adv 2 (2012) 032151.

[LIUX20111] Liu X, Zhang W, Carter M.J, Xiao G, J. Appl. Phys. 110 (2011) 033910.

[LIUX20112] Liu X. H, Liu W, Guo S, Lv X. K, Gong W. J, Zhang Z. D, J. Alloys Compd. 509 (2011) 1448.

[LIUX2012] Liu X.M, Ho P, Chen J.S, Adeyeye A.O, J. Appl. Phys. 112 (2012) 073902.

[LIUY2008] Liu Y, Sellmyer D.J, Shindo D, Handbook of Advanced Magnetic Materials: Vol 1. Nanostructural Effects. Vol 2. Characterization and Simulation. Vol 3. Fabrication and Processing. Vol 4. Properties and Applications, Tsinghua University Press, Springer (2008).

[LIUY2016] Liu Y, Hao L, Cao J, AIP Adv. 6, (2016) 45008.

[LIUZ2006] Liu Z.W, Liu Y, Yan L, Tan C.Y, Ong C.K, J. Appl. Phys. 99 (2006) 043903.

[LIXW2007] Li X.W, Song C, Yang J, Zeng F, Geng K.W, Pan F, J. Magn. Magn. Mater. 315 (2007) 120.

[MAEK2017] Maekawa S, Valenzuela S.O, Saitoh E, Kimura T, Spin Current, OUP Oxford (2017).

[MAJC2007] Majchrak P, Derer J, Lobotka P, Vavra I, Frait Z, Horvath D, J. Appl. Phys. 101 (2007) 113911.

[MAKI1995] Makino A, Inoue A, Masumoto T, Mat. Trans. JIM 36 (1995) 924.

[MALL2012] Mallinson J.C, The Foundations of Magnetic Recording, Elsevier, Academic Press, UK (2012).

[MALL2018] Mallik S, Mattauch S, Dalai M. K, Brückel T, Bedanta S, Scientific Reports 8 (2018) 551.

[MANT2013] Mantovan R, Lamperti A, Tallarida G, Baldi L, Mariani M, Ocker B, Ahn S.-M, Barisic I, Ravelosona D, Thin Solid Films 533 (2013) 75.

[MAPP1991] Mapps D.J, Akhter M.A, Pan G, J. Appl. Phys. 69 (1991) 5178.

[MART1987] Martin Y, Wickramasinghe H.K, Appl. Phys. Lett. 50 (1987) 1455.

[MASO2017] Masood A, McCloskey P, Mathuna C.O, Kulkarni S, AIP Adv. 7 (2017) 055208.

[MCHE1999] McHenry M.E, Willard M.A, Laughlin D.E, Prog. Mater. Sci. 44 (1999) 291.

[MELE2015] Mele P, Endo T, Arisawa S, Li C, Tsuchiya T, Oxide Thin Films, Multilayers, and Nanocomposites, Springer, Switzerland (2015).

[MIDD1963] Middelhoek S, J. Appl. Phys. 34 (1963) 1054.

[MISH2011] Mishra D, Singh A.K, Shyni P.C, Sharma D, Perumal A, J. Appl. Phys. 109 (2011) 07A304.

[MOON1999] Moon K.-S, Fontana Jr. R.E, Parkin S.S.P, Appl. Phys. Lett. 74 (1999) 3690.

[MORA2013] Morán-López J.L., Sánchez J.M, New Trends in Magnetism, Magnetic Materials, and Their Applications, Springer Science & Business Media, New York (2013).

[MORI2004] Moritz J, Garcia F, Toussaint J.C, Dieny B, Nozieres J.P, Europhys. Lett. 65 (2004) 123.

[MUNA2005] Munakata M, Shin-Ichi Aoqui, Yagi M, IEEE Trans. Magn. 41 (2005) 3262.

[MURA1966] Murayama Y, J. Phys. Soc. Jpn. 21 (1966) 2253.

[MURA1997] Murarka S.P, Mater. Sci. Eng. R 19 (1997) 87.

[NAIK2012] Naik V.B, Meng H, Sbiaa R, AIP Adv. 2 (2012) 042182.

[NAKA1997] Nakagawa S, Suemitsu K, Naoe M, J. Appl. Phys. 81 (1997) 3782.

[NAKA2001] Nakamura F, Hikosaka T, Tanaka Y, J. Magn. Magn. Mater. 235 (2001) 64.

[NALW2002] Nalwa H.S, Handbook of Thin Film Materials: Characterization and spectroscopy of thin films. Vol. 2, Academic Press, Florida (2002).

[NAOE1996] Naoe M, Nakagawa S, J. Appl. Phys. 79 (1996) 5015.

[NAOE1998] Naoe M, Matsumiya H, Ichihara T, Nakagawa S, J. Appl. Phys. 83 (1998) 6673.

[NARA2006] Narayan J, Bhosle V, Tiwari A, Gupta A, Kumar P, Wu R, J. Vac. Sci. Tech. A 24 (2006) 1948.

[NAVA2009] Navarro E, Velez M, Huttel Y, Junquera A. P, Martin J. I, Lema O. F. de, Cebollada A, Alameda J. M, Vicent J. L, J. Appl. Phys. 105, 033912 (2009).

[NEAL1994] Neal H.B, Theory of Magnetic Recording, Cambridge University Press, New York (1994).

[NEEL1954] Neel L, J. Phys. Rad. 15 (1954) 376.

[NEEL1962] Néel L, Comptes. Rendus Acad. Sci. 255 (1962) 1676.

[NIST2010] Nistor L.E, Rodmacq B, Auffret S, Schuhl A, Chshiev M, Dieny B, Phys.Rev. B 81 (2010) 220407.

[OEPE1990] Oepen H.P, Benning M, Ibach H, Schneider C.M, Kirschner J, J. Magn. Magn. Matt. 86 (1990) L137.

[OHAN1987] O'Handley R.C, J. Appl. Phys. 62 (1987) R15.

[OHAN2000] O'Handley R.C, Modern Magnetic Materials Principles and Applications, Wiley, New York (2000).

[OHRI1992] Ohring M, Materials Science of Thin Films, Academic Press, London (1992).

[OKUM2003] Okumura H, Twisselmann D. J, McMichael R. D, Huang M.-Q, Hsu Y. N, Laughlin D. E, McHenry M. E, J. Appl. Phys. 93 (2003) 6528.

[OKUM2004] Okumura H, Um C.-Y, Chu S.-Y, McHenry M. E, Laughlin D. E, Kos A. B, IEEE Trans. Magn. 40 (2004) 2700.

[OLIV1999] Oliveira A.J.A.de, Ortiz W.A, Mosca D.H, Mattoso N, Mazzaro I, Schreiner W.H, J. Phys.: Condens. Matter. 11 (1999) 47.

[OSGO1997] Osgood R. M, Clemens B. M, White R. L, Phys. Rev. B 55 (1997) 8990.

[PALU2006] Paluskar P.V, Kohlhepp J.T, Swagten H.J.M, Koopmans B, J. Appl. Phys. 99 (2006) 08E503.

[PAND2016] Pandey H, Perumal A, Wang J, Takahashi Y.K, Hono K, IEEE Trans Magn 52 (2016) 3201004.

[PARK1990] Parkin S.S.P, More N, Roche K.P, Phys. Rev. Lett. 64 (1990) 2305.

[PARK2011] Park J-Y, Kang S-K, Jeon M-H, Jhon M.S, Yeom G-Y, J. Electrochem. Soc. 158 (2011) H1.

[PELL2015] Pellegren J.P, Sokalski V. M, IEEE Trans. Magn. 51 (2015) 3400903.

[PERU2009] Perumal A, Takahashi Y.K, Hono K, J. Appl. Phys. 105 (2009) 07A304.

[PERU2010] Perumal A, Zhang L, Takahashi Y. K, Hono K, J. Appl. Phys. 108 (2010) 083907.

[PESC1987] Pescia D, Stampanoni M, Bona G.L, Vaterlaus A, Willis R.F, Meier F, Phys. Rev. Lett. 58 (1987) 2126.

[PIRA2007] Piramanayagam S.N, J. Appl. Phys. 102 (2007) 11301.

[PIRA2011] Piramanayagam S.N, Chong T.C, Developments in Data Storage: Materials Perspective, John Wiley & Sons, New Jersy (2011).

[PLAT2001] Platt C.L, Minor M.K, Klemmer T.J, IEEE Trans. Magn. 37 (2001) 2302.

[PONG2008] Pong P.W.T, Dennis C.L, Castillo A, J. Appl. Phys. 103 (2008) 07A902.

[PORR2002] Porrati F, Spatially Varying Magnetic Anisotropies in Ultrathin Films, Thesis (PhD) Martin-Luther-University (2002).

[PORT1998] Porthun S, Abelmann L, Lodder C, J. Magn. Magn. Magn. 182 (1998) 238.

[POST1997] Postava K, Jaffres H, Schuhl A, Van Dau F. N, Goiran M, Fert A. R, J. Magn. Magn. Mater. 172 (1997) 199.

[PRAD1997] L.M. Alvarez-Prado, G.T. Perez, R. Morales, F.H. Salas, J.M. Alameda, Phys. Rev. B 56 (1997) 3306.

[PRAD2004] Prado L.M.A, Alamedo J.M, Physica B 343 (2004) 241.

[PRUT1964] Prutton M, Thin Ferromagnetic Films, Butterworth Inc, University of California (1964).

[QIAO2016] Qiao X, Wang B, Tang Z, Shen Y, Yang H, Wang J, Zhan Q, Mao S, Xu X, Li R.-W, AIP Adv. 6 (2016) 56106.

[REIG2013] Reig C, Cardoso S, Mukhopadhyay S.C, Giant Magnetoresistance (GMR) Sensors: From Basis to State-of-the-Art Applications, Springer Science & Business Media, Berlin (2013).

[RUDE1954] Ruderman M.A, Kittel C, Phys. Rev. 96 (1954) 99.

[RUGA1998] Rugar D, Mamin H.J, Guethner P, Lambert S.E, Stern J.E, McFadyen I, Yogi T, J. App. Phys. 68 (1998) 11694.

[SAIT2002] Saitoh E, Matumoto H, Nakamura T, Miyajima H, J. Appl. Phys. 91 (2002) 7215.

[SAKU2013] Sakurai Y, Hamakawa Y, Shirae K, Masumoto T, Suzuki K, Current Topics in Amorphous Materials: Physics & Technology, North-Holland, Elsevier (2013).

[SATO1988] Sato T, Otake H, Miyazaki, T J. Magn. Magn. Mater. 71 (1988) 263.

[SATO2012] Sato H, Yamnouchi M, Ikeda S, Fukami S, Matsukura F, Ohno H, Appl. Phys. Lett. 101 (2012) 022414.

[SATO2014] Sato H, Enobio E.C.I, Yamanouchi M, Ikeda S, Fukami S, Kanai S, Matsukura F, Ohno H, Appl. Phys. Lett. 105 (2014) 62403.

[SATO2015] Sato K, Saitoh E, Spintronics for next generation innovative devices, Wiley Series in materials for electronic & optoelectronic applications, Willoughby A, Capper P, Kasap S (Edts). Wiley, UK (2015).

[SCHA2007] Schäfer R, Novel Techniques for Characterizing and Preparing Samples in Handbook of Magnetism and Advanced Magnetic Materials, ed. H. Kronmüller, Parkin S, Vol. 3, Wiley, Chichester (2007).

[SCHR2000] Schrag B.D, Anguelouch A, Ingvarsson S, Xiao G, Trouilloud Y.L.P.L, Gupta A, Wanner R.A, Gallagher W.J, Rice P.M, Parkin S.S.P, Appl. Phys. Lett. 77 (2000) 2373.

[SEME2004] Sementsov D. I, Shutyi A. M, Crystallography Reports 49 (2004) 1140.

[SERA2011] Serafinczuk J, Pietrucha J, Schroeder G, Gotszalk T.P, Optica Applicata XLI(2) (2011) 315.

[SESH2002] Seshan K, Handbook of Thin-film Deposition Processes and Techniques: Principles, Methods, Equipment, and Applications, Noyes publication, New York (2002).

[SHAH2010] Shah L.R, Fan X, Kou X, Wang W.G, Zhang Y.P, Lou J, Sun N.X, Xiao J.Q, J. Appl. Phys. 107 (2010) 09D909.

[SHAR2006] Sharma P, Kimura H, Inoue A, Arenholz E, Guo J.H, Phys. Rev. B 73 (2006) 052401.

[SHEN2018] Sheng P, Wang B, Li R, J. Semicond. 39 (2018) 011006.

[SHIZ1994] Shi Z-P, Levy P.M, Fry J.L, Phys. Rev. B 49 (1994) 15159.

[SING2012] Singh A.K, Kisan B, Mishra D, Perumal A, J. Appl. Phys. 111 (2012) 093915.

[SING2013] Singh A.K, Mallik S, Bedanta S, Perumal A, J. Phys. D: Appl. Phys. 46 (2013) 445005.

[SING2014] Singh A. K, Mallik S, Bedanta S, Perumal A, IEEE Trans. Magn. 50 (2014) 2000804.

[SING2015] Singh A.K, PhD Thesis, Indian Institute of Technology Guwahati, Guwahati, India (2015).

[SING20161] Singh A.K, Perumal A, J. Phys. D: Appl. Phys. 49 (2016) 085001.

[SING20162] Singh A.K, Hsu J.-H, Perumal A, J. Magn. Magn. Mater. 418 (2016) 21.

[SONG2000] Song D, Nowak J, Larson R, Kolbo P, Chellew R, IEEE Trans. Magn. 36 (2000) 2545.

[SPAL2011] Spaldin N.A, Magnetic Materials: Fundamental and Applications, New York: Cambridge University Press (2011).

[STIL2005] Stiles M.D, Interlayer Exchange Coupling in Ultrathin Magnetic Structures III: Fundamentals of Nanomagnetism ed. Bland J.A.C, Heinrich B, Springer, New York (2005).

[STOB2009] Stobiecki F, Urbaniak M, Szymański B, Kuświk P, Schmidt M, Aleksiejew J, Weis T, Engel D, Lengemann D, Ehresmann A, Kopcewicz M, Acta Phys. Polo. A 115 (2009) 345.

[SULI2015] Su L, Zhang Y, Klein J-O, Zhang Y, Bournel A, Fert A, Zhao W, Sci. Rep. 5 (2015) 14905.

[SUNJ2015] Sun J.Z, Phys. Rev. B 91 (2015) 174429.

[SUNZ2004] Sun Z.G.G, Kuramochi H, Mizuguchi M, Takano F, Semba Y, Akinaga H, Surf. Sci. 556 (2004) 33.

[SVOB2004] Svoboda J, Magnetic Technique for the Treatment of Materials, Kluwer Academic Publishers, Dordrecht (2004).

[TANA2002] Tanahashi K, Kikukawa A, Takahashi Y, Hosoe Y, Futamoto M, J. Magn. Magn. Mater. 242-245 (2002) 325.

[TANA20031] Tanahashi K, Kikukawa A, Hosoe Y, J. Appl. Phys. 93 (2003) 8161.

[TANA20032] Tanahashi K, Kikukawa A, Takahashi Y, Hosoe Y, J. Appl. Phys. 93 (2003) 6766.

[TANG2010] Tang D. D, and Lee Y.-J, Magnetic Memory: Fundamentals and Technology, Cambridge University Press, UK (2010).

[TANG2014] Tang Z, Wang B, Yang H, Xu X, Liu Y, Sun D, Xia L, Zhan Q, Chen B, Tang M, Zhou Y, Wang J, Li R-W, Appl. Phys. Lett. 105 (2014) 103504.

[TATE1998] Tate B.J, Parmer B.S, Todd I, Davies H.A, Gibbs M.R.J, Major R.V, J. Appl. Phys. 83 (1998) 6335.

[TEGE2001] Tegen S, Monch I, Schumann J, Vinzelberg H, Schneider C.M, J. Appl. Phys. 89 (2001) 8169.

[TEHR2000] Tehrani S, Engel B, Slaughter J.M, Chen E, DeHerrera M, Durlam M, Naji P, Whig R, Janesky J, Calder J, IEEE Trans. Magn. 36 (2000) 2752.

[TEIX2006] Teixeira J.M, Silva R.F.A, Ventura J, Pereira A.M, Carpinteiro F, Araújo J.P, Sousa J.B, Cardoso S, Ferreira R, Freitas P.P, Mater. Sci. Eng. B. 126 (2006) 180.

[THOM2000] Thomas L, Lüning J, Scholl A, Nolting F, Anders S, Stöhr J, Parkin S.S.P, Phys. Rev. Lett. 84 (2000) 3462.

[THOM2014] Thomas L, Jan G, Zhu J, Liu H, Lee Y-J, Le S, Tong R-Y, Pi K, Wang Y-J, Shen D, He R, Haq J, Teng J, Lam V, Huang K, Zhong T, Torng T, Wang P-K, J. Appl. Phys. 115 (2014) 172615.

[TORR2014] Torrejon J, Kim J, Sinha J, Mitani S, Hayashi M, Yamanouchi M, Ohno H, Nature Commun. 5 (2014) 4655.

[TSYM2016] Tsymbal E.Y, Zutic I, Handbook of Spin Transport and Magnetism, CRC Press, Tayler & Francis Group, Florida (2016).

[UHRM2008] Uhrmann T, Dimopoulos T, Brückl H, Lazarov V.K, Kohn A, Paschen U, Weyers S, Bär L, Rührig M, J. Appl. Phys. 103 (2008) 63709.

[URSE2005] Urse M, Moga A- E, Grigoras M, Chiriac H, J. Optoelect. Adv. Mater. 7 (2005) 759.

[VEMU2016] Vemulkar T, Mansell R, Fernández-Pacheco A, Cowburn R P, Adv. Funct. Mater. 26 (2016) 4704.

[VILL2010] Villard P, Ebels U, Houssameddine D, Katine J, Mauri D, Delaet B, Vincent P, Cyrille M.-C, Viala B, Michel J.-P, Prouvee J, Badets F, IEEE J. Solid-State Circuits 45 (2010) 214.

[WAGE1994] Wagendristel A, Wang Y, An Introduction to Physics and Technology of Thin Films, World Scientific, Singapore, (1994).

[WANG1999] Wang S.X, Hong J, IEEE Trans. Magn. 35 (1999) 782.

[WANG2014] Wang Y, Wei D, Gao K.-Z., Cao J, Wei F, J. Appl. Phys. 115 (2014) 053901.

[WANG2017] Wang X, Metallic Spintronic Devices, CRC Press, Florida (2017).

[WEHN1955] Wehner G.K, Advance in Electronics and Electron Physics, 7 (1955) 239.

[WEIS2013] Weisbuch C, Physics, Fabrication, and Applications of Multilayered Structures, Springer Science & Business Media, New York (2013).

[WEIV2000] Wei V.F, Wu D, Zheng D, Ma B, Yang Z, Mater. Sci. Engg. B 68 (2000) 156.

[WOLF2001] Wolf S.A, Awschalom D.D, Buhrman R.A, Daughton J.M, Von Molnar S, Roukes M.L, Chtchelkanova A.Y, Treger D.M, Science 294 (2001) 1488.

[WUAY2002] Wua Y, Li K, Qiu J, Guo Z, Han G, Appl. Phys. Lett. 80 (2002) 4413.

[WUDO2015] Wu D, Jin T, Lou Y, Wei F, Appl. Surf. Sci. 346 (2015) 567.

[WUHA2017] Wu H, Khdour M, Apsangi P, Yu H, IEEE Trans. Magn. 53 (2017) 2004507.

[YAMA2011] Yamanouchi M, Jander A, Dhagat P, Ikeda S, Matsukura F, Ohno H, IEEE Magn. Lett. 2 (2011) 3000304.

[YANG2013] Yang F.F, Yan S.S, Yu M.X, Kang S.S, Dai Y.Y, Chen Y.X, Pan S.B, Zhang J.L, Bai H.L, Zhu D.P, Qiao S.Z, Pan W.W, Liu G.L, Mei L.M, J. Alloys Compd. 558 (2013) 91.

[YILD20091] Yildiz F, Przybylski M, Kirschner J, J. Appl. Phys. 105 (2009) 07E129.

[YILD20092] Yildiz F, Przybylski M, Ma X.D, Kirschner J, Phys. Rev. B 80 (2009) 064415.

[YOSH1988] Yoshizawa Y, Oguma S, Yamauchi K, J. Appl. Phys. 64 (1988) 6044.

[YOSH1989] Yoshizawa Y, Oguma S, Hiraki A, Yamuchi K, Hitachi Metals Tech. Rev. 5 (1989) 13.

[YOSI1957] Yosida K, Phys. Rev. 106 (1957) 893.

[YOUC2008] You C.Y, Ohkubo T, Takahashi Y.K, Hono K, Journal of Applied Physics 104 (2008) 033517.

[YOUC2017] You C.-Y, Kim H, IEEE Trans. Magn. 53 (2017) 1400504.

[YUJU2002] Yu J, Chang C, Karns D, Ju G, Kubota Y, Eppler W, Bruker C, Weller D, J. Appl. Phys. 91 (2002) 8357.

[YUL2000] Yu L, Altman R.A, Marley A, Rishton S.A, Trouilloud P.L, Xiao G, Gallagher W.J, Parkin S.S.P, Appl. Phys. Lett. 70 (1997) 2610.

[ZABE2013] Zabel H, Farle M, Magnetic Nanostructures: Spin Dynamics and Spin transport, Springer-Verlag, Berlin (2013).

[ZHAN19961] Zhang J, White R.M, J. Appl. Phys. 79 (1996) 5113.

[ZHAN19962] Zhang J, White R.M, IEEE Trans. Magn. 32 (1996) 4630.

[ZHAN2015] Zhang X, Zhang Y, Cai J. W, J. Appl. Phys. 118 (2015) 143903.

[ZHAN2016] Zhang J, Siddiqui S.A, Ho P, Incorvia J.A.C-, Tryputen L, Lage E, Bono D.C, Baldo M.A, Ross C.A, New Journal of Physics 18 (2016) 053028.

[ZHAO2015] Zhao W, Prenat G, Spintronics-based computing, Springer International Publishing, Switzerland (2015).

[ZHOU2017] Zhou J, Zhao W, Peng S, Qiao J, Klein J.-O, Lin X, Zhang Y, Bournel A, IEEE Trans. Magn. 53 (2017) 1300504.

[ZHUY2012] Zhu Y, Zhang Z, Ma B, Jin Q.Y, J. Appl. Phys. 111 (2012) 07C106.

भारतीय प्रौद्योगिकी संस्थान गुवाहाटी
Indian Institute of Technology Guwahati

Publications

भारतीय प्रौद्योगिकी संस्थान गुवाहाटी
Indian Institute of Technology Guwahati

List of publications

In Journals

Sl.	Published / Under Review and Preparation
[1].	Magnetic properties of single-layer and multilayer structured $Co_{40}Fe_{40}B_{20}$ thin films **Camelia Das,** S. Mohapatra, G. A. Vitthal and Perumal Alagarsamy, *Thin Solid Films 616 (2016) 126.
[2].	Tuning the magnetic properties of stripe domain structured CoFeB films using stack structure with spacer layer thickness dependent interlayer coupling, **Camelia Das** and Perumal Alagarsamy, *Journal of Magnetism and Magnetic Materials 448 (2018) 23.
[3].	Thickness dependent surface topography, magnetic properties and magnetic domain structure of amorphous FeTaC thin films **Camelia Das**, J. Das, T. Vijayabhaskaran, S. Bedanta, A. Talapatra, J. R. Mohanty, Perumal Alagarsamy *Journal of Materials Sciences & Engineering 7 (2018) 100455.
[4].	Temperature dependent magnetization reversal and enhanced magnetic properties in FeTaC/SiO_2 multilayer thin films, **Camelia Das**, Jumal Das, T. Vijayabhaskaran, S. Bedanta, Perumal Alagarsamy, *Physical Review B (under submission).
[5].	Magnetic properties and Magnetic domain structures in single-layer amorphous Fe-Co-Zr-B-Cu thin films **Camelia Das** and Perumal Alagarsamy Manuscript under preparation.
[6].	Soft magnetic properties in multilayer amorphous Fe-Co-Zr-B-Cu / SiO_2 thin films **Camelia Das** and Perumal Alagarsamy Manuscript under preparation.

*Publications from thesis work

In Conferences / Seminars / Workshops:

[1].	Magnetic properties and magnetic domain structures in amorphous FeTaC thin film **Camelia Das**, Jumal Das and Perumal Alagarsamy

	Presented in Research Conclave 2018, An Amalgamation of Academia, Industry and Start-ups, 8 – 10 March, 2018, IIT Guwahati, Guwahati, India and **Received Best poster award**.
[2].	Thickness dependent study of FeTaC single layer film and understanding the role of SiO_2 spacer layer on FeTaC multilayer thin film through interlayer magnetic coupling, **Camelia Das**, Jumal Das and Perumal Alagarsamy, Presented in Condensed Matter Days (CMDAYS-2017), 29th – 31st August, Tezpur University, India.
[3].	Understanding of spacer layer thickness dependent interlayer coupling in FeTaC based multilayer thin films using vibrating sample magnetometer **Camelia Das**, Jumal Das and Perumal Alagarsamy, Presented in The International Conference on Sophisticated Instruments in Modern Research (ICSIMR-2017), 30th June – 1st July, 2017, IIT Guwahati, India.
[4].	Tuning the magnetic properties of stripe domain structured CoFeB films through interlayer magnetic exchange coupling **Camelia Das**, Jumal Das and Perumal Alagarsamy Presented in Research Conclave 2017, An Amalgamation of Academia, Industry and Start-ups, 16 – 19 March, 2017, IIT Guwahati, Guwahati, India.
[5].	Tuning the magnetic properties of stripe domain structured CoFeB films using stack structure with spacer layer thickness dependent interlayer coupling, **Camelia Das** and Perumal Alagarsamy, Presented in The International Conference on Magnetic Materials and Applications (ICMAGMA-2017), 1st -3rd February, 2017, Hyderabad, India.
[6].	Magnetic properties of single-layer and multilayer structured CoFeB thin films **Camelia Das,** Sambit Mohapatra, G.A. Vitthal and Perumal Alagarsamy, Presented in The International Conference on Magnetic Materials and Applications (ICMAGMA-2015), 2nd – 4th December, 2015, VIT University, Vellore, India and **Received Best poster Award**.

* * * * * * * * * *